ISSN: 0120-1425 • Diciembre de 2020

SERVICIO
GEOLÓGICO
COLOMBIANO

Boletín Geológico

47

revistas.sgc.gov.co

Boletín
Geológico

Boletín Geológico
Núm. 47, 2020
Periodicidad anual
ISSN impreso: 0120-1425
ISSN digital: 2711-1318
Servicio Geológico Colombiano

Oscar Paredes Zapata
Director general
Mario Andrés Cuéllar
Director de Geociencias Básicas
Marta Lucía Calvache Velasco
Directora de Geoamenazas
Gloria Prieto Rincón
Directora de Recursos Minerales
Hernán Olaya Dávila
Director de Asuntos Nucleares
Humberto Andrés Fuenzalida
Director de Hidrocarburos
Hernando Camargo
Director de Laboratorios
Jaime Alberto Garzón
Director de Gestión de Información

SERVICIO GEOLÓGICO COLOMBIANO
Diagonal 53 N.º 34-53
Bogotá, Colombia
Teléfono: 220 0200, ext.: 3048
boletingeologico@sgc.gov.co

Mario Maya
Editor
Boletín Geológico

CORRECCIÓN DE ESTILO EN ESPAÑOL
Édgar Ordóñez

CORRECCIÓN DE ESTILO EN INGLÉS
American Journal Experts

DISEÑO Y DIAGRAMACIÓN
Leonardo Cuéllar V.

DIBUJO GIS
Cristian Hernández

EDITORA GENERAL
Carolina Hernández O.

FOTO DE CUBIERTA
Bloques rocosos con meteorización esferoidal del Neis de Termales, Complejo Guaviare, vereda San Lucas, municipio de El Retorno, Guaviare, Colombia. Autora: Claudia Marcela Ríos.

INCLUIDA EN LOS SIGUIENTES ÍNDICES Y BASES DE DATOS:
Ulrich
REDIB
GeoRef
Periódica
Google Scholar

PÁGINA WEB:
https://revistas.sgc.gov.co/index.php/boletingeo

IMPRESIÓN
Imprenta Nacional de Colombia
Carrera 66 N.º 24-09
PBX: 457 8000
www.imprenta.gov.co
Bogotá, D. C., Colombia

Diciembre, 2020

Boletín Geológico

SERVICIO
GEOLÓGICO
COLOMBIANO

CONTENIDO

Boletín Geológico

SERVICIO GEOLÓGICO COLOMBIANO

EDITORIAL

Boletín Geológico presents issue number 47, the second issue published in 2020, with five articles on basin evolution, stratigraphy, economic geology, geothermochronology, and geoarchaeology.

Amaya et al. present a lithological, petrographic, geochemical, and geochronological characterization of the Guaviare Complex, a new unit defined in the Colombian Amazonian Craton, which is part of the Precambrian basement located in southeastern Colombia (Figure 1). This work is the result of the systematic geological mapping of the Servicio Geológico Colombiano carried out near San José del Guaviare. The Guaviare Complex is divided into three units according to their textural and compositional characteristics, which are termed the Termales Gneiss, Unilla Amphibolite, which present protoliths that were formed in the Mesoproterozoic at 1.3 Ga, and La Rompida Quartzite, with a maximum age of 1.28 Ga.

Martínez et al. describe the base of the Guadalupe Group in the Tunja area, Colombia (Figure 1). The base of the Guadalupe Group consists of cherts and porcellanites in the NW region of the study area (Alto del Gavil*á*n section) and mudstones, siltstones, quartz-arenites, and, to a lesser extent, porcellanites and cherts towards the SE (Vereda Salitre section). Paleontological analyses performed on the two stratigraphic sections measured in this study indicate that the base of the Guadalupe Group partly represents the Upper Santonian and mostly the Lower Campanian.

Castrillón and Guerrero describe the mineralogical and geochemical characterization of an association of rocks in the Cerro Matoso nickel laterite deposit, Montelíbano, Colombia, that could correspond to listvenite (Figure 1). This term is used principally by Russian geologists to describe the carbonate +/- sericite +/- pyrite alteration of mafic and ultramafic ophiolitic assemblages, which indicates the hydrothermal involvement of quartz +/- carbonate veins.

Cetina et al. review radiometric and thermobarometric techniques used to construct cooling curves or paths to characterize intrusive bodies and calculate cooling and exhumation rates. These cooling curves or paths in intrusive bodies are highly relevant when studying compressive or extensional areas because they partly represent the local thermal history, thereby providing data on the magmatic and tectonic evolution of a region.

Triana et al. present a detailed micromorphological and micromorphometric analysis of sediments collected in archaeological excavations conducted at the Tequendama and Aguazuque sites near Bogotá, Colombia (Figure 1). The analysis quantifies the contents of archaeological materials, such as bones and coal, as well as carbonates remains, which are associated with various activities. Based on paleoenvironmental interpretation, the presence of secondary carbonates indicates arid conditions in the Sabana de Bogot*á* region, which coincide with the regional climatic records.

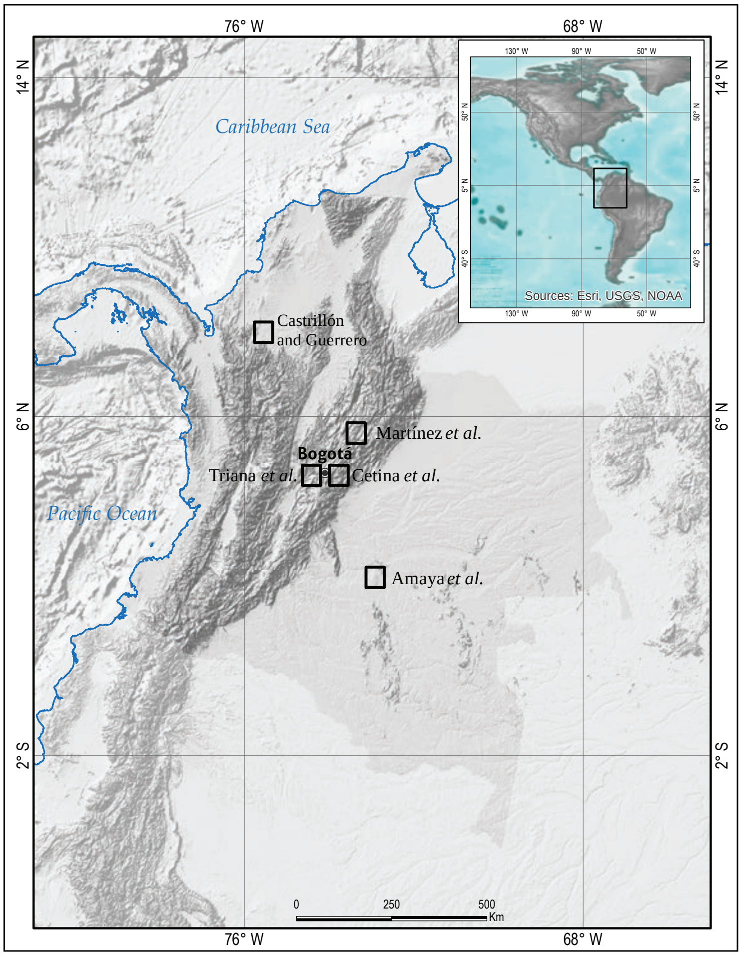

Figure 1. Location of the areas with contributions presented in this issue

Boletín Geológico acknowledges the collaboration of the reviewers and their commitment to the peer-review process involved in this issue. Thank you to Umberto Cordani (Universidade de Sao Paulo), Salomon Kroonenberg (Delft University of Technology), Silvina Claudia Carretero (Universidad Nacional de La Plata), Patricia Villamarín (Ecopetrol), María Marta Sampietro (Universidad Nacional de Tucumán), Luis Ignacio Quiroz (Ecopetrol), Laura Perucca (Universidad Nacional de San Juan), Julio Cezar Rubin (Universidade de Goias), Juan Rodríguez (Helmholtz Centre Potsdam), Jorge López (Logea), Germán Reyes (Consultant), César Valladares (University of Texas), Carlos Alberto Tello (Universidade Estadual Paulista), Basilios Tsikouras (Universiti Brunei Darussalam) and Airton Natael Coelho (Universidade Federal de Sao Carlos).

Mario Maya
Editor
mmaya@sgc.gov.co
boletingeologico@sgc.gov.co

Boletín Geológico

Boletín Geológico, 47, 5-34, 2020
https://doi.org/10.32685/0120-1425/boletingeo.47.2020.502

Received: May 17, 2020
Revised: July 9, 2020
Accepted: August 20, 2020

The Guaviare Complex: new evidence of Mesoproterozoic (ca. 1.3 Ga) crust in the Colombian Amazonian Craton

El Complejo Guaviare: nueva evidencia de corteza continental del Mesoproterozoico (ca. 1,3 Ga) en el Cratón Amazónico colombiano

Carolina **Amaya López**[1], Jorge Julián **Restrepo Álvarez**[1], Marion **Weber Scharff**[2], Federico Alberto **Cuadros Jiménez**[3], Nilson **Francisquini Botelho**[3], Mauricio **Ibáñez Mejía**[4], Mario **Maya Sánchez**[5], Orlando Manuel **Pérez Parra**[6], Carlos **Ramírez Cárdenas**[7]

1 Universidad Nacional de Colombia, Medellín, Colombia
2 Departamento de Geociencias y Medio Ambiente, Universidad Nacional de Colombia, Medellín, Colombia
3 Institute of Geosciences, Universidade de Brasília, Brazil
4 Department of Earth and Environmental Sciences, University of Rochester, New York, USA
5 Servicio Geológico Colombiano, Bogotá, Colombia
6 Université Grenoble-Alpes, France
7 Faculty of Earth Sciences, Universitat de Barcelona – UB, Spain
Corresponding author: Carolina Amaya, caro.geologia@gmail.com

ABSTRACT

The Guaviare Complex is a new unit defined in the Colombian Amazonian Craton, which is part of the Precambrian basement located in southeastern Colombia. It is divided into three units according to their textural and compositional characteristics, termed Termales Gneiss, Unilla Amphibolite, and La Rompida Quartzite.

Termales Gneiss rocks are petrographically classified as gneisses and quartz-feldspar granofels, with the local formation of blastomylonite-like dynamic rocks. The Unilla Amphibolite consists of only amphibolites, and La Rompida Quartzite consists of muscovite quartzites, quartz-feldspar granofels, and quartz-muscovite schists.

The protoliths of Termales Gneiss and Unilla Amphibolite were formed in the Mesoproterozoic at 1.3 Ga due to bimodal magmatism (felsic and mafic) derived from mantle material, with some crust contamination that was probably related to the formation of extensional arcs associated with trans-arc basins in the NW section of the Amazon Craton. La Rompida Quartzite rocks originated from sediments derived from granite rocks and from other, older areas of the craton. These rocks have a maximum age of 1.28 Ga.

The low-to-medium grade metamorphism that affected these units occurred from 1.28 to 0.6 Ga, most likely concurrently with the Putumayo orogeny of approximately 1.0 Ga, although it may have been an independent event.

Keywords: Metamorphic Complex, Amazonian Craton, Proterozoic, Orogeny, geochemistry, geochronology.

Citation: Amaya López, C., Restrepo Álvarez, J. J., Weber Scharff, M., Cuadros Jiménez, F. A., Botelho, N. F., Ibáñez Mejía, M., Maya Sánchez, M., Pérez Parra, O. M., & Ramírez Cárdenas, C. (2020). The Guaviare Complex: new evidence of Mesoproterozoic (ca. 1.3 Ga) crust in the Colombian Amazonian Craton. *Boletín Geológico, 47*, 5-34, https://doi.org/10.32685/0120-1425/boletingeo.47.2020.502

RESUMEN
El Complejo Guaviare es una unidad nueva definida en el Cratón Amazónico colombiano, que hace parte del basamento precámbrico situado en el suroriente del territorio colombiano. Está dividido en tres unidades, según sus características texturales y composicionales, denominadas Neis de Termales, Anfibolita de Unilla y Cuarcita de La Rompida.

Las rocas del Neis de Termales se clasifican petrográficamente como neises y granofelsas cuarzo-feldespáticas, localmente con formación de rocas dinámicas tipo blastomilonitas. La Anfibolita de Unilla está representada únicamente por anfibolitas, y la Cuarcita de La Rompida, por cuarcitas moscovíticas, granofelsas cuarzo-feldespáticas y esquistos cuarzo-moscovíticos.

Los protolitos del Neis de Termales y la Anfibolita de Unilla se formaron en el Mesoproterozoico, hace 1,3 Ga, por un magmatismo bimodal (félsico y máfico) derivado de material mantélico con alguna contaminación cortical, probablemente relacionado con la formación de arcos extensionales asociados a cuencas trasarco en la parte NW del Cratón Amazónico. Las rocas de la Cuarcita de La Rompida se originaron a partir de sedimentos derivados de las rocas graníticas y de otras áreas más antiguas del cratón. Estas rocas tienen una edad máxima de 1,28 Ga.

El metamorfismo de bajo a medio grado que afectó estas unidades tuvo lugar entre 1,28 Ga y 0,6 Ga, y es probable que ocurriera al mismo tiempo que la Orógeno Putumayo, alrededor de 1,0 Ga, aunque no se puede descartar que sea un evento independiente.

Palabras clave: Complejo Metamórfico, Cratón Amazónico, Proterozoico, Orogenia, Geoquímica, Geocronología.

1. INTRODUCTION

In the department of Guaviare, Colombia, in an area between the Mitú Complex (López et al., 2007; Rodríguez et al., 2011a, 2011b) and the Garzón Complex (Rodríguez et al., 2003), metamorphic rocks have been identified, consisting of quartz-feldspar gneisses, amphibolites, quartzites, and granofels. By their compositional and textural characteristics, they are grouped into three lithological units, termed here Termales Gneiss, Unilla Amphibolite, and La Rompida Quartzite.

These rocks were first studied by Buchely et al. (2015) in Plate 371, Puerto Cachicamo, located west of Plate 372. They performed a macroscopic and microscopic description of rocks with gneissic structure. Despite their distance from the Garzón Massif, these rocks were termed the Garzón Complex.

In this study, petrographic characterization, geochemical analysis of major and trace elements, and uranium–lead (U-Pb) zircon geochronology was performed for each of the lithological units that make up the Guaviare Complex. The findings enable to understand the formation environment and petrogenesis of the complex with an eye towards defining a new metamorphic unit.

2. METHOD

2.1 Field geology and petrography

The field study was conducted in the Amazon region between the municipalities of San José del Guaviare and Calamar, in the department of Guaviare, during the geological mapping project of Plate 372 – El Retorno, conducted by Serviminas S. A. S. from 2017 to 2019 for the Servicio Geológico Colombiano – SGC. The geological survey was performed on topographic maps of the Instituto Geográfico Agustín Codazzi (Geographic Institute Agustín Codazzi) at a 1:25,000 scale following the parameters for field data collection proposed by Caicedo (2003) and updated by Serviminas S. A. S. (Maya et al., 2019). In total, at 40 field stations, 47 rock samples of gneiss, granofels, amphibolite, quartzite, schist, and blastomylonite were collected in the Guaviare Complex. 42 thin sections were prepared and analyzed by transmission light microscopy at 300 points for each sample. The minerals, textures, paragenesis, protoliths, metamorphic facies, and type and degree of metamorphism were described based on Heinrich (1965), Winkler (1976), Bowie and Simpson (1977), Winter (2001), and Schmid et al. (2007).

2.2 Geochemistry

Geochemical analyses of major and trace elements, including rare-earth elements, were performed by X-ray fluorescence (XRF) and inductively coupled plasma mass spectrometry

(ICP-MS) at ALS Global Ltd., according to the internal code specifications of the laboratory (ME-XRF26 and ME-MS81). The samples were crushed and pulverized, and the fraction smaller than 200 mesh was collected. The analyses were performed following laboratory standards, including sample fusion with $LiBO_2$ and acid digestion for ICP-MS.

2.3 Total rock analysis

Isotopic analyses of Sm, Nd, and Sr were performed at the Geochronology and Isotopic Geochemistry Laboratory of the Universidad de Brasilia. The analytical procedures applied in this study to determine the $^{147}Sm/^{144}Nd$, and $^{143}Nd/^{144}Nd$ isotopic ratios were described by Gioia and Pimentel (2000). ^{149}Sm and ^{150}Nd spike solutions were added to the crushed and pulverized rock samples. Sm and Nd were separated using cation exchange columns. Then, two drops of 0.025N H_3PO_4 were added to the resulting fractions for subsequent evaporation. The residue was dissolved in 1 µl of 5% HNO_3 distillate and mounted on a double-rhenium filament inside a Finnigan MAT 262 mass spectrometer with seven collectors in static mode. The uncertainties of the $^{147}Sm/^{144}Nd$ and $^{143}Nd/^{144}Nd$ isotopic ratios were lower than 0.2% and 0.0029% (2σ), respectively, based on the analysis of the international standard BHVO-2. The $^{143}Nd/^{144}Nd$ ratio was normalized using the ratio $^{146}Nd/^{144}Nd = 0.7219$ and the decay constant 6.54×10^{-12} a^{-1} (Lugmair and Marti, 1978).

The procedures followed for the Sr isotopic analyses were as described by Gioia et al. (1999). The samples were pulverized and subjected to acid attack under different solutions of HF, HNO_3, and HCl, with subsequent separation in cation exchange columns. Then, fractions containing Sr were deposited together with 1 µl of H_3PO_4 in a tantalum filament in the mass spectrometer described above. Based on the analysis of the international standard NBS-987, the uncertainties assessed for the $^{87}Sr/^{86}Sr$ ratio were lower than 0.0078% (2σ). The $^{87}Rb/^{86}Sr$ ratio was calculated based on the concentrations of Rb and Sr determined by ICP-MS in the samples (annex 1), according to the procedure indicated by Faure and Mensing (2005).

2.4 LA-ICP-MS U-Pb zircon geochronology

The samples were initially prepared at the Universidad EAFIT, where zircon crystals were separated and then subjected to standard ore crushing, sieving, and concentration methods. Later, at the University of Rochester, several crystals of each sample were mounted in epoxy resin and polished to expose an internal face on which textural and isotopic analyses would be performed. Cathodoluminescence images, acquired to reveal the internal structure of the zircons and to guide the geochronological analyses, were recorded under a Jeol 7100FT scanning electron microscope with a field emission source and a Deben panchromatic cathodoluminescence detector at the Mackay Microbeam Laboratory, University of Nevada, Reno.

The U-Pb isotopic analyses were conducted at the University of Rochester using an Agilent 7900 ICP-MS coupled to a Photon Machine Analyte G2 laser ablation system, which features a HelEx2 quick-purge tunable two-volume LA-ICP-MS cell system and generates pulses lasting approximately 8 ns using an excited ArF dimer. During the analyses, the laser was operated at a 7-Hz repetition rate and at a spot diameter of 30 µm, generating a constant energy density of approximately 7 J/cm² on the surface of the analyzed crystals. The ablations were conducted in an ultra-high-purity helium atmosphere, which was the gas used to transport the ablation aerosol to the ICP-MS. Each analysis consisted of 15 seconds of measurement of the "analytical blank" with the laser off, immediately followed by a 20-second measurement of the isotopic composition of the crystals with the laser on. ^{202}Hg, $^{204}(Pb+Hg)$, ^{206}Pb, ^{207}Pb, ^{208}Pb, ^{232}Th, and ^{238}U isotopes were measured in the mass spectrometer, and instrumental bias was corrected using the standard-sample bracketing method and using fragments of a zircon from Sri Lanka (SL2) with a known age of 563.6 ± 3.2 Ma, assessed following the reference manual Isotope Dilution - Thermal Ionization Mass Spectrometry, (Gehrels et al., 2008).

U-Pb data were processed using the procedures and algorithms described by Pullen et al. (2018) to make the necessary linearity corrections of the detection system. In addition to the primary reference material and to zircons from the Guaviare Complex, during our analytical session, several zircon fragments from Plešovice and FC-1 (Duluth gabbro, Minnesota, USA) were also analyzed to evaluate the precision, accuracy, and reproducibility of the method. These secondary materials yielded weighted mean ages of $^{206}Pb/^{238}U = 335.0 \pm 1.2/3.9$ (2σ, n = 21, mean squared weighted deviation (MSWD) = 0.8) for Plešovice and $^{207}Pb/^{206}Pb = 1098 \pm 8/11$ (2σ, n = 23, MSWD = 0.3) for FC-1, where the first level of uncertainty reported represents only internal analytical uncertainties, and the second level of uncertainty includes the propagation of systematic and standardization-related sources of uncertainty. After including systematic uncertainties, the values from our analytical session were indistinguishable from the reference ages of 337.13 ± 0.37 Ma for Plešovice (Sláma et al., 2008) and of 1099.96 ±

0.58 Ma for FC-1 (Ibáñez Mejía and Tissot, 2019), assessed following the Chemical Abrasion - Isotope Dilution - Thermal Ionization Mass Spectrometry reference, which confirms that the geochronological results reported in this study are accurate and that the analytical uncertainties have been correctly assigned.

3. GEOLOGICAL FRAMEWORK

The Guaviare Complex is the lithodemic unit that forms the crystalline basement of southeastern Colombia and groups the regional metamorphic rocks of the Mesoproterozoic described in Plate 372 – El Retorno (Maya et al., 2018) and Plate 371 – Puerto Cachicamo (Buchely et al., 2015). In southeastern Colombia, two main units of Precambrian metamorphic rocks have been regionally defined, the Mitú Migmatite Complex (Galvis et al., 1979; Rodríguez et al., 2011a) or Mitú Complex (López et al., 2007) in the NW section of the Amazonian Craton (or Guiana Shield) and the Garzón Complex in the Andes mountain range (Rodríguez et al., 2003; Cordani et al., 2005; Ibáñez Mejia et al., 2011, 2015).

In the Mitú Complex, the initial Rb-Sr and K-Ar radiometric dates were reanalyzed by Cordani et al. (2016) and complemented with new, more robust zircon U-Pb dating, which identified two belts of different ages: the Atabapo Belt to the north, with ages from 1800 to 1740 Ma, and the Vaupés Belt to the south, with granitoids of 1580 to 1520 Ma. The metamorphic rocks of Araracuara have ages similar to those of the Vaupés Belt. In this area, K-Ar dating has recorded an intraplate heating event dated from 1200 to 1300 Ma, termed the *Nickerian event*. Based on the nomenclature developed by Cordani et al. (1979) and by Tassinari and Macambira (1999), by age and position, the rocks of the Mitú Complex are part of the Rio Negro-Juruena province. With these new dating results, the concept of a Mitú Complex or Mitú Migmatitic Complex becomes obsolete and should no longer be used (see also Ibáñez Mejía and Cordani, 2020).

In studies of the Garzón Massif, the Macarena mountain range, and the basement of the Putumayo basin, Ibáñez Mejía et al. (2011, 2015, 2018) have reported ages that show that this area was formed between 1300 and 990 Ma. Thus, a juvenile intraoceanic magmatic arc developed from 1300 to 1200 Ma, followed by two metamorphic events: a migmatization event in amphibolite facies, which occurred between approximately 1050 and 1010 Ma, and another event in granulite facies, which occurred approximately 990 Ma. Although this area is chronologically similar to the Amazonian province of Sunsás, its origin and location are very different. For this reason, the aforementioned authors consider that this area is a new province of the Amazonian Craton, which they term *Putumayo Orogen*.

The Guaviare Complex is located in an intermediate area between the outcrops of the Atabapo and Vaupés Belts to the east and the Garzón Complex to the west (Figure 1 a, b). Therefore, it may be correlated with some of these units. Buchely et al. (2015) considered that the gneissic metamorphic rocks exposed in Plate 371 - Puerto Cachicamo are part of the Garzón Complex, but they did not perform radiometric dating.

4. RESULTS

4.1 Lithology

In the Guaviare Complex, the most common lithologies are quartz-feldspar gneisses and quartzites, with local amphibolites and granofels. These rocks compose three lithological units that crop out in an elongated belt of approximately 32 km in length in a north–south direction and that stand out from the Phanerozoic sedimentary cover (Figure 2).

The Termales Gneiss encompasses gneisses and quartz-feldspar granofels. The gneisses have homogeneous foliation, ranging from slight to well marked (Figure 3 a, b), without defining a tectonic layer and with medium to very coarse grain size. They consist of feldspar, quartz, biotite, and, in small amounts, amphibole. The granofels are similar in composition to the gneisses and are found in the form of lenses with sharp contacts and a metric character. They are characterized by the absence of schistosity. Their grain size is medium, and they consist of feldspars and quartz. These rocks are associated with veins and medium-grain quartz lenses, fractured and stained by iron oxides.

The amphibolites are dark gray with medium grain size (Figure 3 c, d). They are homogeneous and slightly foliated, consisting of dark areas of amphibole and light areas of plagioclase. The quartzites are recognized for their fine to medium grain size. When somewhat weathered, they are very similar to sandstone, with a color ranging from gray to white. Some are granoblastic, and others exhibit a slight lepidoblastic schistosity. They are composed of quartz, feldspars, and muscovite, with certain levels of iron oxides. These rocks are traversed by quartz veins (Figure 3 e, f) and by a syenogranite dike.

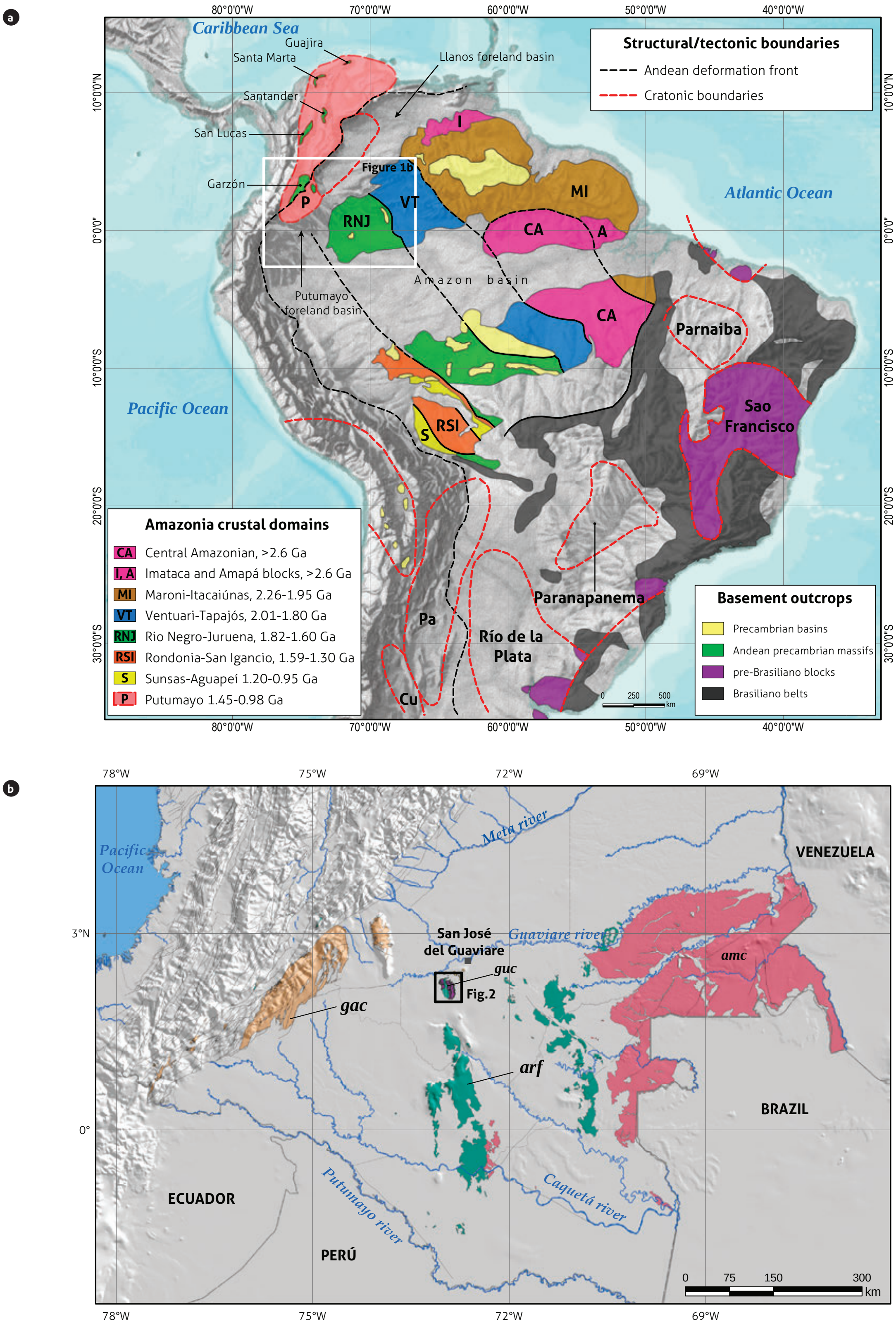

Figure 1. a) Location map of the Guaviare Complex in northwestern South America; b) Location map of the Guaviare Complex and metamorphic rocks located in southeastern Colombia
guc: Guaviare Complex; gac: Garzón Complex; amc: exposed Amazonian Craton (Atabapo and Vaupés belts); arf: Araracuara Formation. Source: Modified from Ibáñez Mejía and Cordani (2020)

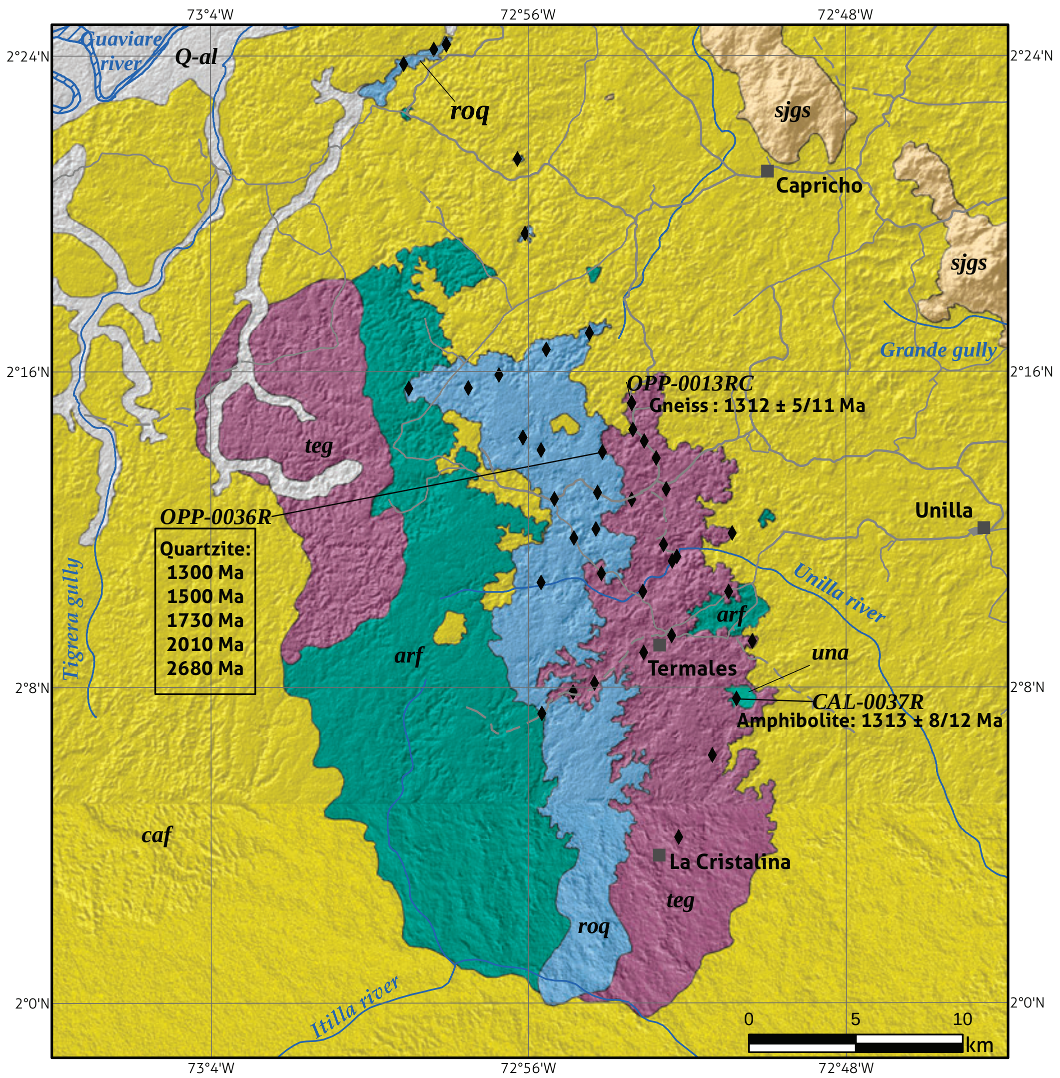

Figure 2. Distribution of lithological units of the Guaviare Complex
teg: Termales Gneiss; una: Unilla Amphibolite; roq: La Rompida Quartzite; sjgs: San José del Guaviare Syenite; arf: Araracuara Formation; caf: Caja Formation; Q-al: alluvial deposits; ♦ black diamond: rock sample. Source: Modified from Maya et al. (2018)

In the Guaviare Complex, foliation is more evident in the Termales Gneiss and in the Unilla Amphibolite than in La Rompida Quartzite. In gneisses and in amphibolite, foliation ranges from N10° to 46°E, with dips ranging from 45° to 80° to the SE. The granofels contain a slight foliation of a N–S tendency with a dip to the W, in contrast to the main trend of the gneisses. In the quartzites, the N5°-to-50°E foliation with dips to the SE matches the main arrangement of the gneisses, but the dips tend to be less angled, with values ranging from 5° to 48°. A second trend, N20°-30°W, has dips to the SW and NE and could suggest a slight folding in the quartzites.

Contact between the different lithologies of the Guaviare Complex could not be established in the field due to the scarcity of outcrops. Sharp contact could only be observed between the gneisses and the granofels of Termales Gneiss. The contact between the quartzites and the gneisses could be considered discordant because the latter was a source of the sediments of the quartzite protoliths. The Araracuara Formation is located between the two metamorphic belts of the Guaviare Complex. No contact between the two units was observed in the field, but the Paleozoic sedimentary rocks likely overlay the Mesoproterozoic basement rocks (nonconformity).

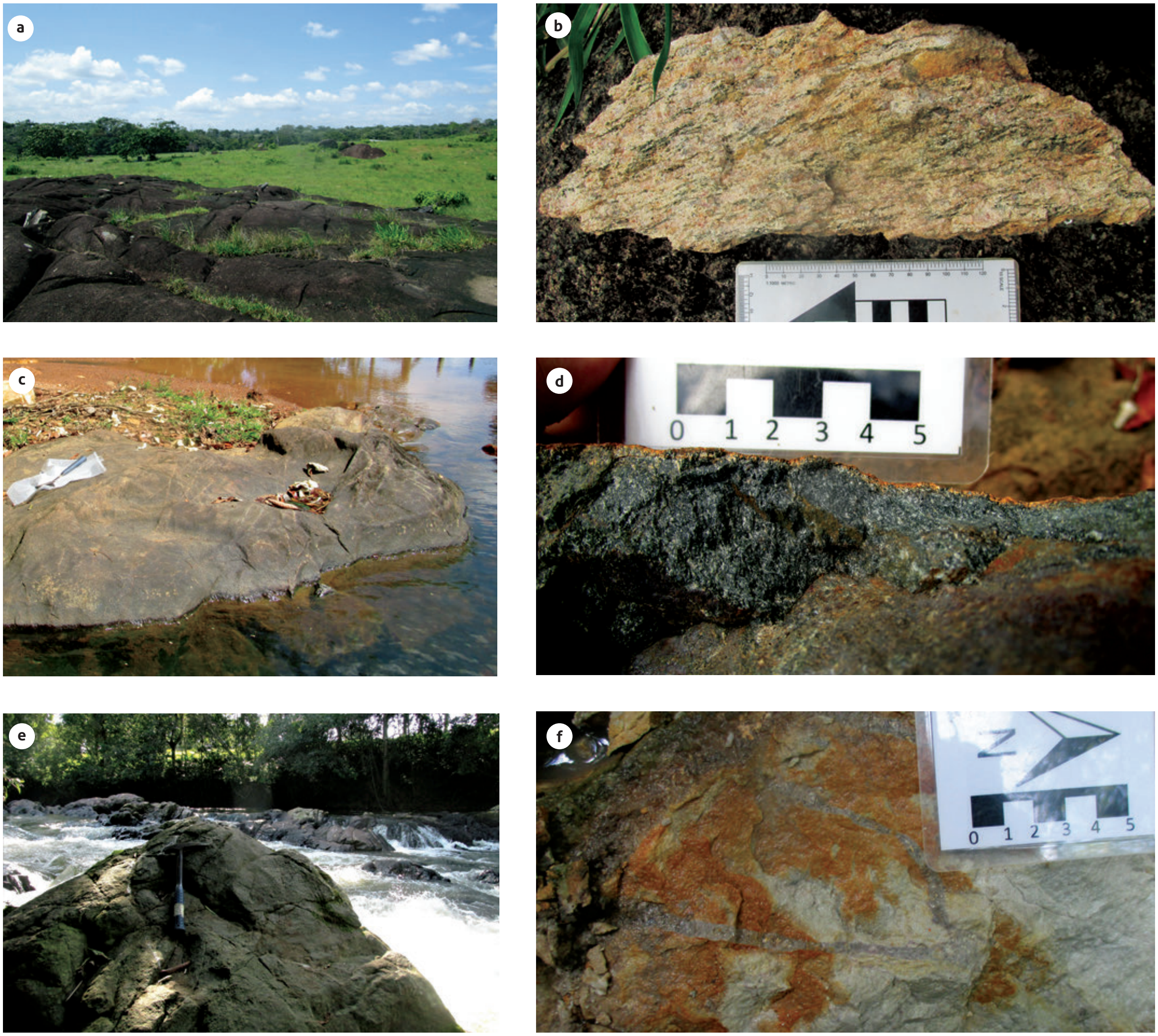

Figure 3. Texture and lithology of the rocks of the Guaviare Complex in macrosamples
a and b) Quartz-feldspar gneiss. c and d) Medium-grain amphibolite. e and f) Quartzite; note the quartz veins

4.2 Petrography

4.2.1 Termales Gneiss

The Termales Gneiss comprises biotite-quartz-feldspar gneiss with ± hornblende/hastingsite ± epidote ± muscovite ± chlorite, and feldspar and quartz granofels. The mineralogical composition of the progradation consists of microcline, plagioclase, quartz, biotite, hornblende, or hastingsite and, as minor constituents, epidote, zoisite, and clinozoisite (Annex 2). The accessory minerals are titanite, calcite, zircon, apatite, and ilmenite. The muscovite found in gneisses is considered retrograde. Common alterations include mild biotite chloritization and feldspar sericitization.

The gneisses show spaced, discontinuous, parallel and subparallel foliation, defined by micaceous minerals (Figure 4a) and, to a lesser extent, by amphiboles. This foliation is separated by bands of quartz-feldspar composition with a polygonal

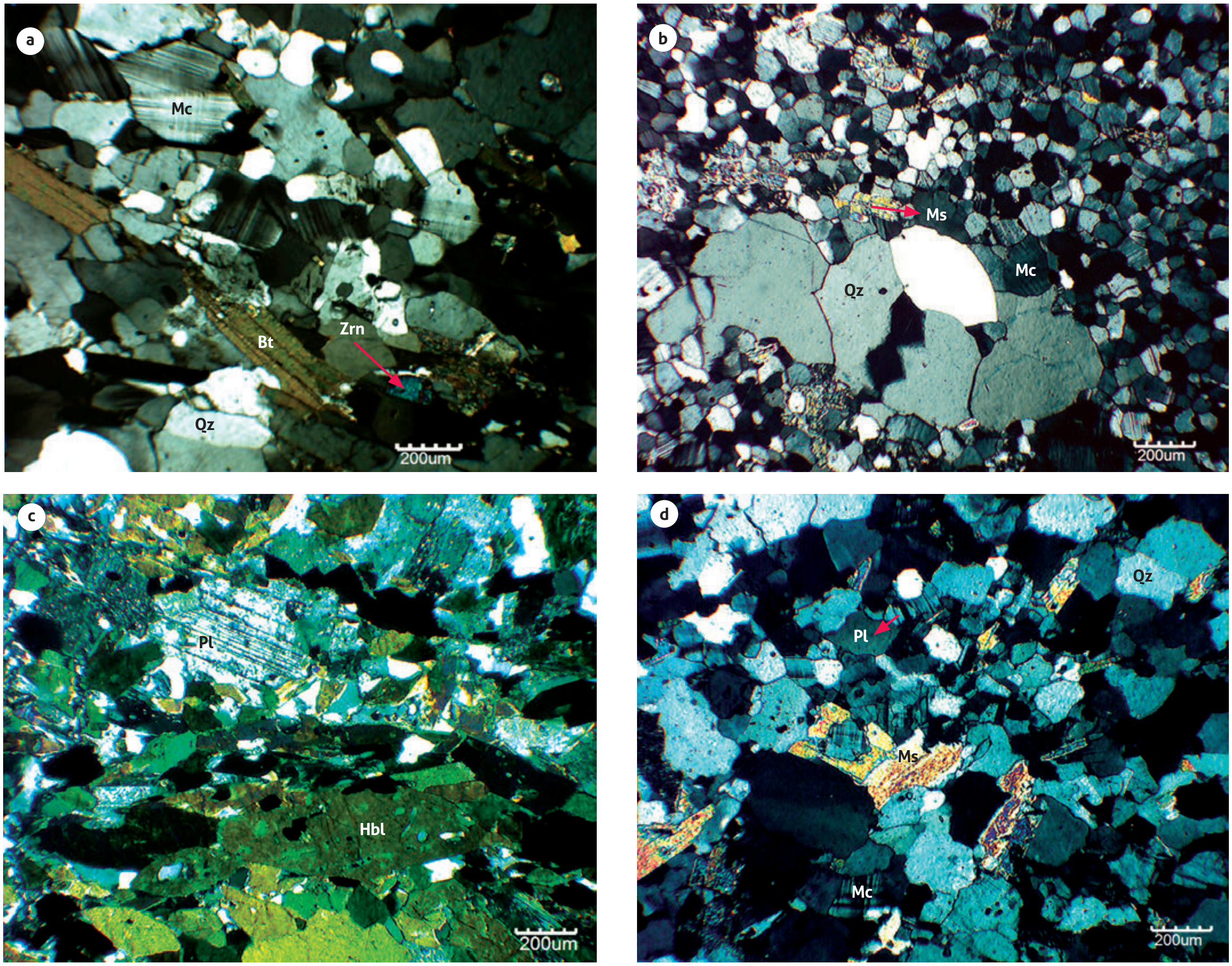

Figure 4. Mineralogy and texture of the rocks of the Guaviare Complex in thin sections
a) Orientation of the biotite (Bt) in the Termales Gneiss. b) Quartz (Qz) augen recrystallized in blastomylonite. c) Foliation defined by the orientation of the hornblende (Hbl) in the Unilla Amphibolite. d) Quartz (Qz), microcline (Mc) and plagioclase (Pl) forming a granoblastic texture in La Rompida Quartzite. Other abbreviations: Zrn: zircon; Ms: muscovite.

granoblastic texture. Some gneisses are characterized by the presence of quartz, plagioclase, and microcline megacrystals, which were defined as porphyroclasts derived (relict) from the original rock. In the granofels, the quartz and the plagioclase form granoblastic mosaics and exhibit deformation twins. Locally, the Termales Gneiss was affected by dynamic metamorphism, which formed blastomylonites (Figure 4b) characterized by quartz + plagioclase + microcline + garnet augen, bent twins in plagioclase, sutured edges in quartz, and embayment and skeletal texture in muscovite.

The microcline and plagioclase crystals range from subidioblastic to xenoblastic, tabular, with poikiloblastic texture (epidote, biotite, quartz and zircon inclusions), and the elongation of the crystals matches the preferential orientation of the rock. The microcline exhibits lattice twinning, whereas the plagioclase presents albite twinning, with a composition ranging from albite to oligoclase as determined using the Michel-Levy method. In the porphyroclastic gneisses, the quartz, plagioclase, and microcline crystals are characterized by their grain size variation, some reaching 7 mm in diameter. They are internally recrystallized and surrounded by quartz crystals, feldspars, and smaller micas and have a polygonal granoblastic texture.

The quartz is xenoblastic, with undulatory extinction and grain size variation. The biotite occurs as laminar, subidioblastic crystals, which define its foliation, and it shows strong pleochroism with X (α): very pale yellowish brown; and Y (β) = Z (γ): dark brownish green. The muscovite ranges from laminar subidioblastic to xenoblastic; some of it follows the preferential orientation of the rock, whereas other parts are disordered and replace biotite and feldspar crystals, suggesting retrograde metamorphic conditions.

The hornblende is the most common amphibole in most samples and defines nematoblastic foliation. The crystals are subidioblastic, columnar, with strong pleochroism with X (α): greenish yellow; Z (γ): bluish green; and Y (β): brownish greenish yellow. The hornblende is associated with biotite, zoisite, and titanite. Only in one sample (CMR-0041R) was the amphibole of the hastingsite type and occurred in subidioblastic to idioblastic, columnar crystals, with strong pleochroism with X (α): light yellow; (β): bluish green; and Z (γ): emerald green and quartz and zircon inclusions. This sample was characterized by high plagioclase content, low quartz content, and almost no potassium feldspar or biotite (Annex 2).

Accessory minerals such as titanite are usually found in granular agglomerations around ilmenite, whereas zircon occurs in very well-formed, prismatic, idioblastic crystals.

The mineral paragenesis of the Termales Gneiss is quartz + microcline + plagioclase (oligoclase or albite) + biotite ± amphibole (hornblende or hastingsite). The protolith of these rocks is igneous plutonic quartz-feldspar, which underwent medium to high regional metamorphism into amphibolite facies with a locally overlayed dynamic metamorphism. Muscovite replacement in feldspars and in biotite indicates retrograde metamorphic conditions.

4.2.2 Unilla Amphibolite

The Unilla Amphibolite shows spaced, coarse, and anastomosed schistosity, defined by a hornblende orientation (Figure 4c). Mineralogically, it consists of plagioclase, hornblende, quartz, biotite, retrograde chlorite, and (retrograde?) epidote and zoisite (Annex 2). The accessory minerals are apatite, titanite, and opaque (ilmenite/magnetite). Moderate plagioclase saussuritization, which makes it difficult to identify the composition, biotite chloritization, and possibly epidote and zoisite formations stand out among the alteration processes.

The plagioclase is found in tabular, subidioblastic to xenoblastic crystals with albite twinning. The quartz is xenoblastic with undulatory extinction and apatite microinclusions. The hornblende crystals range from subidioblastic to idioblastic and are columnar and orientated, with simple twinning, quartz inclusions, and strong pleochroism: X (α): yellowish green; (β): olive green; and Z (γ): bluish green. The biotite is arranged in subidioblastic, laminar crystals with moderate pleochroism: X (α): greenish yellow; (β) = Z (γ): reddish brown. Sometimes the biotite is replaced by xenoblastic to subidioblastic, laminar, oriented, and eventually flexed chlorite. The epidote is related to hornblende and chlorite domains. Among the accessory minerals, titanite is associated with oxides (ilmenite) and with amphibole and chlorite domains; opaque minerals follow foliation.

The mineral paragenesis of the Unilla Amphibolite is hornblende + plagioclase + quartz + biotite. The rock protolith is mafic igneous and was affected by medium to high regional metamorphism (?) in amphibolite facies. Chlorite replacement in biotite indicates retrograde metamorphic conditions. Although the nature of the epidote and zoisite could not be clearly established, if it were retrograde, the rock could have reached the top of the amphibolite facies.

4.2.3 La Rompida Quartzite

These rocks are petrographically classified as muscovite quartzites, quartz, feldspar, and muscovite granofels and quartz and muscovite schist. They have polygonal granoblastic texture (Figure 4d) with sutured edges and embayment between crystals. Sometimes, they show textural variation with parallel to subparallel, discontinuous, anastomosed schistosity defined by muscovite. Mineralogically, they consist of quartz, plagioclase, microcline, muscovite, and chlorite. The accessory minerals include tourmaline, zircon, titanite, apatite, epidote, and opaque minerals. The feldspars are usually altered to sericite, with an intensity ranging from mild to high.

The quartz is arranged as xenoblastic crystals with undulatory extinction, in polygonal granoblastic mosaics, which vary to a granoblastic texture with sutured edges and concave–convex contacts. The feldspars are tabular, ranging from subidioblastic to xenoblastic, with lattice twinning in the microcline and albite twinning in the plagioclase of albite composition, as determined using the Michel-Levy method. The muscovite is prograde, ranging from subidioblastic to xenoblastic; laminar; sometimes disordered, with irregular edges; and usually present in decussate agglomerations. In schist quartzites, the muscovite suggests a folded foliation, which would indicate that the rock is polyphasic. Chlorite is found as subhedral crystals present in alteration zones, interspersed with muscovite, possibly of retrograde origin.

The mineral paragenesis of La Rompida Quartzite is quartz + muscovite ± plagioclase (albite) ± microcline. The compositional and textural characteristics of the rocks suggest sandy sedimentary protoliths of quartzarenites and arkoses with some clay material, which underwent low to medium regional metamorphism in green schist or low-amphibolite facies. Stable muscovite in the presence of quartz indicates that the rock did not reach the top of the amphibolite facies.

4.3 Geochemistry

In the Guaviare Complex, twelve metamorphic rock samples with igneous protoliths were analyzed to determine the major, minor, and trace elements (Annex 1). Eleven of them belong to the Termales Gneiss and one to the Unilla Amphibolite.

The metamorphic rocks of the Termales Gneiss were formed from felsic protoliths, which are mostly classified as granitoids, in addition to a syenite, according to the TAS classification (Cox et al., 1979). The protolith of the Unilla Amphibolite is classified as part of the gabbro field (Figure 5).

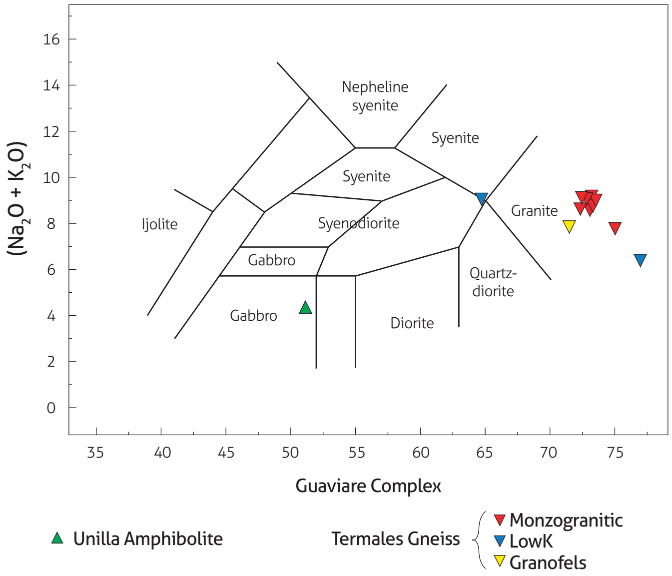

Figure 5. TAS Diagram (Cox et al., 1979) of the protoliths of rocks from the Guaviare Complex

The rocks of the Termales Gneiss generally have a high SiO_2 content (from 64.59% to 77.62%) and are impoverished in Fe_2O_3 (from 2.65% to 3.75%), MgO (from 0.06% to 0.54%), P_2O_5 (from 0.03% to 0.06%), and TiO_2 (from 0.33% to 0.45%). Most of them were chemically classified as monzogranites. These samples have a relatively homogeneous behavior. Three of the samples (CMR-0041R, OPP-0013RA, OPP-0047R) differ from the main group in compounds such as SiO_2, Al_2O_3, CaO, K_2O, and Na_2O. Among them, the samples CMR-0041R and OPP-0047R are chemically classified as tonalites and quartzdiorite, respectively, and petrographically they have a high plagioclase content and the highest modal amphibole content, while the sample OPP-0013RA is trondhjemitic granofels with 70% oligoclase.

The samples of the main group have a SiO_2 content of approximately 73% and a Na_2O content of approximately 3.3%. However, the K_2O content of the samples is more variable, ranging from 3.76% to 6.19%. The tonalite-quartzdiorite samples are characterized by a low K_2O content and the highest Na_2O content. Samples CMR-0041R and OPP-0047R have the lowest and highest SiO_2 values, respectively (64.6% and 77.6%), along with Na_2O values of 5.86% to 8.58% and K_2O values of 0.44% to 0.53%. Sample OPP-0013RA has SiO_2 = 71%, Na_2O = 7.26%, and K_2O = 0.47%. The sample of the Unilla Amphibolite (CAL-0037R) has low levels of SiO_2 (51.0%) and alkali (K_2O = 1.29%; Na_2O = 3.05%) and high levels of CaO (7.14%), Fe_2O_3 (16.01%), MgO (3.36%), and TiO_2 (3.37%).

In the primitive mantle-normalized multielement plots of McDonough et al. (1992) (Figure 6), the pattern of the main group of the Termales Gneiss is homogeneous, and the samples cluster around the same values, except for rare earth elements (REEs) (La, Ce, Nd and Sm), whose values show variable enrichments in light (LREEs) and intermediate rare earth elements (IREEs) (Figure 6a). This diagram shows negative Ba, Sr, and Ti anomalies. The pattern of the samples CMR-0041R and OPP-0047R is homogeneous, with values scattered around some elements. The normalized Rb values are low, in comparison with those of the main group. The Ba anomaly is much more marked, with negative K, Sr, and Ti anomalies (Figure 6b). The sample OPP-0013RA differs from those, having a lower slope and very low U, Th, and Zr values (Figure 6c). The sample from the Unilla Amphibolite has a relatively flat pattern, it slightly enriched in the most incompatible elements, has slight negative Ba and Nb anomalies, and has a markedly negative Sr anomaly (Figure 6c).

The chondrite-normalized REE patterns of McDonough and Sun (1995) in the Termales Gneiss show variable enrich-

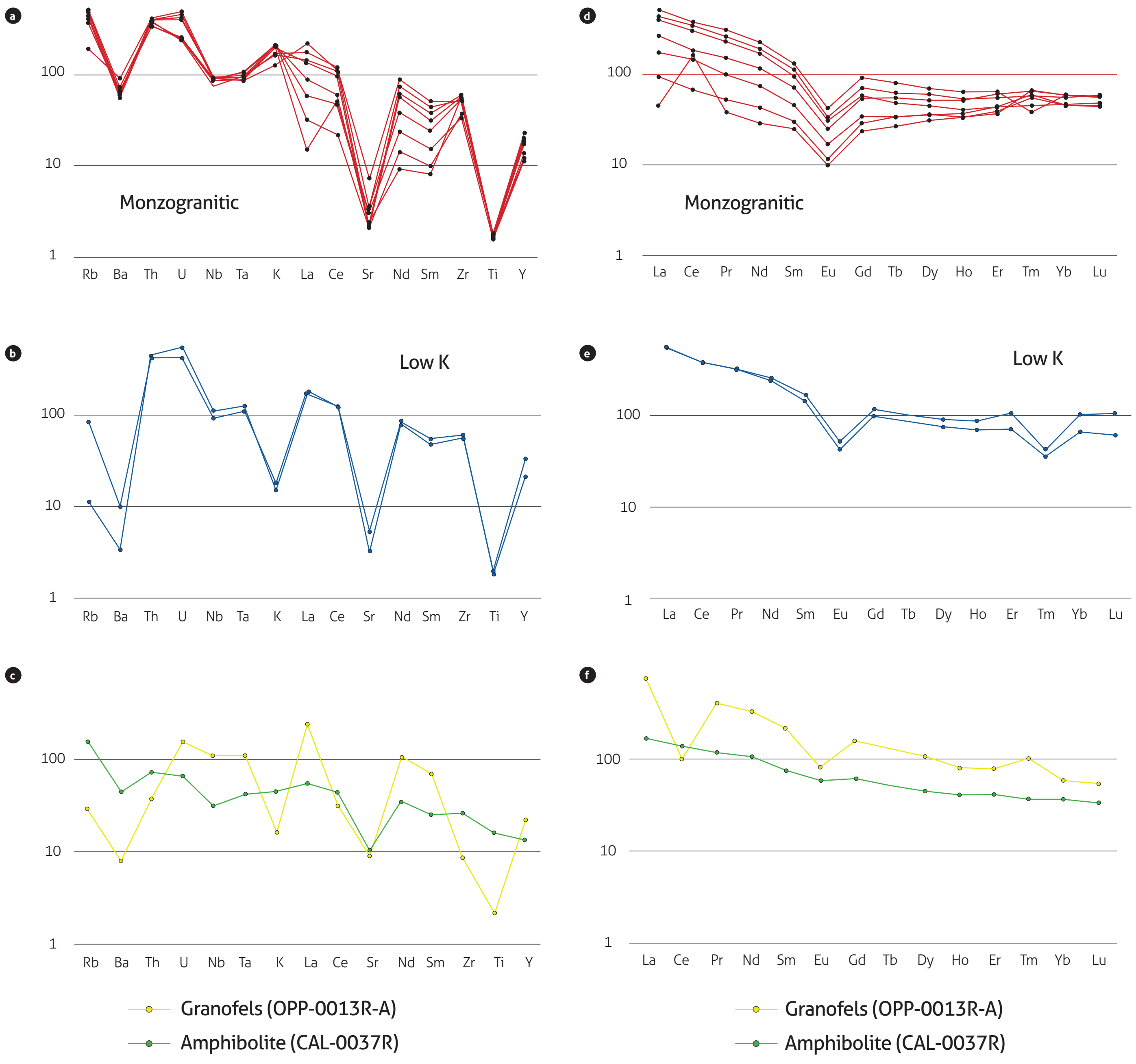

Figure 6. Multielement plots of the Termales Gneiss and Unilla Amphibolite
a, b, and c) Primitive mantle-normalized (McDonough et al., 1992). d, e, and f) Chondrite-normalized (McDonough and Sun, 1995)

ments of LREE (Figure 6). The negative Eu anomaly stands out. This anomaly likely corresponds to rocks from which plagioclase was extracted.

In the main group (Figure 6d), the slope is negative and ranges from gentle to very gentle with $(La/Yb)_N$ = 1.0 to 16.4, with a marked variation in LREEs and little variation in heavy rare earth element (HREEs) (Yb = 5.84 to 9.61). Both characteristics define a fan pattern radiating from the HREEs, which can be interpreted as the result of different degrees of partial fusion from the same source, wherein the samples more enriched in LREEs represent a lower degree of partial fusion than the less enriched samples, although this pattern could also have occurred due to different levels of assimilation of more differentiated materials. The low-K_2O samples (Figure 6e) are similar to the most enriched LREE fraction of the main group and have a similar pattern; the slope is negative and smooth with $(La/Yb)_N = 5.1$ to 12.8. Some samples show a negative Ce anomaly (OPP-0013RA and OPP-0013RB), whereas one shows a positive Ce anomaly (OPP-0037R), which may be related to zircon fractionation.

The amphibolite sample is enriched in LREEs, and the REE pattern has a gentle slope $(La/Yb)_N = 4.5$. The negative Sr (Figure 6c) and very slight Eu anomalies (Figure 6f) also suggest plagioclase removal during the fractional crystallization process of the basaltic protolith. However, these classifications should be viewed with skepticism because they are based on a single sample.

In the classification proposed to define ferrous granitoids (*sensu* Frost and Frost, 2011), also known as type A granites (see Bonin, 2007), the main rock group of the Termales Gneiss is classified as ferrous, calc-alkaline metaluminous rocks (Figure 7). According to Frost and Frost (2011), this type of rock is formed from the differentiation of basaltic magmas that interact with crustal material (Figure 7). One of the samples of the main group is slightly peraluminous (OPP-0013RB), which may be due to increased crustal input. Importantly, this field sample was in contact with granofels. The samples CMR-0041R, OPP-013RA, and OPP-0047R range from ferrous alkaline and calc-alkaline to calcic, which reflects the variability of these three rocks. Nevertheless, the three rocks are peraluminous, and they may belong to the same magmatic suite that originated the main group and may have resulted from a greater assimilation of continental crust or from incomplete mixing with granitic magmas (Frost and Frost, 2011). However, the available data do not allow us to confirm this interpretation.

Immobile elements were used for the tectonic discrimination of the Unilla Amphibolite protolith according to the diagram of Meschede (1986) (Figure 8), in which the sample belongs to the field of within-plate tholeiites or volcanic arc basalts. Due to the primitive mantle- and chondrite-normalized flat pattern of trace elements and REEs, it is considered that the formation environment corresponded to a within-plate or volcanic-arc environment.

The geochemistry of most rocks of the Termales Gneiss is characterized by monzogranitic compositions and presents little geochemical variation. The ASI and Na_2O+K_2O-CaO values differ from those assessed in ferrous magmas in partial fusion experiments of shallow crust (*e.g.*, Patiño-Douce, 1997; Skjerlie and Johnston, 1993), suggesting a mantle contribution in the formation of the protoliths of these rocks. Only the sample of granofels with a trondhjemitic composition resembles this type of melted material.

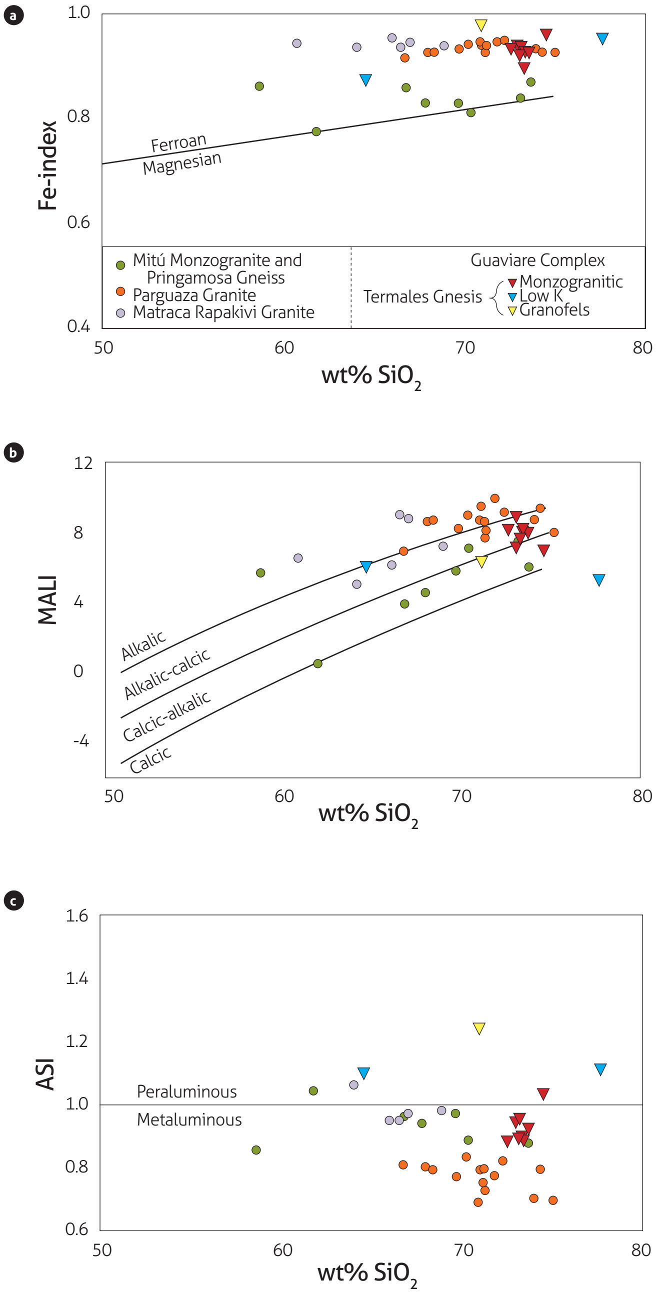

Figure 7. Classification diagrams of ferrous granitoid rocks (type A) (Frost and Frost, 2011) of protoliths of the Termales Gneiss and of rocks of the Mitú Migmatite Complex by Rodríguez et al. (2011b), of the Parguaza Granite by Bonilla et al. (2013), and of the Matraca Rapakivi Granite by Bonilla et al. (2016)

The classification diagrams of Frost and Frost (2011) show that the samples from the Mitú Migmatitic Complex (Mitú Monzogranite and Pringamosa Gneiss) are mainly part of the field of metaluminous calc-alkaline granitoids, which indicates formation processes different from those of the rock suite of the Guaviare Complex. In turn, the protolith of the Termales Gneiss is more similar to the rocks of the Parguaza Granite (Figure 7), which are also of Mesoproterozoic age and which are alkaline and calc-alkaline metaluminous ferrous granites (Bonilla et al., 2013).

In the Y_N-vs.-$(La/Y)_N$ diagram (Figure 9), the rocks of the Termales Gneiss are at an intermediate point between two extreme REE compositions of the Mitú Migmatite Complex and have lower values than those reported for the Parguaza Granite. The Mitú Migmatite Complex values suggest that these samples comprise different groups and that the rocks of the Guaviare Complex and those of the southern section of the geochronological province of Rio Negro-Juruena (Vaupés Belt) resulted from different formation processes.

4.4 Isotopes

The results from the Sm-Nd and Sr isotope analysis of a sample of gneiss with biotite and hornblende (OPP-0042RA), from the main geochemical group, and of a sample of amphibolite (CAL-0037R) are outlined in Table 1. Based on the geochronological data (Annex 3), magmatic crystallization ages of 1312 and 1313 Ma (see section 4.4) were used to calculate the $\varepsilon_{Nd}(T)$ and the initial $^{87}Sr/^{86}Sr$ ratio of the gneiss and amphibolite, respectively.

Both samples have slightly positive values of $\varepsilon_{Nd}(T)$ of +0.1 and +1.5, respectively, with T_{DM} model ages of 1810 and 1590 Ma (Figure 10). The initial $^{87}Sr/^{86}Sr$ ratios of 0.7086 and 0.6427 are quite different from those of most known isotopic reservoirs, particularly the mantle. These initial $^{87}Sr/^{86}Sr$ ratios likely reflect a Rb-Sr isotopic system imbalance, which commonly occurs due to the highly mobile character of Rb; some of this element may have been locally remobilized during metamorphism due to the action of interstitial or hydrothermal metamorphic fluids.

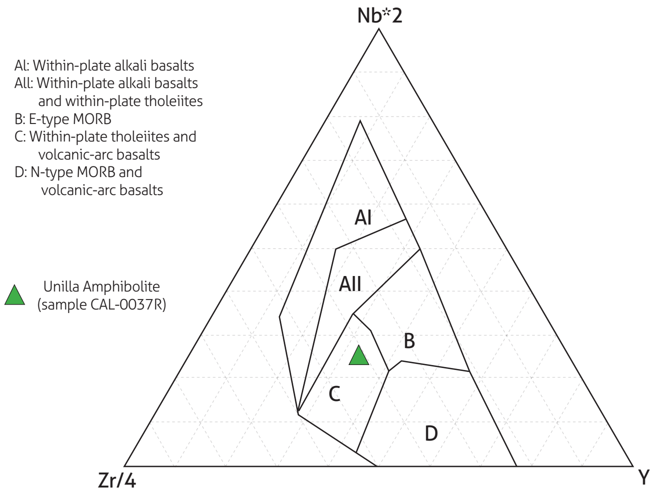

Figure 8. Nb-Zr-Y tectonic discrimination diagram (Meschede, 1986) of the Unilla Amphibolite. MORB: mid-ocean ridge basalts

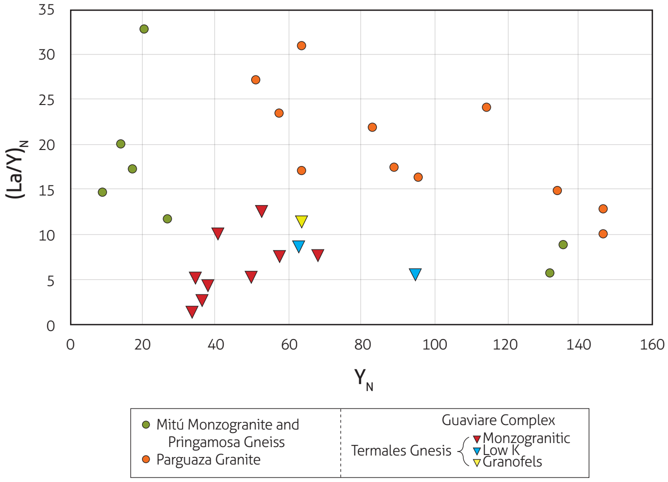

Figure 9. Y_N-vs.-$(La/Y)_N$ diagram of rocks of the Guaviare Complex and Mitú Migmatite Complex

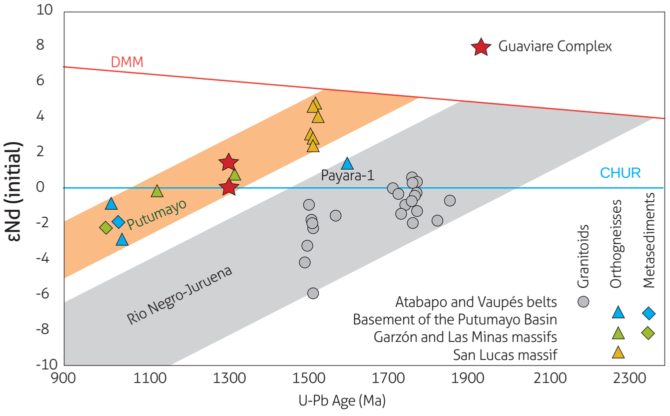

Figure 10. $\varepsilon Nd_{(t)}$-vs.-age plot comparing the new results of the Guaviare Complex with previously determined values for the Atabapo and Vaupés belts (Cordani et al., 2016), the basement of the Putumayo basin (Ibáñez Mejía et al., 2015), and the Garzón, Las Minas (Ibáñez Mejía et al., 2015), and San Lucas massifs (Cuadros et al., 2014)
The Nd isotopic composition of the Guaviare Complex suggests that this lithodemic unit has no affinity to the exposed basement of the Rio Negro-Jurueña province, instead showing higher affinity to the lithospheric domain involved in the Putumayo Orogen. Depleted MORB mantle (DMM) curve according to the model by DePaolo (1981).

4.5 Geochronology

Three samples (Table 2, Figure 2, Annex 3) of the Guaviare Complex were selected for analysis by LA ICP-MS Zircon U-Pb dating. The resulting data correspond to the crystallization ages of the igneous protoliths of the Termales Gneiss and Unilla Amphibolite and to the ages of the detritic zircons included in the sediments that form La Rompida Quartzite (Figure 11). Although some of the zircons, both igneous and detritic, show seemingly thin edges of metamorphic overgrowth or recrystallization, they could not be dated because they are significantly smaller than the analytical spot used, so the metamorphism age could not be accurately determined. The absence of clear edges of thicker metamorphic overgrowth may be due to the degree of metamorphism of the rocks. As mentioned in the petrography, the quartzite was formed in green schist or low-amphibolite facies and the gneisses and amphibolite in low- or high-amphibolite facies, without being able to define it as one or the other. According to Rubatto (2017), green schist or low amphibolite facies do not commonly form metamorphic overgrowths.

Table 1. Sm-Nd and Sr isotopic data of the Termales Gneiss and Unilla Amphibolite

Sample	Sm (ppm)	Nd (ppm)	^{143}Nd/^{144}Nd	^{147}Sm/^{144}Nd	ε_{Nd} (T)	T_{DM} (Ga)	Rb (ppm)	Sr (ppm)	^{87}Sr/^{86}Sr	^{87}Rb/^{86}Sr	^{87}Sr/^{86}Sr$_i$	T (Ga)	Lithological unit
OPP-0042RA	7.86	41.53	0.512005 (±10)	0.1144	+1.5	1.59	317.0	45.0	1.03156 (±8)	21.08454	0.64267	1.312	Termales Gneiss
CAL-0037R	11.65	51.62	0.512123 (±15)	0.1365	+0.1	1.81	95.1	218.0	0.73200 (±1)	1.26871	0.70858	1.313	Unilla Amphibolite

The uncertainties in the last two digits of the ^{143}Nd/^{144}Nd ratios and in the last digit of the ^{87}Sr/^{86}Sr ratio are 2σ. The values of the ^{143}Nd/^{144}Nd$_{CHUR}$ and ^{147}Sm/^{144}Nd$_{CHUR}$ ratios used in the current calculations were 0.512630 and 0.1960, respectively (Bouvier et al., 2008). T_{DM} model ages according to the impoverished mantle model by DePaolo (1981). The concentrations of Rb and Sr were assessed by ICP-MS (Annex 1). The ^{87}Rb/^{86}Sr ratio was calculated according to the procedure described by Faure and Mensing (2005)

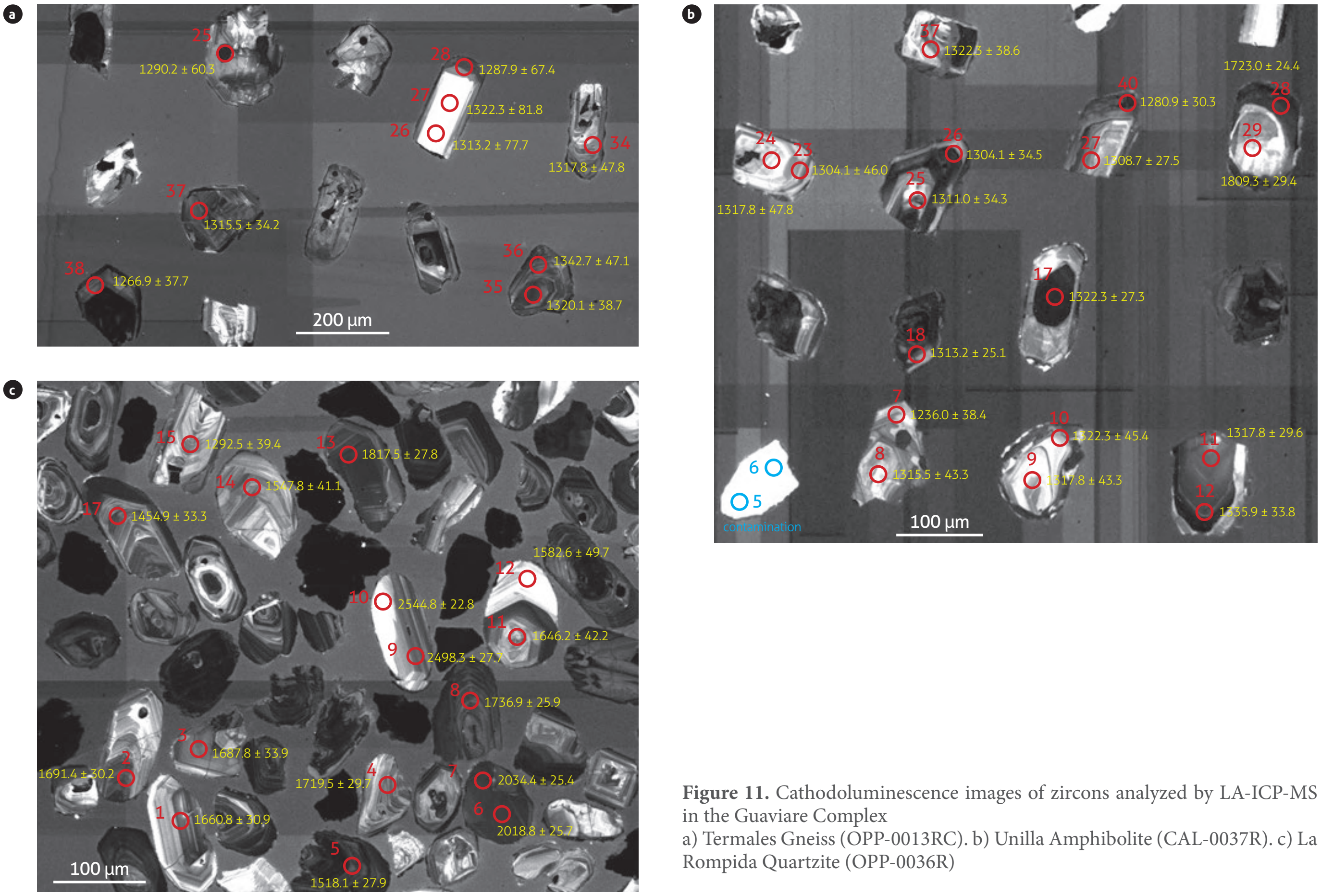

Figure 11. Cathodoluminescence images of zircons analyzed by LA-ICP-MS in the Guaviare Complex
a) Termales Gneiss (OPP-0013RC). b) Unilla Amphibolite (CAL-0037R). c) La Rompida Quartzite (OPP-0036R)

Table 2. Samples with U-Pb geochronology analysis of the Guaviare Complex

Sample	IGM	North	East	Age $^{207}Pb/^{206}Pb$ (Ma)	main U-Pb peaks (Ma)	Method	Lithological unit
OPP-0013RC	5075619	740 964	1 132 115	1312 ± 5/11		U-Pb Zircon	Termales Gneiss
CAL-0037R	5075337	727 157	1 137 003	1313 ± 8/12		U-Pb Zircon	Unilla Amphibolite
OPP-0036R	5075642	738 681	1 130 738	Between 1238.4 ± 74.4 and 2849.7 ± 28.9	1300, 1500, 1730, 2010, 2680	U-Pb Zircon	La Rompida Quartzite

4.5.1 Termales Gneiss (OPP-0013RC)

The study zircons show subhedral to euhedral shapes and a prismatic and bipyramidal habit, sometimes with radial fractures, and others are metamict (Figure 11a, Annex 4). They mostly present well-marked, fine, oscillatory igneous zoning, although a few have patchy textures, which according to Corfu et al. (2003) are commonly found in rocks under relatively high pressure. Some zircons have inherited nuclei that may represent xenocrystals; others have thin edges of metamorphic overgrowth.

Most analyses indicated an age of approximately 1.3 Ga (Figure 12a), whereas a few others presented seemingly younger ages, due to either Pb loss or partial recrystallization. The matching analyses, illustrated in a Wetherill concordia diagram in Figure 12b, yielded a weighted mean $^{206}Pb^*/^{207}Pb^*$ age = 1.312 ± 5/11 (2σ, n = 66, MSWD = 1.3) (Figure 13), which is considered the age of crystallization of the igneous protolith during the Middle Mesoproterozoic (Ectasian).

The dated sample OPP-0013RC could be considered a member of the main group of gneisses described above based on geochemistry considering its similarities in modal mineralogical composition with the other gneisses of this group. As discussed below, the youngest age peak of La Rompida Quartzite, approximately 1.3 Ga, allows us to assume that most igneous protoliths in the area are close to that age, although it cannot rule out that the ages of low-K rocks, and even granofels, are somewhat different.

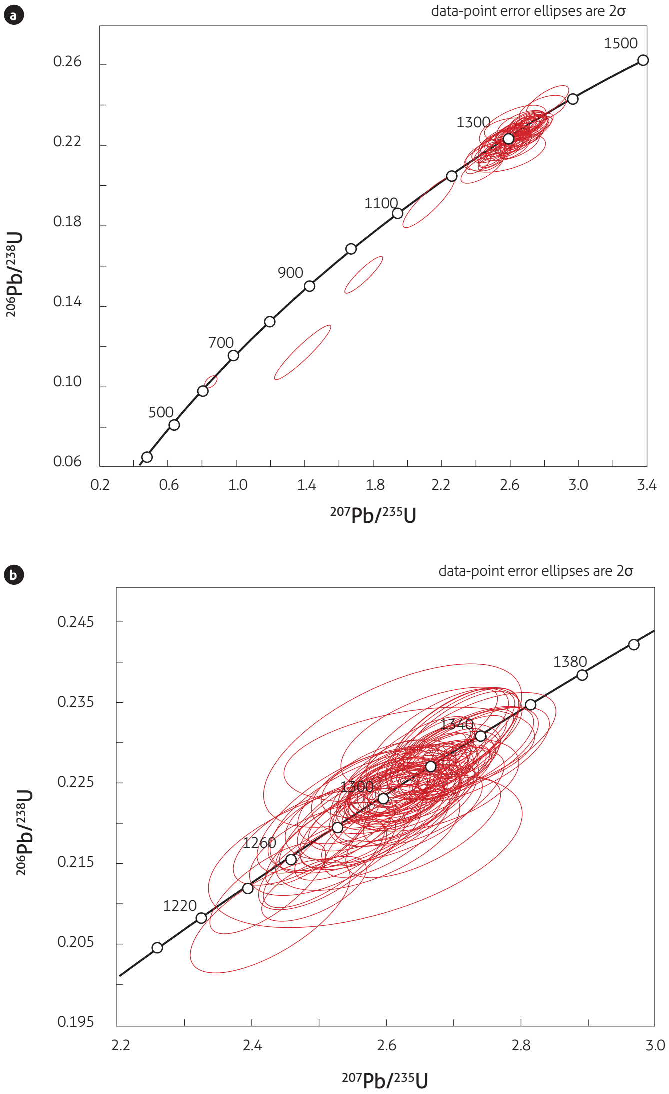

Figure 12. Wetherill concordia curve of the Termales Gneiss. Sample OPP-0013RC
a) All zircons. b) Igneous ages of the sample protolith.

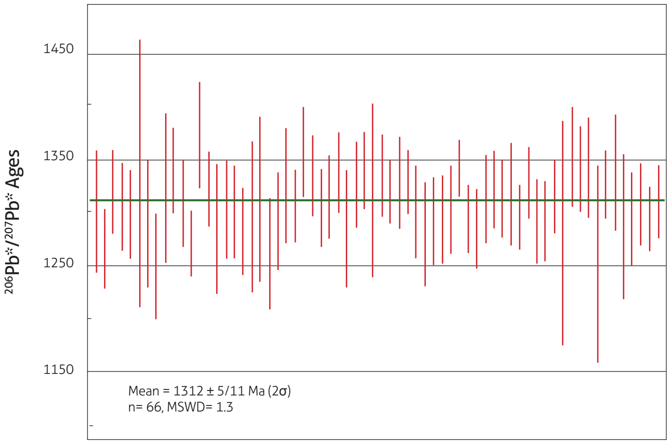

Figure 13. Mean $^{206}Pb^*/^{207}Pb^*$ age of the sample from the Termales Gneiss. Sample OPP-0013RC

4.5.2 Unilla Amphibolite (CAL-0037R)

The zircons collected from the Unilla Amphibolite are euhedral and prismatic, with fine to thick, oscillatory, igneous zoning and thin dark edges, which could be considered to have formed by metamorphism (Figure 11b, Annex 5). The vast majority of the analyses corroborated each other's findings (Figure 14a), and the spots located in nuclei with oscillatory zoning (as shown in Figure 14b) resulted in a weighted mean $^{206}\text{Pb}^{*}/^{207}\text{Pb}^{*}$ age = 1313 ± 8/12 (2σ, n = 19, MSWD = 0.9) (Figure 15). This age, interpreted as the age of crystallization of the igneous protolith of this amphibolite during the Middle Mesoproterozoic (Ectasian), is indistinguishable, within analytical uncertainties, from the age of crystallization assessed for the Termales Gneiss.

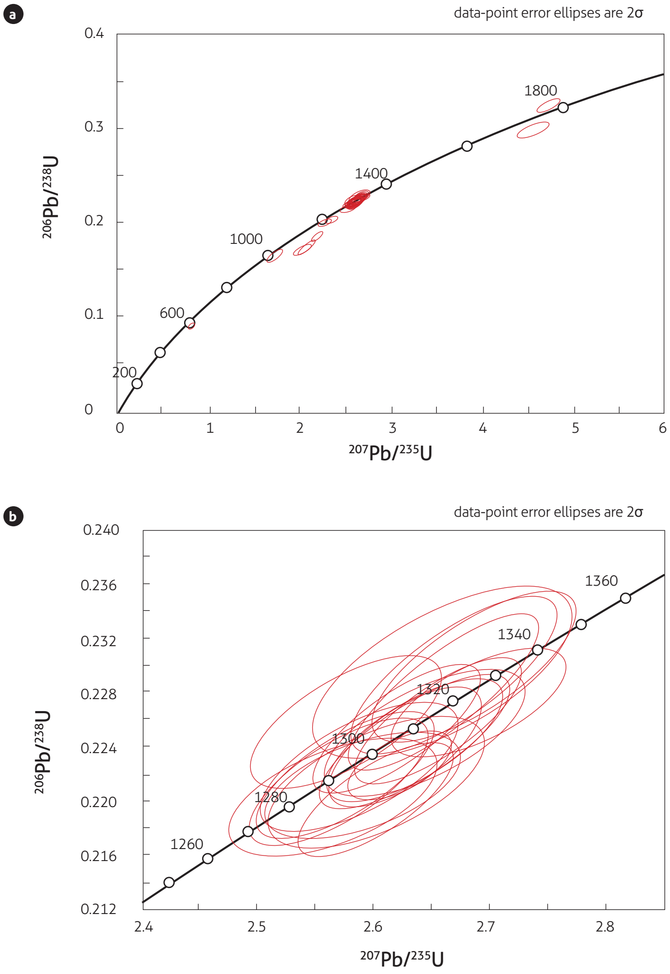

Figure 14. Wetherill concordia curve of the Unilla Amphibolite; Sample CAL-0037R
a) All zircons. b) Igneous ages of the sample protolith.

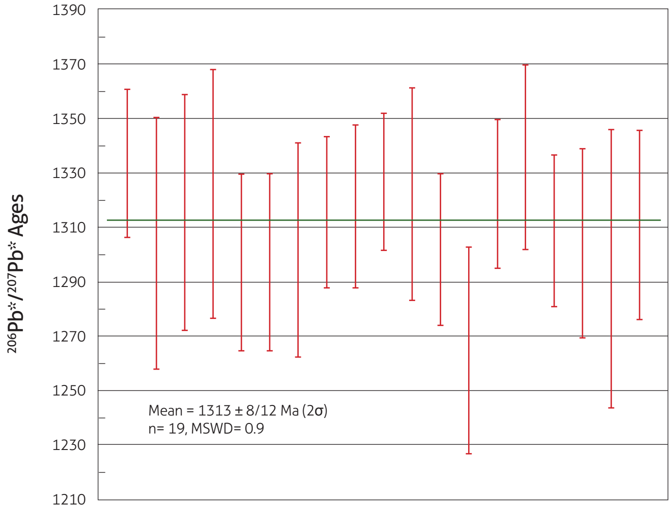

Figure 15. Mean $^{206}\text{Pb}^{*}/^{207}\text{Pb}^{*}$ age of the CAL-0037R sample from the Unilla Amphibolite

Two inherited zircon xenocrystals resulted in apparent $^{206}\text{Pb}/^{207}\text{Pb}$ ages of approximately 1.7-1.8 Ga, which indicates the assimilation of Paleoproterozoic materials, either at the source of the magmas or during the rise/eruption of the basaltic protoliths of this amphibolite. These ages match those indicated by Cordani et al. (2016) for the Atabapo Belt. Other, younger ages recorded in the zircons, between 607 and 1224 Ma, likely correspond to recrystallization or partial loss of Pb.

4.5.3 La Rompida Quartzite (OPP-0036R)

The zircons in this sample are fractured and detrital, with shapes ranging from rounded to subangular, some from euhedral to subhedral, and with a prismatic and bipyramidal habit, which indicates variation in the input sources. The vast majority of them present fine oscillatory igneous zoning (Figure 11c, Annex 6); only some crystals have a thin edge, which may correspond to metamorphic growth. A few crystals have more complex zoning similar to sector zoning (Corfu et al., 2003), possibly due to metamorphic events.

The analytical results, illustrated in a Wetherill concordia plot (Figure 16a), show that most analyses indicated individual $^{206}\text{Pb}/^{207}\text{Pb}$ ages ranging from 1238 ± 74 Ma (youngest age) to 2850 ± 29 Ma (oldest age). The main distribution peaks are located at approximately 1300, 1500, 1730, 2010, and 2680 Ma (Figure 16b), with the main peak at 1730 Ma, followed by the peak at 1500 Ma. The $^{206}\text{Pb}/^{207}\text{Pb}$ ages older than 1829 Ma were

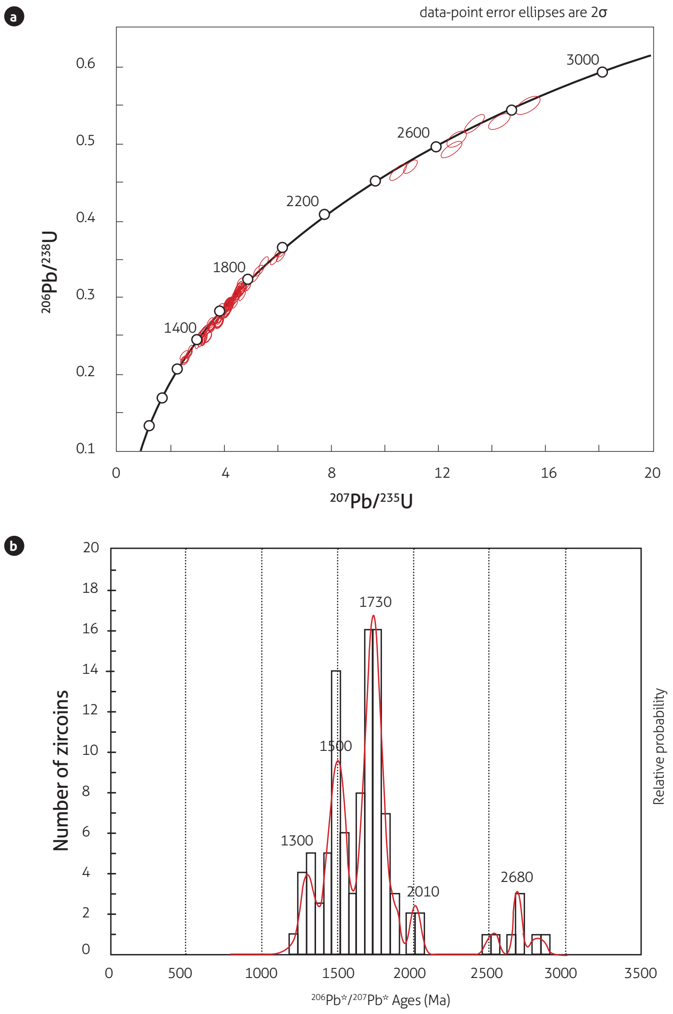

Figure 16. La Rompida Quartzite; OPP-0036R sample
a) Wetherill concordia curve. b) Probability plot of the $^{206}Pb/^{207}Pb$ ages of dendritic zircons showing the maximum age distribution peaks.

assessed in rounded grains, whereas the oldest $^{206}Pb/^{207}Pb$ age of the euhedral grains was 1827.2 Ma.

5. Discussion

The geochemical patterns and the geochronological ages assessed for rocks from the Termales Gneiss and the Unilla Amphibolite indicate that a primarily bimodal magmatism, mostly with a ferrous calc-alkaline granitic (type A) and, at a smaller volume, mafic composition occurred in the extreme NW of the Amazonian Craton at 1.3 Ga (Figures 13 and 15), in the Ectasian period of the Mesoproterozoic. This magmatism could be related to extensional environments, to the formation of rifts over long periods, or to a Mesoproterozoic extensional arc whose tectonic regime may have resulted in the opening of a back-arc basin ca. 1.3 Ga.

In addition, evidence of a more peraluminous, calc-alkaline, granitic magmatism indicates variations in magmatic processes, which could be related to changes in mantle and crustal inputs over time.

Magmatism from ca. 1.3 Ga had not yet been discovered in outcrops of the Amazonian Craton in eastern Colombia. The findings of this study clearly document the existence of this bimodal magmatism in the NW reaches of the Craton, represented by the crystallization ages assessed in igneous protoliths of the Guaviare Complex. The magmatism ages overlap with the beginning of the intraplate heating of the Nickerian event in the northern section the Amazon Craton (Cordani et al., 2016). Near the NW edge of the Amazonian Craton, Ibáñez Mejía et al. (2011) documented the existence of magmatism dated between 1.3 and 1.2 Ga, recorded in igneous protoliths from the Garzón and Las Minas massifs.

In the Proterozoic, from 1800 to 1300 Ma, the magmatism of ferrous granites (type A) were apparently quite common in the NW of the Amazonian Craton because each of the granitic protoliths of Termales Gneiss, the Parguaza Granite (Gaudette et al., 1978; Bonilla et al., 2013), the Matraca Granite (Bonilla et al., 2016), and the granitic protoliths of the Mitú Migmatite Complex (Rodríguez et al., 2011a, 2011b) have these compositions (Figure 7).

Regarding the ages assessed for the quartzites (Figure 16b), the youngest peak, at 1300 Ma, marks the maximum age of deposition of its sedimentary protolith and is close to the igneous ages of the gneisses and amphibolites of the Guaviare Complex. Given this similarity, these rocks—or other units of similar age in the region—may have contributed detrital material to nearby sedimentary basins, thereby forming the protoliths of La Rompida Quartzite during the Ectasian or later. The peak at approximately 1500 Ma is in line with the magmatism found in the Vaupés Belt and in Caquetá (Araracuara), and the main peak at approximately 1730 Ma matches the ages of the Atabapo Belt (Cordani et al., 2016), which clearly shows that the basin where the sedimentary protolith of La Rompida Quartzite was formed received detrital from the interior of the craton derived from those belts.

The peak at 2680 Ma, corresponding to the Neoarchean, matches the dates present in the Central Amazonian province, which would indicate that the current area of Guaviare was bathed by rivers that either were born in the core of the Amazonian Craton or that drained ancient sedimentary rocks that had been formed with contributions from the core of the craton. Zircons older than 1829 Ma have good roundness, indicating good transport conditions. The detrital zircons of those ages are very scarce in the dates assessed so far in the Colombian part of the Amazonian Craton. Cordani et al. (2016) reported no Archean zircons, whereas Ibáñez Mejía et al. (2011) reported scarce inherited zircons aged approximately 2.5 Ga when dating samples from the Vaupés and Apaporis rivers.

The basin most likely also received sedimentary contributions from the craton, in contrast to most metasedimentary units known to date of the Putumayo Orogen, in which no magmatic events derived from the craton were recorded between 1.59 and 1.01 Ga (Ibáñez Mejía et al., 2011). This situation could be explained if the current area of the Guaviare were over or immediately adjacent to the craton, whereas the Putumayo Orogen would have been formed some distance from the craton, where the sediments derived from this craton did not reach.

From the late Mesoproterozoic to the early Neoproterozoic, during the formation of the supercontinent Rodinia, the Mirovoi Ocean was completely consumed, and the continents Laurentia, Amazonia, and Baltica collided, which generated orogenies in the different blocks (Cawood and Pisarevsky, 2017). The Laurentia collision with the western section of the Amazonia formed the Grenvillian Orogeny in Laurentia and the Sunsás Orogeny in Amazonia (Ibáñez Mejía et al., 2011). The collision between the northwestern part of Amazonia and the southern edge of Baltica produced the Putumayo Orogen in Amazonia, the Zapotec Orogeny in the Oaxaquia block—currently part of Mexico—and the Sueconoruega Orogeny in southern Scandinavia (Weber and Schulze, 2014; Ibáñez Mejía et al., 2011, 2015; Cawood and Pisarevsky, 2017).

After 1.28 Ga, which is age of the youngest detrital zircons, but before the Ediacaran, a period during which the rocks of the San José del Guaviare Nepheline Syenites were intruded (Maya et al., 2018), the igneous and sedimentary protoliths of the Guaviare Complex underwent regional metamorphism over a length of time still undetermined because the metamorphic event recorded in the rocks produced only small overheating edges in the zircons, which could not be dated. Two Proterozoic metamorphic events younger than 1.28 Ga are known in the Colombian section of the Amazonian Craton: one from 1.05 to 1.01 Ga and another ca. 0.99 Ga (Ibáñez Mejía et al., 2011). Therefore, the regional metamorphism that affected the basement of the Guaviare Complex likely occurred during one of these Putumayo Orogenic events. However, the possibility that this was an independent event cannot be ruled out.

The difference in age between the Guaviare Complex (~1.3 Ga) and Vaupés Belt (~1.58 to 1.52 Ga) indicates that both groups of rocks were formed at different times. Based on the Nd isotopic data (Table 1 and Figure 10), the igneous protoliths of the rocks from the Guaviare Complex likely derive from the partial fusion of rocks belonging to the same lithospheric segment (which would probably correspond to an underplate of mafic rocks at the base of the crust), which gave rise to the precursor magmas of the protoliths of the gneisses, amphibolites, and granulites of the San Lucas mountain range (Cuadros et al., 2014). Considering that the gneisses and amphibolites of the San Lucas mountain range have T_{DM} ages ranging from 1.5 to 1.8 Ga (Cuadros et al., 2014), the oldest zircons, with ages of 1.7-1.8 Ga, found in the Unilla Amphibolite may have been inherited from that common source consisting of juvenile rocks of this age, though it cannot rule out the possibility that such zircons represent, conversely, xenocrystals added by assimilation of wall rocks during the emplacement of magmas. In the above scenario, the slightly positive ε_{Nd} values of the rocks from the Guaviare Complex could be explained without the need to invoke a high degree of assimilation of additional crustal material because the mantle rocks derived from the underplate would have ~1.3-Ga Nd isotopic ratios, in line with those found in the gneiss and amphibolite samples (Figure 10).

Another possibility is that the precursor magmas of the Guaviare Complex protoliths are juvenile and were directly derived from impoverished mantle (which, at ~1.3 Ga, would have ε_{Nd} values near +6), after which they underwent contamination with less radiogenic crustal material that had markedly negative ε_{Nd} values, which would have resulted in hybrid magmas with the observed values of ε_{Nd} ranging from 0 to +1.5. If this is true, two questions arise: 1) Had such contamination occurred at the source or during the emplacement of the magmas? 2) What crust was responsible for the contamination? More data are needed to answer these questions. Importantly, for example, the rocks from the Atabapo and Vaupés Belts, of the Rio Negro-Juruena province (Cordani et al., 2016), would have, at ~1.3 Ga old, ε_{Nd} values negative enough to be considered possible outliers in the origin of the protoliths of the rocks from the Guaviare Complex, through contamination of juvenile magma.

6. Conclusions

In the department of Guaviare, the Proterozoic metamorphic rocks are represented by granitic orthogneisses and granofels, amphibolites, and muscovite quartzites, which together form the Guaviare Complex. The Guaviare Complex is a new Proterozoic unit of crystalline basement located in southeastern Colombia that crops out in an intermediate position between known Precambrian rock locations in Colombia, with the Amazonian Craton (Atabapo and Vaupés belts) to the east and El Garzón Complex to the west. The rocks of the Guaviare Complex are divided into three lithological units termed Termales Gneiss, Unilla Amphibolite, and La Rompida Quartzite, which were characterized in Plate 372 – El Retorno during the geologic mapping conducted by Serviminas and the SGC. The gneissic metamorphic rocks described in the Plate 371 - Puerto Cachicamo are also included in this complex.

The protoliths of the metamorphic rocks of the Guaviare Complex indicate magmatism of ferrous granitoids (type A) of monzogranitic and tonalitic-quartzdioritic composition and a mafic magmatism of gabbroic composition. This magmatism would have been part of an orogeny after which the granites were exposed by erosion, subsequently producing sediments that incorporated materials both from the granite and from distant areas of the craton. These psammitic, quartzarenitic, and arkosic sediments, with pelitic content, underwent regional metamorphism of half a degree in amphibolite facies, although this regional metamorphism could have been partly of a low degree, in green schist facies for the quartzite. Some of these rocks present a dynamic component superimposed on regional metamorphism.

The zircon U-Pb ages assessed for the igneous protoliths of the rocks from the Guaviare Complex are 1312 ± 5/11 Ma for the Termales Gneiss and 1313 ± 8/12 Ma for the Unilla Amphibolite. In La Rompida Quartzite, the youngest detrital age is 1238 ± 74 Ma, and the oldest age is 2850 ± 29 Ma, with main peaks of 1300, 1500, 1730, 2010, and 2680 Ma. This metasedimentary unit, whose deposition occurred in the Ectasian or later, does not seem to have known equivalents in the Colombian Amazonian Craton.

The metamorphism age is not yet known with precision, and it ranges from 1.3 to 0.6 Ga. Given the regional geology of the NW of the Amazonian Craton, this metamorphism is likely related to the Putumayo province, coming either with the event recorded between 1.05 and 1.01 Ga or with the event closer to 0.99 Ga. However, the possibility that a different, perhaps slightly older, metamorphic event occurred cannot be ruled out.

The chemical characteristics of the metaigneous rocks of the Guaviare Complex, Termales Gneiss and Unilla Amphibolite, suggest that most of the rocks originated as part of a bimodal magmatism formed in an extensional environment associated with a backarc basin. The source of the magmatism, dated at 1.3 Ga, could comprise the mixture between mantle material that is possibly differentiated and older, continental, “inherited” material that was reworked during the Ectasian. The Nd isotopic ratios of the Termales Gneiss and Unilla Amphibolite are in line with the above, so the above explanation is the preferred interpretation of this work, although the hypothesis that such isotopic ratios reflect an older and dominant mantle source, analogous to that responsible for the bimodal association of precursor magmas of basement rocks of the San Lucas mountain range, should not be completely ruled out.

Acknowledgements

This study summarizes part of the results from the project entitled “*Elaboración de la cartografía geológica en un conjunto de planchas a escala 1:100.000 ubicadas en dos zonas del territorio colombiano, zona sur*” [“Preparation of the geologic map of a set of plates located in two areas of southern Colombia at a 1:100,000 scale”] of the Dirección de Geociencias Básicas of the Servicio Geológico Colombiano – SGC, developed by the Geology team of the company Serviminas under contract number 508 of 2017. We thank the SGC geologists and the Ingetec team for reading the manuscript and making recommendations, which allowed us to improve the geologic map and the explanatory memorandum of Plate 372 – El Retorno. Finally, the authors thank the anonymous reviewers for their recommendations, that helped to improve this article.

Supplementary data

Supplementary data to this article can be found online at https://doi.org/10.32685/0120-1425/boletingeo.47.2020.502

References

Bonilla, A., Frantz, J., Charão-Marques, J., Cramer, T., Franco, J., & Amaya, Z. (2016). Magmatismo rapakivi en la cuenca media del río Inírida, departamento de Guainía, Colombia. *Boletín de Geología*, *38*(1), 17-32. https://doi.org/10.18273/revbol.v38n1-2016001

Bonilla, A., Frantz, J., Charão-Marques, J., Cramer, T., Franco, J., Mulocher, E., & Amaya, Z. (2013). Petrografía, geoquímica y geocronología del Granito de Parguaza en Colombia. *Boletín de Geología*, *35*(2), 83-104.

Bonin, B. (2007). A-type granites and related rocks: evolution of a concept, problems and prospects. *Lithos*, *97*(1-2), 1-29. https://doi.org/10.1016/j.lithos.2006.12.007

Bouvier, A., Vervoort, J., & Patchett, P. (2008). The Lu-Hf and Sm-Nd isotopic composition of CHUR: Constraints from unequilibrated chondrites and implications for the bulk composition of terrestrial planets. *Earth and Planetary Science Letters*, *273*(1-2), 48-57. https://doi.org/10.1016/j.epsl.2008.06.010

Bowie, S., & Simpson, P. (1977). Microscopy: reflected light. In J. Zussman (ed.), *Physical methods in determinative mineralogy* (2nd ed., pp. 109-165). Academic Press, Ltd.

Buchely, F., Gómez, L., Reyes Abril, J., Buitrago, J., Ibáñez, R., Tovar, A., Velasco, D., Berg, T., Nota, L., Culebra, D., Becerra, L., Silveira, B., Valencia, D., & Arias, O. (2015). *Geología de la plancha 371 - Puerto Cachicamo. Memoria explicativa. Escala 1: 100.000*. Servicio Geológico Colombiano.

Caicedo, J. C. (2003). *Toma de datos en la libreta de campo*. Ingeominas.

Cawood, P., & Pisarevsky, S. (2017). Laurentia-Baltica-Amazonia relations during Rodinia assembly. *Precambrian Research*, *292*, 386-397. https://doi.org/10.1016/j.precamres.2017.01.031

Cordani, U., Cardona, A., Jimenez, D., Liu, D., & Nutman, A. (2005). Geochronology of proterozoic basement inliers in the Colombian Andes: tectonic history of remnants of a fragmented Grenville belt. *Geological Society of London, Special Publications*, *246*, 329-346. https://doi.org/10.1144/GSL.SP.2005.246.01.13

Cordani, U., Sato, K., Sproessner, W., & Fernandes, F. (2016). U-Pb zircon ages of rocks from the Amazonas territory of Colombia and their bearing on the tectonic history of the NW sector of the Amazonian Craton. *Brazilian Journal of Geology*, *46*, 5-35. https://doi.org/10.1590/2317-4889201620150012

Cordani, U., Tassinari, C., Teixeira, W., Kawashita, K., & Basei, M. (1979). *Evolução tectônica da Amazônia com base nos dados geocronológicos. Actas II. Congreso Geologico Chileno*.

Corfu, F., Hanchar, J., Hoskin, P., & Kinny, P. (2003). Atlas of zircon textures. *Reviews in Mineralogy and Geochemistry*, *53*(1), 469-500. https://doi.org/10.2113/0530469

Cox, K., Bell, J., & Pankhurst, R. (1979). *The interpretation of igneous rocks* (First). Springer Science & Business Media. https://doi.org/10.1007/978-94-017-3373-1

Cuadros, F., Botelho, N., Ordóñez-Carmona, O., & Matteini, M. (2014). Mesoproterozoic crust in the San Lucas Range (Colombia): An insight into the crustal evolution of the northern Andes. *Precambrian Research*, *245*, 186-206. https://doi.org/10.1016/j.precamres.2014.02.010

DePaolo, D. (1981). A neodymium and strontium isotopic study of the mesozoic calc-alkaline granitic batholiths of the Sierra Nevada and Peninsular Ranges, California. *Journal of Geophysical Research*, *86*(B11), 10470-10488. https://doi.org/http://dx.doi.org/10.1029/JB086iB11p10470

Faure, G., & Mensing, T. (2005). *Isotopes: principles and applications* (Third). John Wiley & Sons, Inc.

Frost, C., & Frost, B. (2011). On ferroan (A-type) granitoids: their compositional variability and modes of origin. *Journal of Petrology*, *52*(1), 39-53. https://doi.org/10.1093/petrology/egq070

Galvis, J., Huguett, A., & Ruge, P. (1979). Geología de la Amazonia Colombiana. Informe No. 1792. *Boletín Geológico*, *22*(3), 1-153.

Gaudette, H., Mendoza, V., Hurley, P., & Fairbairn, H. (1978). Geology and age of the Parguaza Rapakivi Granite, Venezuela. *Geological Society of America Bulletin*, *89*(9), 1335-1340. https://doi.org/10.1130/0016-7606(1978)89<1335:GAAOTP>2.0.CO;2

Gehrels, G., Valencia, V., & Ruiz, J. (2008). Enhanced precision, accuracy, efficiency, and spatial resolution of U-Pb ages by laser ablation-multicollector-inductively coupled plasma-mass spectrometry. *Geochemistry, Geophysics, Geosystems*, *9*(3), 1-13. https://doi.org/10.1029/2007GC001805

Gioia, S., Hollanda, M., & Pimentel, M. (1999). *Uso de resinas RE-Spec e Sr-Spec em geoquímica isotópica. En Anais do V congresso de geoquímica dos países de língua portuguesa e VII Congresso Brasileiro de Geoquímica*. 218.

Gioia, S., & Pimentel, M. (2000). The Sm-Nd isotopic method in the geochronology laboratory of the University of Brasília. *Anais da Academia Brasileira de Ciencias*, *72*(2), 219-245. https://doi.org/10.1590/s0001-37652000000200009

Heinrich, E. (1965). *Microscopic identification of minerals*. McGraw-Hill.

Ibañez-Mejía, M., Bloch, E., & Vervoort, J. (2018). Timescales of collisional metamorphism from Sm-Nd, Lu-Hf and U-Pb thermochronology: a case from the Proterozoic Putumayo Orogen of Amazonia. *Geochimica et Cosmochimica Acta*, *235*, 103-126. https://doi.org/10.1016/j.gca.2018.05.017

Ibañez-Mejia, M., & Cordani, U. G. (2020). Zircon U–Pb geochronology and Hf–Nd–O isotope geochemistry of the Paleo– to Mesoproterozoic basement in the westernmost Guiana Shield. In: Gómez, J. & Mateus–Zabala, D. (eds.), *The Geology of Colombia, Volume 1 Proterozoic – Paleozoic*. Publicaciones Geológicas Especiales 35. Servicio Geológico Colombiano. https://doi.org/10.32685/pub.esp.35.2019.04

Ibáñez-Mejia, M., Pullen, A., Arenstein, J., Gehrels, G., Valley, J., Ducea, M., Mora, A., Pecha, M., & Ruiz, J. (2015). Unraveling crustal growth and reworking processes in complex zircons from orogenic lower-crust: the proterozoic Putumayo Orogen of Amazonia. *Precambrian Research*, *267*, 285-310. https://doi.org/10.1016/j.precamres.2015.06.014

Ibáñez-Mejía, M., Ruiz, J., Valencia, V., Cardona, A., Gehrels, G., & Mora, A. (2011). The Putumayo Orogen of Amazonia and its implications for Rodinia reconstructions: new U-Pb geochronological insights into the proterozoic tectonic evolution of northwestern South America. *Precambrian Research*, *191*(1-2), 58-77. https://doi.org/10.1016/j.precamres.2011.09.005

Ibáñez-Mejia, M., & Tissot, F. (2019). Extreme Zr stable isotope fractionation during magmatic fractional crystallization. *Science Advances*, *5*(12), 1-14. https://doi.org/10.1126/sciadv.aax8648

López, J., Khurama, S., Bernal, L., & Cuellar, M. (2007). *El Complejo Mitú: una nueva perspectiva.* Memorias XI Congreso Colombiano de Geología. 1-16.

Lugmair, G., & Marti, K. (1978). Lunar initial 143Nd/144Nd: differential evolution of the lunar crust and mantle. *Earth and Planetary Science Letters*, *39*(3), 349-357. https://doi.org/10.1016/0012-821X(78)90021-3

Maya, M., Amaya, C., Gómez, J., Tabares, G., Palacio, A., García, J., Tabares, F., Camacho, J., Betancur, J., & Duque, J. (2019). *Guía para la elaboración de la libreta de campo de un proyecto de cartografía geológica*. Serviminas.

Maya, M., Amaya, C., Restrepo, J., Duque, J., Palacio, A., Gutiérrez, P., Pérez, O., Ríos, C., Arias, E., & Bedoya, J. (2018). *Memoria explicativa de la Plancha 372 – El Retorno. Escala 1: 100.000*. Servicio Geológico Colombiano.

McDonough, W., & Sun, S. (1995). The composition of the earth. *Chemical Geology*, *120*(3-4), 223-253. https://doi.org/10.1016/0009-2541(94)00140-4

McDonough, W., Sun, S., Ringwood, A., Jagoutz, E., & Hofmann, A. (1992). Potassium, rubidium, and cesium in the earth and moon and the evolution of the mantle of the earth. *Geochimica et Cosmochimica Acta*, *56*(3), 1001-1012. https://doi.org/10.1016/0016-7037(92)90043-I

Meschede, M. (1986). A method of discriminating between different types of mid-ocean ridge basalts and continental tholeiites with the Nb-Zr-Y diagram. *Chemical Geology*, *56*(3-4), 207-218. https://doi.org/10.1016/0009-2541(86)90004-5

Patiño-Douce, A. (1997). Generation of metaluminous A-type granites by low-pressure melting of calc-alkaline granitoids. *Geology*, *25*(8), 743-746. https://doi.org/10.1130/0091-7613(1997)025<0743:GOMATG>2.3.CO;2

Pullen, A., Ibáñez-Mejia, M., Gehrels, G., Giesler, D., & Pecha, M. (2018). Optimization of a laser ablation-single collector-inductively coupled plasma-mass spectrometer (thermo element 2) for accurate, precise, and efficient zircon U-Th-Pb geochronology. *Geochemistry, Geophysics, Geosystems*, *19*(10), 3689-3705. https://doi.org/10.1029/2018GC007889

Rodríguez, G., Sepúlveda, J., Ramírez, C., Ortiz, F., Ramos, K., Bermúdez, J., & Sierra, M. (2011a). *Cartografía geológica y exploración geoquímica de la Plancha 443 Mitú. Memoria explicativa. Escala 1:100.000*. Ingeominas.

Rodríguez, G., Sepúlveda, J., Ramírez, C., Ortiz, F., Ramos, K., Bermúdez, J., & Sierra, M. (2011b). Unidades, petrografía y composición química del Complejo Migmatítico de Mitú. *Boletín de Geología*, *33*(1), 27-42.

Rodríguez, G., Zapata, G., Velásquez, M., Cossio, U., & Londoño, A. (2003). *Geología de las Planchas 367 - Gigante, 368 - San Vicente del Caguán, 389 - Timaná, 390 - Puerto Rico, 391 - Lusitania (parte noroccidental) y 414 - El Doncello, departamentos de Caquetá y Huila. Memoria explicativa*. Ingeominas.

Rubatto, D. (2017). Zircon: the metamorphic mineral. *Reviews in Mineralogy and Geochemistry*, *83*(1), 261-295. https://doi.org/10.2138/rmg.2017.83.9

Schmid, R., Fettes, D., Harte, B., Davis, E., & Desmons, J. (2007). *A systematic nomenclature for metamorphic rocks: 1. How to name a metamorphic rock. Recommendations by the IUGS Subcommission on the Systematics of Metamorphic Rocks: Web version 01/02/07*. 22.

Skjerlie, K., & Johnston, A. (1993). Fluid-absent melting behavior of an F-rich tonalitic gneiss at mid-crustal pressures: implications for the generation of anorogenic granites. *Journal of Petrology*, *34*(4), 785-815. https://doi.org/10.1093/petrology/34.4.785

Sláma, J., Košler, J., Condon, D., Crowley, J., Gerdes, A., Hanchar, J., Horstwood, M., Morris, G., Nasdala, L., Norberg, N., Schaltegger, U., Schoene, B., Tubrett, M., & Whitehouse, M. (2008). Plešovice zircon - A new natural reference material for U-Pb and Hf isotopic microanalysis. *Chemical Geology*, *249*(1-2), 1-35. https://doi.org/10.1016/j.chemgeo.2007.11.005

Tassinari, C., & Macambira, M. (1999). Geochronological provinces of the Amazonian Craton. *Episodes*, *22*(3), 174-182. https://doi.org/10.18814/epiiugs/1999/v22i3/004

Weber, B., & Schulze, C. (2014). Early Mesoproterozoic (>1.4 Ga) ages from granulite basement inliers of SE Mexico and their implications on the Oaxaquia concept - evidence from U-Pb and Lu-Hf isotopes on zircon. *Revista Mexicana de Ciencias Geológicas*, *31*(3), 377-394.

Winkler, H. (1976). *Petrogenesis of metamorphic rocks* (fourth). Springer-Verlag.

Winter, J. (2001). *An introduction to igneous and metamorphic petrology*. Prentice-Hall Inc.

Whitney, D., & Evans, B. (2010). Abbreviations for names of rock-forming minerals. American Mineralogist, 95(1), 185-187. https://doi.org/10.2138/am.2010.3371

SUPPLEMENTARY DATA

ANNEX 1. GEOCHEMICAL DATA OF THE GUAVIARE COMPLEX

	Termales Gneiss											Unilla Amphibolite
	Group 1								Group 2			
Sample	**CAL-0035RA**	**CAL-0036R**	**OPP-0004R**	**OPP-0013RB**	**OPP-0037R**	**OPP-0042RA**	**OPP-0046R**	**OPP-0200R**	**CMR-0041R**	**OPP-0013RA**	**OPP-0047R**	**CAL-0037R**
IGM	**5075334**	**5075336**	**5075606**	**5075618**	**5075643**	**5075648**	**5075653**	**5075696**	**5075415**	**5075617**	**5075654**	**5075337**
Oxide (%)												
SiO_2	73.12	73.37	72.97	74.56	73.23	72.61	73.41	73.65	64.59	71.00	77.62	51.01
TiO_2	0.38	0.33	0.35	0.36	0.37	0.37	0.38	0.37	0.43	0.45	0.39	3.37
Al_2O_3	13.36	13.08	13.16	12.85	13.34	13.00	13.38	12.94	18.26	15.94	11.62	13.61
Fe_2O_3	3.52	2.74	3.42	2.87	3.43	3.49	3.47	3.52	3.75	2.65	3.38	16.01
MnO	0.10	0.05	0.04	0.02	0.06	0.07	0.06	0.07	0.11	0.02	0.05	0.24
MgO	0.31	0.32	0.23	0.12	0.24	0.25	0.27	0.29	0.54	0.06	0.17	3.36
CaO	1.57	0.90	0.29	0.85	0.91	0.92	1.07	0.80	2.97	1.47	1.12	7.14
Na_2O	3.69	2.74	3.36	3.95	2.63	2.77	3.33	3.95	8.58	7.26	5.86	3.05
K_2O	4.99	6.18	5.73	3.76	5.89	6.19	5.83	4.78	0.44	0.47	0.53	1.29
P_2O_5	0.06	0.06	0.05	0.05	0.05	0.04	0.05	0.05	0.05	0.03	0.05	0.57
Cr_2O_3	<0.01	<0.01	<0.01	<0.01	<0.01	<0.01	<0.01	<0.01	<0.01	<0.01	<0.01	<0.01
LOI	0.33	0.11	0.27	0.39	0.49	0.11	0.08	0.43	0.02	0.27	0.10	0.64
Total	101.43	99.88	99.87	99.78	100.64	99.82	101.33	100.85	99.74	99.62	100.89	100.29
Element (ppm)												
Ba	379.00	517.00	454.00	644.00	435.00	461.00	435.00	406.00	23.60	54.90	68.60	308.00
Rb	261.00	323.00	311.00	121.00	309.00	317.00	234.00	232.00	7.00	17.70	52.90	95.10
Sr	70.90	62.90	42.10	150.50	50.10	45.00	78.10	42.20	114.00	187.00	68.60	218.00
Cs	0.96	2.09	0.86	0.50	1.66	4.03	1.62	0.59	0.16	0.28	1.79	0.43
Ga	25.20	21.10	23.80	21.70	24.10	23.10	22.80	22.20	32.50	23.10	19.60	26.50
Ta	3.90	4.00	3.70	3.60	3.90	4.40	4.40	4.10	5.10	4.50	4.50	1.70
Nb	66.50	53.10	61.60	65.20	64.70	62.30	63.70	65.50	78.20	77.80	64.90	22.40
Hf	14.10	9.40	15.70	14.80	15.30	15.80	15.80	16.10	16.90	2.50	16.20	7.40
Zr	597.00	377.00	660.00	587.00	662.00	625.00	608.00	662.00	674.00	94.00	635.00	293.00
Y	107.00	54.20	63.90	82.50	52.80	56.50	78.40	90.40	148.50	99.80	98.30	60.00
Th	34.10	31.80	34.20	35.60	34.60	28.20	32.80	34.10	38.10	3.27	36.10	6.06
U	8.52	4.99	9.06	10.45	9.38	5.40	5.09	9.69	11.65	3.20	8.96	1.36
Cr	<10	10.00	10.00	10.00	<10	40.00	40.00	10.00	40.00	40.00	40.00	40.00
Ni	2.00	1.00	4.00	7.00	<1	<1	2.00	1.00	1.00	4.00	2.00	11.00
Co	1.00	2.00	2.00	2.00	1.00	1.00	1.00	2.00	2.00	1.00	1.00	29.00
Sc	1.90	1.90	2.70	1.60	3.70	2.80	2.10	2.70	2.90	0.80	3.00	12.90
V	22.00	21.00	19.00	30.00	17.00	18.00	18.00	19.00	31.00	30.00	16.00	235.00
Cu	2.00	2.00	3.00	1.00	1.00	2.00	2.00	1.00	2.00	1.00	10.00	77.00
Pb	28.00	31.00	27.00	24.00	33.00	23.00	23.00	24.00	22.00	15.00	9.00	11.00
Zn	104.00	57.00	56.00	20.00	55.00	74.00	63.00	99.00	74.00	16.00	33.00	142.00
Tl	0.42	0.48	0.29	0.05	0.44	0.46	0.30	0.15	<0.02	<0.02	0.05	0.04
Bi	0.05	0.16	0.08	0.02	0.07	0.07	0.05	0.04	0.08	0.01	0.05	0.01
Cd	<0.5	<0.5	<0.5	<0.5	<0.5	<0.5	<0.5	<0.5	<0.5	<0.5	<0.5	0.70
Sn	8.00	7.00	7.00	9.00	7.00	8.00	8.00	8.00	10.00	12.00	8.00	2.00
W	<1	<1	2.00	1.00	2.00	4.00	4.00	2.00	2.00	3.00	2.00	4.00
Li	10.00	<10	10.00	<10	10.00	<10	<10	<10	<10	<10	<10	10.00
Mo	2.00	1.00	2.00	<1	2.00	4.00	3.00	1.00	<1	<1	1.00	<1
Hg	0.01	<0.005	0.01	<0.005	<0.005	<0.005	<0.005	<0.005	<0.005	<0.005	<0.005	<0.005
As	0.30	0.20	<0.1	0.10	0.20	0.40	0.30	0.10	0.20	<0.1	0.80	0.30
Se	<0.2	<0.2	<0.2	0.20	0.20	0.20	0.30	<0.2	0.30	0.20	0.30	0.40
Sb	<0.05	<0.05	<0.05	<0.05	<0.05	<0.05	<0.05	<0.05	<0.05	<0.05	0.07	<0.05
In	0.06	0.05	0.07	0.05	0.09	0.07	0.05	0.08	0.07	0.01	0.07	0.05

	Termales Gneiss											**Unilla Amphibolite**
	Group 1								**Group 2**			
Sample	**CAL-0035RA**	**CAL-0036R**	**OPP-0004R**	**OPP-0013RB**	**OPP-0037R**	**OPP-0042RA**	**OPP-0046R**	**OPP-0200R**	**CMR-0041R**	**OPP-0013RA**	**OPP-0047R**	**CAL-0037R**
IGM	**5075334**	**5075336**	**5075606**	**5075618**	**5075643**	**5075648**	**5075653**	**5075696**	**5075415**	**5075617**	**5075654**	**5075337**
Te	<0.01	0.01	<0.01	<0.01	<0.01	0.01	0.01	0.01	<0.01	<0.01	<0.01	<0.01
La	123.50	41.00	96.10	156.50	10.60	22.50	62.50	103.00	123.00	171.50	128.00	37.80
Ce	229.00	89.20	183.00	209.00	101.00	41.10	113.00	210.00	229.00	59.30	232.00	81.40
Pr	28.30	9.04	21.20	33.50	3.50	4.87	14.05	23.90	29.30	35.80	29.30	10.45
Nd	102.50	33.20	77.60	122.50	12.80	19.60	52.90	86.40	115.00	144.00	110.00	47.80
Sm	19.50	6.72	13.90	22.60	3.58	4.40	10.55	16.70	24.20	30.40	21.10	10.95
Eu	2.30	0.93	1.75	3.13	0.55	0.64	1.39	1.89	2.95	4.48	2.40	3.17
Gd	18.30	6.97	11.55	21.90	4.62	5.82	11.00	14.05	22.80	30.00	19.30	12.05
Tb	2.89	1.20	1.74	3.14	0.93	1.21	1.97	2.20	3.65	4.55	3.08	1.81
Dy	17.20	8.71	11.00	18.40	7.69	8.72	12.85	14.65	22.30	25.30	18.60	10.85
Ho	3.42	1.84	2.21	3.20	1.86	2.02	2.86	2.93	4.71	4.34	3.79	2.18
Er	10.20	5.79	6.88	8.43	6.25	6.88	9.54	8.82	16.35	12.25	11.20	6.51
Tm	1.44	0.93	1.07	1.10	1.06	1.05	1.48	1.35	2.43	1.67	1.63	0.88
Yb	9.61	5.84	7.39	6.50	7.22	7.25	9.25	8.92	16.35	9.13	10.45	5.71
Lu	1.40	0.95	1.17	1.02	1.10	1.08	1.37	1.44	2.52	1.28	1.47	0.80

Annex 2. Modal composition of the Guaviare Complex rocks

Sample	IGM	Qz	Pl	Fsp	Bt	Ms	Hbl	Hst	Chl	Opq	Zrn	Ttn	Ep	Grt	Others	Petrographic classification	Subgroup
CMR-0027R-2	5075396	17.70	30.70	7.30	37.00					2.30	0.30	3.30			1.30	Quartz-biotite-feldspar gneiss	Gneiss
OPP-0013R-B	5075618	26.70	4.00	59.70	4.70	0.01			0.01	5.00	0.01				0.01	Biotite bearing quartz-feldspar gneiss	Gneiss
OPP-0013R-C	5075619	22.30	28.00	42.70	4.00	0.01			0.70	2.00	0.30				0.01	Biotite bearing quartz-feldspar gneiss	Gneiss
OPP-0029R	5075635	27.00	4.30	59.40	0.01				6.00	2.00	1.00					Chlorite-quartz-feldspar gneiss	Gneiss
OPP-0037R	5075643	28.70	5.70	45.30	16.70					2.70	1.00				0.02	Biotite-quartz-feldspar gneiss	Gneiss
CAL-0035R-A	5075334	32.70	33.30	14.00	8.70				2.00	2.70	0.30		5.30		1.02	Epidote-biotite-quartz-feldspar gneiss	Porphyroclastic gneiss
CAL-0036R	5075336	28.30	36.00	17.20	11.50	1.30			0.80	1.30	0.01		3.30		0.32	Muscovite-epidote bearing biotite- quartz-feldspar gneiss	Porphyroclastic gneiss
CMR-0036R	5075410	32.00	16.70	28.30	17.00	0.70				1.30	0.01	0.70	3.30		0.02	Epidote bearing biotite-quartz-feldspar gneiss	Porphyroclastic gneiss
CMR-0041R	5075415	13.70	53.70	0.30				17.3		3.00	1.70	1.70	7.30		1.30	Epidote-amphibole-quartz-feldspar gneiss	Porphyroclastic gneiss
OPP-0004R	5075606	27.00	7.00	55.70	9.00	0.01				1.30	0.01				0.03	Biotite-quartz-feldspar gneiss	Porphyroclastic gneiss
OPP-0041R	5075647	27.70	1.00	57.00	12.70				0.01	1.30	0.01				0.31	Biotite-quartz-feldspar gneiss	Porphyroclastic gneiss
OPP-0042R-A	5075648	21.00	5.30	60.70	9.00		1.30			1.30	0.01	0.30			1.01	Zoisite-hornblenda bearing biotite-quartz-feldspar gneiss	Porphyroclastic gneiss
OPP-0043R	5075650	27.00	3.70	66.70	0.70					1.70	0.01	0.30			0.02	Biotite bearing quartz-feldspar gneiss	Porphyroclastic gneiss
OPP-0044R	5075651	29.70	2.70	54.30	10.70	1.30				0.70	0.30	0.30			0.02	Muscovite bearing biotite-quartz-feldspar gneiss	Porphyroclastic gneiss
OPP-0046R	5075653	27.70	29.70	24.00	6.30		7.00		0.01	1.00	0.01	0.70	3.70		0.01	Epidote bearing biotite-hornblende-quartz-feldspar gneiss	Porphyroclastic gneiss
OPP-0047R	5075654	30.00	42.00	11.00	1.00		11.70		0.01	2.70	0.01	1.70			0.01	Biotite bearing hornblende-quartz-feldspar gneiss	Porphyroclastic gneiss
OPP-0200R	5075696	19.00	21.70	48.50	5.70	1.30			1.00	1.70	0.01	0.70			0.71	Chlorite- muscovite bearing biotite-quartz-feldspar gneiss	Porphyroclastic gneiss
OPP-0013R-A	5075617	29.00	70.70	0.01						0.30	0.01				0.01	Quartz-feldspar granofels	Granofels
CAL-0038R	5075338	51.20	23.10	8.30	0.01	14.90				1.70	0.60				0.23	Feldspar-quartz blastomylonite	Blastomylonite
OPP-0045R	5075652	41.50	29.40	4.30	9.00	6.70			1.30	1.30	0.40	0.01	3.70	1.70	0.72	Garnet bearing biotite- feldspar-quartz blastomylonite	Blastomylonite
CAL-0037R	5075337	5.00	24.00		0.01		60.70		2.30	5.00		1.30	1.00		0.73	Amphibolite	Amphibolite
ENA-0003R-A	5075465	71.00	20.30			5.40				2.30	0.70	0.30			0.01	Muscovite- feldspar-quartz granofels	Granoblastic quartzite
ENA-0003R-C	5075467	70.30	20.30			7.70				1.70	0.01				0.01	Muscovite- feldspar-quartz granofels	Granoblastic quartzite
ENA-0004R	5075468	75.30	16.30	1.30		6.00				0.01	0.01	0.01			1.00	Muscovite-feldspar quartzite	Granoblastic quartzite
ENA-0008R	5075472	77.00	14.30	3.70		1.30				3.70	0.01				0.02	Muscovite bearing feldspar quartzite	Granoblastic quartzite
ENA-0021R	5075485	68.70	13.00			5.00				0.01	0.60				12.7	Muscovite- feldspar-quartz granofels	Granoblastic quartzite
JDB-0026R-B	5075563	77.00				22.30				0.01	0.01	0.01			0.02	Muscovite quartzite	Granoblastic quartzite
PAG-0009R	5075708	55.60	24.90	2.40		9.40				1.00		0.01			6.7	Muscovite- feldspar-quartz granofels	Granoblastic quartzite
PAG-0017R	5075717	75.30	10.30	3.30		11.00				0.01	0.01				0.01	Muscovite-feldspar quartzite	Granoblastic quartzite
PAG-0019R	5075719	68.40	10.60	4.40		15.60				1.00	0.01				0.01	Muscovite- feldspar-quartz granofels	Granoblastic quartzite
PAG-0023R	5075723	60.30	25.70	5.30		7.00				1.70	0.01	0.01			0.01	Muscovite- feldspar-quartz granofels	Granoblastic quartzite
PAG-0025R	5075725	68.00	17.00	2.30		10.70				0.01	0.01	0.01			2.01	Muscovite- feldspar-quartz granofels	Granoblastic quartzite
JDB-0026R-A	5075562	76.70				23.30				0.01	0.01				0.01	Muscovite quartzite	Schist quartzite
OPP-0030R	5075636	77.70	6.00	2.00		14.30				0.01					0.01	Feldspar-muscovite quartzite	Schist quartzite
OPP-0034R	5075640	84.70				11.70				0.01					3.70	Muscovite quartzite	Schist quartzite
OPP-0035R	5075641	82.00				14.00			4.00	0.01						Muscovite quartzite	Schist quartzite
OPP-0036R	5075642	75.00				23.70				0.01	0.01	0.01			1.32	Muscovite quartzite	Schist quartzite
OPP-0038R	5075644	88.30				10.30				0.01	0.01				1.31	Muscovite quartzite	Schist quartzite
OPP-0039R	5075645	61.10	8.30			23.90				0.70					6.00	Feldspar-muscovite-quartz schist	Schist quartzite
OPP-0040R	5075646	76.00	0.01			14.30									9.71	Muscovite-quartz schist	Schist quartzite
OPP-0052R	5075659	81.90				2.70					0.01				15.4	Muscovite-quartz schist	Schist quartzite
PAG-0020R	5075720	75.30	10.30	2.00		10.30				2.00	0.01					Muscovite-feldspar quartzite	Schist quartzite

Qz: quartz, Pl: plagioclase, Fsp: feldspar, Mc: microcline, Bt: biotite, Ms: muscovite, Hbl: hornblende, Hst: hastingsite, chl: chlorite, Opq: opaque, Zrn: zircon, Ttn: titanite, Ep: epidote, Grt: garnet. Abbreviations according to Whitney and Evans (2010).

ANNEX 3. ANALYTICAL DATA FOR U/PB AGE OF THE GUAVIARE COMPLEX

OPP-0013RC (Feldspar-quartz gneiss)																	
	Isotope ratios									Apparent ages (Ma)							
Analysis	U (ppm)	U/Th	206Pb*/ 207Pb*	± (%)	207Pb*/ 235U*	± (%)	206Pb*/ 238U	± (%)	error **corr.**	206Pb*/ **238U***	± **(Ma)**	207Pb*/ **235U**	± **(Ma)**	206Pb*/ **207Pb***	± **(Ma)**	Conc (%)	**Observations**
OPP_0013RC_60	182	0.8	16.6389	2.7	0.8465	3.5	0.1022	2.3	0.65	627.3	13.5	622.7	16.2	607.2	57.6	103.3	Partial Pb-loss? Recrystallization?
OPP_0013RC_07	237	3.4	11.6414	3.1	1.3851	9.9	0.1170	9.4	0.95	713.3	63.5	882.6	58.5	1335.9	60.8	53.4	Partial Pb-loss? Recrystallization?
OPP_0013RC_15	311	3.8	12.3305	2.0	1.7425	5.1	0.1559	4.7	0.92	934.0	41.3	1024.4	33.2	1223.9	38.8	76.3	Partial Pb-loss? Recrystallization?
OPP_0013RC_45	225	5.5	12.4688	2.7	2.1222	5.9	0.1920	5.2	0.88	1132.2	54.1	1156.0	40.6	1201.9	54.1	94.2	Partial Pb-loss? Recrystallization?
OPP_0013RC_66	43	1.9	11.8483	3.0	2.4264	4.1	0.2086	2.8	0.68	1221.4	30.9	1250.5	29.2	1301.8	57.6	93.8	Igneous protolith
OPP_0013RC_38	204	1.4	12.0627	1.9	2.4221	2.9	0.2120	2.2	0.75	1239.5	24.5	1249.2	20.9	1266.9	37.7	97.8	Igneous protolith
OPP_0013RC_35	365	1.2	11.7371	2.0	2.4905	2.6	0.2121	1.6	0.63	1240.0	18.1	1269.3	18.5	1320.1	38.7	93.9	Igneous protolith
OPP_0013RC_50	186	1.8	11.8203	2.1	2.5068	3.0	0.2150	2.1	0.70	1255.4	23.9	1274.0	21.7	1306.4	41.3	96.1	Igneous protolith
OPP_0013RC_18	112	1.7	11.8624	2.1	2.5002	3.0	0.2152	2.1	0.71	1256.5	24.4	1272.1	21.9	1299.5	41.5	96.7	Igneous protolith
OPP_0013RC_30	9	1.6	11.6279	6.5	2.5684	7.4	0.2167	3.6	0.48	1264.4	41.3	1291.7	54.4	1338.2	126.0	94.5	Igneous protolith
OPP_0013RC_25	156	1.9	11.9190	3.1	2.5103	3.8	0.2171	2.2	0.57	1266.5	24.9	1275.0	27.5	1290.2	60.3	98.2	Igneous protolith
OPP_0013RC_48	111	1.0	12.1655	2.6	2.4753	3.4	0.2185	2.2	0.66	1273.9	25.9	1264.8	24.6	1250.3	50.0	101.9	Igneous protolith
OPP_0013RC_49	83	1.7	11.7096	3.6	2.5717	4.4	0.2185	2.5	0.56	1273.9	28.6	1292.6	32.1	1324.6	70.3	96.2	Igneous protolith
OPP_0013RC_65	127	1.5	11.6144	2.1	2.5987	2.9	0.2190	2.1	0.70	1276.6	23.8	1300.3	21.5	1340.4	40.4	95.2	Igneous protolith
OPP_0013RC_70	139	1.9	11.8064	2.1	2.5599	3.2	0.2193	2.3	0.74	1278.2	27.0	1289.3	23.0	1308.7	41.2	97.7	Igneous protolith
OPP_0013RC_51	271	1.4	12.0337	1.6	2.5139	3.0	0.2195	2.6	0.86	1279.2	30.1	1276.0	22.0	1271.6	30.5	100.6	Igneous protolith
OPP_0013RC_46	60	1.5	11.4155	2.6	2.6536	3.5	0.2198	2.4	0.67	1280.8	27.5	1315.6	26.1	1373.7	50.5	93.2	Igneous protolith
OPP_0013RC_64	197	1.9	11.7233	1.8	2.5839	2.5	0.2198	1.8	0.72	1280.8	21.1	1296.1	18.5	1322.3	34.1	96.9	Igneous protolith
OPP_0013RC_55	56	1.8	11.9474	3.1	2.5389	3.8	0.2201	2.1	0.57	1282.4	24.8	1283.3	27.5	1285.6	60.5	99.8	Igneous protolith
OPP_0013RC_54	142	1.9	11.8343	2.4	2.5702	3.2	0.2207	2.2	0.68	1285.6	25.9	1292.2	23.7	1304.1	46.0	98.6	Igneous protolith
OPP_0013RC_17	159	1.8	11.8483	2.3	2.5706	2.8	0.2210	1.6	0.58	1287.2	18.5	1292.3	20.1	1301.8	43.7	98.9	Igneous protolith
OPP_0013RC_56	438	1.5	11.9617	2.2	2.5509	3.1	0.2214	2.2	0.72	1289.3	25.9	1286.7	22.5	1283.2	41.9	100.5	Igneous protolith
OPP_0013RC_42	109	1.7	11.8765	3.7	2.5715	4.6	0.2216	2.8	0.61	1290.3	32.7	1292.6	33.8	1297.2	71.6	99.5	Igneous protolith
OPP_0013RC_26	42	1.1	11.7786	4.0	2.5941	4.6	0.2217	2.3	0.50	1290.9	26.9	1299.0	33.9	1313.2	77.7	98.3	Igneous protolith
OPP_0013RC_59	108	2.1	12.0919	2.7	2.5268	3.9	0.2217	2.8	0.72	1290.9	32.7	1279.8	28.1	1262.1	52.0	102.3	Igneous protolith
OPP_0013RC_43	126	1.7	11.9048	2.4	2.5723	3.4	0.2222	2.4	0.71	1293.5	28.5	1292.8	24.9	1292.5	46.3	100.1	Igneous protolith
OPP_0013RC_05	109	2.1	11.6959	2.8	2.6242	3.4	0.2227	2.0	0.58	1296.1	23.2	1307.4	25.2	1326.9	54.4	97.7	Igneous protolith
OPP_0013RC_04	122	1.9	11.8203	1.8	2.6024	2.7	0.2232	2.0	0.74	1298.8	23.2	1301.3	19.5	1306.4	34.4	99.4	Igneous protolith
OPP_0013RC_09	116	1.7	11.5075	2.2	2.6755	3.0	0.2234	2.1	0.69	1299.8	24.8	1321.7	22.4	1358.3	42.2	95.7	Igneous protolith
OPP_0013RC_10	244	1.7	11.6414	2.0	2.6447	2.4	0.2234	1.4	0.59	1299.8	16.9	1313.2	18.0	1335.9	38.3	97.3	Igneous protolith
OPP_0013RC_53	153	1.8	11.8343	1.9	2.6040	2.7	0.2236	2.0	0.72	1300.9	23.2	1301.8	20.0	1304.1	36.8	99.8	Igneous protolith
OPP_0013RC_72	83	2.0	11.7647	2.0	2.6217	2.8	0.2238	2.0	0.70	1301.9	23.2	1306.7	20.6	1315.5	38.8	99.0	Igneous protolith
OPP_0013RC_08	194	1.8	11.6279	2.0	2.6537	2.6	0.2239	1.7	0.64	1302.4	19.5	1315.7	19.0	1338.2	38.2	97.3	Igneous protolith
OPP_0013RC_58	83	1.5	11.9474	2.9	2.5828	3.6	0.2239	2.2	0.61	1302.4	26.3	1295.8	26.6	1285.6	55.8	101.3	Igneous protolith
OPP_0013RC_63	184	1.8	11.6959	2.1	2.6383	2.6	0.2239	1.6	0.61	1302.4	19.0	1311.4	19.5	1326.9	40.8	98.2	Igneous protolith
OPP_0013RC_67	119	2.0	11.6144	1.9	2.6616	3.0	0.2243	2.4	0.79	1304.6	27.9	1317.9	22.2	1340.4	35.9	97.3	Igneous protolith
OPP_0013RC_27	37	1.2	11.7233	4.2	2.6427	4.8	0.2248	2.2	0.47	1307.2	26.3	1312.6	35.2	1322.3	81.8	98.9	Igneous protolith
OPP_0013RC_21	183	1.3	11.6414	2.0	2.6637	2.6	0.2250	1.7	0.66	1308.2	20.5	1318.4	19.4	1335.9	38.3	97.9	Igneous protolith
OPP_0013RC_13	544	1.4	11.7371	1.5	2.6443	2.3	0.2252	1.8	0.76	1309.3	21.0	1313.1	17.3	1320.1	29.6	99.2	Igneous protolith
OPP_0013RC_03	135	1.6	11.6822	2.2	2.6579	3.0	0.2253	2.0	0.66	1309.8	23.1	1316.8	21.8	1329.1	43.0	98.5	Igneous protolith
OPP_0013RC_12	186	1.6	11.6822	1.5	2.6591	2.3	0.2254	1.8	0.76	1310.3	21.0	1317.2	17.2	1329.1	29.4	98.6	Igneous protolith
OPP_0013RC_19	165	1.8	11.8483	2.3	2.6253	3.1	0.2257	2.2	0.69	1311.9	25.8	1307.8	23.0	1301.8	43.7	100.8	Igneous protolith
OPP_0013RC_16	78	1.6	11.9760	2.5	2.5996	3.1	0.2259	1.7	0.57	1313.0	20.5	1300.5	22.4	1280.9	49.0	102.5	Igneous protolith
OPP_0013RC_44	111	1.9	11.9048	2.1	2.6152	2.8	0.2259	1.7	0.63	1313.0	20.5	1304.9	20.2	1292.5	41.7	101.6	Igneous protolith
OPP_0013RC_11	136	1.7	11.8906	2.1	2.6195	2.7	0.2260	1.7	0.62	1313.5	20.0	1306.1	20.0	1294.8	41.6	101.4	Igneous protolith
OPP_0013RC_71	88	1.8	11.8343	2.1	2.6319	2.9	0.2260	2.0	0.69	1313.5	24.2	1309.6	21.7	1304.1	41.4	100.7	Igneous protolith
OPP_0013RC_73	213	1.6	11.6009	1.4	2.6849	2.4	0.2260	1.9	0.81	1313.5	23.1	1324.3	17.7	1342.7	26.9	97.8	Igneous protolith
OPP_0013RC_62	323	1.7	11.8906	1.7	2.6218	2.4	0.2262	1.8	0.73	1314.6	21.0	1306.8	17.9	1294.8	32.4	101.5	Igneous protolith
OPP_0013RC_22	125	0.9	11.9474	1.9	2.6105	3.0	0.2263	2.3	0.77	1315.1	27.3	1303.6	21.9	1285.6	37.2	102.3	Igneous protolith

OPP-0013RC (Feldspar-quartz gneiss)

	Isotope ratios									Apparent ages (Ma)							
Analysis	U	U/Th	206Pb*/	±	207Pb*/	±	206Pb*/	±	error	206Pb*/	±	207Pb*/	±	206Pb*/	±	Conc	**Observations**
	(ppm)		207Pb*	(%)	235U*	(%)	238U	(%)	**corr.**	**238U***	**(Ma)**	**235U**	**(Ma)**	**207Pb***	**(Ma)**	**(%)**	
OPP_0013RC_75	109	1.9	11.7786	2.1	2.6479	2.8	0.2263	1.8	0.65	1315.1	21.6	1314.1	20.6	1313.2	41.1	100.1	Igneous protolith
OPP_0013RC_69	134	1.8	11.7233	1.9	2.6674	2.5	0.2269	1.7	0.67	1318.2	20.0	1319.5	18.6	1322.3	36.3	99.7	Igneous protolith
OPP_0013RC_40	128	1.7	11.7786	1.9	2.6584	2.6	0.2272	1.8	0.70	1319.8	22.1	1317.0	19.5	1313.2	36.6	100.5	Igneous protolith
OPP_0013RC_34	122	1.7	11.7509	2.5	2.6682	3.1	0.2275	1.8	0.60	1321.4	22.1	1319.7	22.8	1317.8	47.8	100.3	Igneous protolith
OPP_0013RC_74	248	1.9	11.8765	1.5	2.6446	2.5	0.2279	2.0	0.79	1323.5	23.6	1313.1	18.5	1297.2	30.0	102.0	Igneous protolith
OPP_0013RC_61	263	1.8	11.6822	1.8	2.6898	2.7	0.2280	2.0	0.75	1324.0	24.1	1325.6	19.8	1329.1	33.9	99.6	Igneous protolith
OPP_0013RC_06	128	2.1	11.9048	2.0	2.6430	2.6	0.2283	1.7	0.64	1325.6	19.9	1312.7	19.3	1292.5	39.4	102.6	Igneous protolith
OPP_0013RC_02	105	1.6	11.9048	1.9	2.6453	2.6	0.2285	1.8	0.69	1326.6	21.5	1313.3	19.3	1292.5	37.0	102.6	Igneous protolith
OPP_0013RC_37	171	1.6	11.7647	1.8	2.6779	2.3	0.2286	1.5	0.64	1327.2	17.8	1322.4	17.1	1315.5	34.2	100.9	Igneous protolith
OPP_0013RC_29	13	1.4	11.9760	5.4	2.6330	5.8	0.2288	2.1	0.37	1328.2	25.7	1309.9	42.7	1280.9	105.1	103.7	Igneous protolith
OPP_0013RC_20	165	1.8	11.5340	2.4	2.7351	3.2	0.2289	2.1	0.65	1328.7	25.2	1338.0	23.8	1353.8	46.7	98.1	Igneous protolith
OPP_0013RC_47	82	1.8	11.6009	2.1	2.7193	3.0	0.2289	2.1	0.71	1328.7	25.2	1333.7	22.0	1342.7	40.3	99.0	Igneous protolith
OPP_0013RC_36	150	1.8	11.6009	2.4	2.7205	3.2	0.2290	2.0	0.64	1329.3	24.1	1334.1	23.4	1342.7	47.1	99.0	Igneous protolith
OPP_0013RC_23	75	1.6	12.1507	4.7	2.6076	6.0	0.2299	3.7	0.61	1334.0	44.0	1302.8	43.9	1252.6	92.8	106.5	Igneous protolith
OPP_0013RC_14	647	1.6	11.6959	1.6	2.7102	2.3	0.2300	1.7	0.71	1334.5	19.9	1331.3	17.3	1326.9	31.7	100.6	Igneous protolith
OPP_0013RC_68	117	2.1	11.6279	2.8	2.7320	3.5	0.2305	2.2	0.61	1337.1	26.2	1337.2	26.3	1338.2	54.0	99.9	Igneous protolith
OPP_0013RC_28	67	1.9	11.9332	3.5	2.6667	4.1	0.2309	2.3	0.55	1339.2	27.2	1319.3	30.5	1287.9	67.4	104.0	Igneous protolith
OPP_0013RC_39	117	2.0	11.8906	2.3	2.6786	3.1	0.2311	2.1	0.68	1340.3	25.7	1322.6	22.9	1294.8	43.9	103.5	Igneous protolith
OPP_0013RC_57	221	1.7	11.8064	2.0	2.6977	2.9	0.2311	2.1	0.73	1340.3	25.7	1327.8	21.6	1308.7	39.0	102.4	Igneous protolith
OPP_0013RC_01	267	2.1	11.8906	1.5	2.6844	2.4	0.2316	1.9	0.78	1342.9	23.0	1324.2	18.1	1294.8	30.1	103.7	Igneous protolith
OPP_0013RC_24	271	1.6	11.7925	1.8	2.7079	2.5	0.2317	1.8	0.71	1343.4	21.5	1330.6	18.6	1311.0	34.3	102.5	Igneous protolith
OPP_0013RC_31	314	1.2	22.0264	5.3	0.0910	5.8	0.0146	2.3	0.39	93.1	2.1	88.5	4.9	-34.1	128.3	NA	Contamination?
OPP_0013RC_32	128	2.3	21.2314	8.5	0.0968	9.0	0.0149	3.0	0.33	95.4	2.9	93.8	8.1	54.3	202.9	NA	Contamination?
OPP_0013RC_33	230	1.3	15.0602	8.1	0.1385	8.4	0.0151	2.2	0.27	96.8	2.2	131.7	10.4	819.0	170.1	NA	Contamination?

CAL-0037R (Amphibolite)

	Isotope ratios									Apparent ages (Ma)							
Analysis	**U**	**U/Th**	**206Pb*/**	**±**	**207Pb*/**	**±**	206Pb*/	±	error	206Pb*/	±	207Pb*/	±	206Pb*/	±	Conc	**Observations**
	(ppm)		207Pb*	(%)	235U*	(%)	238U	(%)	corr.	**238U***	**(Ma)**	**235U**	**(Ma)**	**207Pb***	**(Ma)**	**(%)**	
CAL_0037R_03	228	1.1	15.6740	2.8	0.8151	3.8	0.0927	2.5	0.66	571.5	13.6	605.3	17.1	735.0	59.7	77.8	Partial Pb-loss? Recrystallization?
CAL_0037R_20	474	3.7	13.3511	2.3	1.7249	3.8	0.1671	3.0	0.80	996.1	27.6	1017.9	24.1	1065.8	45.6	93.5	Partial Pb-loss? Recrystallization?
CAL_0037R_24	281	1.0	11.7509	2.5	2.0267	3.7	0.1728	2.7	0.74	1027.5	25.8	1124.5	25.0	1317.8	47.8	78.0	Partial Pb-loss? Recrystallization?
CAL_0037R_13	766	1.6	11.6686	1.5	2.0799	3.8	0.1761	3.5	0.92	1045.6	33.4	1142.2	25.9	1331.4	29.4	78.5	Partial Pb-loss? Recrystallization?
CAL_0037R_18	953	1.8	11.7786	1.3	2.1869	2.3	0.1869	1.9	0.83	1104.6	19.6	1176.9	16.2	1313.2	25.1	84.1	Partial Pb-loss? Recrystallization?
CAL_0037R_07	219	3.2	12.2549	2.0	2.2728	2.6	0.2021	1.6	0.64	1186.6	17.7	1203.9	18.0	1236.0	38.4	96.0	Partial Pb-loss? Recrystallization?
CAL_0037R_40	352	2.3	11.9760	1.6	2.3499	2.2	0.2042	1.6	0.71	1197.8	17.1	1227.5	15.7	1280.9	30.3	93.5	Partial Pb-loss? Recrystallization?
CAL_0037R_09	161	1.7	11.7509	2.2	2.5321	2.6	0.2159	1.3	0.52	1260.2	15.4	1281.3	19.0	1317.8	43.3	95.6	Partial Pb-loss? Recrystallization?
CAL_0037R_34	581	1.7	11.6550	1.4	2.6026	2.1	0.2201	1.5	0.74	1282.4	18.0	1301.4	15.3	1333.7	27.1	96.2	Igneous protolith
CAL_0037R_23	180	1.8	11.8343	2.4	2.5655	2.9	0.2203	1.6	0.56	1283.5	18.5	1290.9	20.8	1304.1	46.0	98.4	Igneous protolith
CAL_0037R_08	147	1.6	11.7647	2.2	2.5913	2.7	0.2212	1.4	0.54	1288.2	16.9	1298.2	19.5	1315.5	43.3	97.9	Igneous protolith
CAL_0037R_10	101	2.3	11.7233	2.3	2.6028	2.9	0.2214	1.8	0.60	1289.3	20.6	1301.4	21.5	1322.3	45.4	97.5	Igneous protolith
CAL_0037R_02	144	1.7	11.8765	1.7	2.5727	2.3	0.2217	1.6	0.70	1290.9	19.0	1292.9	17.0	1297.2	32.3	99.5	Igneous protolith
CAL_0037R_14	811	1.1	11.8765	1.7	2.5727	2.5	0.2217	1.8	0.74	1290.9	21.6	1292.9	18.2	1297.2	32.3	99.5	Igneous protolith
CAL_0037R_35	188	1.7	11.8483	2.0	2.5881	2.7	0.2225	1.8	0.66	1295.1	20.6	1297.3	19.6	1301.8	39.1	99.5	Igneous protolith
CAL_0037R_15	206	1.7	11.7647	1.4	2.6229	2.1	0.2239	1.6	0.75	1302.4	19.0	1307.1	15.7	1315.5	27.4	99.0	Igneous protolith
CAL_0037R_11	378	1.9	11.7509	1.5	2.6342	2.3	0.2246	1.7	0.75	1306.1	20.5	1310.2	17.0	1317.8	29.6	99.1	Igneous protolith
CAL_0037R_21	514	1.3	11.6959	1.3	2.6477	2.1	0.2247	1.7	0.80	1306.7	20.0	1314.0	15.7	1326.9	24.9	98.5	Igneous protolith
CAL_0037R_37	197	1.5	11.7233	2.0	2.6451	2.6	0.2250	1.7	0.66	1308.2	20.5	1313.3	19.5	1322.3	38.6	98.9	Igneous protolith
CAL_0037R_22	539	1.4	11.8483	1.4	2.6207	2.2	0.2253	1.7	0.77	1309.8	20.5	1306.4	16.5	1301.8	27.6	100.6	Igneous protolith
CAL_0037R_01	146	1.6	12.0773	1.9	2.5767	2.6	0.2258	1.8	0.68	1312.4	21.0	1294.0	19.2	1264.5	37.7	103.8	Igneous protolith

CAL-0037R (Amphibolite)

	Isotope ratios									Apparent ages (Ma)							
Analysis	U (ppm)	U/Th	**206Pb*/** 207Pb*	± (%)	**207Pb*/** 235U*	± (%)	206Pb*/ 238U	± (%)	error corr.	206Pb*/ **238U***	± **(Ma)**	207Pb*/ **235U**	± **(Ma)**	206Pb*/ **207Pb***	± **(Ma)**	Conc (%)	**Observations**
CAL_0037R_17	901	1.3	11.7233	1.4	2.6557	2.2	0.2259	1.7	0.77	1313.0	20.0	1316.2	16.2	1322.3	27.3	99.3	Igneous protolith
CAL_0037R_12	931	2.5	11.6414	1.7	2.6909	2.3	0.2273	1.5	0.64	1320.3	17.3	1326.0	16.8	1335.9	33.8	98.8	Igneous protolith
CAL_0037R_27	531	1.6	11.8064	1.4	2.6615	2.5	0.2280	2.1	0.82	1324.0	24.7	1317.8	18.5	1308.7	27.5	101.2	Igneous protolith
CAL_0037R_26	858	1.9	11.8343	1.8	2.6703	2.7	0.2293	2.0	0.76	1330.8	24.6	1320.3	20.0	1304.1	34.5	102.1	Igneous protolith
CAL_0037R_32	82	1.5	11.8906	2.6	2.6600	3.4	0.2295	2.2	0.65	1331.9	26.7	1317.4	25.3	1294.8	50.9	102.9	Igneous protolith
CAL_0037R_25	442	1.3	11.7925	1.8	2.6868	2.7	0.2299	2.0	0.75	1334.0	24.1	1324.8	19.8	1311.0	34.3	101.8	Igneous protolith
CAL_0037R_28	411	2.9	9.4787	1.3	4.7269	2.1	0.3251	1.6	0.78	1814.6	25.8	1772.0	17.6	1723.0	24.4	105.3	Inherit
CAL_0037R_29	141	0.8	9.0416	2.2	4.5576	3.2	0.2990	2.4	0.74	1686.3	35.2	1741.5	26.8	1809.3	39.4	93.2	Inherit
CAL_0037R_05	94	0.9	19.2308	9.0	0.1048	9.3	0.0146	2.3	0.25	93.6	2.2	101.2	9.0	285.4	207.0	NA	Contamination?
CAL_0037R_33	650	1.5	20.3252	4.1	0.0996	4.6	0.0147	2.1	0.46	94.0	2.0	96.4	4.2	157.4	95.2	NA	Contamination?
CAL_0037R_06	71	1.0	20.5761	11.7	0.1019	12.1	0.0152	3.2	0.26	97.3	3.0	98.5	11.4	128.6	276.8	NA	Contamination?
CAL_0037R_36	344	1.7	21.8818	5.9	0.0958	6.5	0.0152	2.6	0.41	97.3	2.5	92.9	5.7	-18.2	143.0	NA	Contamination?

OPP-0036R (Quartzite)

	Isotope ratios									Apparent ages (Ma)							
Analysis	U (ppm)	U/Th	**206Pb*/** 207Pb*	± (%)	**207Pb*/** 235U*	± (%)	**206Pb*/** 238U	± (%)	error corr.	206Pb*/ 238U*	± **(Ma)**	207Pb*/ **235U**	± **(Ma)**	206Pb*/ **207Pb***	± **(Ma)**	Conc (%)	**Observations**
OPP_0036R_01	162	0.7	9.8039	1.7	4.1441	2.3	0.2948	1.5	0.68	1665.5	22.4	1663.1	18.5	1660.8	30.9	100.3	Detrital zircon
OPP_0036R_02	227	1.4	9.6432	1.6	4.1932	2.1	0.2934	1.3	0.63	1658.5	19.4	1672.7	17.3	1691.4	30.2	98.1	Detrital zircon
OPP_0036R_03	119	2.3	9.6618	1.8	4.1395	2.7	0.2902	1.9	0.72	1642.5	28.0	1662.1	21.8	1687.8	33.9	97.3	Detrital zircon
OPP_0036R_04	129	1.6	9.4967	1.6	4.4103	2.3	0.3039	1.6	0.70	1710.6	23.7	1714.3	18.7	1719.5	29.7	99.5	Detrital zircon
OPP_0036R_05	483	0.8	10.5820	1.5	3.2234	2.1	0.2475	1.5	0.71	1425.6	19.1	1462.8	16.3	1518.1	27.9	93.9	Detrital zircon
OPP_0036R_06	346	1.6	8.0451	1.4	6.1705	2.3	0.3602	1.7	0.77	1983.1	29.9	2000.3	19.8	2018.8	25.7	98.2	Detrital zircon
OPP_0036R_07	343	1.5	7.9745	1.4	6.1283	2.3	0.3546	1.7	0.77	1956.5	29.5	1994.3	19.7	2034.4	25.4	96.2	Detrital zircon
OPP_0036R_08	314	1.5	9.4073	1.4	4.3877	2.1	0.2995	1.5	0.73	1688.8	22.3	1710.0	17.0	1736.9	25.9	97.2	Detrital zircon
OPP_0036R_09	170	1.3	6.0938	1.6	10.4667	2.4	0.4628	1.7	0.72	2451.9	34.8	2477.0	22.0	2498.3	27.7	98.1	Detrital zircon
OPP_0036R_10	153	1.2	5.9277	1.4	10.9275	2.0	0.4700	1.5	0.74	2483.6	30.7	2517.0	18.8	2544.8	22.8	97.6	Detrital zircon
OPP_0036R_11	125	1.2	9.8814	2.3	3.7964	2.9	0.2722	1.8	0.63	1552.0	25.3	1592.0	23.5	1646.2	42.2	94.3	Detrital zircon
OPP_0036R_12	67	1.6	10.2249	2.7	3.8360	3.5	0.2846	2.2	0.64	1614.5	31.6	1600.3	27.9	1582.6	49.7	102.0	Detrital zircon
OPP_0036R_13	397	1.5	9.0009	1.5	4.9089	2.3	0.3206	1.7	0.75	1792.7	27.3	1803.8	19.6	1817.5	27.8	98.6	Detrital zircon
OPP_0036R_14	194	1.1	10.4167	2.2	3.3500	2.7	0.2532	1.6	0.59	1455.0	21.1	1492.8	21.3	1547.8	41.1	94.0	Detrital zircon
OPP_0036R_15	149	1.3	11.9048	2.0	2.5307	2.6	0.2186	1.6	0.63	1274.5	19.0	1280.9	19.0	1292.5	39.4	98.6	Detrital zircon
OPP_0036R_16	347	1.0	9.3284	1.6	4.4175	2.4	0.2990	1.8	0.76	1686.3	27.3	1715.6	20.1	1752.3	29.0	96.2	Detrital zircon
OPP_0036R_17	220	0.9	10.9409	1.8	3.2222	2.2	0.2558	1.4	0.62	1468.3	18.0	1462.5	17.2	1454.9	33.3	100.9	Detrital zircon
OPP_0036R_18	188	1.7	11.8906	1.9	2.5430	2.5	0.2194	1.5	0.63	1278.7	18.0	1284.4	17.9	1294.8	37.0	98.8	Detrital zircon
OPP_0036R_19	308	1.2	9.3721	1.4	4.4924	1.9	0.3055	1.3	0.67	1718.5	19.3	1729.6	15.8	1743.8	25.8	98.6	Detrital zircon
OPP_0036R_20	281	0.8	10.9051	1.4	3.1405	2.0	0.2485	1.4	0.71	1430.7	18.6	1442.7	15.6	1461.2	26.9	97.9	Detrital zircon
OPP_0036R_21	31	0.5	10.3093	4.1	3.3207	4.8	0.2484	2.4	0.50	1430.2	30.5	1485.9	37.2	1567.2	77.3	91.3	Detrital zircon
OPP_0036R_22	35	0.5	10.7527	3.0	3.1107	3.9	0.2427	2.4	0.63	1400.7	30.6	1435.3	29.7	1487.9	57.0	94.1	Detrital zircon
OPP_0036R_23	301	1.6	9.1241	1.5	4.7686	2.5	0.3157	2.0	0.81	1768.7	31.4	1779.4	21.0	1792.8	26.6	98.7	Detrital zircon
OPP_0036R_24	159	1.4	9.2421	1.6	4.5720	2.7	0.3066	2.2	0.81	1724.0	32.6	1744.2	22.2	1769.3	28.7	97.4	Detrital zircon
OPP_0036R_25	253	1.2	9.3458	1.6	4.5464	2.5	0.3083	1.9	0.77	1732.3	29.6	1739.5	20.9	1748.9	29.1	99.1	Detrital zircon
OPP_0036R_26	102	1.3	10.9890	2.1	2.9849	2.6	0.2380	1.5	0.59	1376.3	18.7	1403.8	19.6	1446.6	39.8	95.1	Detrital zircon
OPP_0036R_27	240	1.4	11.9904	1.6	2.4885	2.1	0.2165	1.5	0.69	1263.4	17.0	1268.7	15.6	1278.6	30.4	98.8	Detrital zircon
OPP_0036R_28	733	1.3	9.7561	1.6	3.8438	2.2	0.2721	1.5	0.70	1551.5	21.3	1602.0	17.7	1669.9	28.9	92.9	Detrital zircon
OPP_0036R_29	152	1.1	9.7087	1.7	4.1280	2.7	0.2908	2.1	0.76	1645.5	30.0	1659.9	22.1	1678.9	32.3	98.0	Detrital zircon
OPP_0036R_30	163	0.8	9.5329	1.9	3.8311	2.8	0.2650	2.1	0.74	1515.4	28.5	1599.3	22.9	1712.5	35.1	88.5	Detrital zircon
OPP_0036R_31	75	1.5	9.5694	2.3	4.0225	2.9	0.2793	1.8	0.61	1587.8	25.2	1638.7	23.7	1705.5	42.3	93.1	Detrital zircon
OPP_0036R_32	50	1.0	9.8135	3.0	3.7609	3.7	0.2678	2.2	0.58	1529.6	29.5	1584.4	30.0	1659.0	56.3	92.2	Detrital zircon
OPP_0036R_33	160	1.4	10.6157	1.6	3.3832	2.0	0.2606	1.3	0.62	1492.9	16.9	1500.5	15.9	1512.1	30.1	98.7	Detrital zircon
OPP_0036R_34	115	1.9	10.6383	1.8	3.3268	2.5	0.2568	1.8	0.70	1473.4	23.6	1487.4	19.9	1508.1	34.2	97.7	Detrital zircon
OPP_0036R_35	141	3.0	10.4822	2.1	3.4263	2.8	0.2606	1.8	0.66	1492.9	24.5	1510.5	21.9	1536.0	39.5	97.2	Detrital zircon

OPP-0036R (Quartzite)																	
	Isotope ratios									**Apparent ages (Ma)**							
Analysis	**U**	**U/Th**	**206Pb*/**	**±**	**207Pb*/**	**±**	**206Pb*/**	**±**	error	206Pb*/	±	207Pb*/	±	206Pb*/	±	Conc	**Observations**
	(ppm)		207Pb*	(%)	235U*	(%)	238U	(%)	corr.	238U*	**(Ma)**	**235U**	**(Ma)**	**207Pb***	**(Ma)**	**(%)**	
OPP_0036R_36	81	0.9	10.6610	3.0	3.3443	3.5	0.2587	1.9	0.53	1483.2	24.6	1491.5	27.5	1504.1	56.4	98.6	Detrital zircon
OPP_0036R_37	70	1.0	10.2041	2.3	3.3441	3.0	0.2476	1.9	0.63	1426.1	24.3	1491.4	23.6	1586.4	43.9	89.9	Detrital zircon
OPP_0036R_38	268	17.4	5.4377	1.2	12.8092	1.8	0.5054	1.3	0.73	2637.0	27.8	2665.7	16.5	2688.3	19.8	98.1	Detrital zircon
OPP_0036R_39	91	1.2	9.4073	2.2	4.5181	2.9	0.3084	1.9	0.67	1732.8	29.6	1734.3	24.2	1736.9	39.7	99.8	Detrital zircon
OPP_0036R_40	83	2.0	11.7233	2.7	2.6451	3.3	0.2250	1.9	0.57	1308.2	22.1	1313.3	24.2	1322.3	52.2	98.9	Detrital zircon
OPP_0036R_41	291	1.5	9.4877	1.6	4.1399	2.4	0.2850	1.8	0.74	1616.5	25.6	1662.2	19.7	1721.3	29.6	93.9	Detrital zircon
OPP_0036R_42	132	1.5	9.3197	1.8	4.4423	2.3	0.3004	1.5	0.65	1693.3	22.3	1720.3	19.2	1754.0	32.4	96.5	Detrital zircon
OPP_0036R_43	222	1.5	9.7276	1.5	4.0576	2.0	0.2864	1.4	0.69	1623.5	20.0	1645.8	16.5	1675.3	27.0	96.9	Detrital zircon
OPP_0036R_44	86	1.2	10.5042	2.7	3.1777	3.2	0.2422	1.7	0.53	1398.1	21.3	1451.8	24.8	1532.0	51.4	91.3	Detrital zircon
OPP_0036R_45	161	1.5	11.0132	2.1	3.0634	2.8	0.2448	1.8	0.65	1411.6	22.8	1423.6	21.1	1442.4	39.9	97.9	Detrital zircon
OPP_0036R_46	242	7.0	9.4518	1.7	4.5712	2.2	0.3135	1.4	0.64	1757.9	21.6	1744.0	18.4	1728.2	31.2	101.7	Detrital zircon
OPP_0036R_47	60	1.1	11.2233	2.1	3.0453	2.9	0.2480	2.0	0.68	1428.2	25.3	1419.1	22.2	1406.3	40.8	101.6	Detrital zircon
OPP_0036R_48	49	0.7	10.7643	3.1	3.2751	3.7	0.2558	2.1	0.55	1468.3	27.2	1475.2	29.2	1485.8	59.1	98.8	Detrital zircon
OPP_0036R_49	706	2.3	10.5708	1.5	3.3507	2.1	0.2570	1.6	0.72	1474.5	20.5	1492.9	16.8	1520.1	27.9	97.0	Detrital zircon
OPP_0036R_50	159	1.5	11.0742	2.2	3.1312	3.2	0.2516	2.3	0.72	1446.7	29.4	1440.4	24.4	1431.9	42.3	101.0	Detrital zircon
OPP-0036R_51	85	1.0	9.4518	1.5	4.1833	2.3	0.2869	1.7	0.76	1626.0	25.0	1670.8	18.9	1728.2	27.8	94.1	Detrital zircon
OPP_0036R_52	305	1.3	9.4162	1.7	4.4319	2.5	0.3028	1.9	0.74	1705.2	28.2	1718.3	21.0	1735.2	31.1	98.3	Detrital zircon
OPP_0036R_53	180	1.5	9.5694	1.5	4.4949	2.6	0.3121	2.1	0.80	1751.0	31.4	1730.0	21.3	1705.5	28.2	102.7	Detrital zircon
OPP_0036R_54	357	1.8	8.6806	1.3	5.1885	2.2	0.3268	1.8	0.81	1822.9	28.7	1850.7	19.0	1883.0	23.5	96.8	Detrital zircon
OPP_0036R_55	62	1.3	10.2669	3.1	3.5156	3.5	0.2619	1.7	0.48	1499.6	22.5	1530.7	27.7	1574.9	57.7	95.2	Detrital zircon
OPP_0036R_56	25	1.1	12.2399	3.8	2.5188	4.3	0.2237	2.0	0.46	1301.4	23.2	1277.5	31.1	1238.4	74.4	105.1	Detrital zircon
OPP_0036R_57	117	1.2	9.1075	1.8	4.8530	2.4	0.3207	1.5	0.64	1793.1	23.9	1794.1	20.0	1796.1	33.2	99.8	Detrital zircon
OPP_0036R_58	122	1.5	9.5511	1.9	4.6261	2.4	0.3206	1.5	0.62	1792.7	23.4	1754.0	20.3	1709.0	35.2	104.9	Detrital zircon
OPP_0036R_59	355	5.5	9.2678	1.3	4.6337	1.9	0.3116	1.4	0.74	1748.6	21.6	1755.4	16.0	1764.2	23.7	99.1	Detrital zircon
OPP_0036R_60	384	2.1	9.1241	1.6	4.8215	2.4	0.3192	1.8	0.74	1785.8	28.3	1788.7	20.6	1792.8	29.9	99.6	Detrital zircon
OPP_0036R_61	135	1.8	8.6505	1.9	5.4726	2.7	0.3435	1.9	0.71	1903.5	31.7	1896.3	23.2	1889.2	34.3	100.8	Detrital zircon
OPP_0036R_62	87	1.2	5.1073	1.8	14.2911	2.4	0.5296	1.6	0.68	2739.8	36.7	2769.2	23.0	2791.5	29.3	98.1	Detrital zircon
OPP_0036R_63	73	1.4	4.9285	1.8	15.3798	2.5	0.5500	1.8	0.72	2825.2	41.6	2839.1	24.2	2849.7	28.9	99.1	Detrital zircon
OPP_0036R_64	55	0.6	5.4377	1.5	13.3313	2.4	0.5260	1.9	0.79	2724.6	42.2	2703.4	22.7	2688.3	24.3	101.3	Detrital zircon
OPP_0036R_65	153	1.2	9.5420	1.5	4.4327	2.3	0.3069	1.7	0.74	1725.4	25.6	1718.5	18.9	1710.8	28.1	100.9	Detrital zircon
OPP_0036R_66	216	0.8	9.3371	1.9	4.5668	2.5	0.3094	1.7	0.68	1737.8	26.1	1743.2	21.1	1750.6	34.2	99.3	Detrital zircon
OPP_0036R_67	92	0.8	10.6952	2.6	3.2756	3.2	0.2542	1.9	0.60	1460.1	25.2	1475.3	25.0	1498.0	48.6	97.5	Detrital zircon
OPP_0036R_68	32	1.0	10.7066	2.7	3.2013	3.6	0.2487	2.4	0.67	1431.8	31.0	1457.5	27.9	1496.0	50.6	95.7	Detrital zircon
OPP_0036R_69	445	2.4	9.3633	1.6	4.6159	2.4	0.3136	1.8	0.75	1758.4	27.5	1752.1	20.0	1745.5	29.2	100.7	Detrital zircon
OPP_0036R_70	559	1.5	10.6045	1.8	3.4700	2.5	0.2670	1.8	0.70	1525.6	23.9	1520.4	19.9	1514.1	34.0	100.8	Detrital zircon
OPP_0036R_71	146	1.4	11.6822	2.2	2.6957	2.6	0.2285	1.4	0.55	1326.6	17.3	1327.3	19.6	1329.1	43.0	99.8	Detrital zircon
OPP_0036R_72	214	1.2	11.6550	2.0	2.7398	2.6	0.2317	1.7	0.66	1343.4	20.9	1339.3	19.6	1333.7	38.3	100.7	Detrital zircon
OPP_0036R_73	212	4.7	8.1235	1.9	6.0821	2.4	0.3585	1.5	0.63	1975.1	26.1	1987.7	21.1	2001.6	33.2	98.7	Detrital zircon
OPP_0036R_74	163	2.8	5.5127	1.5	12.6776	2.3	0.5071	1.7	0.75	2644.2	36.8	2656.0	21.2	2665.7	24.7	99.2	Detrital zircon
OPP_0036R_75	281	2.2	5.4318	1.6	12.5288	2.3	0.4938	1.7	0.74	2587.1	37.1	2644.9	22.1	2690.1	26.0	96.2	Detrital zircon
OPP_0036R_76	641	1.0	10.6157	1.5	3.3793	2.4	0.2603	1.8	0.78	1491.4	24.6	1499.6	18.6	1512.1	28.1	98.6	Detrital zircon
OPP_0036R_77	104	0.8	9.6246	2.1	4.0237	2.7	0.2810	1.6	0.61	1596.4	23.1	1639.0	21.8	1694.9	39.0	94.2	Detrital zircon
OPP_0036R_78	99	0.8	9.7087	2.0	4.0854	2.4	0.2878	1.3	0.54	1630.5	19.0	1651.4	19.8	1678.9	37.7	97.1	Detrital zircon
OPP_0036R_79	182	1.3	9.8039	1.7	4.1174	2.5	0.2929	1.8	0.74	1656.0	26.4	1657.8	20.1	1660.8	30.9	99.7	Detrital zircon
OPP_0036R_80	318	1.5	9.1912	1.7	4.3814	2.4	0.2922	1.7	0.69	1652.5	24.4	1708.8	20.0	1779.4	31.9	92.9	Detrital zircon
OPP_0036R_81	156	1.3	8.9445	1.8	4.8381	2.5	0.3140	1.8	0.70	1760.4	27.0	1791.6	21.1	1828.9	32.4	96.3	Detrital zircon
OPP_0036R_82	151	1.6	9.2937	1.6	4.5882	2.5	0.3094	2.0	0.78	1737.8	30.0	1747.1	21.1	1759.1	28.9	98.8	Detrital zircon
OPP_0036R_83	442	1.7	8.9526	1.3	4.6737	2.5	0.3036	2.1	0.84	1709.1	31.2	1762.5	20.7	1827.2	24.4	93.5	Detrital zircon
OPP_0036R_84	110	1.2	9.4877	2.4	4.2140	3.1	0.2901	2.0	0.64	1642.0	29.0	1676.7	25.5	1721.3	43.6	95.4	Detrital zircon
OPP_0036R_85	187	1.0	10.7643	1.6	3.2251	2.3	0.2519	1.7	0.72	1448.3	21.6	1463.2	18.0	1485.8	30.6	97.5	Detrital zircon
OPP_0036R_86	79	1.4	10.8460	2.0	3.1094	2.7	0.2447	1.8	0.69	1411.1	23.3	1435.0	20.6	1471.5	37.1	95.9	Detrital zircon
OPP_0036R_87	291	1.6	8.1699	1.3	5.8839	2.0	0.3488	1.5	0.76	1928.9	25.3	1958.9	17.4	1991.5	23.2	96.9	Detrital zircon

OPP-0036R (Quartzite)																	
	Isotope ratios									Apparent ages (Ma)							
Analysis	**U** (ppm)	**U/Th**	**206Pb*/** 207Pb*	**±** (%)	**207Pb*/** 235U*	**±** (%)	**206Pb*/** 238U	± (%)	error corr.	206Pb*/ 238U*	± **(Ma)**	207Pb*/ **235U**	± **(Ma)**	206Pb*/ **207Pb***	± **(Ma)**	Conc **(%)**	**Observations**
OPP_0036R_88	56	1.1	10.8578	2.4	3.2710	3.0	0.2577	1.8	0.61	1478.1	24.1	1474.2	23.4	1469.4	45.4	100.6	Detrital zircon
OPP_0036R_89	167	3.0	9.4518	1.5	4.2548	2.4	0.2918	1.9	0.78	1650.5	27.4	1684.7	19.9	1728.2	27.8	95.5	Detrital zircon
OPP_0036R_90	104	1.5	9.6061	1.9	4.1592	2.6	0.2899	1.8	0.68	1641.0	26.0	1666.0	21.5	1698.5	35.4	96.6	Detrital zircon
OPP_0036R_91	174	1.4	9.0827	1.6	4.7281	2.4	0.3116	1.8	0.73	1748.6	27.0	1772.2	20.2	1801.0	29.7	97.1	Detrital zircon
OPP_0036R_92	44	1.8	12.0627	3.5	2.4975	4.1	0.2186	2.1	0.52	1274.5	24.3	1271.3	29.6	1266.9	68.3	100.6	Detrital zircon
OPP_0036R_93	46	1.1	10.7296	2.5	3.1945	3.2	0.2487	2.0	0.63	1431.8	25.8	1455.8	24.6	1491.9	46.7	96.0	Detrital zircon
OPP_0036R_94	101	1.0	9.2937	2.1	4.5718	3.0	0.3083	2.1	0.70	1732.3	32.0	1744.2	25.0	1759.1	39.1	98.5	Detrital zircon
OPP_0036R_95	87	1.3	9.3897	2.2	4.3534	2.7	0.2966	1.6	0.59	1674.4	23.4	1703.5	22.1	1740.3	39.6	96.2	Detrital zircon
OPP_0036R_96	92	1.6	11.8203	2.2	2.5791	3.0	0.2212	2.0	0.67	1288.2	23.8	1294.7	22.2	1306.4	43.6	98.6	Detrital zircon
OPP_0036R_97	121	1.7	11.8483	2.4	2.5357	2.8	0.2180	1.5	0.53	1271.3	16.9	1282.4	20.3	1301.8	46.0	97.7	Detrital zircon
OPP_0036R_98	97	1.8	8.7260	2.0	5.2752	2.6	0.3340	1.7	0.64	1857.7	27.1	1864.9	22.3	1873.6	36.2	99.2	Detrital zircon
OPP_0036R_99	93	0.9	9.4518	2.2	4.1090	3.1	0.2818	2.2	0.72	1600.4	31.7	1656.1	25.5	1728.2	39.9	92.6	Detrital zircon
OPP_0036R_100	291	1.9	9.2593	1.6	4.5025	2.2	0.3025	1.5	0.69	1703.7	22.3	1731.4	18.0	1765.9	28.8	96.5	Detrital zircon

Boletín Geológico

Boletín Geológico, 47, 35-65, 2020
https://doi.org/10.32685/0120-1425/boletingeo.47.2020.494

Received: May 12, 2020
Revised: July 27, 2020
Accepted: September 17, 2020

Lithology and geochemistry of the Guadalupe Group base around Tunja, Boyacá, Colombia

Litología y geoquímica de la base del Grupo Guadalupe, en los alrededores de Tunja, Boyacá, Colombia

German **Martínez Aparicio**[1], Pedro **Patarroyo**[2] and Roberto **Terraza Melo**[1]

1. Servicio Geológico Colombiano, (SGC), Bogotá, Colombia.
2. Universidad Nacional de Colombia, (UNAL), Bogotá, Colombia.
Corresponding author: German Martínez Aparicio, gamartinez@sgc.gov.co

ABSTRACT

The base of the Guadalupe Group, in the Tunja area of Colombia, contains cherts, porcellanites, mudstones, and siltstones with subordinate quartz arenites. The lithostratigraphic description of two stratigraphic sections showed that the dominant facies have fine granular textures and siliceous compositions, which considerably differ from those of the prevailing sandy terrigenous facies described in the type locality in the Eastern Hills of Bogotá, in the Arenisca Dura Formation, the basal unit of the Guadalupe Group in this sector.

The units that form the Guadalupe Group (base of the Guadalupe Group, Plaeners, and Arenisca Tierna) markedly differ from each other morphologically, which facilitates their mapping because the base and top units generate a steep morphology, and the intermediate units form surface depressions or valleys, similar to the morphology of the Guadalupe Group in its type locality in the Eastern Hills of Bogotá. The base of the Guadalupe Group consists of cherts and porcellanites toward the NW of the study area (Alto del Gavilán section), with mudstones, siltstones, quartz arenites, and to a lesser extent porcellanites and cherts prevailing toward the SE (Vereda Salitre section).

Geochemical analysis of total rock samples by XRD and XRF confirmed the primarily siliceous nature of the base of the Guadalupe Group, with SiO_2 ranging from 62 to 98%, CaO less than 3.0%, and P_2O_5 peaking at 15.0%. Etayo-Serna (2015) conducted paleontological determinations of ammonites found in the stratigraphic section of Alto del Gavilán and assigned the base of the Guadalupe Group mainly to the Lower Campanian.

Keywords: Guadalupe Group, lithology, porcellanites, cherts, Tunja.

RESUMEN

La base del Grupo Guadalupe, en los alredores de Tunja, está representada por *cherts*, porcelanitas, lodolitas y limolitas con cuarzoarenitas subordinadas. A partir de la descripción litoestratigráfica realizada en dos secciones estratigráficas se estableció que

Citation: Martínez Aparicio, G., Patarroyo, P., & Terraza Melo, R. (2020). Lithology and geochemistry of the base of the Guadalupe Group, in the Tunja area, Boyacá, Colombia. *Boletín Geológico*, *47*, 35-65, https://doi.org/10.32685/0120-1425/boletingeo.47.2020.494

las facies dominantes son de textura finogranular con composición silícea, que difieren sustancialmente de las facies terrígenas arenosas predominantes, descritas en la localidad tipo en los cerros orientales de Bogotá, en la Formación Arenisca Dura, unidad basal del Grupo Guadalupe en ese sector.

Las unidades que integran el Grupo Guadalupe (base del Grupo Guadalupe, Plaeners y Arenisca Tierna) presentan contraste morfológico marcado entre ellas, que permite cartografiarlas fácilmente, ya que las unidades de base y techo generan una morfología escarpada y la intermedia depresiones o valles en la superficie, similar a la morfología que presenta el Grupo Guadalupe en su localidad tipo, en los cerros orientales de Bogotá. La base del Grupo Guadalupe hacia el NW del área de estudio (sección Alto del Gavilán) está compuesta por *cherts* y porcelanitas, y hacia el SE (sección vereda Salitre) predominan lodolitas, limolitas y cuarzoarenitas con menor proporción de porcelanitas y *cherts*.

Los análisis geoquímicos realizados en roca total (DRX y FRX) reafirman la naturaleza principalmente silícea de la base del Grupo Guadalupe, con porcentajes entre 62% al 98% de SiO_2, CaO menor al 3,0% y 15,0% máximo de P_2O_5. Etayo-Serna (2015) realizó determinaciones paleontológicas en amonitas encontradas en la sección estratigráfica del Alto del Gavilán, y asignó principalmente al Campaniano Inferior la base del Grupo Guadalupe.

Palabras clave: Grupo Guadalupe, litología, porcelanitas, *cherts*, Tunja.

1. Introduction

From 2012 to 2015, the *Servicio Geológico Colombiano* (SGC) conducted detailed prospecting of 1600 km^2 in the Tunja area, in the department of Boyacá, in a sector of Plate 191, Tunja (Renzoni et al., 1976); such prospecting (Terraza et al., 2016) made it possible to redraw the geologic map of this region of the Eastern Cordillera of Colombia into a new stratigraphic panorama of the Upper Cretaceous corresponding to the Guadalupe Group. This new geological knowledge is partly reported in this article.

The study area is located in the central region of the Eastern Andes (Eastern Cordillera) of Colombia, in the Tunja area, where two stratigraphic sections were measured that included the base of the Guadalupe Group: one in Alto del Gavilán in the municipality of Motavita, and the other in Vereda Salitre in the municipality of Soracá (see the location in the geological framework), where the lithostratigraphic and geochemical characteristics of this unit were described in detail.

1.1 Stratigraphic nomenclature of the Guadalupe Group

The term "Guadalupe" was introduced by Hettner (1892, pp. 1-351), referencing Upper Cretaceous rocks, present in the Eastern Andes of Colombia, or Bogotá mountain range, which he designated the *Guadalupe Stage* (Table 1).

To the east of Cundinamarca and the Bogotá savanna, Hubach (1931, pp. 126-150) divided the Guadalupe Stage into two sets: "an upper set of sandstone and a lower set of schist". The upper set, which is currently known as the Guadalupe Group, was subdivided into three horizons at the time: an upper horizon of soft sandstones, a middle horizon of Plaeners, and a lower horizon of hard sandstones.

Hubach (1951, pp. 10-13) assigned the *formation* rank to the Guadalupe Stage in the Bogotá savanna, dividing it into two sets: an upper set, consisting of sandstones and Plaeners, which is currently known as *Guadalupe Group*; and a lower schistose-clayey set with intercalating quartzitic sandstone horizons and strata, which is currently known as *Chipaque Formation*. He divided the upper set into three horizons: an upper horizon, which he termed *Arenisca Tierna* (*Soft sandstone*); a middle horizon, which he termed Plaeners and which included *Arenisca Labor*; and a lower horizon, designated *Arenisca Dura* (*hard sandstone*). In addition, based on the level of *Exogyra mermeti* and on the fauna of crushed ammonites next to bivalves found in the lower set of the Guaduas Formation, he stratigraphically ranked the Guadalupe Formation between the Coniacian and the Maastrichtian.

Hubach (1957, pp. 39-46) promoted the Guadalupe Formation to the *group* rank, subdividing it into a lower clayey formation, or Lower Guadalupe, and an upper sandy formation, or Upper Guadalupe. The Lower Guadalupe Formation, consisting of clayey and quartzitic sandy facies, currently belongs to the Chipaque Formation; the Upper Guadalupe can be subdivided into Areniscas Duras, Plaeners, and Arenisca Tierna. Hubach (1957, pp. 39-46) assigned to Upper Guadalupe a stratigraphic rank between the Turonian and the Lower Maastrichtian (Table 1).

Bürgl (1959, pp. 2-6) introduced a new stratigraphic nomenclature for the Guadalupe Group, which, from the top to the base, corresponded to "Arenisca Tierna, Plaeners Superiores [Upper Plaeners], Arenisca Dura, Plaeners and Clays, unnamed Sandstone, Plaeners and Sandstones, First Lidita, unnamed Sandstone, Plaeners and Sandstones, and Second Lidita". The Arenisca Dura of Bürgl (1959) corresponds to the Arenisca Labor of Hubach (1957). In the stratigraphic section of Chía-Tabio-Tenjo that Bürgl illustrated (1959, pp. 2-3), Arenisca Tierna represents the Middle Maastrichtian; Arenisca Dura (or Arenisca Labor according to Hubach), the Lower Maastrichtian, characterized by the presence of "*Nostoceras*, *Ostrea tecticosta* and *Siphogenerinoides bramlettei*" (Bürgl, 1959, pp. 2-6); and the First Lidita represents the Lower Campanian.

Pratt et al. (1961) redefined the Guadalupe Group, restricting it to the *Upper Guadalupe or Upper Sandy Set* and dividing it from the base to the top as follows: "Arenisca Raizal, Lower Plaeners, Arenisca Dura, Upper Plaeners and Arenisca Tierna". For these authors, Lower Plaeners contained the First Lidita of Bürgl, and Arenisca Dura corresponded to the Arenisca Labor of Hubach.

Renzoni (1962), based on a purely lithostratigraphic criterion, divided the Guadalupe Group into practical and mappable units easily recognizable in the field. For this reason, he decided to combine Arenisca Labor (which Hubach [1951, pp. 10-13] included in the top of the Plaeners horizon) with Arenisca Tierna into a single sandy lithostratigraphic unit termed the Arenisca Labor-Tierna Formation. Thus, the Guadalupe Group was formed, from the base to the top, by the Arenisca Dura Formation, the Plaeners Formation, and the Arenisca Labor-Tierna Formation.

Etayo-Serna (1964) assigned a Santonian-Campanian rank to the base of the Guadalupe Group (east of the Bogotá savanna), exclusively considering the stratigraphic position of the Raizal Member. Among the typical fauna of the base of the Raizal Member, Etayo-Serna mentioned *Ostrea nicaisei*, which had been described by Hubach (1957, pp. 39-46). Furthermore, Etayo-Serna assigned the Plaeners Level, which overlies the Raizal Member, to the Lower Maastrichtian, based on the following fauna: *Siphogenerinoides clarki* Karsten, *Ostrea tecticosta* Gabb, *Ostrea falcata* Morton, *Siphogenerinoides clarki* Cushman & Campbell, and *Sphenodiscus*, among others.

In the Tunja area, Renzoni (1981) and Renzoni et al. (1976) divided the Guadalupe Group into the Plaeners Formation (kg2) and the Arenisca Labor-Tierna Formation (kg1) and indicated that the Arenisca Dura Formation (kg3) of the Bogotá savanna might correspond to some sandstones found in the top of the Conejo Formation of this locality (Table 1). They described the following fauna: *Baculites* sp. in the Plaeners Formation, *Ostrea abrupta* in the Labor-Tierna Formation, and *Lenticeras baltai* in the top of the Conejo Formation, the last of which is from the Santonian, according to Etayo-Serna (1968b, 1969).

Pérez and Salazar (1978) described in detail the formations that compose the Guadalupe Group, located east of Bogotá (Guadalupe hill and Rajadero páramo), thereby formally defining its units, which from the base to the top are the Arenisca Dura Formation, the Plaeners Formation, the Arenisca Labor Formation, and the Arenisca Tierna Formation (Table 1). Arenisca Dura would range from the Coniacian or Santonian to the Campanian, considering the age of the overlying Plaeners Formation, which these authors assigned to the Lower Maastrichtian based on the observed *Ostrea tecticosta* Gabb, *Orthocarstenia cretacea* (Cushman), *Orthocarstenia clarki* (Cushman and Campbell), and *Globigerinacea*.

Föllmi et al. (1992), in a section in Tausa (Cundinamarca), collected fossil fauna from the Lower Plaeners Member, overlying the Raizal Member (=A. Dura) of the Guadalupe Formation. According to the authors, these fossils included *Nostoceras* (*Nostoceras) liratum*, *Exiteloceras jenneyi*, *Libycoceras* sp., and remains of the dinoflagellate *Andalusiella polymorpha*, dated between the Upper Campanian and the Lower Maastrichtian (Table 1).

In the Llanero foothills (municipality of San Luis de Gaceno), in a section measured in the San Antonio ravine, Guerrero and Sarmiento (1996) divided the Guadalupe Group, from the base to the top, as follows: Lower Guadalupe (Arenitas de San Antonio Formation), Middle Guadalupe (Lodolitas de Agua Caliente Formation), and Upper Guadalupe (Arenitas de San Luis de Gaceno Formation). Based on palynological analyses, they assigned the following stratigraphic ranks to these units: Lower Campanian to Lower Guadalupe, Upper Campanian to Middle Guadalupe and Lower Maastrichtian to Upper Guadalupe.

More recently, in geologic mapping studies of the SGC, Montoya and Reyes (2003 a, b; 2005 a, b; 2007), in the Bogotá savanna and Plate 209, Zipaquirá, Colombia, identified the Upper Lidita Formation (nomenclature of the Upper Magdalena Valley (Valle Superior del Magdalena)) at the base of the Guadalupe Group, a unit considered contemporary to and heteropic with the Arenisca Dura Formation of the Bogotá savanna (Table 1). Montoya and Reyes (2003 a, b) assigned the Upper Lidita Formation to the Lower Campanian, based on the fossil fauna found in the top of the Conejo Formation (municipality of Ubaté), corresponding to "*Texanites (Texanites)* cf. *quinquenodosus* (Redtenbacher) cf. Kennedy et al. (1981); *Glyptoxoceras* sp. cf. *crispatum* (Moberg), cf. Kennedy et al. (1995); *Eulophoceras* sp. indet., cf. Kennedy et al. (1995), and *Baculites* sp. Indet".

Similarly, Terraza et al. (2010), in Plate 210, Guateque, Colombia (NW sector, grid 210: A1), and Terraza et al. (2016), in phosphate exploration in the Tunja area, mapped the Upper Lidita Formation at the base of the Guadalupe Group.

In this article, the informal nomenclature proposed by Martínez (2018) for the area located between Ventaquemada and Toca ("base of the Guadalupe Group") (Table 1) will be used while the SGC decides whether to accept the nomenclature of Montoya and Reyes (2003 a, b; 2005 a, b; 2007).

2. Geological framework

Cretaceous sedimentary rocks of the Conejo Formation and Guadalupe Group crop out in the study area. They are overlaid by the Guaduas, Cacho, and Bogotá formations of the Paleogene. In some sectors, these units are discordantly covered by Neogene and Quaternary deposits. Structurally, the area is influenced by the Combita Syncline, Tunja Syncline, and Puente Hamaca Anticline as well as the Chivatá and Puente Hamaca thrust faults, which place the Upper Cretaceous rocks in contact with the Paleogene rocks (Figure 1). Morphologically, in the Tunja area, as in the Bogotá savanna, the base of the Guadalupe Group and the Arenisca Tierna Formation generate an escarpment, whereas the Plaeners Formation originates a valley.

Conejo Formation. The Conejo Formation crops out toward the northwest of Motavita and the southeast of Soracá, forming belts with a SW-NE direction (Figure 1). The upper part of the unit forms a valley and is clearly distinguishable from the base of the Guadalupe Group, which generates a ridge. Lithologically, the lower section contains thick bundles of mudstones with dark claystones; the middle section shows quartz arenites interspersed with claystones and siliceous siltstones; the upper section reveals claystones and mudstones with frequent intercalations of quartz arenites and sporadic layers of bivalve wackestone, with layers of siliceous siltstones.

Base of the Guadalupe Group. The Base of the Guadalupe Group forms belts oriented in the SW-NE direction, which are part of the flanks of the Tunja Syncline, Cómbita Syncline, and other, minor folds (Figure 1). It is characterized by a succession of porcellanites, fossiliferous cherts with wackestone textures of foraminifera and bioclasts, mudstones, quartz arenites, siltstones, and some silicified phosphatic layers that have benthic foraminifera and bioclasts. It lies concordantly

Table 1. Stratigraphic Nomenclature for the Upper Cretaceous in the central region of the Eastern Andes of Colombia

<table>
<tr><th>Bogotá Savanna Hettner (1982)</th><th colspan="2">Bogotá Savanna Hubach (1957)</th><th>Bogotá Savanna Bürgl (1959, 1960)</th><th colspan="2">Villa de Leyva Etayo-Serna (1968)</th><th colspan="2">J-12 Tunja Renzoni (1981)</th><th>Bogotá Savanna Pérez and Salazar (1978)</th><th colspan="2">Tausa Föllmi et al. (1992)</th><th>Pl-209 Zipaquirá Montoya and Reyes (2003a, 2005a)</th><th colspan="2">Pl-191 Tunja The present study (2020)</th></tr>
<tr><th>Guaduas Stage</th><th colspan="2">Guaduas Formation</th><th>Guaduas Formation</th><th colspan="2">Guaduas Formation</th><th colspan="2">Guaduas Formation</th><th>Guaduas Formation</th><th colspan="2">Guaduas Formation</th><th>Guaduas Formation</th><th colspan="2">Guaduas Formation</th></tr>
<tr><td rowspan="7">Guadalupe Stage</td><td rowspan="4">Upper Guadalupe Formation</td><td>Arenisca Tierna</td><td>Arenisca Tierna</td><td rowspan="3">Unknown formations</td><td>Arenisca Tierna</td><td colspan="2" rowspan="3">Labor and Tierna Formation Kg1</td><td>Arenisca Tierna Formation</td><td rowspan="4">Guadalupe Formation Lower Plaeners</td><td rowspan="2">Tierna Upper Plaeners</td><td rowspan="2">Labor-Tierna Formation</td><td rowspan="4">Guadalupe Group</td><td rowspan="2">Arenisca Tierna Formation</td></tr>
<tr><td rowspan="2">Arenisca Labor-Plaeners</td><td>Upper Plaeners Arenisca Dura</td><td rowspan="2">Clayey siltstone Set</td><td>Arenisca Labor Formation</td></tr>
<tr><td>Plaeners and Arcillas unnamed sandstone</td><td>Plaeners Formation</td><td>Labor</td><td>Plaeners Formation</td><td>Plaeners Formation</td></tr>
<tr><td>Arenisca Dura</td><td>Plaeners and Areniscas First Lidita</td><td colspan="2">Plaeners Formation</td><td colspan="2">Plaeners Formation Kg2</td><td>Arenisca Dura Formation</td><td>Raizal = Dura Upper Chert</td><td>Arenisca Dura/ Lidita Superior</td><td>Base of the Guadalupe Group</td></tr>
<tr><td colspan="2" rowspan="3">Lower Guadalupe Formation</td><td>Unnamed sandstone</td><td rowspan="3">Conejo Formation</td><td>Segment C</td><td rowspan="3">Conejo Formation</td><td>Kg3 (same as Arenisca Dura)</td><td rowspan="3">Villeta Group</td><td colspan="2" rowspan="3">Villeta Formation</td><td rowspan="3">Conejo Formation</td><td colspan="2" rowspan="3">Conejo Formation</td></tr>
<tr><td>Plaeners and Areniscas</td><td rowspan="2">Segment B (Cucaita Member)</td><td rowspan="2"></td></tr>
<tr><td>Second Lidita</td></tr>
</table>

over the Conejo Formation, in rapid transitional contact. The upper contact with the Plaeners Formation is abruptly concordant with mudstones, claystones, and some porcellanites and with abundant benthic foraminifera.

Plaeners Formation. Similarly, to the base of the Guadalupe Group, this unit crops out, forming belts oriented in the SW-NE direction, which are part of the flanks of the Tunja Syncline, San Francisco Anticline, Cómbita Syncline, and other, minor folds (Figure 1). It is identified by its clayey character, with mudstones, some porcellanites, siltstones, quartz arenites, and some phosphatic layers. It lies concordantly over the base of the Guadalupe Group and underlies the Arenisca Tierna Formation.

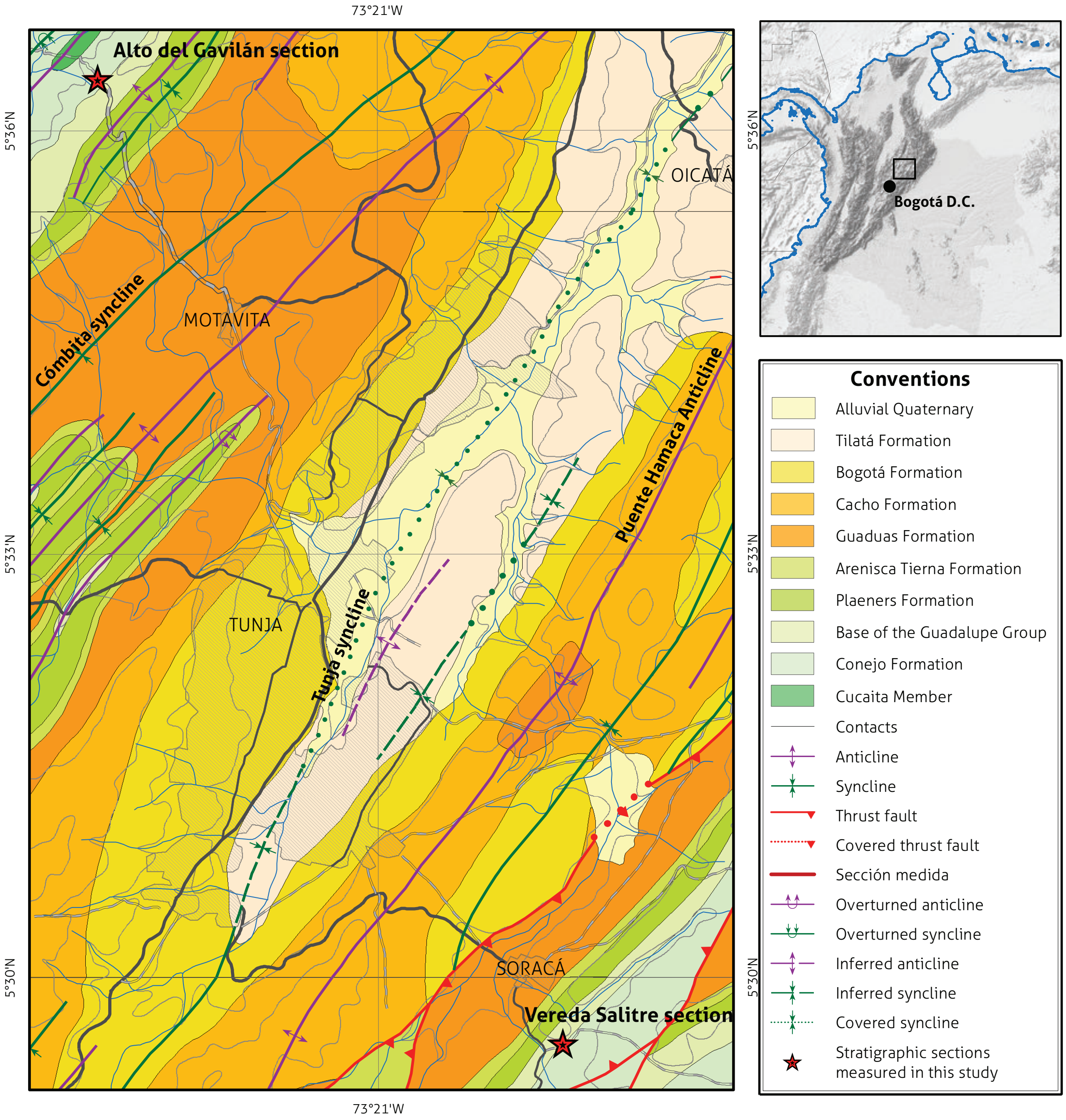

Figure 1. Geology of the study area and location of the stratigraphic sections measured in this study
Source: geologic base map retrieved from Terraza et al. (2016)

3. METHOD

Initially, the two stratigraphic sections in the study area were located and georeferenced using a GPS. Later, a measurement was performed at 1:100 scale using a Jacob's staff and a Brunton compass. We recorded the primary data in the format adapted by the SGC in 2013.

The following proposals were used to describe the stratigraphic sections: layer and lamina thickness according to Campbell (1967); geometric description of layers and laminae according to Reineck and Singh (1980), degree of progressive destruction of lamination by bioturbation according to Moore and Scrutton (1957); rock color according to the Munsell color system of the Geological Society of America (1991); degree of rock weathering according to the terminology of the Geological Society of London (1990); grain-shape and particle-size comparison diagram according to Krumbein and Sloss (1969); particle selection type and descriptive terminology according to Pettijohn, Potter, and Siever (1973); types of contacts between grains according to Taylor (1950); state of textural maturity of siliciclastic rocks according to Folk (1954); percentages of fossils and other allochems according to the charts of Baccelle and Bosellini (1965); textural classification of siliciclastic sedimentary rocks according to Folk (1954); compositional classification according to Folk (1974); and textural classification of calcareous rocks according to Dunham (1962) and Folk (1962).

Siliceous rocks were classified, both texturally and compositionally, according to Williams et al. (1954) and to Lazar et al. (2015), considering the percentage of microcrystalline quartz of the rock, as follows: The rock was classified as chert when the values ranged from 80% to 100%; as porcellanite, from 50% to 80%; and as mudstone or siliceous claystone, from 25% to 50%.

Both stratigraphic sections were systematically sampled for petrographic and geochemical analysis. The samples were sent to the Chemical Laboratory of the SGC, where they were analyzed by X-ray diffraction (XRD) and X-ray fluorescence (XRF) according to the protocols and methods established by the SGC.

The paleontological material collected in the two stratigraphic sections was analyzed by Dr. Etayo-Serna.

4. RESULTS

The results reported in the present article correspond to the detailed lithostratigraphic description of the base of the Guadalupe Group and to XRD and XRF data of the samples collected in the two stratigraphic sections measured in this study.

4.1 Lithostratigraphic Description

This description was performed based on two stratigraphic sections measured by Martínez (2018). The first section is located on the road that connects the municipalities of Soracá and Boyacá (Boyacá), in Vereda Salitre (Figures 1 and 2), and includes the base of the Guadalupe Group and part of the Plaeners Formation. The second section, in Alto del Gavilán, along the road from Motavita to the Honda stream sector (Figures 1 and 17), includes the upper part of the Conejo Formation and the base of the Guadalupe Group.

4.1.1 Stratigraphic section of Vereda Salitre

The measured thickness was 275 m. The coordinates of the starting point are N: 1099136; E: 1083027; Z: 2858 m a.s.l. The coordinates of the end point are N: 1099257; E: 1082621; Z: 2804 m a.s.l. The outcrop has an average N41°E strike and 51° NW dip (Figure 2).

The section was divided into five segments (Figure 3), termed, from the base to the top, A, B, C, D, and E. Segments A, B, and C have a thickness of 99.8 m and correspond to the base of the Guadalupe Group; segments D and E have a thickness of 171.4 m and are part of the Plaeners Formation. The contact with the Conejo and Plaeners formations is covered (Figure 4).

In general, in this stratigraphic section, the base of the Guadalupe Group is characterized by the presence of porcellanites and cherts with a wackestone texture toward the base and a portion of the top. In contrast, mudstones, siltstones, claystones, and sporadic layers of very fine-grained quartz arenites prevail in the middle and higher parts.

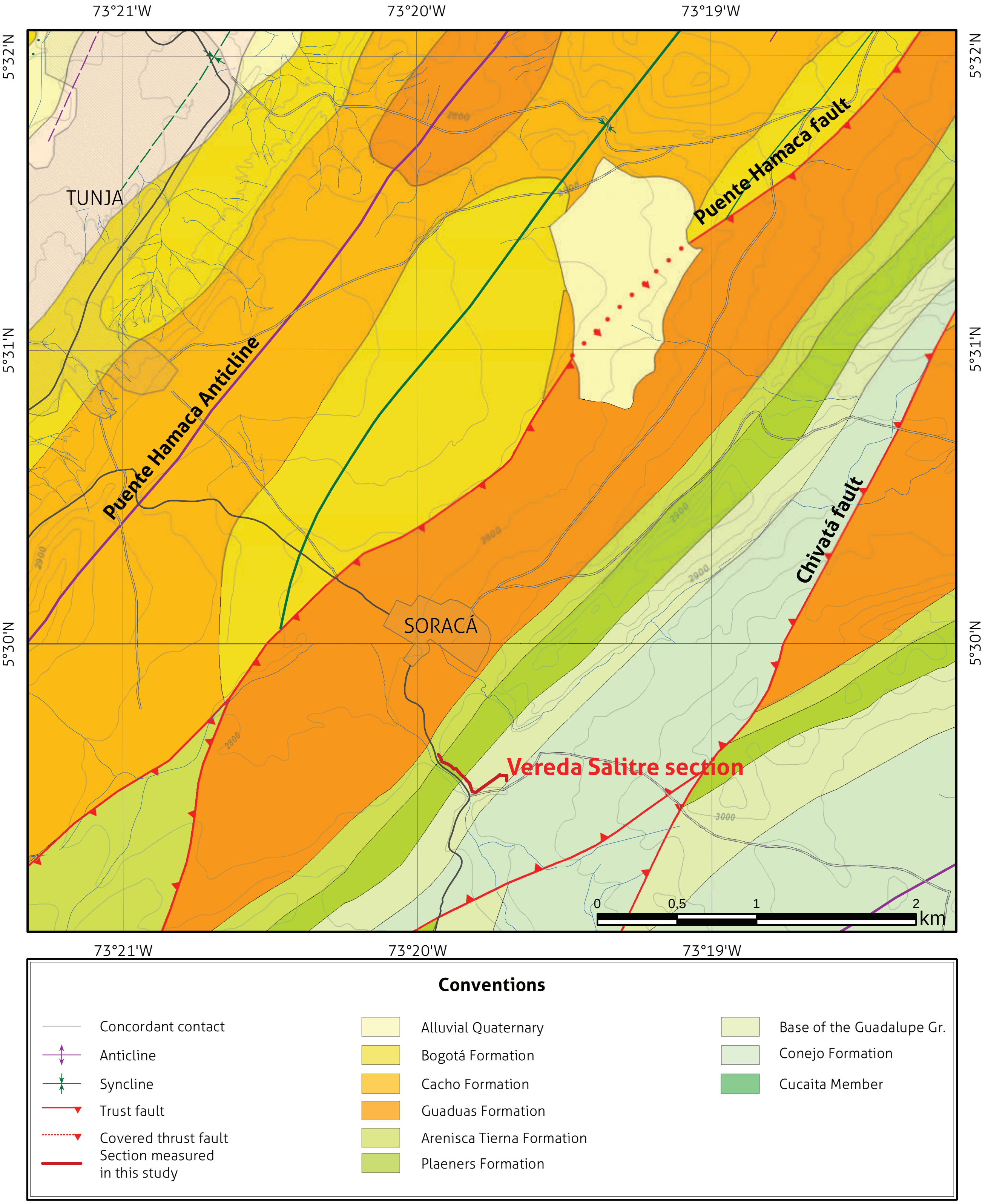

Figure 2. Location and local geology of the Vereda Salitre stratigraphic section
Source: geologic base map retrieved from Terraza et al. (2016)

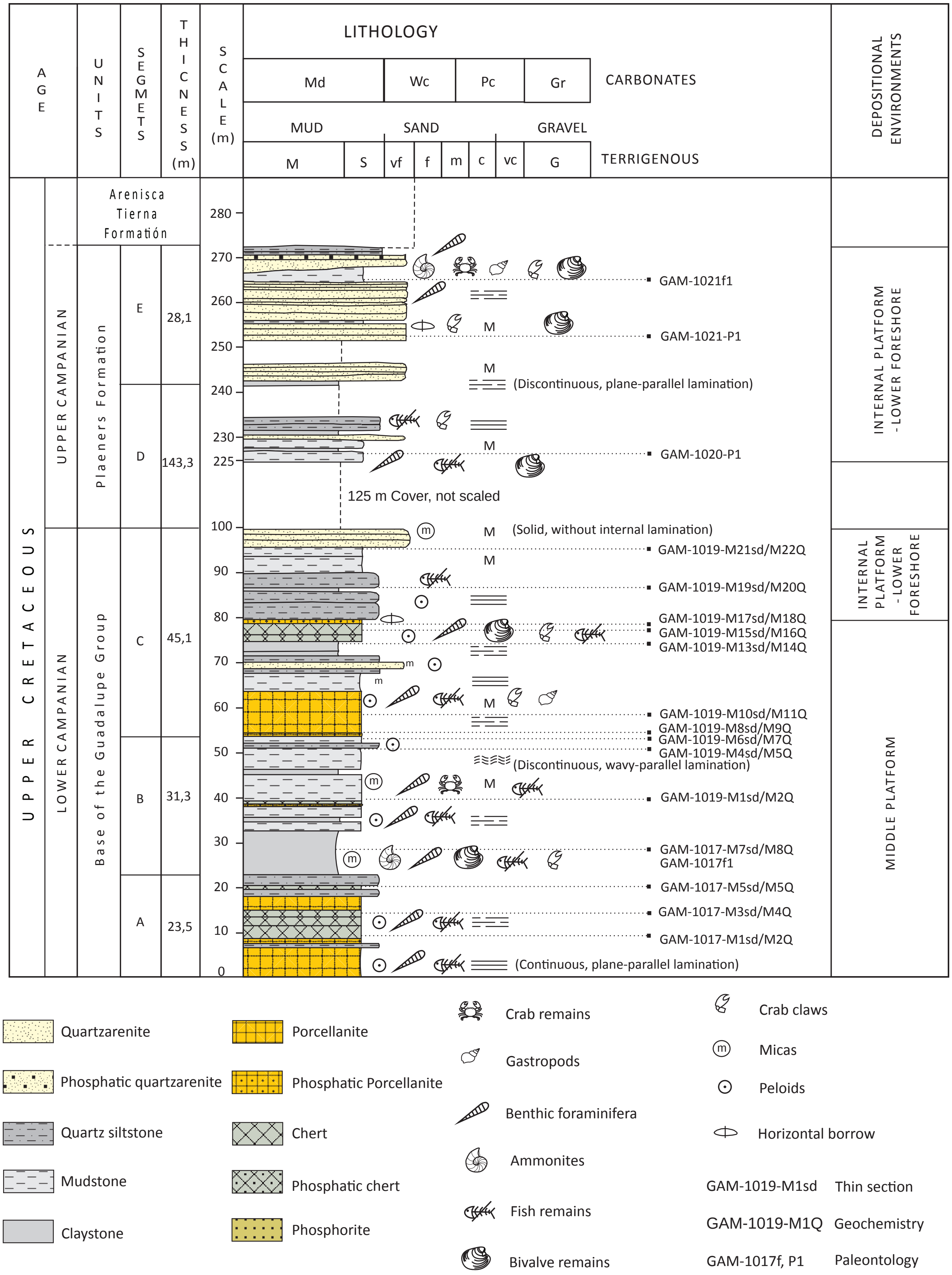

Figure 3. Stratigraphic section of Vereda Salitre

4.1.2 Base of the Guadalupe Group

Segment A (0.0-23.5 m). Segment A was measured in the quarry located by the road from Soracá to the municipality of Boyacá (Figure 5). The layers show continuous, plane-parallel bedding and very thin, discontinuous, plane-parallel lamination. The low part shows 18.5 m of very thin to thin layers of chert with foraminifera and bioclast wackestone texture (Figure 6) and light-gray and orange-grayish-pink porcellanites, with sporadic thin layers of yellowish-gray mature quartz siltstones, without internal lamination. The high part of segment A shows 5 m of thin, medium, and thick layers of bluish-white siltstones and some layers of chert. This interval contains benthic foraminifera, fish remains, and peloids, in addition to some very slightly phosphatic layers. Rocks are moderately weathered with low bioturbation.

Segment B (23.5-53.0 m). Segment B was partly measured in the quarry and partly in the road from Soracá to the municipality of Boyacá (Figures 5 and 9). The layers present continuous plane-parallel bedding and mostly very thin, discontinuous, plane-parallel lamination. From the base to the top, 9.7 m of thick to very thick layers of bluish-white claystones are observed (Figure 7), followed by 4.6 m of medium to thick layers of pale-greenish-yellow mudstones with low bioturbation and sporadic medium, laminated layers of light-brownish-gray claystones. Ascending stratigraphically, a thin, laminated layer of phosphatic porcellanite is found, followed by thin layers of light-brownish-gray chert, with nonvisible lamination and prismatic partitioning. They are followed by 11.6 m of thin to very thin layers of light-brownish-to-brownish gray mudstones, with sporadic layers of siltstones. Segment B ends in a section with 3.2 m of thin to medium, tabular layers of brownish-gray mudstones, with very thin, discontinuous, plane-parallel, lenticular heterolithic lamination and low bioturbation (Figure 8) and medium to thick, tabular layers of yellowish-gray siltstones. This interval contains benthic foraminifera laminae, fish and crab remains, some bivalves, and ammonites, including Campanian "*Didymoceras stevensoni*? (Whitfield, 1877), *Hoploscaphites* sp. Inc.? and *Sphenodiscus* sp.?" (Etayo-Serna, 2015), as well as peloids, siliceous nodules, and muscovite as an accessory mineral.

Figure 4. Morphological contrast of the units of the Guadalupe Group and Conejo Formation in Vereda Salitre (N: 1099147; E: 1083034; Z: 2904; azimuth: 200°)

Figure 5. Abandoned quarry located by the Soracá-Boyacá road, showing segment A and part of segment B (N: 1099175; E: 1082984; Z: 2904; azimuth: 120°)

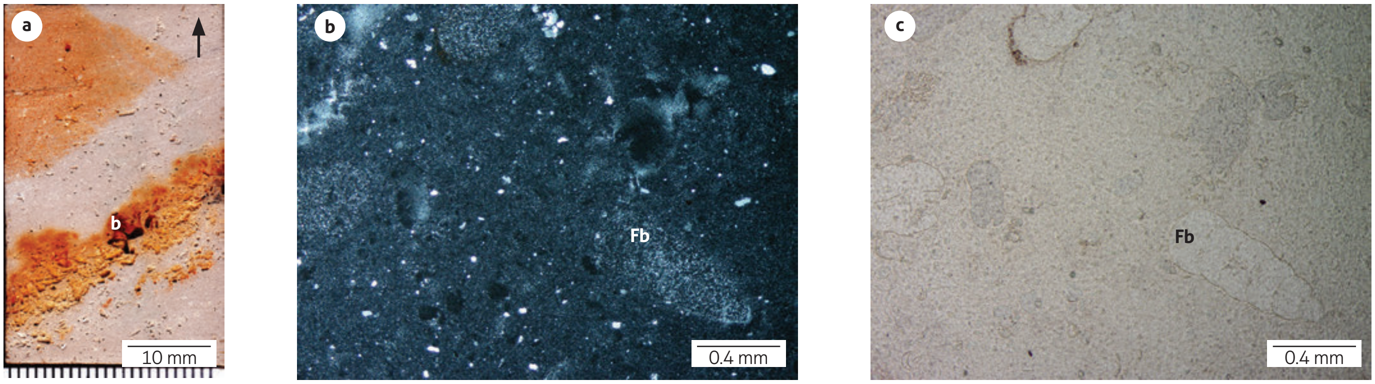

Figure 6. Polished section (a) and micrographs (b, c) of a chert with wackestone texture showing benthic foraminifera (Fb) and bioclasts (b) embedded in microcrystalline quartz
Segment A, sample GAM-1017-M3sd, 14.7 m. Crossed (b) and parallel nicols (c).

Fb

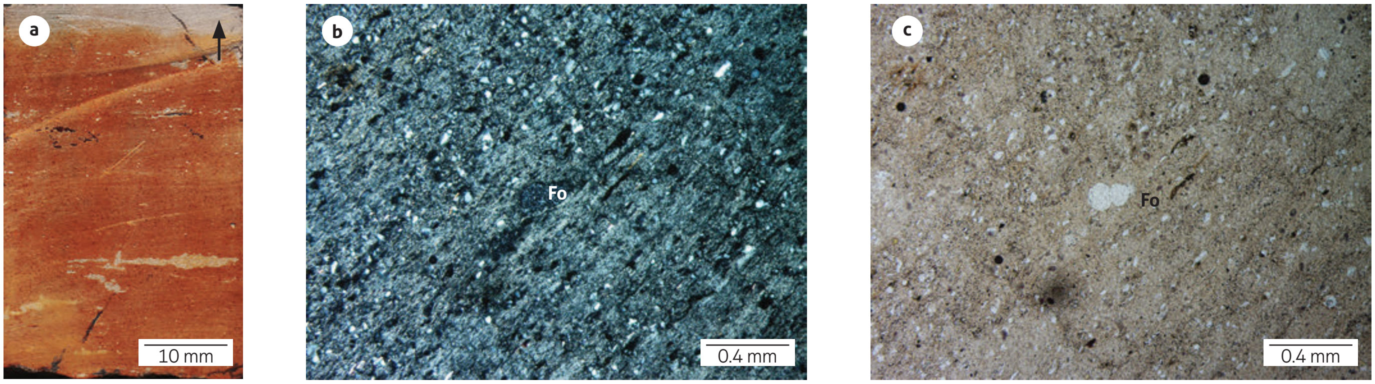

Figure 7. Polished section (a) and micrographs (b, c) of a claystone showing foraminifera (Fo) in a clay mineral framework
Segment B, sample GAM-1017-M7sd, 28.4 m. Crossed (b) and parallel nicols (c).

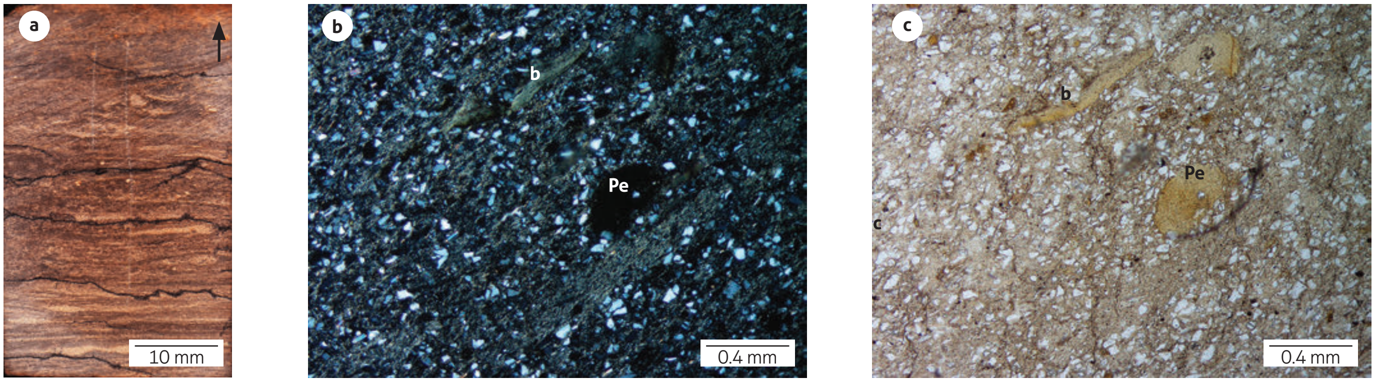

Figure 8. Segment C, sample GAM-1019-M4sd, 51.6 m
(a) Polished section of a mudstone with lenticular heterolithic lamination. B and C show bioclasts (b) and phosphatized peloids (Pe) supported by laminae of clay minerals and quartz grains. Micrograph of crossed (b) and parallel nicols (c).

Segment C (54.7-99.8 m). Segment C was measured in the road from Soracá to the municipality of Boyacá (Figure 9). Most layers show continuous plane-parallel bedding and very thin to thin, discontinuous, plane-parallel lamination. The lower, middle, and upper parts of the segment are described below.

The lower part begins with a 0.3 m layer of phosphatic porcellanite with peloids, followed by 8.7 m of a very thick set of layers, consisting of thin, medium, and thick layers of porcellanites and siltstones without internal lamination (Figure 10); bioturbation ranging from low to high; and sporadic medium layers of phosphatic porcellanites. Ascending stratigraphically, 3.5 m of thin layers of mudstones are found with low bioturbation, followed by 2.9 m of very thin to thin layers of siltstones, with low bioturbation, and then by 4.4 m of thin to medium layers of very fine-grained, somewhat phosphatic, mature quartz arenites, with moderate bioturbation, interspersed with thin to medium, tabular layers of siltstones and some mudstones. This interval is characterized by the presence of benthic foraminifera, fish remains, crab claws, gastropods, peloids, and muscovite as an accessory mineral; the typical colors are very light gray, light medium gray, light brownish gray, and pale greenish yellow.

The middle part of the segment (Figure 11) starts with 4.1 m of very thin, thin, and medium layers of cherts, with low bioturbation, interspersed with tabular, thin, and medium layers of porcellanites, followed by a tabular, (0.3 m) thin layer of phosphatic porcellanite (Figure 12), with peloids and bioclasts, high bioturbation, and horizontal burrows toward the base of the layer. Then we find a 10.6-m-thick section starting with very thin to thin layers of siltstones, low bioturbation, and sporadic layers of chert. This is followed by a tabular, medium layer of very fine-grained, mature quartz arenites, with bioturbation ranging from high to moderate. This layer continues to thin layers of porcellanites with nonvisible lamination, followed by thin to medium layers of siltstones with nonvisible lamination and high bioturbation and, finally, sporadic, thin to medium layers of claystones, porcellanites, and phosphatic mudstones. The typical colors are very light gray, medium gray, greenish yellow, and very pale orange.

The upper part of the segment shows 5.5 m of medium layers of mudstones, with high bioturbation and an interspersed, tabular, medium layer of claystones, followed by thin to medium layers of siltstones with high bioturbation and some layers of mudstones, ending with 3.3 m of tabular, thin to medium layers of very fine-grained quartz arenites with nonvisible lamination and high bioturbation. The rocks of this interval are brownish and yellowish gray. They contain remains of fish, crabs, peloids, crab claws, horizontal burrows, benthic foraminifera, and some bivalves in porcellanites, in addition to mica as an accessory mineral.

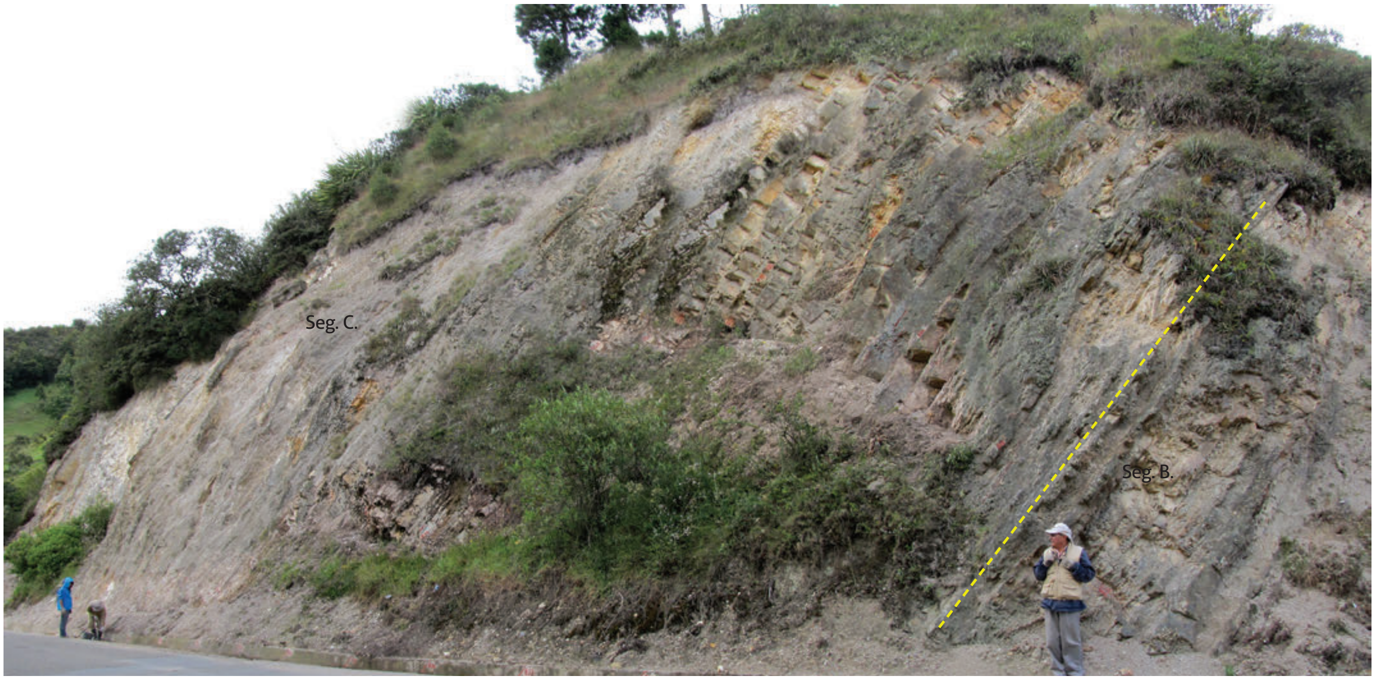

Figure 9. Outcrop in the Soracá-to-Boyacá roadcut showing segment C and the upper part of segment B. (N: 1099067; E: 1082810; Z: 2872; azimuth: 300°)

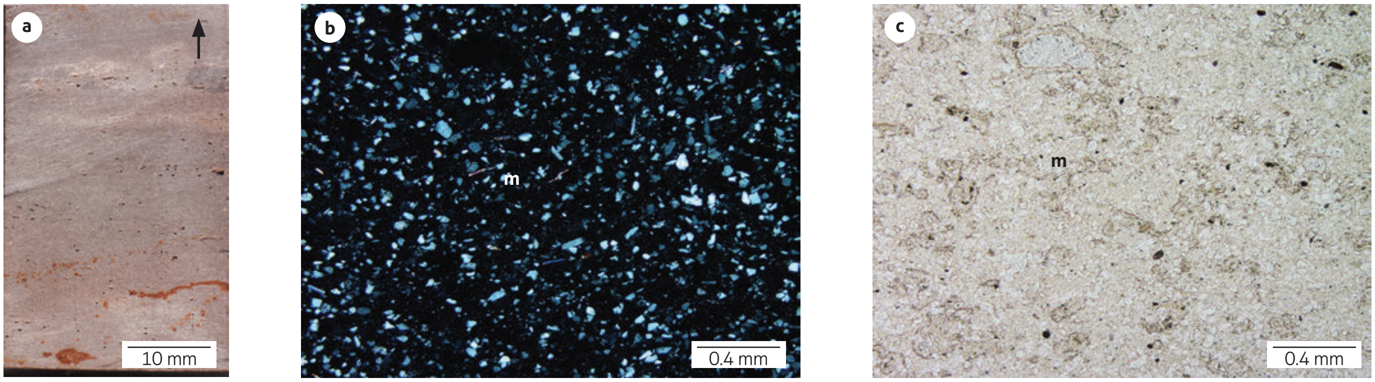

Figure 10. Polished section (a) of porcellanite. The micrographs show grains of muscovite (m) and quartz supported by microcrystalline quartz. Crossed (b) and parallel nicols (c). Segment C, sample GAM-1019-M10sd, 58.4 m.

Figure 11. Contact between the base of the Guadalupe Group, middle and upper part of segment C and the Plaeners Formation, which starts with a cover in segment D (N: 1099115; E: 10827950; Z: 2702; azimuth: 50°).

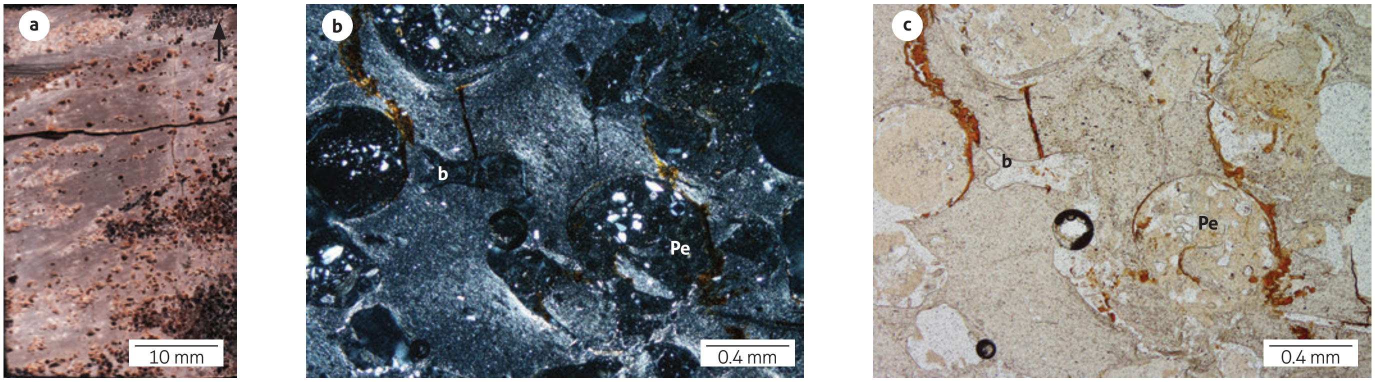

Figure 12. Polished section of a phosphatic porcellanite with wackestone texture
The micrographs show phosphatic peloids (Pe) and bioclasts (b) embedded in microcrystalline quartz. Crossed (b) and parallel nicols (c). Segment C, sample GAM-1019-M17sd, 79.6 m.

4.1.3 Plaeners Formation

Segment D (99.8-243.1 m). Most layers show continuous, plane-parallel bedding and thin to very thin, discontinuous, plane-parallel lamination. Segment D starts with a 125.1-m cover (Figure 13), followed by a 9.9-m-thick stratum consisting of thick and very thick layers of mudstones, with high bioturbation. Next, a tabular, medium layer of siltstones is followed by thick to very thick layers of mudstones; thick layers of claystones; thin to very thin layers of mudstones; a tabular, very thick layer of very fine-grained, mature quartz arenites; a tabular, very thick layer of claystone, with nonvisible lamination; a tabular, very thick layer of mudstone; and, lastly, medium to thick layers of siltstones. Ascending stratigraphically, a 7.3-m cover is then identified in this segment, which ends with 1 m of claystones in thin to medium layers. The rocks of this interval are medium gray, brownish gray, dark gray, and light olive gray and contain benthic foraminifera, fish remains, crab claws, some bivalves, peloids, and micas.

Segment E (243.1-271.2 m). The layers show continuous and discontinuous plane-parallel bedding, starting with 4.1 m of medium to thick layers of very fine-grained, mature quartz arenites with nonvisible lamination and high bioturbation, continuing with a cover of 5.1 m. Ascending stratigraphically, a 12.2-m-thick stratum starts with tabular, medium to thick layers of very fine-grained quartz arenites with discontinuous, nonparallel wavy lamination and medium bioturbation, followed by a very thick cuneiform layer of very fine-grained, mature quartz arenites with horizontal burrows toward the base with high bioturbation and large bivalves (>5 cm) of the Campanian species *Abruptolopha abrupta* (D'Orbigny, 1842) and *Gastrochaenolites socialis* (D'Orbigny, 1842) (Etayo-Serna, 2015), as shown in Figure 14. Next we find medium, thick, and very thick layers of very fine-grained, mature quartz arenites, with medium to high bioturbation and sporadic layers of siltstones. The rocks in this interval are grayish orange, very pale orange, and greenish yellow and contain peloids, crab claws, benthic foraminifera, and muscovite as an accessory mineral.

Higher up stratigraphically, we find 2.6 m of thick to very thick layers of grayish-orange mudstones with discontinuous plane-parallel bedding, high bioturbation, and the following ammonites (Figure 15):

> *Exiteloceras jenneyi jenneyi* (Whitfield, 1880), *Libycoceras* sp. inc. and *Sphenodiscus* sp. Inc.? and the bivalves *Gyrostrea* cf. *glabra* (Meek and Hayden, 1857), *Ostrea cretacea*? *(*Meek and Hayden*,* 1857), *Ostrea tecticosta* (Gabb, 1860), *Paranomia scabra* (Morton, 1834), *Tenuipteria* cf. *argenta* (Conrad, 1858), *Lima* cf. *acutilineata* (Conrad, 1858), and crab remains of the Upper Campanian (Etayo-Serna, 2015).

Segment E ends with a 5.2-m-thick stratum formed by medium to thick cuneiform layers of very fine-grained, pale-greenish-yellow quartz arenites with high bioturbation, followed by a thick, cuneiform layer of phosphatic, light-brown quartz arenites with peloids, then very thick layers of sandy, white siltstone with discontinuous, plane-parallel, thin lamination with bivalves and peloids, then a tabular, medium layer of porcellanite, and lastly medium to thick layers of silicious siltstones (Figure 16) with nonvisible lamination and with some benthic foraminifera and micas.

Figure 13. Contact between the base of the Guadalupe Group and the Plaeners Formation
Segment E is covered and shows soft morphology, typical of silt-clayey lithology (N: 1099140; E: 1 082775; Z: 2864; azimuth: 10°)

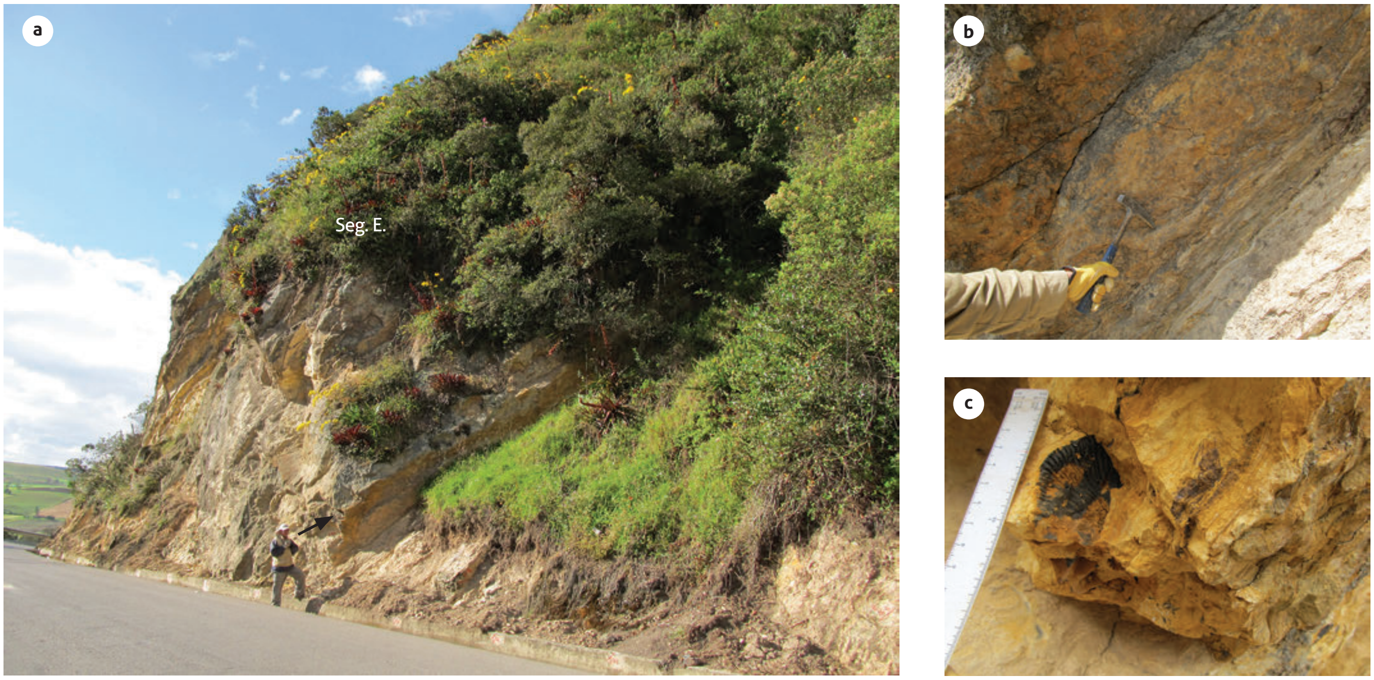

Figure 14. View of segment E of the Plaeners Formation (a)
The first layer of quartz arenites (black arrow) shows horizontal burrows toward the base (b) and *Abruptolopha abrupta* bivalves (c) (E: 1099231, N: 1082625; Z: 2884; azimuth: 30°).

Figure 15. Level of mudstones in segment E; some of the ammonites found in this segment are detailed on the right (N: 1099257; E: 1082621; Z: 2807)

Figure 16. Upper part of segment E of the Plaeners Formation
The contact with the Arenisca Tierna Formation is outlined (N: 1099257; E: 1082621; Z: 2807; azimuth: 20°)

4.1.4 Stratigraphic section of Alto del Gavilán

The measured thickness was 141.6 m. The coordinates of the starting point are N: 1111734; E: 1076950; Z: 2977 m a.s.l. The coordinates of the end point are N: 1111594; E: 1077100; Z: 3172 m a.s.l. The outcrop has an average N 60°E strike and 36° SE dip (Figure 17).

The section was divided into four segments (Figure 18), termed, from the base to the top, A, B, C, and D. Segments A and B, with a thickness of 66 m, correspond to the top of the Conejo Formation, and segments C and D, with a thickness of 75.6 m, correspond to the base of the Guadalupe Group. In this locality, the base of the Guadalupe Group generates a ridge that contrasts with the valleys of the Conejo and Plaeners formations (Figure 19).

In general, in this stratigraphic section, the base of the Guadalupe Group predominantly shows porcellanites and cherts with wackestone texture, with some layers of very fine-grained quartz arenites and quartz siltstones.

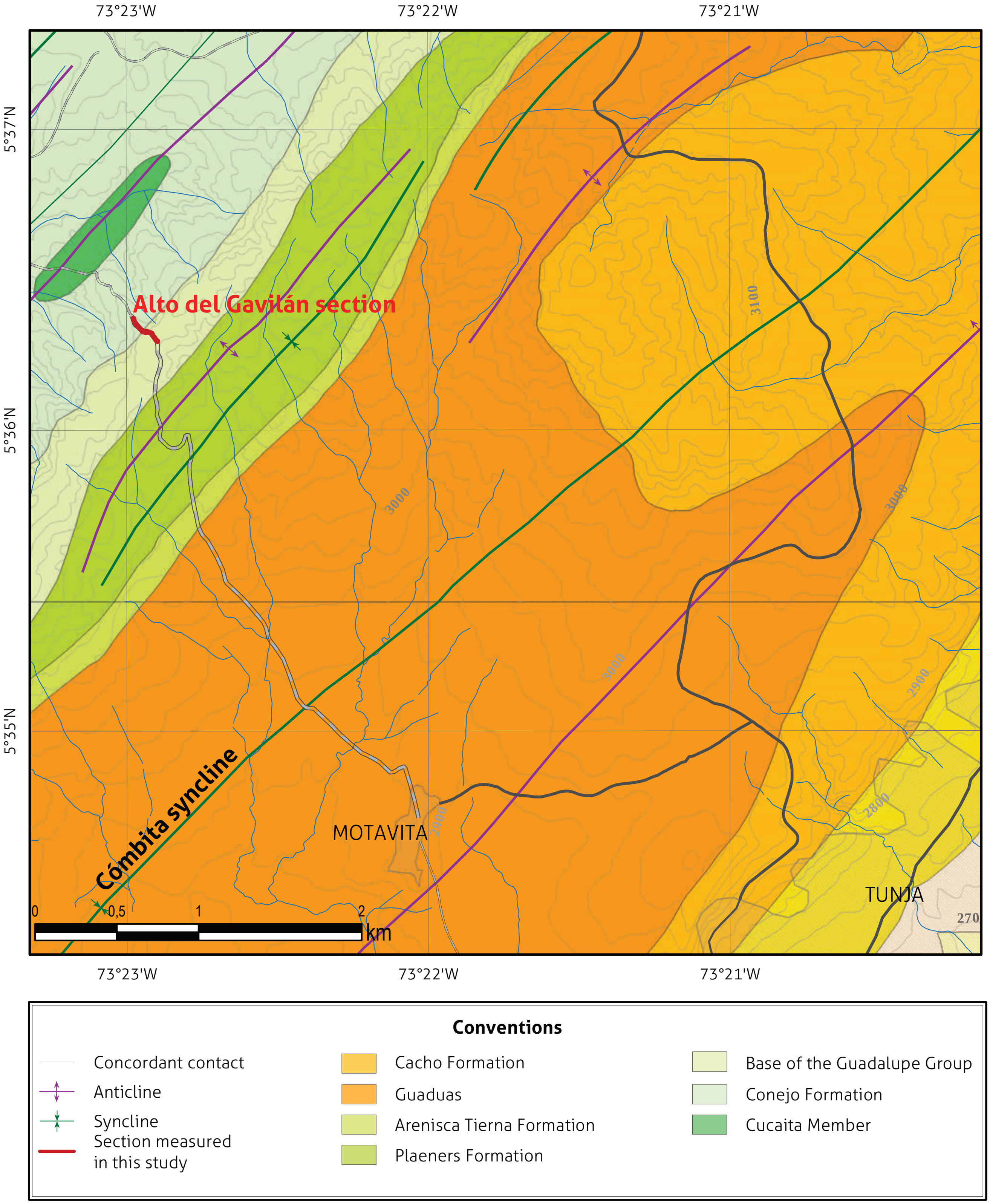

Figure 17. Location and local geology of the stratigraphic section of Alto del Gavilán
Source: geologic base map retrieved from Terraza et al. (2016)

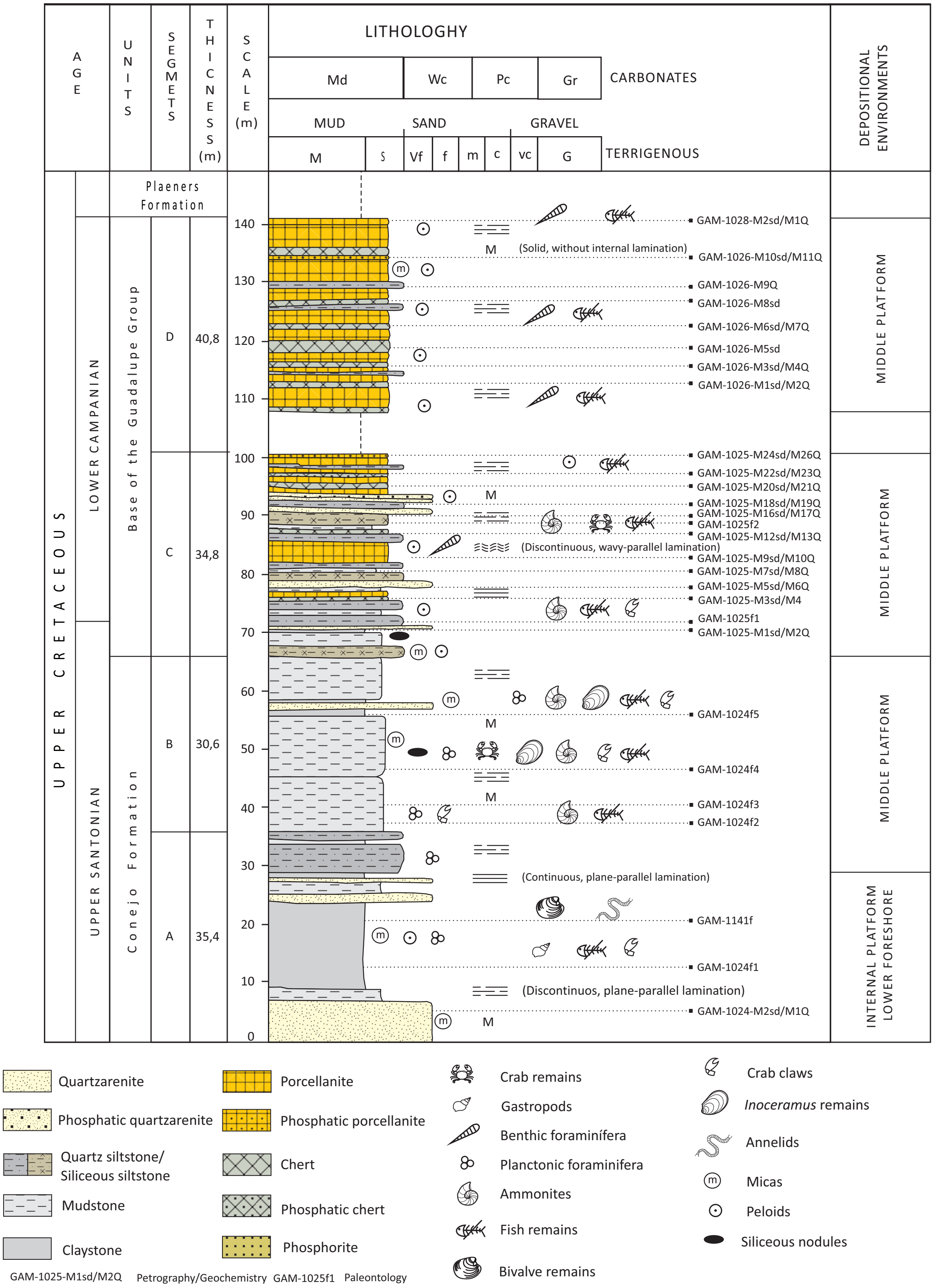

Figure 18. Stratigraphic section of Alto del Gavilán

Figure 19. SW view (Alto del Gavilán) showing the morphological contrast between the Conejo and Plaeners formations and the base of the Guadalupe Group (N: 1115657; E: 1080404; Z: 3081)

4.1.5 Conejo Formation

Segment A (0.0-35.4 m). The layers typically show continuous, plane-parallel bedding and very thin to thin, discontinuous, plane-parallel lamination, and the rocks are highly weathered. From the base to the top, segment A starts with a 6.9-m stratum of medium to very thick layers of very fine-grained, mature, pale-greenish-yellow quartz arenites with high bioturbation and sporadic layers of very fine-grained quartz arenites with discontinuous, wavy, nonparallel lamination, followed by a 2.4-m stratum of thin layers of very light-gray mudstones, continuing with 15 m of thin layers of brownish-gray claystones. Then a 1.7-m tabular layer of very fine-grained quartz arenites is followed by a 2-m layer of pale brown mudstones, by a 0.5-m tabular layer of very fine-grained quartz arenites, and by a 1.2-m layer of light-gray claystones, ending with 5.7 m of thin, medium, thick, and very thick layers of brownish-gray clayey siltstones (Figure 20). This interval contains planktonic foraminifera, fish remains, gastropods, crab claws, peloids, micas, and iron oxides.

Segment B (35.4-66.0 m). Segment B predominantly shows thin, medium, thick, and very thick layers of dark-yellowish-brown, brownish-gray, medium-brown, and medium-dark-gray mudstones with discontinuous to solid plane-parallel lamination and moderate to high bioturbation; sporadic thin, medium, and thick layers of dark-brown claystones; and tabular, medium to very thick layers of very fine-grained, medium-dark-gray quartz arenites with high bioturbation (Figure 21). This segment is characterized by the presence of ammonites such as “*Cocuyites cocuyensis* (Etayo-Serna, 1985), *Paratexanites* sp. inc., *Placenticeras* sp.? and the Upper Santonian bivalves *Meretrix eufaulensis*? (Conrad, 1860) and *Platyceramus* ex gr. *P. cycloides* (Wegner, 1905)” (Etayo-Serna, 2015). Some of these fossils are illustrated in Figures 21 and 22. Segment B also contains iron oxide concretions, siliceous nodules, planktonic foraminifera, crab claws, fish remains, organic matter, and micas.

Figure 20. Upper part of segment A and start of segment B of the Conejo Formation (N: 1111704; E: 1076962; Z: 3177; azimuth: 100°)

Figure 21. Base of segment B showing tabular, medium to thin layers of mudstones (a), with ammonites (b) and inoceramids (c) (N: 1111649; E: 1076026; Z: 3188)

Figure 22. Top of segment B of the Conejo Formation with layers of claystone (a) containing ammonite impressions shown in (b) and (c) (N: 1111676; E: 1076987; Z: 3186; azimuth: 95°)

4.1.6 Base of the Guadalupe Group

Segment C (66.0-100.8 m). The contact with the Conejo Formation (segment B) is net concordant (Figure 23). Segment B is characterized by continuous plane-parallel bedding and by very thin to thin, discontinuous, plane-parallel lamination.

The lower part of segment C starts with 1.7 m of thin to medium layers of siliceous siltstones, followed by 7.7 m of stratigraphic thickness with the following components: thin layers of mudstones and claystones (Figure 24) with siltstone nodules, followed by medium to thin layers of siliceous siltstones, with Lower Campanian ammonites such as "*Submortoniceras* sp. cf. *uddeni* (Young, 1963)" (Etayo-Serna, 2015), interspersed with tabular, thin layers of mudstones (Figure 25). Ascending stratigraphically, 1.5 m of thin to medium layers of porcellanites and cherts are followed by 5.7 m of the following lithology: medium layers of siltstones, followed by thin to medium layers of somewhat fossiliferous, very fine-grained quartz arenites with tabular geometry, and then thin to medium layers of siltstones with sporadic layers of porcellanites. Subsequently, 3.4 m of medium to thin layers of porcellanites containing quartz arenite nodules are followed by layers with chert nucleation, by a very thin layer of ferruginous grayish red siltstones, by a 0.9-m-thick stratum of thin to medium layers of siltstones, and by a 1.8-m-thick stratum of thin to medium layers of porcellanites and chert with foraminifera and peloid wackestone texture (Figure 26). These are interspersed with sporadic layers of quartz arenites and siliceous siltstones. Most rocks of this interval show the following colors: very light gray, brownish gray, pinkish gray and pale greenish yellow.

In the upper part of segment C, a fossil level of 1.2 m (Figure 27) consists of medium to thick layers of yellowish-gray mudstones, with impressions of ammonites such as *Submortoniceras uddeni*? (Young, 1963), suggesting the Lower Campanian (Etayo-Serna, 2015), and, as shown in Figure 27, fish and crab remains and peloids, followed by subtabular, thin to medium layers of sandy mudstone with high bioturbation (Figure 28). The upper part of segment C continues with a 7.8-m-thick stratum with the following structure: a thick and somewhat fossiliferous layer of quartz arenites, with nonvisible lamination, followed by thin layers of porcellanites with continuous, plane-parallel bedding and sporadic layers of chert; above, tabular, thin to medium layers of siliceous siltstones interspersed with a tabular, medium layer of chert with peloid wackestone texture (Figure 29) and nonvisible lamination, which are followed by thin to medium layers of porcellanites and by a tabular, medium layer of phosphatic porcellanite with peloid wackestone texture and nonvisible lamination. In this interval, the rocks are very light gray and pale greenish yellow. The upper part of segment C also contains benthic foraminifera, ammonite impressions, crabs, fish remains, peloids, micas, and iron oxides.

Figure 23. Contact between the Conejo Formation and the base of the Guadalupe Group, which corresponds to the boundary between segments B and C (N: 1111697; E: 1076987; Z: 3186; azimuth: 160°)

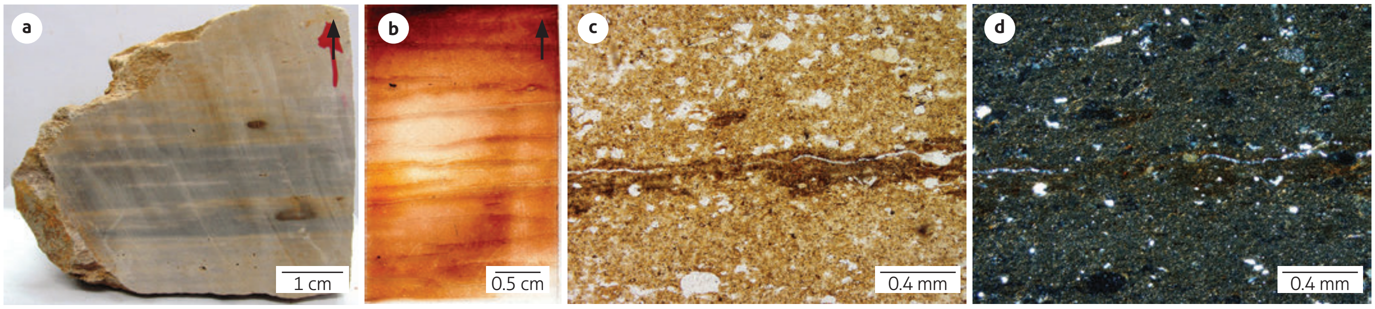

Figure 24. Sample GAM-1025-M1 sd of segment C, at 70.7 m
(a) Polished section of a laminated claystone. (b) Thin lamina of claystone showing discontinuous, wavy to plane-parallel lamination. Micrographs show crossed (c) and parallel nicols (d) showing clayey minerals with some floating quartz.

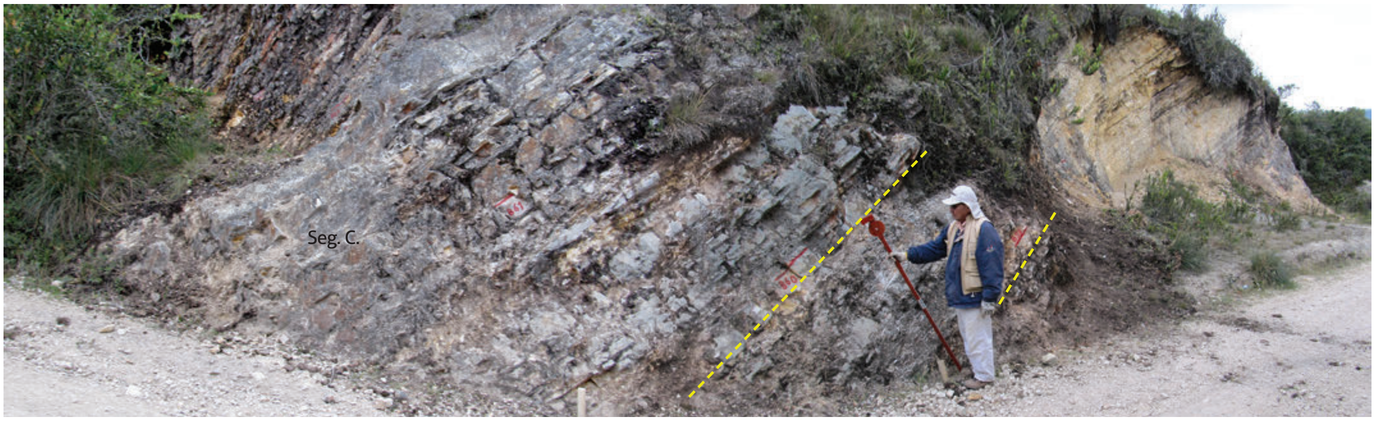

Figure 25. Base of segment C showing a fossiliferous level with ammonites in layers of siliceous siltstones and porcellanites (N: 1111649; E: 1077026; Z: 3188; azimuth: 255°)

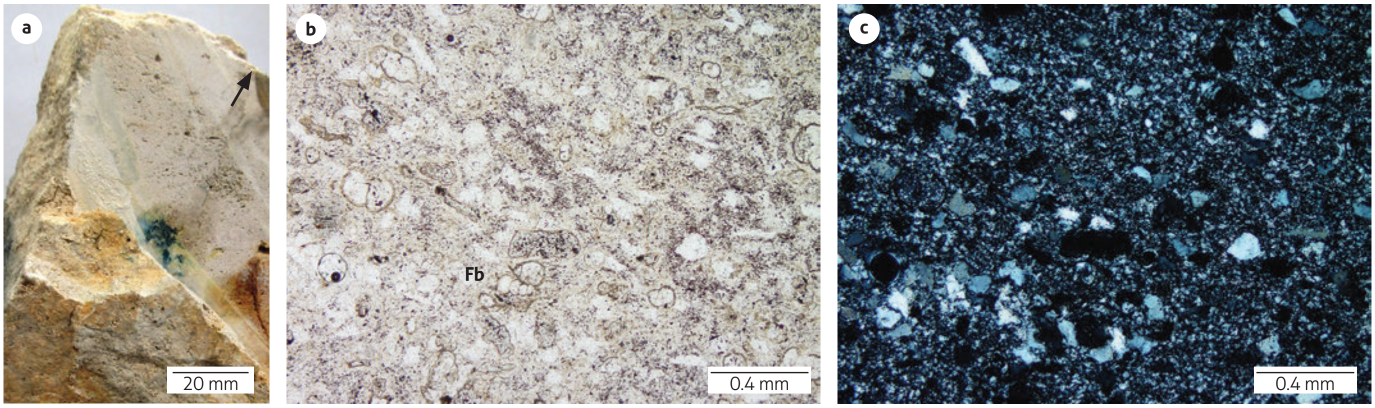

Figure 26. Sample GAM-1025-M12sd, 83.7 m, segment C
Polished section of a chert (a). The micrographs show benthic foraminifera (Fb) and bioclasts supported on finely crystalline quartz. Parallel (b) and crossed nicols (c).

Figure 27. Fossiliferous level of segment C (a) showing layers of siltstones and porcellanites, with ammonites magnified in b and c

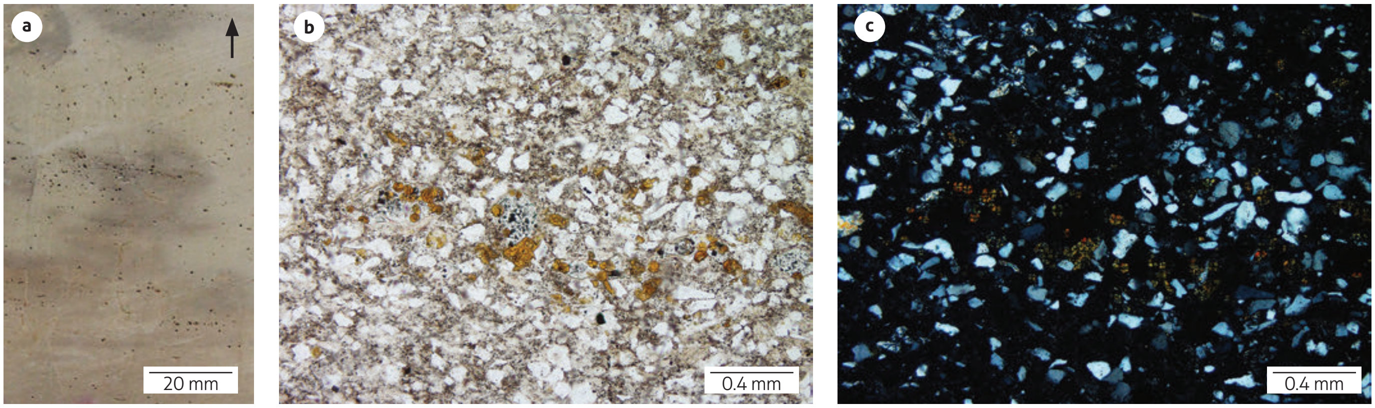

Figure 28. Sample GAM-1025-M14sd, segment C, 90 m
Polished section of a sandy mudstone (a). The micrographs show yellow grains of quartz and phosphates, supported by microcrystalline quartz and clayey minerals. Parallel (b) and crossed nicols (c).

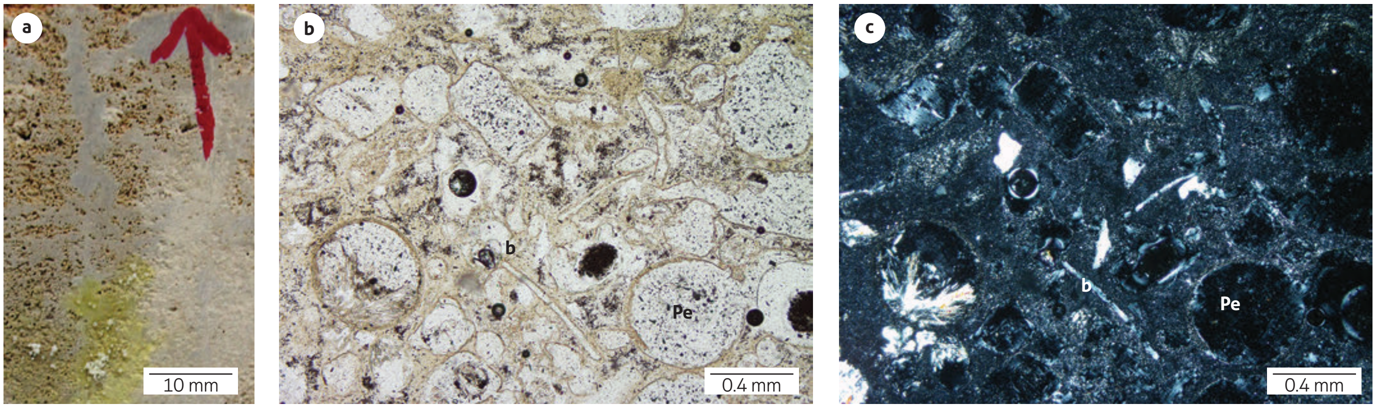

Figure 29. Sample GAM-1025-M22sd, segment C, 96.6 m
Polished section of a chert with peloid and bioclast wackestone texture (a). The micrographs show peloids (Pe) and bioclasts (b), supported by microcrystalline quartz (with chalcedony replacing peloids). Parallel (b) and crossed nicols (c).

Segment D (100.8-141.6 m). The outcrop generally presents continuous, plane-parallel bedding, and the layers show very thin to thin, nonvisible, discontinuous, plane-parallel lamination, predominantly with porcellanites (Figure 30). From the base to the top, the following sequence is identified: First, thin layers of porcellanites are interspersed with sporadic layers of chert and three wavy, intercalated, very thin layers of ferruginous, grayish-red siltstone. Then, thin to medium layers of siltstones are followed by thin to medium layers of porcellanites with tabular geometry, with sporadic layers of chert, siliceous siltstones, and two very thin layers of ferruginous siltstones. Next, a tabular, medium layer of fossiliferous porcellanite shows a peloid wackestone texture. At the top of the segment, tabular, thin to medium layers of fossiliferous porcellanite with a benthic foraminifera wackestone texture, interspersed with layers of chert, are followed by a covered zone with soft morphology that belongs to the Plaeners Formation. In this interval, the rocks show the following colors: very light gray, white, pinkish gray, and bluish white. The top of segment D also contains benthic foraminifera, fish remains, peloids, micas, and iron oxides.

Figure 30. Segment D, predominantly with tabular, thin, medium, and thick layers of porcellanites (N: 1111585; E: 1077080; Z: 3199; azimuth: 340°)

4.2 Results from XRD and XRF analysis

Within the stratigraphic interval that corresponds to the base of the Guadalupe Group, in the two stratigraphic sections measured in this study, systematic sampling was performed as follows: seventeen samples were collected in Vereda Salitre and nineteen in Alto del Gavilán. These samples were sent to the Laboratory of the SGC, where they were characterized mineralogically and geochemically by XRD and XRF. The results are outlined in Tables 2, 3, 4, and 5. The dashes shown in some of the cells of these tables indicate values below the detection limits of the diffraction and fluorescence equipment.

From the batch of samples collected at the base of the Guadalupe Group, in Vereda Salitre (Tables 2 and 3), the mineralogical analyses determined that eight samples are siliceous rocks (cherts and porcellanites) and that nine samples are siliciclastic rocks (claystones, mudstones, and quartz arenites). They have (detritic and silica) quartz contents ranging from 66.7 to 99.8%, as corroborated by geochemical data, which shows that silica (SiO_2) ranges from 62.6 to 95.7% (Figure 31). In conclusion, although the texture determined by petrographic analysis is typical of calcareous and phosphatic rocks (wackestone), minerals with calcium and phosphorus, such as hydroxyapatite and carbonatofluoroapatite, are only present in two samples. In general, throughout the stratigraphic interval, the values of calcium oxide (CaO) are lower than 4.0% (Figure 31), and the values of phosphoric oxide (P_2O_5) range from 0.2 to 5.4%.

Kaolinite is also detected, with values ranging from less than 2.0 to 21.3%, in line with the values of aluminum oxide (Al_2O_3), which range from 2.0 to 14.4%, as possible alteration products of aluminum silicates (Figure 31).

Table 2. Mineralogical results (XRD) of the samples collected in Vereda Salitre

Sample	Equivalent petrographic sample	In the section (m)	Quartz (%)	Kaolinite (%)	Muscovite (%)	Goethite (%)	Hydroxyapatite (%)	Wavellite (%)	Microcline (%)	Carbonate fluorapatite (%)	Rock classification, Folk (1954, 1974) y Williams et al. (1954)
GAM-1019-M22Q	GAM-1019-M21 sd	95.7	83.9	13.5	0.0	0.0	0.0	0.0	2.6	0.0	Mudstone
GAM-1019-M20Q	GAM-1019-M19sd	88.7	85.2	11.9	0.0	0.0	0.0	0.0	0.0	3.0	Mudstone
GAM-1019-M18Q	GAM-1019-M17sd	79.6	84.7	6.8	0.0	0.0	0.0	8.5	0.0	0.0	Porcellanite
GAM-1019-M16Q	GAM-1019-M15sd	77.7	90.5	_	3.1	0.0	0.0	0.0	4.6	0.0	Chert
GAM-1019-M14Q	GAM-1019-M13sd	74.6	81.2	7.2	5.7	0.0	0.0	0.0	5.9	0.0	Mudstone
GAM-1019-M12Q	Not collected	71.3	76.1	23.3	0.0	0.0	0.0	0.0	_	0.0	Quartz arenite
GAM-1019-M11Q	GAM-1019-M10sd	58.4	92.5	7.2	0.0	0.0	0.0	0.0	_	0.0	Porcellanite
GAM-1019-M9Q	GAM-1019-M8sd	54.8	80.2	10.4	0.0	0.0	7.4	0.0	_	0.0	Porcellanite
GAM-1019-M7Q	GAM-1019-M6sd	53.2	85.1	9.6	0.0	0.0	0.0	0.0	5.3	0.0	Mudstone
GAM-1019-M5Q	GAM-1019-M4sd	51.6	80.9	4.5	5.9	0.0	0.0	0.0	8.7	0.0	Mudstone
GAM-1019-M3Q	Not collected	43.5	66.7	20.6	12.7	0.0	0.0	0.0	0.0	0.0	Mudstone
GAM-1019-M2Q	GAM-1019-M1 sd	39.3	99.3	0.0	0.0	_	0.0	0.0	0.0	0.0	Chert
GAM-1018-M1Q	Not collected	39.0	70.3	14.7	0.0	15.1	0.0	0.0	0.0	0.0	Porcellanite
GAM-1017-M8Q	GAM-1017-M7sd	28.4	78.7	21.3	0.0	0.0	0.0	0.0	0.0	0.0	Claystone
GAM-1017-M6Q	GAM-1017-M5sd	20.8	91.4	8.6	0.0	0.0	0.0	0.0	0.0	0.0	Chert
GAM-1017-M4Q	GAM-1017-M3sd	14.7	93.2	6.8	0.0	0.0	0.0	0.0	0.0	0.0	Chert
GAM-1017-M2Q	GAM-1017-M1 sd	12.2	99.8	_	0.0	0.0	0.0	0.0	0.0	0.0	Chert

Table 3. Geochemical results (XRF) of the samples collected in Vereda Salitre

Sample	Equivalent petrographic sample	In the section (m)	SiO_2 (%)	TiO_2 (%)	Al_2O_3 (%)	Fe_2O_3 (%)	MgO (%)	CaO (%)	Na_2O (%)	K_2O (%)	P_2O_5 (%)	FeO (%)
GAM-1019-M22Q	GAM-1019-M21 sd	95.7	84.5	0.4	8.2	1.9	0.2	0.1	_	0.8	0.6	0.1
GAM-1019-M20Q	GAM-1019-M19sd	88.7	83.9	0.3	7.9	1.0	0.3	1.0	_	0.6	1.5	_
GAM-1019-M18Q	GAM-1019-M17sd	79.6	75.6	0.2	10.8	0.6	0.1	0.6	_	0.4	5.4	_
GAM-1019-M16Q	GAM-1019-M15sd	77.7	94.5	0.1	3.0	0.2	0.1	0.1	_	0.3	0.2	_
GAM-1019-M14Q	GAM-1019-M13sd	74.6	82.7	0.5	10.0	1.4	0.3	0.1	_	1.0	0.3	_
GAM-1019-M12Q	Not collected	71.3	77.1	0.6	13.4	1.7	0.5	0.1	_	1.2	0.6	_
GAM-1019-M11Q	GAM-1019-M10sd	58.4	90.2	0.3	5.0	1.5	0.1	0.1	_	0.4	0.3	_
GAM-1019-M9Q	GAM-1019-M8sd	54.8	78.4	0.4	7.1	2.2	0.2	3.6	_	0.7	3.7	_
GAM-1019-M7Q	GAM-1019-M6sd	53.2	86.2	0.4	6.9	1.6	0.1	0.1	_	0.9	0.9	_
GAM-1019-M5Q	GAM-1019-M4sd	51.6	81.7	0.4	8.6	3.3	0.3	0.1	_	1.1	0.8	_
GAM-1019-M3Q	Not collected	43.5	75.5	0.6	14.4	1.7	0.5	0.1	_	1.2	0.4	0.2
GAM-1019-M2Q	GAM-1019-M1 sd	39.3	91.7	0.1	2.0	3.8	0.1	0.1	_	0.2	0.2	_
GAM-1018-M1Q	Not collected	39.0	62.6	0.2	4.6	22.1	0.1	0.6	_	0.2	3.8	0.1
GAM-1017-M8Q	GAM-1017-M7sd	28.4	79.3	0.4	11.9	2.2	0.4	0.0	_	1.0	0.2	_
GAM-1017-M6Q	GAM-1017-M5sd	20.8	92.7	0.2	4.1	0.6	0.1	0.1	_	0.3	0.2	_
GAM-1017-M4Q	GAM-1017-M3sd	14.7	95.7	0.1	2.5	0.3	0.1	0.1	_	0.2	0.1	_
GAM-1017-M2Q	GAM-1017-M1 sd	12.2	95.7	0.1	2.4	0.4	0.1	0.1	_	0.2	0.1	_

Mineralogical analysis of the batch of samples collected at the base of the Guadalupe Group, in Alto del Gavilán (Tables 4 and 5), shows that 10 samples are siliceous (cherts and porcellanites) and six are siliciclastic, (claystones, mudstones, and quartz arenites). Their (detritic and silica) quartz at percentages range from 80.8% to 100%, as corroborated by the geochemical data, which show that silica (SiO_2) ranges from 79.2% to 98.5% (Figure 32). The three remaining samples (ferruginous siltstones) show quartz percentages lower than 50.0%, but they have high values of kaolinite (53.0%, 66.0% and 67.3%), hematite, and anatase. Although the texture of siliceous rocks, as determined by petrographic analysis, is typical of calcareous and phosphate rocks (wackestone), minerals with calcium are absent, and minerals with phosphorus, such as wavellite and variscite, are only present in seven samples, at very low percentages, lower than 6.8% (Figure 32). Calcium oxide (CaO) is present in amounts lower than 2.4%, and phosphoric oxide (P_2O_5) ranges from 0.04% to 15.1% (Figure 32).

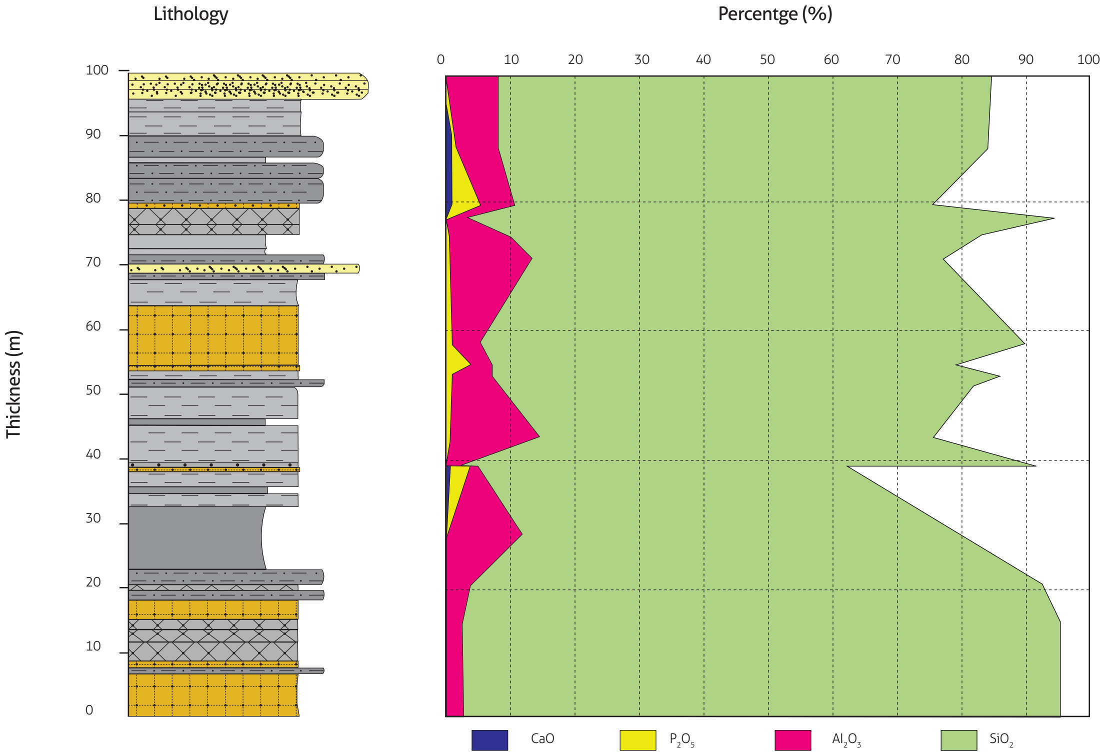

Figure 31. Curves of the percentages of major elements, SiO_2, Al_2O_3, CaO, and P_2O_5, determined by XRF, representing vertically the thickness of the base of the Guadalupe Group in Vereda Salitre

Table 4. Mineralogical results (XRD) of the samples collected in Alto del Gavilán

Sample	Equivalent petrographic sample	In the section (m)	Quartz (%)	Kaolinite (%)	Muscovite (%)	Sepiolite (%)	Greenalite (%)	Hematite (%)	Wavellite (%)	Microcline (%)	Variscite (%)	Anatase (%)	Rock classification, Folk (1954, 1974) and Williams et al. (1954)
GAM-1028-M1Q	GAM-1028-M2sd	141.0	91.3	8.7	0.0	0.0	0.0	0.0	0.0	0.0	0.0	0.0	Porcellanite
GAM-1026-M11Q	GAM-1026-M10sd	134.5	98.8	_	0.0	0.0	_	0.0	0.0	_	0.0	0.0	Chert
GAM-1026-M9Q	Not collected	129.1	12.5	66.0	0.0	2.3	0.0	15.2	0.0	0.0	0.0	4.0	Ferruginous Siltstone
GAM-1026-M7Q	GAM-1026-M6sd	122.8	35.7	53.0	0.0	0.0	0.0	6.3	0.0	0.0	0.0	5.0	Ferruginous Siltstone
GAM-1026-M4Q	GAM-1026-M3sd	115.4	100.0	0.0	0.0	0.0	0.0	0.0	0.0	0.0	0.0	0.0	Chert
GAM-1026-M2Q	GAM-1026-M1 sd	112.9	99.7	0.0	0.0	0.0	0.0	0.0	0.0	_	0.0	0.0	Chert
GAM-1025-M26Q	GAM-1025-M24sd	100.3	80.8	0.0	0.0	0.0	0.0	0.0	18.5	0.0	_	0.0	Porcellanite
GAM-1025-M23Q	GAM-1025-M22sd	96.6	93.2	0.0	0.0	0.0	0.0	0.0	6.8	_	0.0	0.0	Chert
GAM-1025-M21Q	GAM-1025-M20sd	95.4	100.0	0.0	0.0	0.0	0.0	0.0	0.0	0.0	0.0	0.0	Chert
GAM-1025-M19Q	GAM-1025-M18sd	93.8	94.0	0.0	4.1	0.0	0.0	0.0	_	0.0	0.0	0.0	Quartz arenite
GAM-1025-M17Q	GAM-1025-M16sd	91.1	98.6	0.0	0.0	0.0	0.0	0.0	_	_	0.0	0.0	Quartz arenite
GAM-1025-M15Q	GAM-1025-M14sd	90.0	94.1	0.0	4.8	0.0	0.0	0.0	_	0.0	0.0	0.0	Mudstone
GAM-1025-M13Q	GAM-1025-M12sd	87.3	98.4	0.0	0.0	0.0	0.0	0.0	_	0.0	0.0	0.0	Porcellanite
GAM-1025-M11Q	Not collected	85.8	25.9	67.3	0.0	0.0	0.0	6.9	0.0	0.0	0.0	0.0	Ferruginous Siltstone
GAM-1025-M10Q	GAM-1025-M9sd	83.0	92.1	7.5	0.0	0.0	_	0.0	0.0	0.0	0.0	0.0	Chert
GAM-1025-M8Q	GAM-1025-M7sd	80.8	91.8	3.1	4.6	_	0.0	0.0	0.0	0.0	0.0	0.0	Mudstone
GAM-1025-M6Q	GAM-1025-M5sd	77.9	91.6	7.7	0.0	0.0	0.0	0.0	0.0	0.0	0.0	0.0	Mudstone
GAM-1025-M4Q	GAM-1025-M3sd	76.0	100.0	0.0	0.0	0.0	0.0	0.0	0.0	0.0	0.0	0.0	Chert
GAM-1025-M2Q	GAM-1025-M1 sd	70.7	88.5	11.5	0.0	0.0	0.0	0.0	0.0	0.0	0.0	0.0	Claystone

Table 5. Geochemical results (XRF) of the samples collected in Alto del Gavilán

Sample	Equivalent petrographic sample	In the section (m)	SiO_2 (%)	TiO_2 (%)	Al_2O_3 (%)	TFe_2O_3 (%)	MgO (%)	CaO (%)	P_2O_5 (%)	K_2O (%)	Na_2O (%)	FeO (%)
GAM-1028-M1Q	GAM-1028-M2sd	141.0	91.1	0.2	5.1	0.7	0.1	0.1	0.2	_	_	0.3
GAM-1026-M11Q	GAM-1026-M10sd	134.5	93.8	0.1	3.7	0.4	0.1	0.1	0.1	_	_	0.3
GAM-1026-M9Q	Not collected	129.1	36.3	0.8	25.2	26.5	0.3	0.1	0.6	_	_	1.1
GAM-1026-M7Q	GAM-1026-M6sd	122.8	50.0	1.0	19.0	19.6	0.3	0.1	0.8	_	_	0.7
GAM-1026-M4Q	GAM-1026-M3sd	115.4	84.8	0.1	6.9	0.7	0.4	2.4	1.9	_	_	0.3
GAM-1026-M2Q	GAM-1026-M1 sd	112.9	95.8	0.1	2.3	0.4	0.1	0.1	0.1	0.2	_	0.2
GAM-1025-M26Q	GAM-1025-M24sd	100.3	55.4	0.1	17.7	1.1	0.1	0.1	15.1	0.3	_	0.3
GAM-1025-M23Q	GAM-1025-M22sd	96.6	79.2	0.1	8.7	0.6	0.1	0.1	5.3	_	_	0.4
GAM-1025-M21Q	GAM-1025-M20sd	95.4	98.5	0.0	0.7	0.3	0.1	0.1	0.0	_	_	_
GAM-1025-M19Q	GAM-1025-M18sd	93.8	84.1	0.2	6.9	1.2	0.2	0.1	3.2	0.2	_	0.4
GAM-1025-M17Q	GAM-1025-M16sd	91.1	92.5	0.2	3.5	0.6	0.1	0.1	1.4	_	_	0.2
GAM-1025-M15Q	GAM-1025-M14sd	90.0	88.7	0.3	5.4	1.1	0.3	0.1	1.0	_	_	0.6
GAM-1025-M13Q	GAM-1025-M12sd	87.3	88.8	0.2	5.4	1.3	0.2	0.1	1.1	_	_	0.6
GAM-1025-M11Q	Not collected	85.8	46.4	0.7	26.0	13.9	0.7	0.1	0.9	0.2	_	2.2
GAM-1025-M10Q	GAM-1025-M9sd	83.0	91.4	0.2	4.9	0.6	0.2	0.1	0.3	_	_	0.5
GAM-1025-M8Q	GAM-1025-M7sd	80.8	90.1	0.1	5.1	0.9	0.2	0.1	0.8	_	_	0.6
GAM-1025-M6Q	GAM-1025-M5sd	77.9	89.3	0.1	5.3	1.2	0.2	0.1	1.2	0.2	_	0.4
GAM-1025-M4Q	GAM-1025-M3sd	76.0	95.9	0.0	2.4	0.3	0.1	0.1	0.1	0.2	_	0.2
GAM-1025-M2Q	GAM-1025-M1 sd	70.7	87.7	0.2	7.1	0.9	0.3	0.1	0.2	0.2	_	0.8

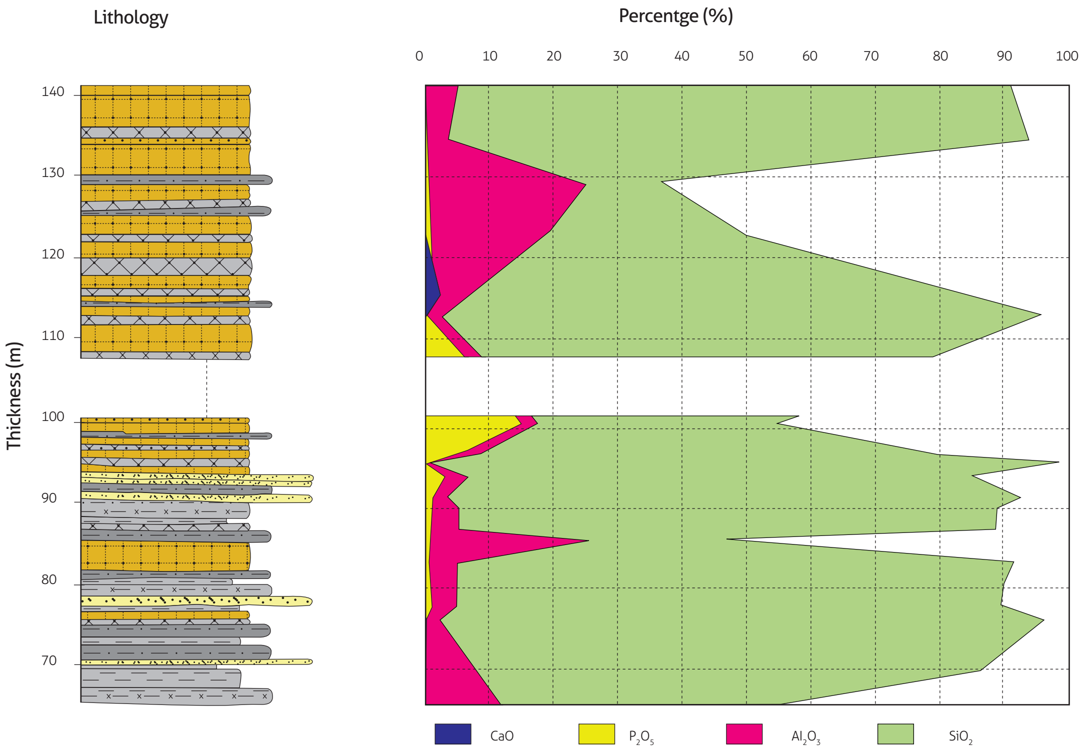

Figure 32. Curves of the percentages of major elements, SiO_2, Al_2O_3, CaO, and P_2O_5, determined by XRF represented horizontally, representing vertically the thickness of the base of the Guadalupe Group in Alto del Gavilán

5. Discussion

The stratigraphic nomenclature corresponding to the Guadalupe Group, in the Tunja area of Colombia, established by Renzoni (1981) and by Renzoni et al. (1976), divided the Guadalupe Group into the Plaeners Formation (kg2) in the base and the Labor-Tierna Formation (kg1) in the top. These authors thought that the Arenisca Dura Formation (kg3) of the Bogotá savanna would be included in the layers of sandstones of the top of the Conejo Formation of this locality. However, the base of the Guadalupe Group, the object of this study, mostly dates back to the Lower Campanian (Etayo-Serna, 2015) and corresponds to the Plaeners Formation (kg2) of Renzoni (1981). In addition, stratigraphically, above the base of the Guadalupe Group, a soft unit of the Upper Campanian (Etayo-Serna, 2015) is overlaid by a set of quartz arenites representing the Plaeners and Arenisca Tierna formations of the Bogotá savanna, included by Renzoni in unit kg1, in this part of the eastern Andes of Colombia (see Figure 1). In the Guadalupe Group of Tunja and its surrounding area, three clearly distinguishable and easily recognizable units can be lithologically and geomorphologically identified. The base of these units (described in this article) differs substantially from the type section in the Eastern Hills of Bogotá. To avoid confusion with the nomenclature proposed by Renzoni (1981), for the moment, the unit in question should be informally designated as “base of the Guadalupe Group” while deciding whether to maintain the nomenclature of Montoya and Reyes (2003 a, b; 2005 a, b; 2007) for this area of the Eastern Andes of Colombia.

The petrographic analysis performed by Martínez (2018) at the base of the Guadalupe Group, in the two stratigraphic sections described in this study, showed that most cherts and porcellanites with wackestone or mudstone texture with allochems replaced by microcrystalline quartz and chalcedony, with microcrystalline quartz support, correspond to calcareous or phosphate rocks (biomicrites and biopelmicrites), which underwent a process of replacement of the calcareous mud (micrite) and pre-existing allochems by silica, possibly during the final stage of diagenesis (compaction).

6. Conclusions

In the Tunja area of Colombia, the Guadalupe Group has morphologically and lithologically differentiated into three units: two hard units that originate ridges corresponding to the base of the Guadalupe Group and the Arenisca Tierna Formation, respectively, with a soft unit in the middle that generates a characteristic valley in the Plaeners Formation.

The paleontological analyses performed on the two stratigraphic sections measured in this study (Etayo-Serna, 2015) indicate that the base of the Guadalupe Group partly represents the Upper Santonian and mostly the Lower Campanian.

Acknowledgments

The authors thank Gloria Prieto Rincón, the Director of the Dirección de Recursos Minerales of the SGC, for the unconditional support for our research group during the activities conducted in this study and the assessment of the results; doctor Fernando Etayo Serna for the valuable contribution through the paleontological determination of the ammonites collected in the two stratigraphic sections measured in this study; the staff members of the Dirección de Laboratorios of the SGC, for the geochemical analysis and preparation of thin sections from samples collected in the two stratigraphic sections; the geographer Hernán Guillermo Cifuentes, for his help with the Geographic Information System; the geologists Nadia Rojas and Claudia Martín, for their help with the geologic mapping of the Tunja area; doctor Mario Maya Sánchez, editor of the journal *Boletín Geológico* of the SGC, for his recommendations and suggestions about the writing of this manuscript; and Mr. Franklin Lugo Buendía (“*Chicharrito*”), for his help with the field work and wise advice.

References

Baccelle, L., & Bosellini. A. (1965). Diagrammi per la stima visiva della composizione percentuale nelle rocce sedimentarie. *Annali della Universitá di Ferrara*, Sezione IX, Science Geologiche e Paleontologiche.

Bürgl, H. (1959). *Estratigrafía y estructura de la región entre Chía y Tenjo, Cundinamarca. Revisión del informe 1299*. Servicio Geológico Nacional.

Campbell, C. (1967). Lámina, laminaset, bed and bedset. Sedimentology. Oxford. https://doi.org/10.1111/j.1365-3091.1967.tb01301.x

Conrad, T. (1858). Observations on a group of Cretaceous fossil shells, found in Tippah County, Miss., with descriptions of fifty-sis new species. *Journal of the Academy of Natural Sciences of Philadelphia*, *3*(2), 323-336.

Conrad, T. (1860). Description of new species of Cretaceous and Eocene fossils of Mississippi and Alabama. *Journal of the Academy of Natural Sciences of Philadelphia*, *2*(4), 275-298.

D'Orbigny, A. D., & Boussingault, J. B. (1842). *Coquilles el échinodermes fossiles de Colombie (Nouvelle-Grenade), recueillis de 1821 à 1833*. P. Bertrand.

Dunham, R. (1962). Classification of carbonate rocks according to depositional textures. In W. E. Ham (Ed.), *Classification of carbonate rocks* (pp. 108-121). Memoir 1. American Association of Petroleum Geologists.

Etayo-Serna, F. (1964). Posición de las faunas en los depósitos cretácicos colombianos y su valor en la subdivisión cronológica de los mismos. *Boletín de Geología*, (16-17), 36-37.

Etayo-Serna, F. (1968a). Sinopsis estratigráfica de la región de Villa de Leyva y zonas próximas. Universidad Industrial de Santander. *Boletín de Geología*, (21), 19-32.

Etayo-Serna, F. (1968b). El sistema Cretáceo en la región de Villa de Leyva y zonas próximas. Universidad Nacional de Colombia. *Geología Colombiana* (5), 5-74.

Etayo-Serna, F. (1969). *Lenticeras baltai* Lisson en Colombia y su probable posición zonal santoniana. Universidad Nacional de Colombia. *Geología Colombiana*, 6, 17-32.

Etayo-Serna, F. (1985). *Paleontología estratigráfica del Sistema Cretácico en la Sierra Nevada del Cocuy. Proyecto Cretácico, contribuciones.* Publicaciones Geológicas Especiales. Ingeominas.

Etayo-Serna, F. (2015). *Estudios paleontológicos y bioestratigráficos de apoyo a la "Exploración de fosfatos en la cordillera Oriental, bloque Boyacá. Proyecto de investigación y exploración de recursos minerales no metálicos e industriales"*. Servicio Geológico Colombiano.

Folk, R. (1954). The distinction between grain size and mineral composition in sedimentary rock nomenclature. *Journal of Geology*, *62*(4), 344-359. https://doi.org/10.1086/626171

Folk, R. (1962). Spectral subdivision of limestone types. In W. E. Ham (Ed.), *Classification of carbonate rocks* (pp. 62-84). Memoir 1. American Association of Petroleum Geologists.

Folk, R. (1974). *Petrology of sedimentary rocks*. Hemphill Publishing Co.

Föllmi, K., Garrison, R., Ramírez, P., Zambrano F., Kennedy, W., & Lehner, B. (1992). Cyclic phosphate- rich successions in the upper Cretaceous of Colombia. *Paleogeography, Paleoclimatology, Paleoecology*, *93*(3-4), 151-182. https://doi.org/10.1016/0031-0182(92)90095-M

Geological Society of America. (1991). *Rock color chart. With genuine Munsell® color chips*.

Geological Society of London. (1990). Tropical residual soils: Geological Society Engineering Group Working Party Report. *Quarterly Journal of Engineering Geology and Hydrogeology*, *23*(1), 4-101. https://doi.org/10.1144/GSL.QJEG.1990.023.001.01

Guerrero, J., & Sarmiento, G. (1996). Estratigrafía física, palinológica, sedimentológica y secuencial del Cretáceo Superior y Paleoceno del piedemonte llanero. Implicaciones en exploración petrolera. *Geología Colombiana*, *20*, 3-66.

Hettner, A. (1892). *La cordillera de Bogotá: Resultado de viajes y estudios* (Trad. E. Gühl). Spanish version published in 1966. Banco de la República.

Hubach, E. (1931). *Geología petrolífera del departamento de Norte de Santander. Compilación de Estudios Geológicos Oficiales en Colombia.* Vol. XII. Ingeominas.

Hubach, E. (1951). *Estratigrafía de la sabana de Bogotá y sus alrededores*. Report 785. Servicio Geológico Nacional.

Hubach, E. (1957). *Contribución a las unidades estratigráficas de Colombia*. Internal report I-1212. Instituto Geológico Nacional.

Kennedy, W., Herbert, C., & Herber, S. (1981). Cretaceous faunas from Zululand and Natal, South Africa. Additional observations on the ammonite subfamily Texanitinae Collignon, 1948. *Annals of the South African Museum*, 8, 1-357.

Kennedy, W., Michel, B., & Patrice, M. (1995). Ammonite faunas, biostratigraphy and sequence stratigraphy of the Coniacian – Santonian of the Corbières (NE Pyrénées). *Bulletin des Centres de Recherches, Exploration et Production Elf-Aquitaine*, 19.

Krumbein, W., & Sloss, L. (1969). *Estratigrafía y sedimentación*. Ed Uteha.

Lazar, O., Bohacs, K., Macquaker, J., Schieber, J., & Demko, T. (2015). Capturing key attributes of fine-grained sedimentary rocks in outcrops, cores, and thin sections: Nomenclature and description guidelines. *Journal of Sedimentary Research*, *85*(3), 230-246. https://doi.org/10.2110/jsr.2015.11

Martínez, G. (2018). *Estudio de la base del Grupo Guadalupe en la región central de la cordillera Oriental, entre Ventaquemada y Toca, Boyacá, Colombia* (tesis de maestría). Universidad Nacional de Colombia.

Meek, F., & Hayden, F. (1857). Descriptions of new species and genera of fossils, collected by Dr. F. V. Hayden in Nebraska Territory, under the direction of lieut. GK Warren, US topographical engineer; with some remarks on the Tertiary and Cretaceous formations of the North-West, and the parallelism of the latter with those of other portions of the United States and territories. *Proceedings of the Academy of Natural Sciences of Philadelphia*, *9*, 117-133.

Montoya, D., & Reyes, G. (2003a). *Geología de la Plancha 209-Zipaquirá*. Ingeominas.

Montoya, D., & Reyes, G. (2003b). *Mapa geológico de la Plancha 209, Zipaquirá, escala 1:100.000*. Ingeominas.

Montoya, D., & Reyes, G. (2005a). *Geología de la sabana de Bogotá*. Ingeominas.

Montoya, D., & Reyes, G. (2005b). *Mapa geológico de la sabana de Bogotá, escala 1:100.000*. Ingeominas.

Montoya, D., & Reyes, G. (2007). *Geología de la sabana de Bogotá*. Publicaciones Geológicas Especiales, vol. 28. Ingeominas.

Moore, D., & Scrutton, P. (1957). Minor internal structures of recent unconsolidated sediments. *AAPG Bulletin*, *41*(12), 2753-2751. https://doi.org/10.1306/0BDA59DB-16BD-11D7-8645000102C1865D

Pérez, G., & Salazar A. (1978). Estratigrafía y facies del Grupo Guadalupe. *Geología Colombiana*, *10*, 6-85.

Pettijohn, F., Potter, P., & Siever, R. (1973). *Sand and sandstone*. Springer-Verlag.

Pratt, S., Rowlinson, N., Aitken, B., Anderson, W., Babcock, C., Campbell, C., & Maher, P. (1961). *The Muzo emerald mine.* Second Anual Field Conference. Colombian Society of Petroleum Geologists and Geophysicists.

Reineck, H., & Singh, I. (1980). *Depositional sedimentary environments*. Springer-Verlag.

Renzoni, G. (1962). Apuntes acerca de la litología y tectónica de la zona al este y sureste de Bogotá. *Boletín Geológico*, *10*(1-3), 73-75.

Renzoni, G. (1981). Geología del cuadrángulo J-12, Tunja. *Boletín Geológico*, *24*(2), 31-48.

Renzoni, G., Rosas, H., & Etayo-Serna, F. (1976). *Geología de la Plancha 191, Tunja*. Ingeominas.

Taylor, J. (1950). Pore-espace reduction in sandstone. *AAPG Bulletin*, *34*(4), 701-706. https://doi.org/10.1306/3D933F47-16B1-11D7-8645000102C1865D

Terraza, R., Martin, C., Martínez, G., & Rojas, R. (2016). *Exploración geológica de fosfatos en el Bloque Boyacá, planchas 191 y 210*. Servicio Geológico Colombiano.

Terraza, R., Moreno, G., Buitrago, J., Pérez, A., & Montoya, D. (2010). *Geología de la Plancha 210, Guateque*. Ingeominas.

Wegner, T. (1905). Die Granulatenkreide des westlichen Münsterlandes. *Zeitschrift der Deutschen Geologischen Gesellschaft Band*, 57, 112-232.

Whitfield, R. (1877). *Preliminary report on the paleontology of the Black Hills, containing descriptions of new species of fossils from the Potsdam, Jurassic, and Cretaceous formations of the Black Hills of Dakota*. Geologial Survey of the Rocky Mountain region. https://doi.org/10.5962/bhl.title.55132

Whitfield, R. (1880). Paleontology of the Black Hills of Dakota. In H. Newton y W. P. Jenney (Eds.), *Report on the geology and resources of the Black Hills of Dakota* (pp. 325-468). Government Printing Office. https://doi.org/10.3133/70039917

Williams, H., Turner, F., & Gilbert, C. (1954). *Petrography and introduction to the study of rocks in thin sections*. University of California.

Young, K. (1963). *Upper Cretaceous ammonites from the Gulf Coast of the United States.* The University of Texas, Austin, Bureau of Economic Geology, Publication 6304.

Vertical faults controling Nickel enrichment in hich Mg green saprolite from peridotite Cores, Cerro Matoso nickel mine. Montelíbano, Colombia. Photo by Andrés Castrillón.

Boletín Geológico

Boletín Geológico, 47, 67-84, 2020
https://doi.org/10.32685/0120-1425/boletingeo.47.2020.492

Received: May 14, 2020
Revised: June 2, 2020
Accepted: September 28, 2020

Listvenites: new insights of a hydrothermal system fossilized in Cerro Matoso peridotites, Montelíbano, Córdoba Department, Colombia

Listvenitas: nuevos vestigios de un sistema hidrotermal fosilizado en las peridotitas de Cerro Matoso, Montelíbano, departamento de Córdoba, Colombia

Andrés **Castrillón**[1], Javier **Guerrero**[1]

1 Departamento de Geociencias, Universidad Nacional de Colombia, Bogotá, Colombia
Corresponding author: Andrés Castrillón, acastrillon@unal.edu.co

ABSTRACT

The products of metasomatic alteration (e.g., carbonation) of peridotites are called listvenites. Based on a description of the outcrops in the laterite deposit at Cerro Matoso located in the NW of Colombia, the mineralogical composition confirmed by petrography, and a chemical analysis performed with XRF and WDS/EDS, the previous unit called tachylite is redefined as listvenite. Two types of listvenites are described: listvenite A, with the mineralogical association of quartz + siderite + phyllosilicates + goethite +/- magnetite, and listvenite B, with the association of siderite + phyllosilicates + goethite. Cr-spinel relics accompanied by Mn-siderite and neoblastic textures, indicate their origin from peridotites, where Mn-Fe would have been deposited by hydrothermal fluids. Hydrothermal reducing environments with alkaline fluids and low temperatures should have favored the formation of listvenites that are observed along a fracture zone, oriented WNW-ESE at Pit-1 in Cerro Matoso. Due to exposure to climatic conditions since the Eocene, but definitively since the last Andean Orogeny, listvenites were affected, like all the rocks in the Cerro Matoso deposit, by intense supergene weathering and leaching processes, which could make their true origin unclear.

Keywords: Listvenite, metasomatism, hydrothermal systems, Cerro Matoso, spinel.

RESUMEN

El producto de alteración metasomatica (e.g., carbonation) de peridotitas son listvenitas. Basados en una descripción de los afloramientos en el depósito de lateritas niquelíferas de Cerro Matoso, localizado al NW de Colombia, la composición mineralógica confirmada con XRD y análisis químicos con XRF y WDS/EDS, se redefine una unidad previamente llamada tachyilita como listvenita. Se describen dos tipos de listvenitas; listvenita A con la asociación mineralógica: cuarzo + siderita + filosilicatos + goetita

Citation: Castrillón, A., & Guerrero, J. (2020). Listvenites: new insights of a hydrothermal system fossilized in Cerro Matoso peridotites, Montelibano, Córdoba Department, Colombia. *Boletín Geológico*, *47*, 67-84, https://doi.org/10.32685/0120-1425/boletingeo.47.2020.492

+/- magnetita, y listvenita B con la asociación: siderita + filosilicatos + goetita. Relictos de Cr-espinela, acompañados por Mn-siderita y texturas neoblásticas, indican un origen a partir de peridotitas, en donde Mn-Fe serían aportados por fluidos hidrotermales. Ambientes hidrotermales reductores con fluidos alcalinos y de bajas temperaturas debieron favorecer la formación de listvenitas, que se observan a lo largo de una zona de fracturas orientada WNW-ESE en el Pit-1 de Cerro Matoso. Expuestas a condiciones climáticas quizás desde el Eoceno pero definitivamente desde la última Orogenia Andina, las listvenitas fueron afectadas al igual que todas las rocas en el depósito de Cerro Matoso por intensos procesos de meteorización y lixiviación mineral ocultando el verdadero origen de algunas.

Palabras clave: Listvenita, metasomatismo, sistemas hidrotermales, Cerro Matoso, espinelas.

1. Introduction

Listvenite (from the Russian "listvenity", Rose, 1837) is a term used principally by Russian geologists to describe the carbonate +/- sericite +/- pyrite alteration of mafic and ultramafic ophiolitic assemblages, which indicates the hydrothermal involvement of quartz +/- carbonate veins (Rose, 1837). This alteration is due to carbonation occurring in rocks that are susceptible to interactions with CO_2-rich fluids, resulting in the alteration and precipitation of carbonate and other minerals (Halls and Zhao, 1995). Some authors recommend that the term listvenite be used strictly in cases where potassium metasomatism has been verified in ultramafic rocks (serpentinites, serpentinized peridotites) and where this potassium metasomatism is evidenced by the development of micas (e.g., fuchsite) as components of the mineralogical association included in "listwaenite" (Halls and Zhao, 1995; Abuamarah, 2020). Mafic and ultramafic rocks are particularly prone to carbonation due to abundant olivine $(Mg, Fe)_2SiO_4$ and pyroxene $(Ca, Mg, Fe)_2Si_2O_6$, which react with H_2O and CO_2 to form hydrous silicates, such as serpentine, Fe-oxides (magnetite) and carbonates (Kelemen and Matter, 2008). According to Halls and Zhao (1995), the correct spelling of the word listwaenite is listvenite, and it was proposed to describe the formations in Beresovsk in the Ural Mountains of central Russia (Halls and Zhao, 1995) and in Europe and North America (Bates and Jackson, 1987).

The term listvenite has been used for the following mineral assemblages: a quartz + magnesite rock derived from serpentinite at low temperatures by full conversion of all original Mg-silicates to carbonate and residual quartz (Bucher and Stober, 2019); quartz (45-55%) and carbonates (40-60%) with minor amounts of serpentine, chlorite, chromite, and Cr-rich sericite (fuchsite) (e.g., upper mantle peridotites in the Cryogenian Bir Umq ophiolite, Arabian Shield, Saudi Arabia, Abuamarah, 2020); and listvenites (silica-type) mainly consisting of opal, quartz, cristobalite, chalcedony, and relicts of serpentine, Cr-spinel and secondary iron hydroxides, where magnesite, dolomite, calcite and clay minerals are minor phases (e.g., Khoy ophiolite complex, northwestern Iran, Imamalipour et al., 2018). The term listvenite has also been used to describe the mineral association of metamorphosed amphibole-bearing listvenites (e.g., Bayazeh Paleozoic ophiolite, Nosouhian et al., 2016, 2019). In this text, the term listvenite refers to a variation of carbonated and silicified serpentinite to denote rocks that are strictly the metasomatic product of low-grade hydrothermal alteration of ultramafic rocks and can be defined as one rock type or a mixture of rock types that are genetically related to the same hydrothermal event but can vary depending on the intensity of the alteration and the composition of the protoliths (e.g., Kashkai and Allakhverdiev, 1965; Buisson and Leblanc, 1987; Leblanc, 1991; Halls and Zhao, 1995).

According to Ucurum (2000), the movement of hydrothermal fluids along fractures of ultramafic rocks produces dikes of listvenites whose length can vary by hundreds of meters, and whose thickness can vary by tens of meters. These rocks have been found in altered mafic and ultramafic rocks in British Columbia (Ash and Arksey, 1990), Turkey (Ucurum, 1998, 2000), Canada (Jutras and Geol, 2002), Mali, Morocco and Saudi Arabia (Buisson and Leblanc, 1987; Leblanc, 1991) and are now identified in the deposit of Cerro Matoso, NW Colombia. Listvenites in Cerro Matoso are covered by marine deposits of black conglomeratic mudstone and are located along a fracture zone oriented WNW-ESE.

The Cerro Matoso ultramafic rocks, developed a Ni laterite profile by weathering with different characteristics in the south (or Pit-2) (Figure 1), with nickel grades not exceeding 4%, compared with the laterite profile developed in the north (or Pit-1), where nickel grades reached 9%. The higher nickel grades at Pit-1

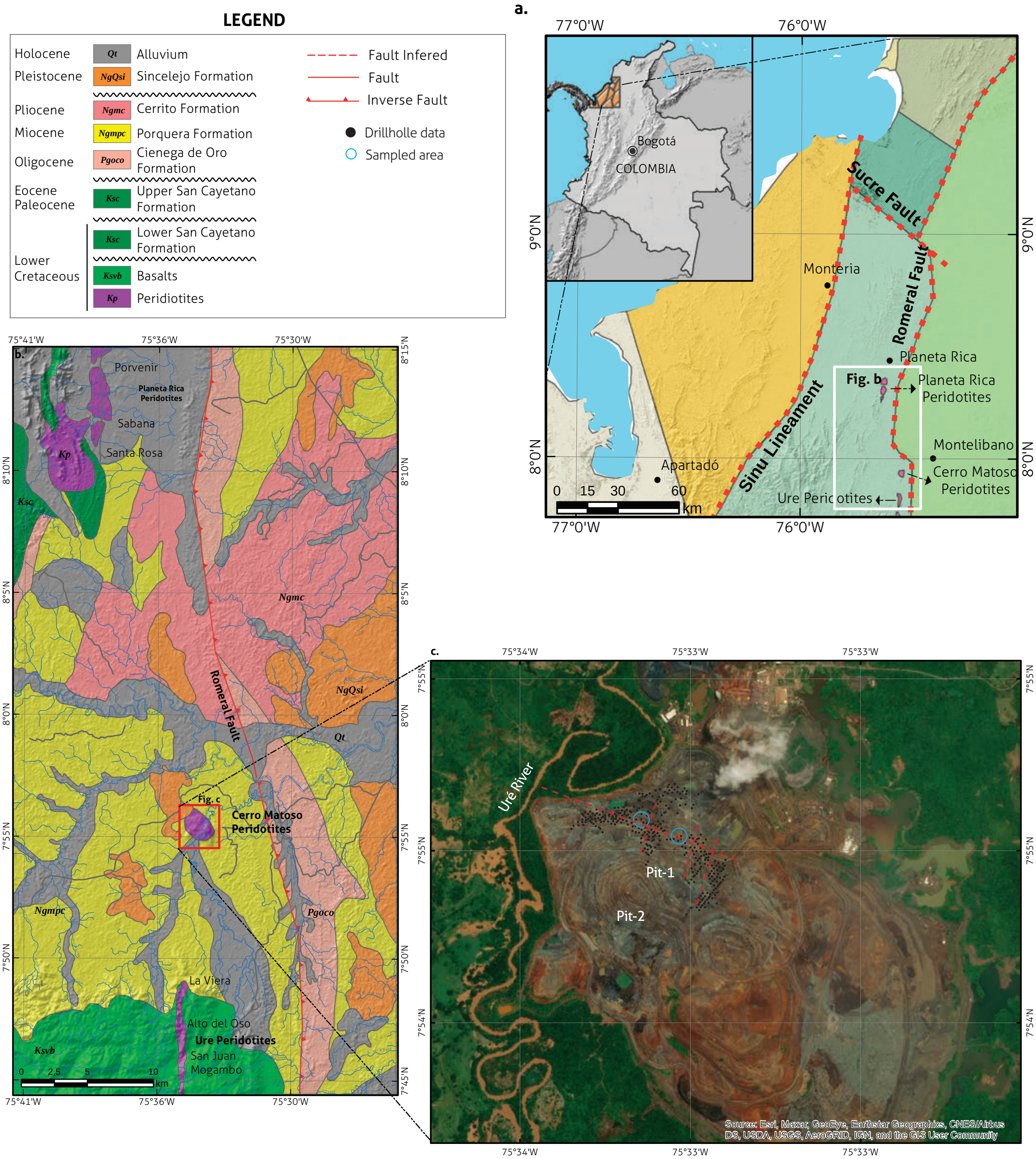

Figure 1. Regional geology and location of the Cerro Matoso Ni laterite deposit and of Pit-1 and Pit-2
Location of listvenites along Pit-1 in the Cerro Matoso open pit mine, illustrating the WNW-ESE general trend (modified from Londoño and González, 1997; Gleeson et al., 2004). The peridotites of Cerro Matoso are surrounded by basalts (Ksvb) (outcropped 30 km to the south), which are unconformably covered by early- and mid-Miocene sediments from the Ciénaga de Oro Formation (Pgoco), Porquera Formation (Ngmpc), Cerrito Formation (Ngmc) and Sincelejo Formation (NgQsi).

are related to the influence of hydrothermal systems, and the "tachylite" (a term used by mine geologists to describe an enigmatic Fe-oxide horizon) was assigned to the laterite profile, although it was not considered to be a normal product of peridotite weathering (Gleeson et al., 2004). A detailed petrological and geochemical study of "tachylite" occurrence was published by Sumicol (2002). This paper describes the characteristics, mineralogy, and geochemistry of an association of rocks in the Cerro Matoso nickel laterite deposit that could correspond to listvenites.

2. REGIONAL GEOLOGICAL SETTING

The Cerro Matoso deposit is located in the department of Córdoba, northwest Colombia. Nickeliferous laterites are the product of supergene weathering of peridotites (principally harzburgites with varying degrees of serpentinization). Peridotites of Cerro Matoso are defined as an isolated body of outcrops that have been assigned to an Early Cretaceous ophiolite complex (Mejia and Durango, 1981). The ultramafic rocks are associated with the ancient oceanic crust that existed in the Pacific Ocean, west of its present position (Pindell and Barrett, 1990; Pindell and Kennan, 2009), where it is suggested that the mantle rocks were exhumed as an Oceanic Core Complex (OCC) (Castrillón, 2013). The OCC is part of the ophiolites accreted during the pre-Andean orogeny along the Romeral Fault System, which is considered an important boundary between the oceanic crust to the west and the continental crust to the east (Barrero, 1974; Meissener et al., 1976). As the American continent moved west and the oceanic plate moved east during the Late Cretaceous, ocean segments accreted in the western part of the continent (Lewis et al., 2006) were eventually exposed to supergene weathering conditions beginning in the late Eocene (López-Rendón, 1986). Locally, the CM peridotites are overlaid by a deep marine sedimentary succession (Castrillón, 2013). These sediments were interpreted to be part of the ultramafic weathering profile (López-Rendón, 1986; Gonçalves et al., 1999; Gleeson et al., 2004, Lelis et al., 2004). Recently, Castrillón (2019) suggested that fossils and black conglomeratic mudstone found at Pit-1 represent ocean floor sediments associated with hydrothermal systems hosted by ultramafic rocks.

The variably serpentinized ultramafic rocks of Cerro Matoso that developed a complete laterite profile, where iron and nickel alloy is produced in the mining process, are exposed in the form of an elongated isolated hill approximately 2.5 km long and 1.5 km wide at the northern limit of the Western Cordillera and are considered the northernmost extension of the allochthonous oceanic crustal terranes (Mora-Bohórquez et al., 2017). The peridotites of Cerro Matoso are surrounded by basalts (Ksvb) (outcropped 30 km to the south), which are unconformably covered by sediments from the early and mid-Miocene, including a transgressive succession consisting of fluvial and shore sandstones of the Ciénaga de Oro Formation (Pgoco), followed by marine shales of the Porquera Formation (Ngmpc), which are unconformably covered by Cerrito Formation (Ngmc) and Sincelejo Formation (NgQsi) sediments. The Cerro Matoso peridotites have been exposed on the surface since the middle Eocene and have therefore been affected by intense weathering (e.g., López-Rendón, 1986; Gleeson et al., 2004). According to López-Rendón (1986), lateritization probably started in the late Eocene-early Oligocene, and chemical weathering and erosion continued throughout the Oligocene (Figure 1).

3. SAMPLE AND METHOD

According to the field description, listvenites are very fine-grained and extremely friable; they have conchoidal fractures and high porosity, a violet-brown to black color when dry, and a dark-green color when wet, and have locally abundant quartz veins (Figure 2a). Listvenites underlie the black conglomeratic mudstone (Figure 2b) and are a very uniform unit, consisting of lenses capping altered peridotites (i.e., green saprolites). Two listvenite varieties can be differentiated according to their veinlets and brecciated texture (Figure 2a-2c). A representative set of samples (Figure 3a-3f) was collected at the 49 Bench level of Pit-1, where two varieties coexist (A: CM-3, CM-4, CM-6, CM-7; and B: CM-27, CM-56, samples) overlaying green saprolites along transitional contacts (Figure 3g-3h), altered peridotites (Figure 3i), peridotites with magnesite veins (Figure 3j) and peridotites (Figure 3k-l). Petrographic classification and analysis were performed using a Carl ZEISS Primo Star HD/cam Full Köhler microscope, 100x, SF2, from the Instituto de Geología of the Universidad Nacional Autónoma de México (UNAM). Scanning electron microscopy (SEM) and X-ray diffraction (XRD) patterns were further used for the identification of minerals in listvenites. According to their textures and silica content, three samples of listvenite were selected for further analysis: sample CM-6 (brecciated texture) and samples CM-27 and CM-56, also named DRX14 (non-brecciated texture); these were analyzed at the UNAM labs, and sample CM-3 was selected for XRF and analyzed at the Gmas labs (code name CM-14).

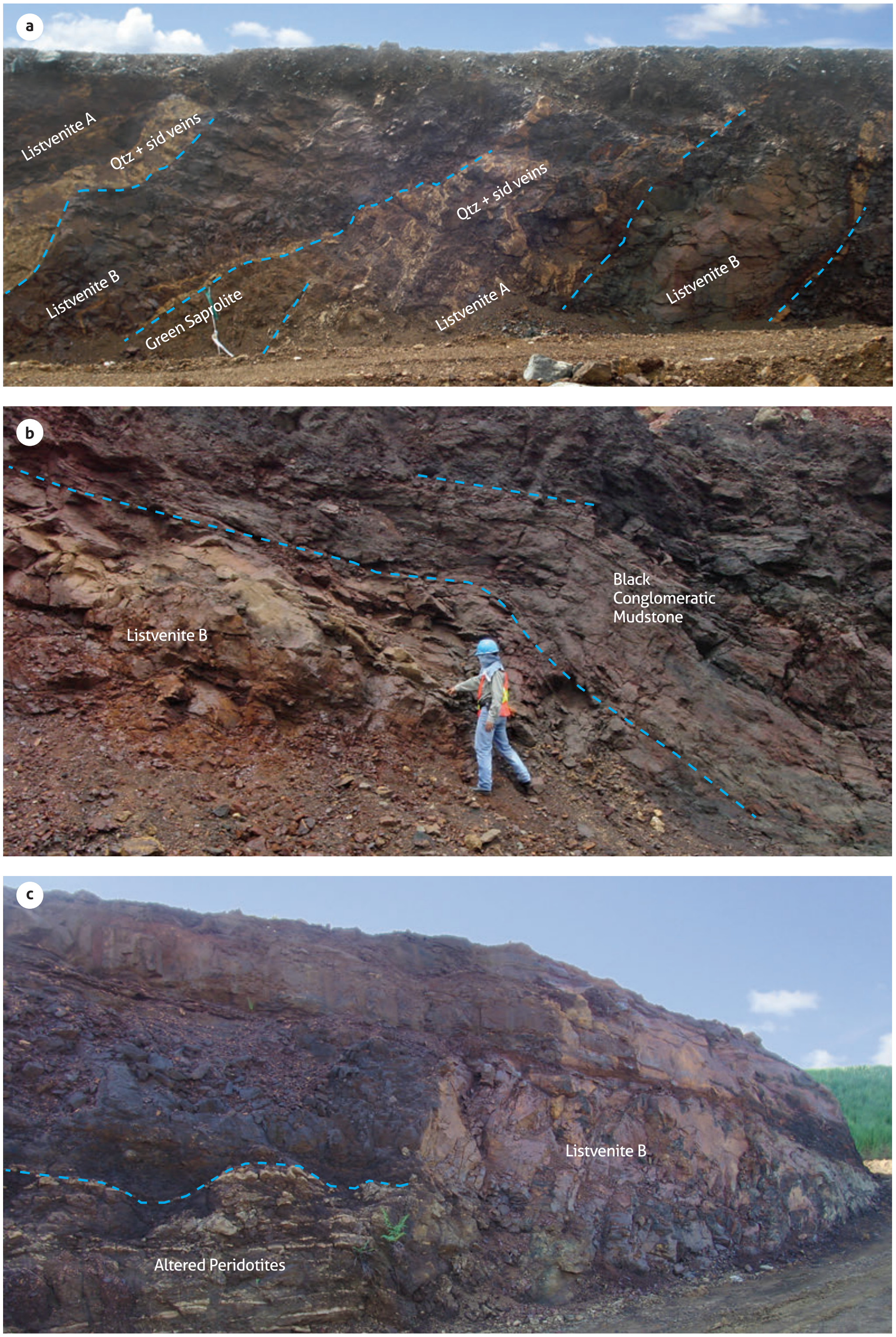

Figure 2. Listvenites outcrops at Pit-1 of Cerro Matoso
a) Western orientation of the main fractures presented by the listvenites (varieties A and B). Variety A presents a complex vein pattern on top of the green saprolite. Variety B, with a dark purple color, has lenses with or without silica/siderite veins. b) Black conglomeratic mudstone (BCM) overlying listvenites. c) Altered peridotites underlying a listvenite cap (Bench level 49 of Pit-1; outcrop is 8 m high). A purple color is also observed with bronze tones, typical of listvenites when dry (Bench level 56 of Pit-1; outcrop is 7 m high).

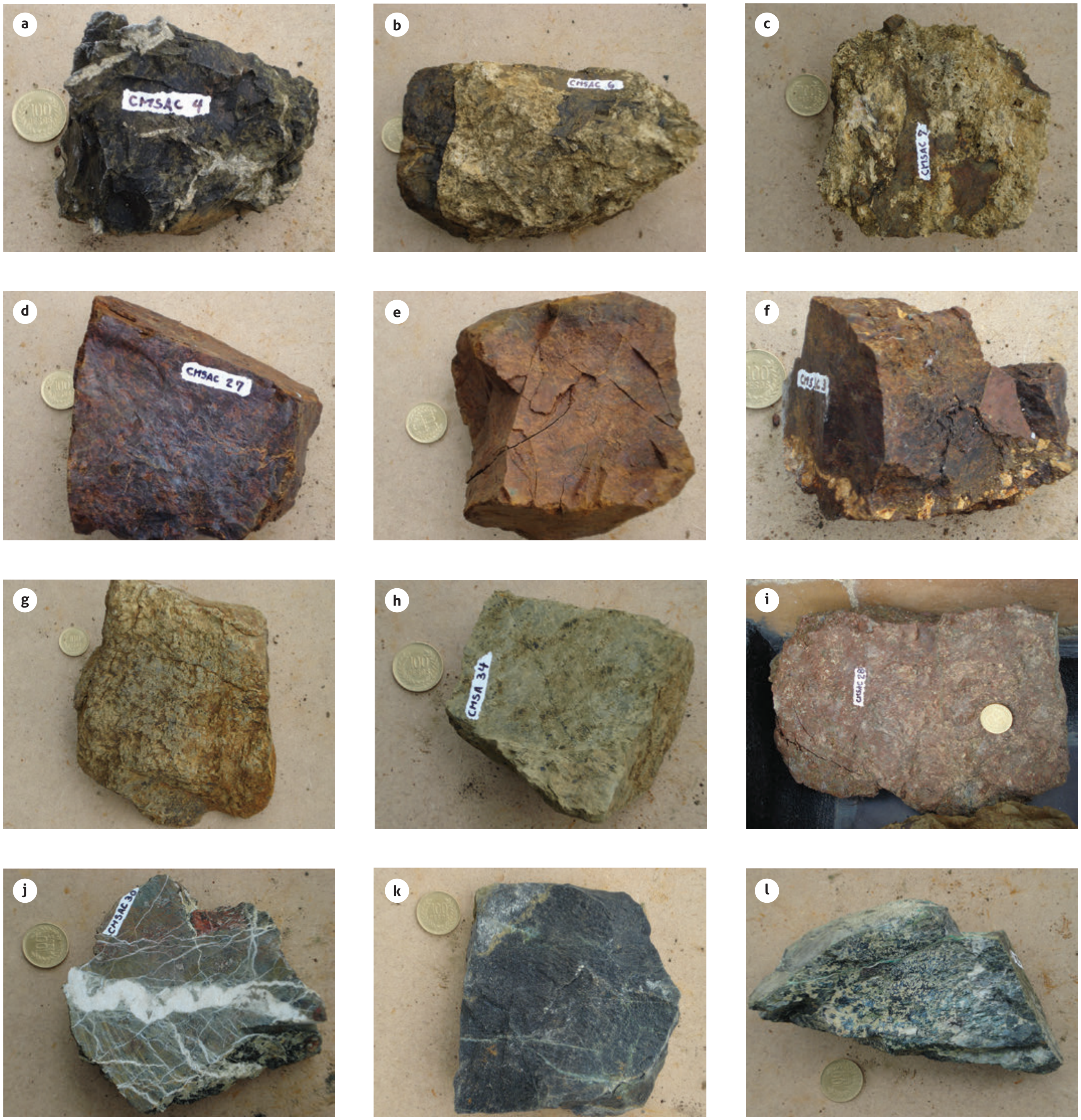

Figure 3. Hand samples collected from the Cerro Matoso deposit at Pit-1
a-c, f) Listvenite variety A is characterized by brecciated textures with high silica/siderite vein content. In some cases, listvenite was fractured into angular clasts several mm to 20 cm in size and cemented by quartz veins. d-e) Listvenite variety B is characterized by a purple color. g) Low-Mg green saprolite. h) High-Mg green saprolite. i) Saprolitized peridotite. j) Magnesite and silica veins in peridotite. k) Fresh peridotite. l) Serpentinized peridotite.

Selected samples for bulk-rock mineralogical analysis were ground with an agate mortar and pestle to >200 µm and mounted in aluminum holders for X-ray powder diffraction analysis following the standard XRD procedures (Brindley and Brown, 1980; Moore and Reynolds, 1997). Measurements were made using an EMPYREAN diffractometer at the Instituto de Geología LANGEM, Universidad Nacional Autónoma de México and Gmas labs in Bogotá. The equipment was operated with an accelerating voltage of 45 kV and a probe current of 40 mA using CoKα radiation (cobalt tube) without a monochromator and iron filter in the incident optics of the equipment. The detector used is of solid state (PIXCel 3D). The preparations were measured over a 2θ angle range of 5-80° (air-dried) and 5-40° (glycolated and heated) in steps of 0.003° and 40 second integration time. Peak positions were standardized against the quartz 100 peak of relative intensity taken at 4.26 Å. The databases used for identification were the Inorganic Crystal Structure database (ICCD, V2016) and the International Center for Diffraction Data (ICDD). Phase identification and quantification by the Rietveld refinement method were performed with a PDF-2 database using HighScore 7 V4.5 software. Relevant data from the diffractometer used in the refinement are shown in Table 1. The refined specimen-dependent parameters included zero error, displacement error, polynomial fitting for the background with six coefficients, cell parameters, crystallite size, atomic coordinates, and isotropic temperature factors. The GOF (goodness of fit) values show the fit between the Rietveld refinement and the experimental profile.

Table 1. Data from the diffractometer used in the refinement

Geometry	Bragg-Brentano
Goniometer Radius	220 mm
Radiation Source	CoKα
Generator	45 kV, 40 mA
Tube	Fine Focus
Divergence Slit	1⁄2° (fixed)
Soller Slits	0.04° (incident and diffracted beam)
Incident Beam Optics	Parallel Mirror
Filter	Iron Filter
Detector	Solid State (PIXcel 3D)
Step Size	0.002°
Integration Time	40 s

The composition of major elements was obtained by X-ray fluorescence (XRF) in fused $LiBO_2/Li_2B_4O_7$ disks using a Bruker_S4_Explorer X-ray fluorescence spectrometer with a Rh-anode X-ray tube as a radiation source in the Gmas labs in Bogotá. Semiquantitative and quantitative analyses were performed using the QUANT-EXPRESS method (fundamental parameters; He, 1991) based on the certified USGS standard samples AGV1, BCR2, DST2, QLO1, G2 and W2A, with which the equipment is calibrated. Chemical composition of carbonates and oxides in the listvenite carbon-coated thin section were analyzed under energy dispersive spectroscopy (EDS), wavelength dispersion spectrometry (WDS) and X-ray spectroscopy (XRD) with an electronic probe microanalyzer (EPMA) JEOL JXA-8900XR and an SEM model JSM-6300 (both from the Instituto de Geología - UNAM) operated at 15 kV accelerating voltage. Measurements were performed on different minerals of the sample, and the compositions were obtained from different points on each mineral (i.e., siderite: 12 points, magnetite: 7 points, spinel: 6 points, and orthopyroxene: 6 points) to determine their usual chemical composition. The textural classification of the quartz considered the quartz type and the individual grain size as well as its crystal shapes and textures and the way the quartz related to the surrounding rock (Demoustier, 1995; Demoustier and Castroviejo, 1997; Demoustier et al., 1998).

4. RESULTS

4.1 Listvenite mineralogy and petrography

Listvenite A corresponds principally to the matrix-supported brecciated textures with quartz + siderite + serpentine + goethite assemblages; zonate microcrystalline coarse quartz (Qvxg) (<10 mm) crystallized into posthumous cavities in symmetric and radiated plumose textures. Microcrystalline fine quartz (Qvxf) (0.1-1 mm) is usually crystallized in the inner parts of plumose textures. Siderite (Sid) is present in zonate textures and works as cement with quartz. Serpentine (Ser) and goethite (Go) are products of peridotite alteration. A massive replacement quartz (QeM) in the housing rock forms heterogeneous angular and subangular fragments in breccia samples CM3 and CM7 (Figure 4a-4e). Listvenites of type A are characterized by their siderite + quartz vein systems in the field.

Listvenite B consists mainly of smectite with goethite and siderite and relic spinel. The smectite is nontronite. Siderite occurs as subhedral crystals with high birefringence. Goethite occurs as opaque earthy black aggregates, usually in fissures and with magnetite. Relic subangular olivines with blueish to purple colors are scarce. The light green yellowish fibrous crystals are phyllosilicates (Figure 4f).

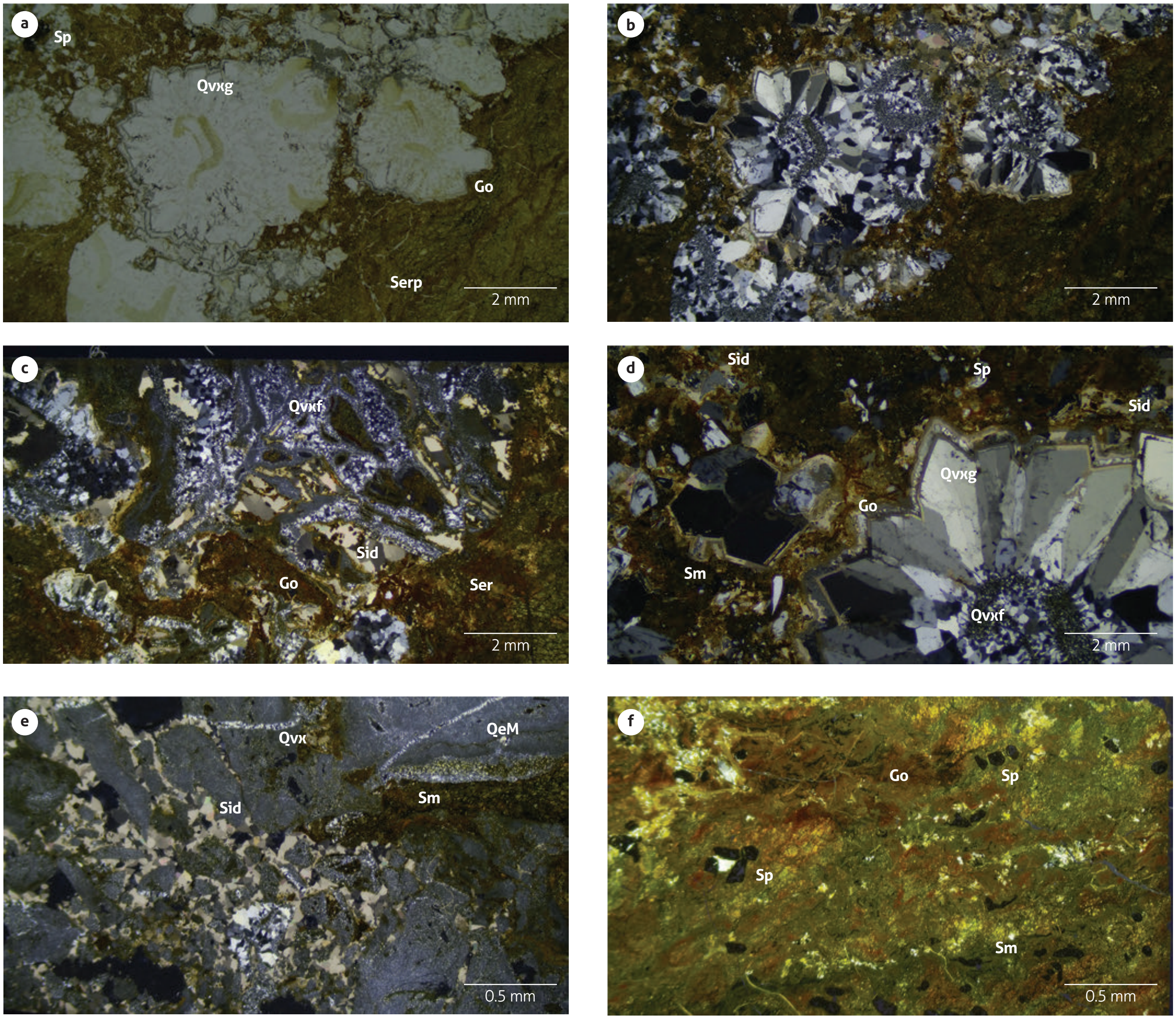

Figure 4. Listvenite thin sections
a and b) Listvenite A. Association of quartz + siderite + green serpentine (Ser) + quartz (Q)+ reddish goethite (Go). Posthumous cavities filled with thick microcrystalline quartz (Qvxg) in a symmetric feathery structure and radially zoned on the edges with fine microcrystalline quartz inside (Qvxf). Samples CM3_np_10x and nc. c) Listvenite A. Fine microcrystalline quartz (Qvxf) and siderite (Sid) as cement surrounded by goethite and serpentine (Ser). Sample CM3_nc_10x. d) Listvenite A. Detail of the feathery texture and zoned texture with siderite (Sid) on the edge of thick microcrystalline quartz (Qvxg). Fine microcrystalline quartz (Qvxf) with puzzled texture surrounded by smectite (Sm) and goethite (Go). Sample CM3_nc_20x. e) Brecciated matrix-supported texture with quartz and massive replacement of the host rock (QeM) forming fragments of heterogeneous subhedral to anhedral quartz with impure edges, siderite (Sid) as cement and micro veins of quartz (Q). Sample CM3_nc_40x. f) Listvenite B. Association of serpentine (Ser) + goethite (Go) +/- siderite (Sid), with euhedral spinels (Sp) as accessories. Sample CM27_nc_10x.

4.2 XRD Diffractometry

XRD for fractions >200 µm indicate siderite and phyllosilicates as the common minerals. In sample CM-56, siderite (5.7%), goethite (3.6%) and phyllosilicates 15 Å pbb-type smectite (90.7%) are the principal components. A more suitable smectite with a 15 Å peak was identified by the Green-Kelly test as nontronite (Sumicol, 2002). Sample CM-3 consists of quartz, siderite, goethite and phyllosilicates (serpentine). Sample CM-6 is composed of quartz, siderite, goethite, magnetite and phyllosilicates (serpentine) (Figure 5).

4.3 Electron microscopy

Sample CM-56 was analyzed under a scanning electron microscope. Cr-spinel relicts are very fractured and surrounded by Mn-siderite + smectite (Figure 6a and b). In Figure 6c, siderite occurs as subhedral to anhedral crystals in a neoblastic texture. Magnetite is tabular and appears in smaller amounts, typically < 5 vol. Orthopyroxene relics with border alteration of serpentine are commonly rimmed by magnetite (Figure 6d). In general, the dominant phase is smectite, which replaces serpentine. Olivine relics are also present in minor amounts as anhedral crystals.

4.4 Geochemistry

4.4.1 Major oxides

Geochemical analyses of sample CM-56 are shown in Table 2. For comparison, four representative analyses of listvenites, named “tachylites,” from the Cerro Matoso open pit mine are also provided; all samples were collected from Pit-1. Listvenites contain silica between 27.5 and 65.3 wt% and Fe between 21.5 and 61.8 wt%, which are their principal components. Al_2O_3 (2.7 to 6.5 wt%) and Mg (<3.7 wt%) are low, resulting in lower MgO/SiO_2 ratios (0.02–0.46 wt%). The Ni content is between 1.6. and 6.1 wt%.

4.4.2 Microprobe chemical composition of siderite

The chemical composition (wds/eds) of siderite in the listvenite sample CM-56 indicates carbonates with high Fe content (33%) and Mn (12%) content and low contents of Mg and Ca (<1%) for 12 analyses. Normalizing these data for carbonates shows a considerable amount of $MnCO_3$ (11–39.2 mole%) (Table 3). Spinels that occur as small undeformed grains (0.1–0.3 mm) generally show pitted dissolution textures (Figure 6a) with Fe (17.6%) and Mg (14%) as the principal components. The composition of magnetite crystals reaches 83.2% Fe.

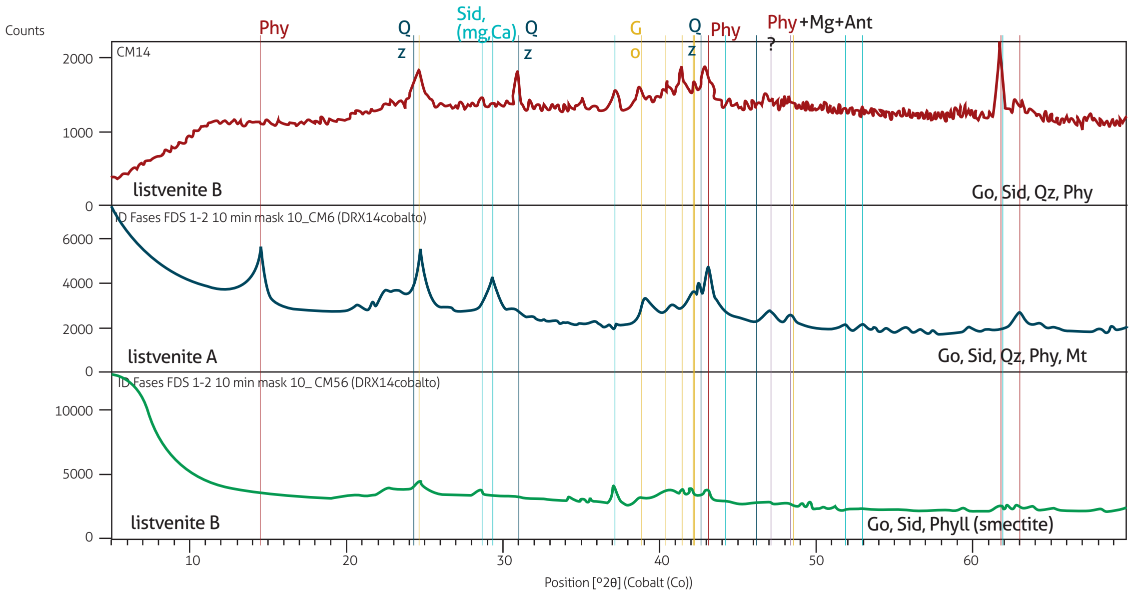

Figure 5. XRD diffractograms
XRD for fractions (>200 microns). Sample CM-3 contains the following: quartz (Qz), siderite (Sid), goethite (Go) and phyllosilicates (Phy). Sample CM-6 is composed of quartz, siderite, goethite, magnetite (Mt) and phyllosilicates. Sample CM-56 contains siderite, goethite and phyllosilicates.

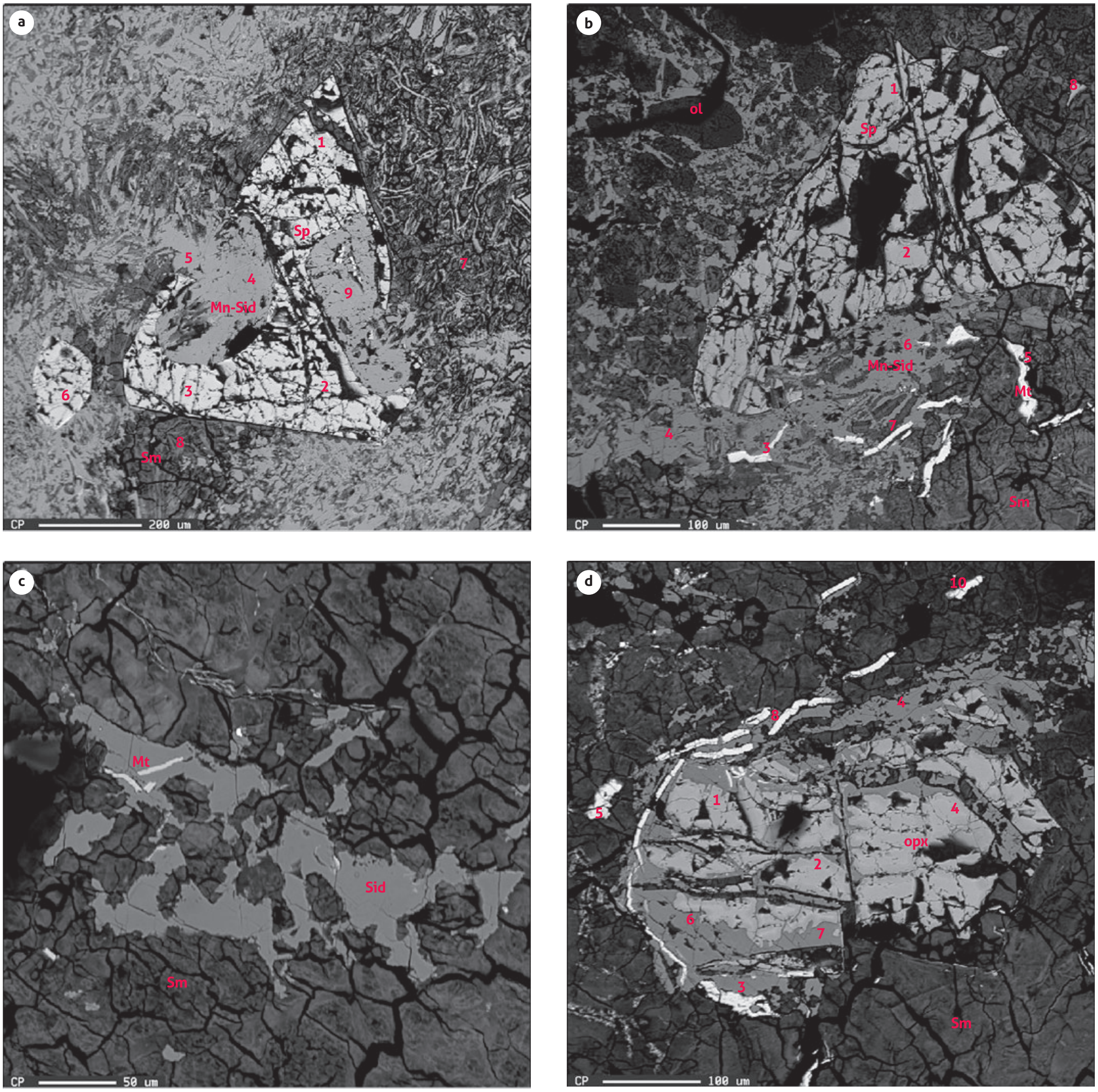

Figure 6. Scanning electron microscope analysis of the listvenite components in detail
a) Neoblastic texture of listvenite composed of smectite (Sm) and Mn-siderite (Mn-Sid) surrounding a euhedral Cr-spinel (Sp) fractured crystal that is partially altered. b) Smectite (Sm) and Mn-siderite (Mn-Sid) surrounded by Cr-spinel (Sp) euhedral crystals, magnetite (Mt), and olivine (Ol), which are accessories. c) Fractured smectite (Sm) with a substantial amount of siderite (Sid). d) Orthopyroxene (opx) altered to serpentine surrounded by smectite (Sm) and euhedral crystals of magnetite (Mt).

Table 2. Listvenites chemical composition in wt%

Name	wt (%)								MgO/SiO_2	Sample ID
	SiO_2	Al_2O_3	Fe_2O_3	MgO	CaO	MnO	TiO_2	Ni		
Listwaenite	27.54	4.2	61.8	2.3	0.2	0.8	0.05		0.086	CM-14
Tachylite	28	6.5	44.9	3.0	0.0	0.3	0.07	2.6	0.109	Gleeson et al. (2004)
Tachylite	37.1	3.8	25.2	17.4	0.2	0.1	<0.01	4.2	0.469	Gleeson et al. (2004)
Tachylite	53.1	2.9	22.9	3.7	0.1	1.6	<0.01	6.1	0.069	Gleeson et al. (2004)
Tachylite	65.3	2.7	21.5	1.8	<0.01	0.3	<0.01	1.6	0.027	Gleeson et al. (2004)
Peridotite	41.2	0.3	9	42.6	0.2	0.1	<0.01	0.2	1.033	Gleeson et al. (2004)
Peridotite	42	0.3	9	41.9	0.3	0.1	<0.01	0.2	0.997	Gleeson et al. (2004)
Peridotite	43.8	0.4	9.1	42.1	0.4	0.1	<0.01	0.2	0.962	Gleeson et al. (2004)
Tachylite A	42.8	3.4	28.4	4.1	0.5	0.4	N.D.	1.8	0.098	Sumicol (2002)
Tachylite B	39.5	2.2	34.3	1.0	0.3	1.3	N.D.	1.5	0.027	Sumicol (2002)

Comparation between listvenite (sample CM-56, XRF) and "tachylites" (ICP-AES) composition, data from Sumicol (2002) and Gleeson et al. (2004), both of which are given in wt%.

Table 3. Microprobe mean chemical composition of Mn-siderite in the Cerro Matoso listvenite sample CM-56.

Chemical composition of Mn-siderite in CM listvenites										
wt %	K_2O	Na_2O	MnO	SrO	CaO	MgO	FeO	BaO	CO_2	Total
Mean	0.01	0.09	12.44	0.01	0.16	0.97	33.00	0.01	29.18	75.86
Desv	0.01	0-04	3.90	0.01	0.06	0.28	6.82	0.02	1.77	4.77
mole %	K_2CO_3	Na_2CO_3	$MnCO_3$	$SrCO_3$	$CaCO_3$	$MgCO_3$	$FeCO_3$	$BaCO_3$	Total	
Mean	0.02	0.42	26.85	0.01	0.43	3.64	68.63	0.,01	100.00	
Desv	0.03	0.19	9.33	0.01	0.19	1.09	10.10	0.02	100.00	

Mn-siderite: 12 points analyzed

5. DISCUSSION

The term listvenite has been used to principally describe the assemblage of carbonate + silica as the product of carbonation in mantle rocks (Buisson and Leblanc, 1987; Leblanc, 1991; Halls and Zhao, 1995; Nasir et al., 2007; Kelemen and Matter 2008; Bucher and Stober, 2019) but also in metamorphosed rocks (e.g., amphibole-bearing listvenites, Nosouhian et al., 2016). Listvenites can be classified based on their SiO_2 content as silica, silica-carbonate, and carbonate listvenites (e.g., Nasir et al., 2007; Aftabi and Zarrinkoub, 2013; Azer, 2013;) with mineralogical compositions similar to those described by Ucurum (2000) with the assemblage of quartz + calcite + dolomite + ankerite ± magnesite as major rock-forming minerals in silica-carbonate listvenites (Type I) and carbonate listvenite (Type II) composed of calcite + dolomite + ankerite with only trace amounts of quartz and magnesite; or with the assemblage of quartz + calcite + magnetite + goethite + hematite ± talc ± ankerite (e.g., listvenites in Turkey; Central Eastern Desert, Egypt; Tavreh mercury prospect, northwestern Iran; Sartohay ophiolitic mélange, Xinjiang, NW China; and Semail Ophiolite, Oman). At Cerro Matoso, on the contrary, listvenites are composed of siderite ± phyllosilicates and can either be accompanied by quartz or not accompanied by quartz. Commonly, the siderite is a Mn-siderite.

The Mn-carbonate in listvenites could be formed by replacing calcium carbonate with CO_2 derived from hydrothermal fluids, as suggested by Zierbeng and Shanks (1988). Furthermore, Mn enrichment has been associated with hydrothermal systems, hydrothermal deposits and hydrothermal sulfides (e.g., Von Damm, 1995; Dekov et al., 2004; Taitel-Goldman et al., 2008). Siderite and Mn-siderite crystallize better under reducing conditions of high CO_2 and partial pressure and at elevated dissolved iron or manganese concentrations. Nevertheless, additional chemical and geochemical analysis of the Mn-siderite at Cerro Matoso is necessary to confirm this formation mechanism.

The Mn-siderite in the type B listvenites (CM-56) conforms to a neoblastic texture with spinels and smectite instead of forming veins or filling fractures and is likely a product of metasomatic alteration. Additionally, type A listvenites (CM-3, CM-4, CM-6, CM-7) with siderite and quartz forming vein systems indicate a pattern of fluid flow into the rocks.

Supported matrix breccia textures reflect the intensity of fracturing and hydrothermal vein fills and therefore the activity of fluids in the host rock. On the other hand, modified (QeM) and recrystallization textures (e.g., feathery texture) represent different hydrothermal phases or changes in the fluid conditions that allow morphological evolution of quartz, which, according to the presence of zoning textures, reflects abrupt changes in fluids and very advanced recrystallization processes.

In Cerro Matoso peridotites, weathering developed a complete laterite profile with complex silica vein stockwork at different topographic levels. It is commonly admitted that weathering of mantle peridotites tectonically exposed to the atmosphere commonly leads to natural carbonation processes through a mechanism that involves the infiltration of meteoric waters enriched in dissolved atmospheric CO_2. Mg and Si commonly released during the laterization of peridotites are usually represented by extensive cryptocrystalline silica/magnesite veins and widespread stockwork in the laterite profile, similar to the lowest area of Pit-1 in Cerro Matoso or in the New Caledonia ophiolites (Ulrich et al., 2014).

Based on field and textural observations at Bench level 42 and uppers, the carbonation of peridotites at Cerro Matoso must have gone through two stages to form the two types of listvenites that are associated with fracture zones, which act as pathways for altering and mineralizing fluids (e.g., Ucurum and Larson, 1999; Tsikouras et al., 2006). As suggested by Ucurum (2000), silica-carbonate listvenite is an early alteration product and is followed by non-quartz listvenites, which are formed as a final product from the alteration. The first stage produces a silica/carbonate vein system with brecciated textures affecting the type A listvenites at Cerro Matoso, and later the type B listvenites must have been formed. Listvenites of type A and B were apparently contemporaneous with the emplacement of the mantle section into the oceanic lithosphere, according to field relations. Abundant quartz veins (1 cm to 0.3 m wide) generated along fault zones with a regular pattern appear to have formed simultaneously with or slightly later than the listvenite. The most characteristic feature of listvenites is their relative resistance against weathering compared with the surrounding rocks.

The high silica content (65%) in the samples of listvenites (i.e., tachylites from Gleeson et al., 2004) compared with their possible precursors (peridotite, 45%) suggest an extra SiO_2 input in a metasomatic system. Additionally, it is associated with the intense quartz vein system pattern at the Cerro Matoso outcrops. Listvenites without quartz represent a second stage of metasomatic alteration. The latter are named carbonate listvenites (Type II) by Ucurum (2000), while those with quartz are named silica-carbonate listvenites (Type I) in the Karakuz area in Turkey. The lower content of SiO_2 in listvenite B (sample CM-3) (Table 2), although not identified by XRD, is part of the silica in phyllosilicates. This makes sense because silica is more soluble at higher pH levels, a setting that makes the formation of siderite favorable. This suggests that the hydrothermal solution to form the listvenites at Cerro Matoso was characterized by low to moderate temperatures under a reduced environment instead of an oxidized environment or supergene.

Although Barnes et al. (1973) suggest that in a supergene listvenitization, the amount of carbonate, silica, and the pH of the groundwaters favor the precipitation and recrystallization of carbonate and/or silica after or coincident with dissolution to create carbonated and/or silicified peridotites, Nasir et al. (2007) suggest that this process is more efficient with hydrothermal fluids at alkaline pHs. Stanger (1985) indicates that silicification of listvenites is a low-temperature chemical replacement feature and not a weathering phenomenon, although some effects leading to the formation of listvenite are aqueous precipitates from bicarbonate-rich groundwaters (Neal and Stanger, 1984, 1985; Stanger and Neal, 1984; Stanger, 1985).

However, the details about the petrogenesis of listvenites at Cerro Matoso are complicated and still not clearly defined, although fluids required for listvenitization will probably be related to low temperature hydrothermal systems of Type II (Kelley and Shank, 2010) in Castrillón (2019).

A low-temperature, alkaline, and highly reduced fluid, probably drained from serpentinite, could favor siderite formation instead of another carbonate. The low silica content (27-65%) compared with that of other listvenites (e.g., 85-92% in Koracakaya, Turkey; 81-83%, in the Iti ophiolite, Greece) also suggests that these rocks were affected by hydrothermal systems, increasing silica content in some cases (i.e., near veins) or reducing it in others. In the latter case, the possibility is that silica will dissolve from serpentinite and/or harzburgite into the hydrothermal fluid during the formation of type B listvenites and will be taken from the system by the remaining silica-rich fluid in a high-pH and low-temperature environment. This is possible because silica is more soluble at high pH levels (>9) and could therefore indicate which listvenite is formed first.

Hydrothermal fluids apparently induced alteration of Cr-spinel to siderite. This fluid allowed an intense water-rock interaction resulting in carbonation, partial silicification, and less serpentinization of the peridotite (Nasir et al., 2007). The intensity of the alteration at the local level varies from small veins of carbonate and quartz to complex stockwork systems that replace the original structure of the rock. These vein structures can also be precipitated by weathering. To clarify this point, isotope analyses of siderite would be useful. Meanwhile, it is clear that listvenite lenses in Cerro Matoso can reach 20 m of thickness, can vary from a few meters to 200 m, and can vertically grade to the serpentinized harzburgites from which they were derived; these harzburgites had also suffered an intense supergene weathering process, which converted peridotites into green saprolites that also present siderite (Sumicol, 2002).

High Cr and Ni contents and the occurrence of Cr-spinel plus Mn-carbonate, olivine, and orthopyroxene relics indicate an ultramafic protolith for the Cerro Matoso listvenites. Ucurum (2000) indicates that elements such as As, Ba, Cr and Ni are more enriched in silicate-carbonate listvenites that were probably controlled by the amount and the presence of silica, which creates an increase in their concentration compared with the serpentinites' Co, Cr and Ni content. In this sense, Ni grades (reaching 6.1 wt%) of listvenites at Cerro Matoso could be associated with hydrothermal alteration of peridotites, as also happened for Co, Hg and Au, (Koc and Kadiglu, 1996) or for Ni, Mn, Pb, Co and SiO_2 (Aydal, 1990), rather than a supergene origin.

Differences in the amounts of Fe_2O_3, SiO_2 and MgO in the listvenites (A and B, Table 2) suggest differences in the alteration, intensity or composition of the protolith and/or the chemistry of the ancient hydrothermal fluids affecting the peridotites. High concentrations of Fe-Mn in the fluids should have favored the formation of siderite and Mn-siderite. Once exposed to supergene weathering conditions (since the Eocene), the chemistry of listvenites was possibly affected as well.

The difference of the presence of siderite instead of other carbonates in the Cerro Matoso listvenites may be because they are derived from fresh ultramafic rocks, such as those reported in Central Euboea, Greece (Capedri and Rossi, 1973). Listvenites generally comprise part of the hydrothermal transformation of ophiolitic melánges that contain a chaotic accumulation of harzburgite, lherzolite, dunite, chromitite, gabbro, diabase, basalt, tuff, and chert blocks (e.g., serpentinite bodies in the Divrigi and Kuluncan ophiolitic mélange, Turkey [Ucurum, 2000]; Sartohay ophiolitic mélange in west Junggar, Xinjiang, China [Qiu and Zhu, 2015, 2018]), which can contribute to the amount of carbonates it contains. The Egyptian ophiolites are described as variably dismembered, deformed, altered, and metamorphosed peridotites due to serpentinization and interaction with a large flux of CO_2-bearing fluids (Gahlan et al., 2018) that led to the formation of various types of carbonate-bearing meta-ultramafics, but also were tectonically incorporated in a mélange with metasediments and metavolcaniclastics (Gahlan et al., 2018). Siderite deposits are reported at the contact between Caltu ultramafic rock and the Buldudere Formation in the Kuluncak ophiolite mélange (Ucurum, 2000).

According to Kashahi and Allakverdiev (1965), listvenites are formed, with a few exceptions, by the metasomatic/hydrothermal alterations of serpentine to evolve as products in two successive stages of the same process: the serpentinization of ultrabasites followed by metasomatic alteration. Similarly, Ucurum (2000) shows that listvenite is formed later than serpentinization and is superimposed on earlier serpentinite, which means that lisvenitization occurs by metasomatism of weakly serpentinized or completely serpentinized mafic minerals.

A fossilized Type II hydrothermal system (Kelly and Shank, 2010) was proposed as part of the geological history of Cerro Matoso (Castrillón, 2019) based on the isotope composition in bulk samples in black conglomeratic mudstone (BCM) overlying listvenites. Although negative $\delta^{13}C$ (-21.6 to -8.1‰ V-PDB) values are compatible with meteoric waters, $\delta^{18}O$ (25.1 to 29.8 ‰ V-SMOW) values indicate a low-temperature hydrothermal/diagenetic system and could only be explained by oxidation of methane processes. It is possible that hydrothermal fluid activity metasomatized the Cerro Matoso peridotites. According to information from a hole drilled at Pit-1 (Figure 1), listvenites have always been associated with BCM; unfortunately, some rocks with a similar chemical composition to listvenites were assigned the same name (i.e., tachylites by the mine geologists), and later, they were identified as marine sediments, generating confusion about the origin of both.

The $\delta^{18}O$ values at Cerro Matoso differ from the isotopic composition values of typical smectites of weathered clays (Savin and Epstein, 1970), which are consistent with $\delta^{18}O$ values (20.3 to 24.3 ‰ SMOW) in nickel smectites in Murrin Murrin, Western Australia (Gaudin et al., 2005), and represent water-rock interactions at low temperatures by the contact of meteoric fluid during mineral leaching processes in which laterites are formed. These $\delta^{18}O$ isotope values in siderite form the BCM II facies, and some intraclasts indicate temperatures over 90°C that can be associated with diagenetic/hydrothermal fluids. These values are similar in temperature to the calculation from the $\delta^{18}O$ content of carbonate of silica-carbonate alteration (between 56°C and 163°C) of the Cretaceous ophiolite at Narman (Ucurum, 2000).

Most likely, as suggested (Kim et al., 2007), the slight difference of 0.00042 at 75°C in the fractionation factor between aragonite ($\Delta = 1.00856$) and siderite ($\Delta = 1.00898$) permitted the siderite to replace the original carbonate, inheriting its isotopic composition; however, according to Rosenbaum and Sheppard (1986), the minimal difference of 0.0002 at 100°C in the fractionation factor between ankerite ($\Delta = 1.00901$) and siderite ($\Delta = 1.00881$) could make it possible that siderite replaces ankerite, inheriting its isotopic composition. This would explain the presence of siderite instead of another carbonate in listvenites. Zheng (1998) also suggests that carbonates may prefer to be formed in the first state of crystallization of $CaCO_3$ and subsequently converted to another carbonate without isotopic reset.

Some ultramafic bodies in western Colombia have been associated with Pacific oceanic crust (Pindell and Barrett, 1990; Pindell and Kennan, 2009), as is the case for Cerro Matoso peridotites, where listvenites could have been formed in the oceanic domain in a pre- or syn-obduction context similar to the one suggested by Kishida and Kerrich (1987), Buisson and Leblanc (1987), Auclair et al. (1993) or Tsikouras et al. (2006), and would be the unusual expression of metasomatism in the ocean floor. Nevertheless, Nasir et al. (2007) suggest that the metasomatism process can take place either while an ophiolite is part of the oceanic lithosphere or during its detachment from it and be reflected along major thrust and fracture zones where the metasomatic alteration of the peridotite is more intense and complete.

Specifically, in an oceanic geological setting where the ophiolites are exposed at the seafloor, the peridotites undergo serpentinization reactions, and it is very possible that Type II hydrothermal systems (Kelley and Shanks, 2010) have been hosted in peridotites (e.g., Logatchev and Rainbow at the Mid-Atlantic Ridge). The additional geological setting, including the hydrothermal system hosted by the Cerro Matoso peridotites, in an ancient mid-oceanic ridge far west of its present location could have originated the metasomatic alteration of peridotites, and listvenites would be proof of that. After being accreted during the Cretaceous to the continent and strongly affected by weathering and mineral leaching processes since the late Eocene (López-Rendón, 1986), all of the rocks at Cerro Matoso changed chemically and physically, probably confusing the origins of some of them (i.e., black conglomeratic mudstone and listvenites).

6. CONCLUSIONS

The previously described unit has been defined since the end of the 20th century by geologists at Cerro Matoso S.A. (today, South32) as "tachylite", and it has been mineralogically and chemically described in studies by Sumicol (2002) and Gleeson et al. (2004), among others. Now, the term "listvenite" is assigned to this unit, meaning, in a broad sense, a product of siliceous-carbonated alteration of serpentinized ultramafic protolith by hydrothermal fluids.

The listvenite bodies at Cerro Matoso present a WNW-ESE orientation can be associated with fault zones through which hydrothermal fluids could have affected the original protolith (i.e., variably serpentinized harzburgite), altering the peridotite composition to produce an assemblage of Mn-siderite (12 wt%, MnO) +/- quartz, accompanied by nontronite, serpentine (lizardite ± chrysotile), goethite, and magnetite, with Cr-spinel relicts, olivine and orthopyroxene.

Field relations and textural evidence along with the occurrence of Cr-spinel relics suggest a hydrothermal metasomatism process that occurred before the supergene weathering of peridotite (of harzburgitic origin), perhaps during serpentinization processes once the Cerro Matoso peridotites were exposed in the ocean deep.

ACKNOWLEDGMENTS

This article is part of the doctoral thesis of Andrés Castrillón, who gives thanks for a grant from Colciencias (Scholarship 647, National Doctorate) and Universidad Nacional de Colombia. This work was also possible thanks to the support of Dr. Vanessa Cole from the Universidad Nacional Autónoma de México and their team at the Instituto de Geología. Special acknowledgments go to the Cerro Matoso S.A. company for allowing the development of this research.

References

Abuamarah, B. A. (2020). Geochemistry and fore-arc evolution of upper mantle peridotites in the Cryogenian Bir Umq ophiolite, Arabian Shield, Saudi Arabia. *International Geology Review*, *62*(5), 630-648. https://doi.org/10.1080/00206814.2019.1652942

Aftabi, A., & Zarrinkoub, M. H. (2013). Petrogeochemistry of listvenite association in metaophiolites of Sahlabad region, eastern Iran: Implications for possible epigenetic Cu–Au ore exploration in metaophiolites. *Lithos*, *156-159*, 186-203. https://doi.org/10.1016/j.lithos.2012.11.006

Ash, C. H., & Arksey, R. L. (1991). *The listwaenites-lode gold association in British Columbia. Geological Fieldwork 1989*, paper 1990-1991.

Ash, C. H. (2001). *Relationship between ophiolites and gold–quartz veins in the North American Cordillera*. Bulletin 108. British Columbia, Ministry of Energy and Mines.

Auclair, M., Gauthier, M., Trottier, J., Jébrak, M., & Chartrand, F. (1993). Mineralogy, geochemistry, and paragenesis of the Eastern Metals serpentinite-associated Ni–Cu–Zn deposit, Quebec Appalachians. *Economic Geology*, *88*(1), 123-138. https://doi.org/10.2113/gsecongeo.88.1.123

Aydal, D. (1989). Gold-bearing listwanites in Arac Massif, Kastamonu, Turkey. *Terra Nova*, *2*(1), 43-52. https://doi.org/10.1111/j.1365-3121.1990.tb00035.x

Azer, M. K. (2013). Evolution and economic significance of listwaenites associated with Neoproterozoic ophiolites in South Eastern Desert, Egypt. *Geologica Acta*, *11*(1), 113-128. https://doi.org/10.1344/105.000001777

Barnes, I., O'Neil, J. R., Rapp, J. B., & White, D. E. (1973). Silica-carbonate alteration of serpentine: wall rock alterations in mercury deposits of the California Coast Ranges. *Economic Geology*, *68*(3), 388-398. https://doi.org/10.2113/gsecongeo.68.3.388

Barrero, D. (1974). *Metamorfismo regional en el Occidente Colombiano*. Simposio sobre ofiolitas Medellín, Colombia, Medellín.

Bates, R., & Jackson, J. (1987). *Glossary of Geology* (Third Ed.). American Geological Institute.

Boskabadi, A., Pitcairn, I. K., Broman, C., Boyce, A., Teagle, D. A. H., Cooper, M. J., Azer, M. K., Mohamed, F. H., Stern, R. J., & Majka, J. (2017). Carbonate alteration of ophiolitic rocks in the Arabian–Nubian Shield of Egypt: sources and compositions of the carbonating fluid and implications for the formation of Au deposits. *International Geology Review*, *59*(4), 391-419. https://doi.org/10.1080/00206814.2016.1227281

Bucher, K., & Stober, I. (2019). Interaction of Mantle Rocks with Crustal Fluids: Sagvandites of the Scandinavian Caledonides. *Journal of Earth Science*, *30*, 1084-1094. https://doi.org/10.1007/s12583-019-1257-2

Buisson, G., & Leblanc, M. (1987). Gold in mantle peridotites from Upper Proterozoic ophiolites in Arabia, Mali, and Morocco. *Economic Geology*, *82*(8), 2092-2097. https://doi.org/10.2113/gsecongeo.82.8.2091

Capedri, S., & Rossi, A. (1973). Conditions governing the formation of ophicalcites and listwaenites (Central Euboea/Greece). *Bulletin of Geological Society of Greece*, *10*(2), pp. 78-297.

Castrillón, A. (2013). *Determinación de las estructuras tubulares presentes en el Pit 6 en el depósito laterítico de níquel de Cerro Matoso* (Master thesis). Universidad Nacional de Colombia.

Castrillón, A. (2019). *Carbonatos y otros minerales autigénicos asociados a las lateritas niquelíferas de Cerro Matoso y su posible relación con actividad hidrotermal y reducción de sulfatos* (Doctoral Thesis) Universidad Nacional de Colombia.

Dekov, V. M., & Savelli, C. (2004). Hydrothermal activity in the SE Tyrrhenian Sea: an overview of 30 years of research. *Marine Geology*, *204*(1-2), 161-185. https://doi.org/10.1016/S0025-3227(03)00355-4

Demoustier, A. (1995). *Contribution ala caractérisation des quartz auriferes de la région de Cabo de Gata, province d'Almería, Espagne. Pétrographie-thermoluminescence-inclu-sions fluides. Travail de fin d'études*, Faculté Polytechnique de Mons.

Demoustier, A., & Castroviejo, R. (1997). *Fluid inclusion characterization of the Carneros epithermal ores (Cabo de Gata, Almería, SE Spain): preliminary results*. XIV ECROFI (European Current Research on Fluid Inclusions), Nancy, France.

Demoustier, A., Castroviejo, R., & Charlett, J. M. (1998). Clasificación textural del cuarzo epitermal (Au-Ag) de relleno filoniano del area volcánica de Cabo de Gata, Almeria. *Boletín Geológico y Minero*, *109*(5-6), 449-468.

Gahlan, H. A., Azer, M. K., & Asimow, P. D. (2018). On the relative timing of listwaenite formation and chromian spinel equilibration in serpentinites. *American Mineralogist*, *103*(7), 1087-1102. https://doi.org/10.2138/am-2018-6473

Gaudin, A., Decarreau, A., Noack, Y., & Grauby, O. (2005). Clay mineralogy of the nickel laterite ore developed from serpentinised peridotites at Murrin Murrin, Western Australia. *Australian Journal of Earth Sciences*, *52*(2), 231-241. https://doi.org/10.1080/08120090500139406

Gleeson, S., Herrington, R., Durango, J., & Velazquez, C. (2004). The Mineralogy and Geochemistry of the Cerro Matoso S.A. Ni Laterite Deposit, Montelíbano, Córdoba. *Economic Geology, 99*(6), 1197-1213. https://doi.org/10.2113/gsecongeo.99.6.1197

Gonçalves, C., Fabris, J., & Pacheco Serrano, W. (1999). Chemical and mineralogical analyses of a weathering mantle developing on peridotite of the mining area for nickel in Cerro Matoso, Colombia. *Hyperfine Interactions*, 122, 171-176. https://doi.org/10.1023/A:1012658009195

Halls, C., & Zhao, R. (1995). Listvenite and related rocks: perspectives on terminology and mineralogy with reference to an occurrence at Cregganbaun, Co. Mayo, Republic of Ireland. *Mineralium Deposita*, *30*(3-4), 303-313. https://doi.org/10.1007/BF00196366

Imamalipour, A., Karimlou, M., & Hajalilo, B. (2018). Geochemical zonality coefficients in the primary halo of Tavreh mercury prospect, northwestern Iran: implications for exploration of listwaenitic type mercury deposits. *Geochemistry: Exploration, Environment, Analysis*, *19*(4), 347-357. https://doi.org/10.1144/geochem2018-048

Jutras, J., & Geol, P. (2002). Ultramafic nickel-bearing magmas of the Nadaleen river area (106C/3) and associated listwaenites: new exploration targets in Mayo Mining District, Yukon. In D. Emond, & L. Lewis, *Exploration and Geological Service Division, Yukon Region, Indian and Northerb Affairs, Canada*. Manson Creek Resources Ltda.

Kashkai, M., & Allakverdiev, S. (1965). *Listwaenites, their origin and classification.* (U. G. Survey, Ed.) Baku, Izdat. Akad, Nauk Azerbaidzhanskoi: Translated by Vi-taliano, D.B.

Kelemen, P. B., & Matter, J. M. (2008). In situ carbonation of peridotite for CO_2 storage. *PNAS*, *105*(45), 17295-17300. https://doi.org/10.1073/pnas.0805794105

Kelley, D. S., & Shank, T. M. (2010). Hydrothermal systems: a decade of discovery in slow spreading environments. In P.a. Rona, C.w. Devey, J. Dyment, & B.j. Murton (Eds.), *Diversity Of Hydrothermal Systems On Slow-Spreading Ocean Ridges*. Agu Geophysical Monograph Series. https://Doi.org/10.1029/2010Gm000945

Kim, S-T., Mucci, A., & Taylor, B. E. (2007). Phosphoric acid fractionation factors for calcite and aragonite between 25 and 75 °C: Revisited. *Chemical Geology*, *246*(3-4), 135-146. https://doi.org/10.1016/j.chemgeo.2007.08.005

Kishida, A., & Kerrich, R. (1987). Hydrothermal alteration zoning and gold concentration at the Kerr–Addison Archean lode gold deposit, Kirkland Lake, Ontario. *Economic Geology*, *82*(3), 649-690. https://doi.org/10.2113/gsecongeo.82.3.649

Koc, S., & Kadioglu, Y. K. (1996). Mineralogy, geochemistry, and precious metal content of Karacakaya (Yunusemre-Eskisehir) Listwaenites. *Ofioliti*, *21*(2), 125-130.

Leblanc, M. (1991). Platinum-group elements and gold in ophiolitic complexes: distribution and fractionation from mantle to oceanic floor. In T. Peters, A. Nicolas, & R. Coleman, *Ophiolite Genesis and Evolution of the Oceanic Lithosphere*. Springer. https://doi.org/10.1007/978-94-011-3358-6_13

Lelis, M.deF., Gonçalvesa C. M., Fabris, J. D., Mussel, W. N., & Pacheco-Serrano, W. A. (2004). Effectiveness of Selective Chemical Treatments on Concentrating Magnetic Minerals of Samples from a Nickel-Ore Peridotite Mantle. *Journal of the Brazilian Chemical Society*, *15*(6), 884-889. https://doi.org/10.1590/S0103-50532004000600015

Lewis, J., Draper, G., Proenza, J., Epaillat, J., & Jiménez, J. (2006). Ophiolite-Related Ultramafic Rocks (Serpentinites) in the Caribbean Region: A Review of their ocurrence, composition, origin, emplacement and Ni-laterite soil formation. *Geológica Acta, 4*(1-2), 237-263. https://doi.org/10.1344/105.000000368

Londoño, A. C., & González, H. (1997). *Geología del Departamento de Córdoba*, Scale 1:250.000. Ingeominas.

López-Rendón, J. (1986). *Geology, Mineralogy and Geochemistry of the Cerro Matoso Nicheliferous Laterite, Córdoba, Colombia.* Montelibano (Master Thesis). Colorado State University.

Meissner, R., Flueh, E., Stibane, F., & Berg, E. (1976). Dynamics of the active plate boundary in soutwest Colombia according to recent geophysical measurements. *Tectonophysics*, *35*(1-3), 115-136. https://doi.org/10.1016/0040-1951(76)90032-9

Mejia, V., & Durango, J. (1981). Geologia de las lateritas niquelíferas de Cerro Matoso. *Boletin de Geología, 15*(29), 117-123.

Mora-Bohórquez, J., Ibáñez-Mejía, M., Oncken, O., de Freitas, M., Vélez, V., Mesa, A., & Serna, L. (2017). Structure and age of the Lower Magdalena Valley basin basement, northern Colombia: New reflection-seismic and U-Pb-Hf insights into the termination of the central andes against the Caribbean basin. *Journal of South American Earth Sciences*, 74, 1-26. https://doi.org/10.1016/j.jsames.2017.01.001

Nasir, S., Al Sayigh, A., Al Harthy, A., Al-Khirbash, S., Al-Jaaidi, O., Musllam, A., Al-Mishwat, A., & Al-Bu'saidi, S. (2007). Mineralogical and geochimical characterization of listwaenite from the Semail Ophiolite, Oman. *Geochemistry*, *67*(3), 213-228. https://doi.org/10.1016/j.chemer.2005.01.003

Neal, C., & Stanger, G. (1983). Hydrogen generation from mantle source rocks in Oman. *Earth and Planetary Science Letters*, *66*, 315-320. https://doi.org/10.1016/0012-821X(83)90144-9

Neal, C., & Stanger, G. (1984). Calcium and magnesium hydroxide precipitation from alkaline groundwaters in Oman, and their significance to the process of serpentinization. *Mineralogical Magazine*, *48*(37), 237-241. https://doi.org/10.1180/minmag.1984.048.347.07

Neal, C., & Stanger, G. (1985). Past and present serpentinization of ultramafic rocks; an example from the Semail ophiolite nappe of northern Oman. In J.I. Drever (ed.), *The Chemistry of Weathering. Reidel*, Dordrecht

Nosouhian, N., Torabi, G., & Arai, S. (2016). Amphibole-bearing listwaenites from the Paleozoic Bayazeh ophiolite (Central Iran). *Italian Journal of Geosciences*, *135*(1), 109-119. https://doi.org/10.3301/IJG.2015.04

Nosohuian, N., Torabi, G., & Arai, S. (2019). Petrological aspects of the Bayazeh Paleozoic ophiolite (Central Iran); implications for Paleo-Tethys subduction. *Periodico di Mineralogia*, *88*(2), 155-184.

Pindell, J., & Barrett, S. (1990). Geological evolution of the Caribbean region: a plate tectonic perspective. In J. Pindell, & S. Barrett, *The Caribbean Decade of North American Geology*. Geological Society of America.

Pindell, J., & Kennan, L. (2009). Tectonic evolution of the Caribbean and northern South America in the mante reference frame. In J. Pindell, & L. Kennan, *The geology and evolution of theh region between North and South America* (Special Publication ed., p. 60). Geological Society of London.

Qiu, T., & Zhu, Y. F. (2015). Geology and geochemistry of listwaenite-related gold mineralization in the Sayi gold deposit, Xinjiang, NW China. *Ore Geology Reviews*, *70*, 61-79. https://doi.org/10.1016/j.oregeorev.2015.03.017

Qiu, T., & Zhu, Y. F. (2018). Chromian spinels in highly altered ultramafic rocks from the Sartohay ophiolitic mélange, Xinjiang, NW China. *Journal of Asian Earth Sciences*, *159*, 155-184. https://doi.org/10.1016/j.jseaes.2017.08.011

Rose, G. (1837). Mineralogisch-geognostiche Reise nach dem Ural, dem Altai und dem Kaspischen Meere. In C. Berlin, *Eichoff (Verlag der Sanderchen Buchhandl)* (Vols. I-VII).

Rosenbaum, J., & Sheppard, S. (1986). An isotopic study of siderites, dolomites and ankerites at high temperatures. *Geochimica et Cosmochimica Acta*, *50*(6), 1147-1150. https://doi.org/10.1016/0016-7037(86)90396-0

Savin, S. M., & Epstein, S. (1970). The oxygen and hydrogen isotope geochemistry of clay minerals. Geochimica et Cosmochimica Acta, *34*(1), 25-42. https://doi.org/10.1016/0016-7037(70)90149-3

Stanger, G., & Neal, C. (1984). A new occurrence of suoluinte, from Oman. *Mineralogical Magazine*, *48*, 143-146.

Stanger, G. (1985). Silicified serpentinite in the Semail nappe of Oman. *Lithos*, *18*, 13-22. https://doi.org/10.1016/0024-4937(85)90003-9

Sumicol S.A. (2002). *Caracterización mineralógica de los tipos de roca de la laterita niquelífera de Cerro Matoso S.A., Colombia*. Informe privado para Cerro Matoso S.A., 2 vols.

Taitel-Goldman, N., Ezersky, V., & Mogilyanski, D. (2008). Study of Mn-siderite–rhodochrosite from the hydrothermal sediments of the Atlantis II Deep, Red Sea. *Israel Journal of Earth Sciences*, *57*, 45-54.

Tsikouras, B., Karipi, S, Grammatikopoulos, T. A., & Hatzipanagiotou, K. (2006). Listwaenite evolution in the ophiolite mélange of Iti Mountain (continental Central Greece). *European Journal of Mineralogy*, *18*(2), 243-255. https://doi.org/10.1127/0935-1221/2006/0018-0243

Ucurum, A. (1998). Application of the correspondence-type geoestatistical analysis on the Co, Ni, As, Ag, and Au concentrations of the listwaenites from serpentinites in the Diveru and Kulunack ophiolitic mélanges. *Turkish Journal of Earth Sciences*, *7*(2), 87-95.

Ucurum, A., & Larson, L. T. (1999). Geology, Base-Precious Metal Concentration and Genesis of the Silica-Carbonate Alteration (Listwaenites) From Late Cretaceous Ophiolitic Mélanges at Central East Turkey. *Chemie der Erde*, 59, 77-104.

Ucurum, A. (2000). Listwaenites in Turkey: perspectives on formation and precious metal concentration with referene to occurrences in East-Central Anatolia. *Ofioliti*, *25*(1), 15-29.

Ulrich, M., Muñoz, M., Guillot, S., Cathelineau, M., Picard, C., Quesnel, B., Boulvais, P., & Couteau, C. (2014). Dissolution–precipitation processes governing the carbonation and silicification of the serpentinite sole of the New Caledonia ophiolite. *Contributions to Mineralogy and Petrology*, *167*. https://doi.org/10.1007/s00410-013-0952-8

Von Damm, K. L. (1995). Controls on the chemistry and temporal variability of seafloor hydrothermal fluids. In S. Humphris, J. Lupton, L. Mullineaux, & R. Zierenberg, (eds.), *Physical, Chemical, Biological, and Geological Interactions within Seafloor Hydrothermal Systems*, vol. 91, 222-247. https://doi.org/10.1029/GM091p0222

Zheng, Y. F., Fu, B., Li, Y., Xiao, Y., & Li, S. (1998). Oxygen and hydrogen isotope geochemistry of ultra-high pressure eclogites from the Dabie mountains and the Sulu terrane. *Earth and Planetary Science Letters*, *155*(1-2), 113-129. https://doi.org/10.1016/S0012-821X(97)00203-3

Zierenberg, R. A., & Shanks, W. C. (1988). Isotopic studies on epi- genetic features in metalliferous sediment Atlantis II Deep, Red Sea. The Canadian Mineralogist, 26(3), 737-753.

Boletín Geológico

Boletín Geológico, 47, 85-105, 2020
https://doi.org/10.32685/0120-1425/boletingeo.47.2020.527

Received: June 1, 2020
Revised: September 24, 2020
Accepted: October 23, 2020

Review of geothermochronological and thermobarometric techniques for the construction of cooling and exhumation curves or paths for intrusive igneous rocks

Revisión de técnicas geotermocronológicas y termobarométricas para la construcción de curvas o trayectorias de enfriamiento y exhumación en rocas ígneas intrusivas

Lina María **Cetina**[1], Julián Andrés **López-Isaza**[1], Mario Andrés **Cuéllar-Cárdenas**[1], Anny Julieth **Forero-Ortega**[1]

1. Dirección Técnica de Geociencias Básicas, Servicio Geológico Colombiano (SGC), Bogotá, Colombia.
Corresponding autor: Lina María Cetina, lcetina@sgc.gov.co

ABSTRACT

The present study reviews radiometric and thermobarometric techniques used to construct cooling curves or paths to characterize intrusive bodies and to calculate cooling and exhumation rates. To construct these curves or paths, the temperature, time and depth variables must be estimated in intrusive bodies by applying various analytical techniques, including thermobarometry and U-Pb zircon, Ar-Ar hornblende and muscovite, fission track and (U-Th)/He zircon and apatite dating, in combination with a geological framework of reference for each intrusive body. The authors recommend to determine the crystallization age by zircon U-Pb dating, to quantify the emplacement depth using thermobarometry methods according to the composition of the intrusive body, to calculate the initial cooling ages with hornblende and muscovite Ar-Ar methods, as well as to calculate the cooling/exhumation ages in the upper crust using low-temperature thermochronology methods. These cooling curves or paths in intrusive bodies are highly relevant when studying compressive or extensional areas because they partly represent the thermal history of the era, thereby providing data on the magmatic and tectonic evolution of the region. Thus, these studies are highly important for designing geodynamic models and for their possible application in developing the tectonic model of the country.

Keywords: cooling and exhumation curves or paths, geochronology, thermochronology, thermobarometry in igneous rocks.

RESUMEN

El presente trabajo expone una revisión de técnicas radiométricas y termobarométricas para construir curvas o trayectorias de enfriamiento aplicadas a la caracterización de intrusivos, así como el cálculo de tasas de enfriamiento y exhumación. Para la construcción de estas curvas o trayectorias se deben estimar en los intrusivos las variables de temperatura, tiempo y profundidad,

Citation: Cetina, L. M., López-Isaza, J. A., Cuéllar-Cárdenas, M. A., & Forero-Ortega, A. J. (2020). Review of geothermochronological and thermobarometric techniques for the construction of cooling and exhumation curves or paths for intrusive igneous rocks. *Boletín Geológico, 47*, 85-105, https://doi.org/10.32685/0120-1425/boletingeo.47.2020.527

aplicando diversas técnicas analíticas que incluyen termobarometría y geotermocronología U-Pb en circón, Ar-Ar en hornblenda y moscovita, y trazas de fisión y (U-Th)/He en circón y apatito, esto integrado a un marco geológico de referencia para cada intrusivo. Se recomienda determinar la edad de cristalización mediante U-Pb en circón, cuantificar la profundidad del emplazamiento utilizando métodos de termobarometría según la composición del intrusivo, calcular edades de enfriamiento inicial con los métodos Ar-Ar en hornblenda y moscovita, y calcular edades de enfriamiento/exhumación en corteza superior mediante métodos de termocronología de baja temperatura. Estas curvas o trayectorias de enfriamiento en intrusivos son de gran relevancia para estudiar áreas compresivas o extensionales, pues representan en parte la historia termal de la zona y, por lo tanto, proporcionan información sobre la evolución magmática y tectónica de la región. Por lo expuesto, estos estudios son de gran importancia para la formulación de modelos geodinámicos y su posible aplicación en la construcción del modelo tectónico del país.

Palabras clave: curvas o trayectorias de enfriamiento y exhumación, geocronología, termocronología, termobarometría en rocas ígneas.

1. Introduction

Cooling processes inside the earth's crust result from geological events, and their characterization makes it possible to learn the thermal history of a region and to obtain information about their magmatic, metamorphic and tectonic evolution (cf. Dodson, 1979; Harrison et al., 1979; Zeitler, 1985; Green, Duddy, Laslett et al., 1989, Corrigan, 1991; Gallagher et al., 1998, Reiners and Brandon, 2006). In recent decades, different radiometric dating techniques have been combined to construct cooling curves or paths in rock bodies (since isotopic systems are essentially a form of geothermometry) in order to understand the dynamics of orogenic belts and sedimentary basins, as well as their relationships with mineral deposits and petroleum systems (cf. Zeitler, 1985; Green, Duddy, Gleadow et al., 1989; Hunziker et al., 1992; Gallagher et al., 1998; McInnes et al., 1999; Armstrong, 2005; Bernet et al., 2006, Peyton and Carrapa, 2013 a, b; Bernet et al., 2019).

In regions with tectonic deformation, applying various radiometric techniques may help to constrain the exhumation time and rates, and if the exhumation results from tectonic activity, these techniques may help to determine the time of the tectonic events occurred (cf. Zeitler et al., 1982; Bernet et al., 2006; Deeken et al., 2006; Peyton and Carrapa, 2013a); however, exhumation processes are also related to erosion and climatic effects, as well as the combination of these processes to a greater extent (cf. Zeitler, 1985; Brandon et al., 1998; England and Molnar, 1990; Ring et al., 1999; Reiners and Brandon, 2006; Peyton and Carrapa, 2013a; Bernet et al., 2019).

Constructing cooling and exhumation curves for intrusive igneous rocks is an excellent opportunity to partly retrace the thermal and tectonic evolution of a region due to its extensive exposure. In addition, determining the formation age of the intrusive body can constrain deformation and post-deformation times, and offer a first-order view of the uplift or subsidence of the crust during tectonic processes (Harrison et al., 1979; Zeitler, 1985; Hurford, 1986; Anderson et al., 1988; Clarke, 1992; Anderson, 1996; Foster et al., 2001; Anderson et al., 2008; Glorie et al., 2017; Nieto Samaniego et al., 2019).

In Colombia, various radiometric techniques have been used in intrusive rocks to determine crystallization and cooling ages (e.g., *Catalogo de dataciones radiometricas de Colombia*, cf. Gomez et al., 2015), as well as cooling and exhumation studies in intrusive bodies using low-temperature thermochronology techniques (e.g., Sáenz et al., 1996; Sáenz, 2003; Restrepo-Moreno et al., 2009; Villagómez et al., 2011; Cardona et al., 2011; Villagómez and Spikings, 2013; Van der Lelij et al., 2016; León et al., 2018; Restrepo-Moreno et al., 2019). In turn, few thermobarometry studies have estimated the emplacement depth of igneous bodies exposed in the country (Martínez and Zuluaga, 2010; Gil-Rodríguez, 2014; Cortés-Calderón, 2015).

Despite the large volume of geothermochronological data on intrusive units published in the literature, few studies have focused on constructing the cooling and exhumation curves or paths of these units for understanding the evolution of areas with magmatic belts. For this purpose, the authors of this review suggest to consider that: a) reported radiometric data should be statistically validated to increase the reliability of crystallization and cooling ages of intrusive units, b) thermobarometry studies should be performed in intrusive rocks to quantify the emplacement levels of these bodies and c) carrying out systematic studies that combine the different techniques used to the construction of cooling curves or paths in intrusive rocks.

The aim of this review is to present a proposal to construct cooling curves or paths for studying the thermal history of intrusive units in Colombia, to perform a literature review on the currently used analytical techniques, and to highlight the importance of these cooling curves or paths as a complementary tool for determining the geological evolution of the respective units through geodynamic concepts. These approaches are useful to systematically calculate cooling and exhumation rates, and these inputs may be applied to complete the tectonic model of the country.

1.1 History of cooling and exhumation of intrusive igneous rocks

The exposure of large intrusive bodies in the continental crust suggests that these types of rocks play a key role in the evolution of the continents. Therefore, knowing their cooling and exhumation histories is crucial for understanding the crustal evolution that continental masses experience during tectonic events (cf. Anderson, 1996; Foster et al., 2001; Anderson et al., 2008; Mutch et al., 2016; Reiners et al., 2017, p. 197).

The history of cooling and exhumation of intrusive igneous bodies (cf. Harrison et al., 1979; Harrison and Clarke, 1979; Hurford, 1986; England and Molnar, 1990; Foster et al., 1992; George, 1993; Caggianelli et al., 2000; Parada et al., 2005; Glorie et al., 2017; Bernet et al., 2019; Nieto-Samaniego et al., 2019) can be determined by constructing cooling curves or paths, thereby assessing the temperature, time and depth variables that characterize the body from its initial emplacement to its final exposure on the surface (Figures 1 and 2).

These cooling curves or paths are based on the fact that mineral phases dated by some isotopic method, show typical closing temperatures. Therefore, cooling ages associated with different temperature ranges can be determined in a sample, and to perform temperature vs. age plots. In addition, by thermal field modeling or by assuming a geothermal gradient in the study area, the temperature-time data can be converted into depth-time to estimate the cooling/exhumation rates that are partly associated with tectonic events (cf. Wagner et al., 1977; Zeitler et al., 1982; Zeitler, 1985; Hunziker et al., 1992; Bernet et al., 2006; Reiners et al., 2017, pp. 105-122).

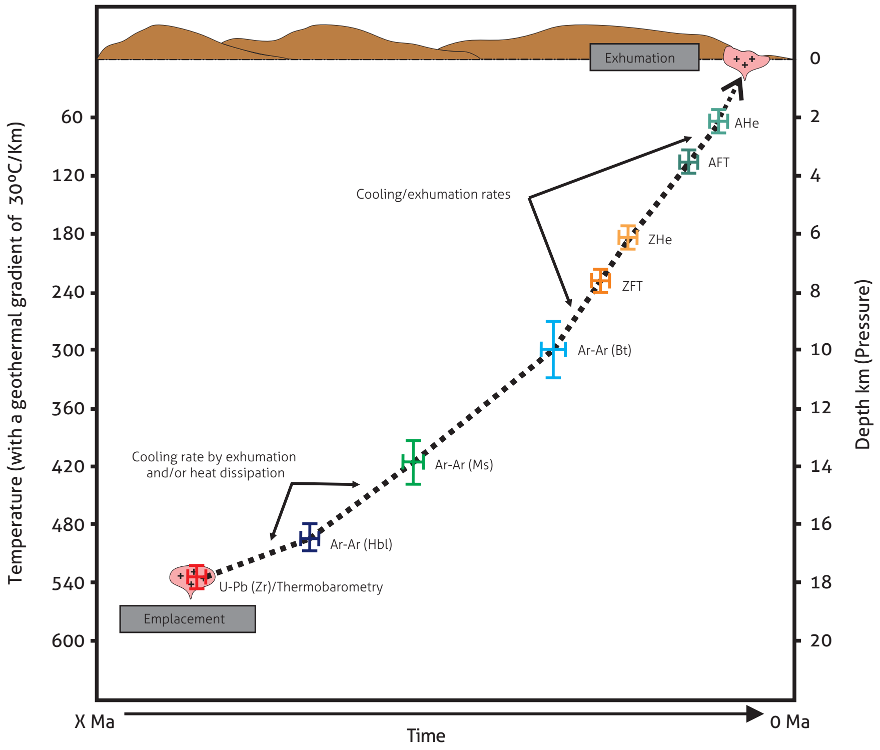

Figure 1. Representative diagram of a hypothetical cooling curve or path of an intrusive body from its emplacement to its final exposure on the surface, indicating the various geothermochronological and thermobarometric methods recommended for determining its cooling/exhumation history. The bars that accompany each method correspond to the uncertainty associated with age and depth. The temperature shown correspond to the hypothetical temperatures of the host rock, according to a geothermal gradient of 30 °C/km. Abbreviations: Zr: zircon; Hbl: hornblende; Ms: muscovite; Bt: biotite; ZFT: fission track in zircon; ZHE: (U-Th)/He in zircon; AFT: fission track in apatite; and AHe: (U-Th)/He in apatite.

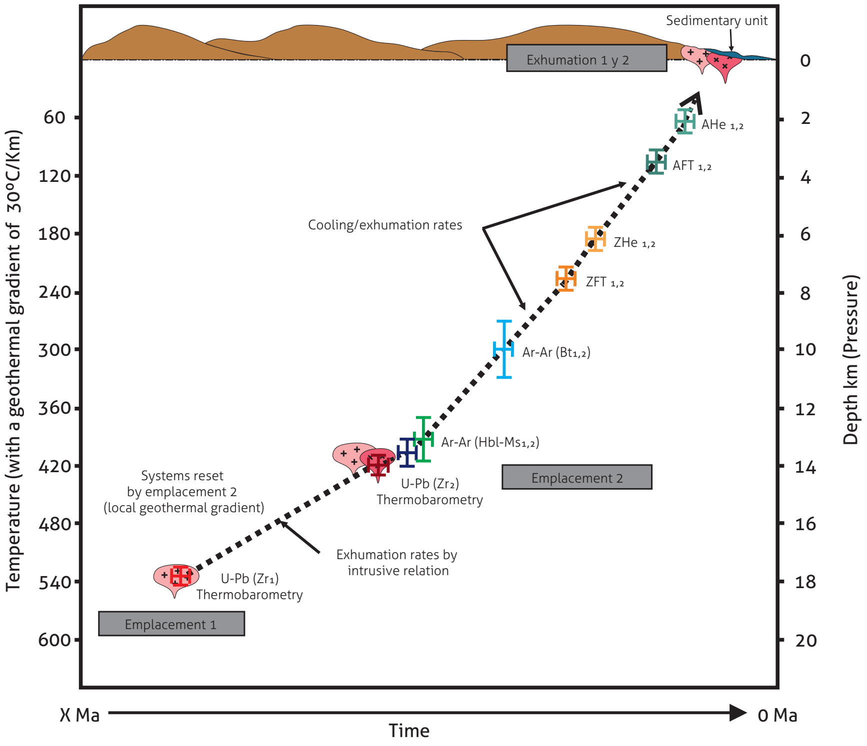

Figure 2. Representative diagram of the cooling curve or path of two intrusive bodies from their emplacement to their final exhumation on the surface showing the field relationships and the geothermochronological and thermobarometric methods recommended for determining their cooling/exhumation history. The bars that accompany each method correspond to the uncertainty associated with age and depth. The temperature shown corresponds to the hypothetical temperature of the host rock according to a geothermal gradient of 30 °C/km. Abbreviations are described in Figure 1.

These cooling curves or paths were initially considered empirically because they represent net histories, which involves simplifying a scenario that may have actually had more complex cooling paths (Zeitler, 1985). However, with sufficient samples and geological data, these curves or paths are highly reliable (Zeitler, 1985) using high-resolution and high-reliability ages and onsidering some type of thermal modeling (cf. Zeitler, 1985; Ehlers, 2005; Ketcham, 2005; Braun et al., 2012).

To properly construct this type of curve or path, the intrusive body should first be geologically characterized, identifying the field relationships with adjacent rocks and the type of contact observed to establish its geological context for reference (Figure 2). This step establishes valid geological criteria that support the interpretation of the findings through various analytical methods. If the unit geological context is clear, cooling and exhumation curves or paths can be constructed by integrating various geothermochronological and thermobarometric methods and by calculating the cooling and exhumation rates of the intrusive body.

2. PROPOSAL FOR THE CONSTRUCTION OF COOLING AND EXHUMATION CURVES OR PATHS OF INTRUSIVE BODIES

The following proposal combines various geothermochronological and thermobarometric methods for determining emplacement (or crystallization) and cooling and/or exhumation ages, according to the closure temperature of each mineral system (Figure 3). These methods also provide key data on the depth associated with each geological process. The application of these analytical methods is conditioned to the nature of the study bodies, that is, they depend on the presence of minerals, such as hornblende, biotite, muscovite, zircon, apatite, and so on. Thus, a sequence of steps is proposed below to gather the necessary data to construct the cooling curves or paths of intrusive rocks:

1. Geological characterization of the intrusive units, determining their nature, geological context and field relationships with adjacent units.

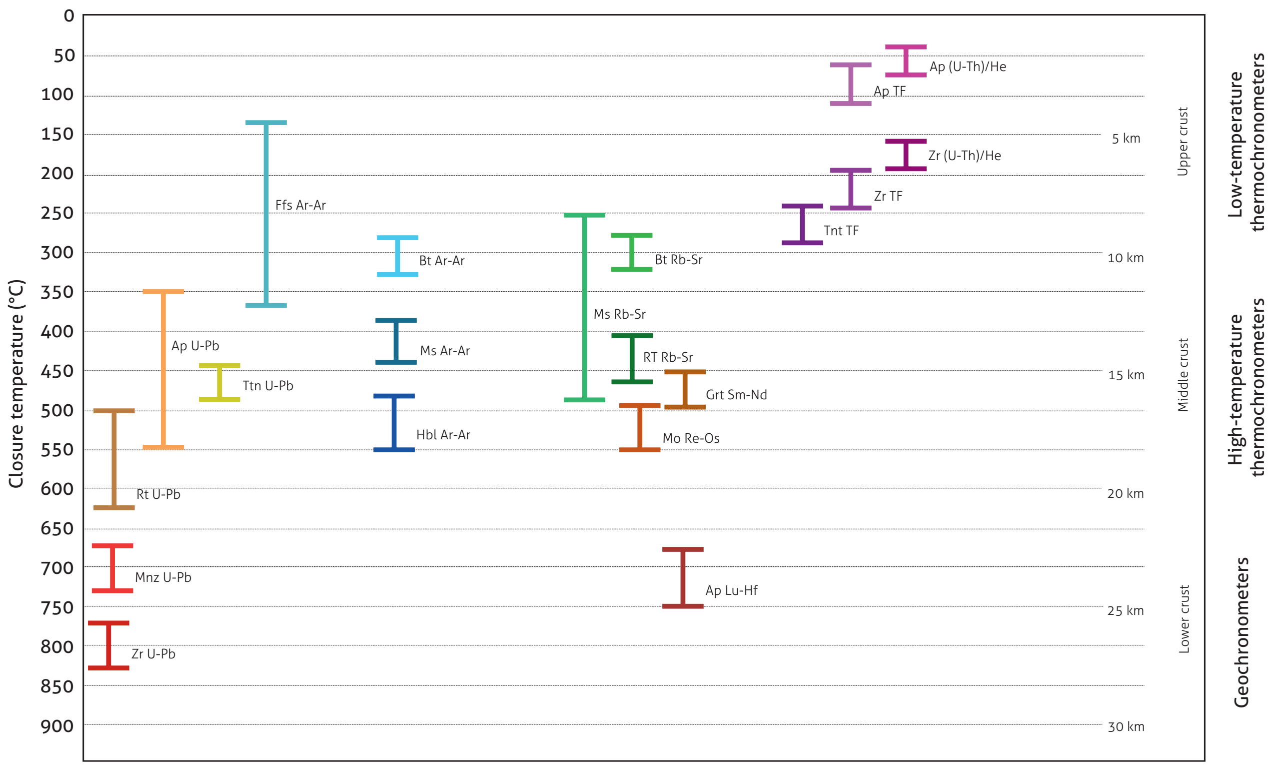

Figure 3. Average closure temperatures of different geothermochronometers and their potential depths, assuming a geothermal gradient of 30 °C/km. Temperature thresholds retrieved from Harrison (1982), Grove and Harrison (1996), Harrison et al., (2009), Chew and Spikings (2015), Bernet et al. (2019) and references therein. Abbreviations: Zr: zircon; Mnz: monazite; Rt: rutile; Ap: apatite; Ttn: titanite; Hbl: hornblende; Ms: muscovite; Bt: biotite; Kfs: potassium feldspar; Mo: molybdenite; Grt: garnet; and FT: fission track.

2. Geological characterization of the units adjacent to the intrusive bodies.
3. Calculation of emplacement (or crystallization) ages using the zircon U-Pb method.
4. Quantitative estimation of emplacement depths using thermobarometry techniques (e.g., aluminum in hornblende barometer), which are also applied to the host rock to estimate the geothermal paleogradient of the emplacement environment.
5. Calculation of initial cooling ages using high-temperature thermochronometers (hornblende and muscovite Ar-Ar).
6. Calculation of cooling ages in the upper crust levels using high-temperature thermochronometers (fission track and zircon and apatite (U-Th)/He dating).
7. Determination of the thermal history of intrusive bodies by combining geothermochronological and thermobarometric data, assuming a geothermal gradient or from thermal field modeling.
8. Calculation of cooling (Δtemperature/Δtime) and exhumation (Δtemperature/geothermal gradient/Δtime) rates.
9. Evaluation of the possible cooling/exhumation mechanisms associated with tectonic events, erosion or both processes.

3. ANALYTICAL METHODS

Obtaining the necessary data to determine the cooling curve or path of intrusive rocks requires applying specific analytical methods, whose particular characteristics will influence the possible interpretations of the results. The methods used to obtain data for constructing the cooling curve or path are described below.

3.1. Zircon U-Pb geochronology: emplacement age

The emplacement age of an intrusive body can be correlated with its crystallization age, which is determined by zircon U-Pb dating (cf. Faure and Messing, 2005; Reiners et al. 2017, pp. 197-199). Also, the crystallization age of zircon is assumed to be the crystallization age of the igneous body because the mineral has a closure temperature of approximately 900-700 °C (Cherniak and Watson, 2001; Harrison et al., 2007) and an average of 800 °C (Figure 3), at which a melt of intermediate composition would reach 50% crystallization (Carroll and Wyllie, 1990; Harrison et al., 2007).

However, the emplacement of plutonic bodies may involve multiple intrusive facies (cf. Miller et al., 2007; Reiners et al. 2017, pp. 198-199), and due to the crystallization of a zircon mineral depends on zirconium saturation and on the composition and temperature of the melt (Harrison et al., 2007) a granite body may contain zircon xenocrysts, anticrysts and autocrysts, which gives rise to a wide range of zircon U-Pb ages (cf. Coleman et al., 2004; Miller et al., 2007). Xenocrysts are zircons that are foreign to the magmatic melt, which can be derived, for example, from the source rock (in this case, termed inherited zircons) or from the host rock. Anticrysts are zircons formed in the initial magma pulses, and autocrysts are zircons that grow within the main intrusive pulse (Figure 4; Miller et al., 2007).

Based on the above information, the crystallization age of the intrusive body (or emplacement age) corresponds to the population of ages in zircons interpreted as autocrysts, with statistically reliable parameters (cf. Vermeesch, 2018). Thus, to correctly interpret the U-Pb ages in zircon crystals, the following tasks are recommended: a) characterize the mor-

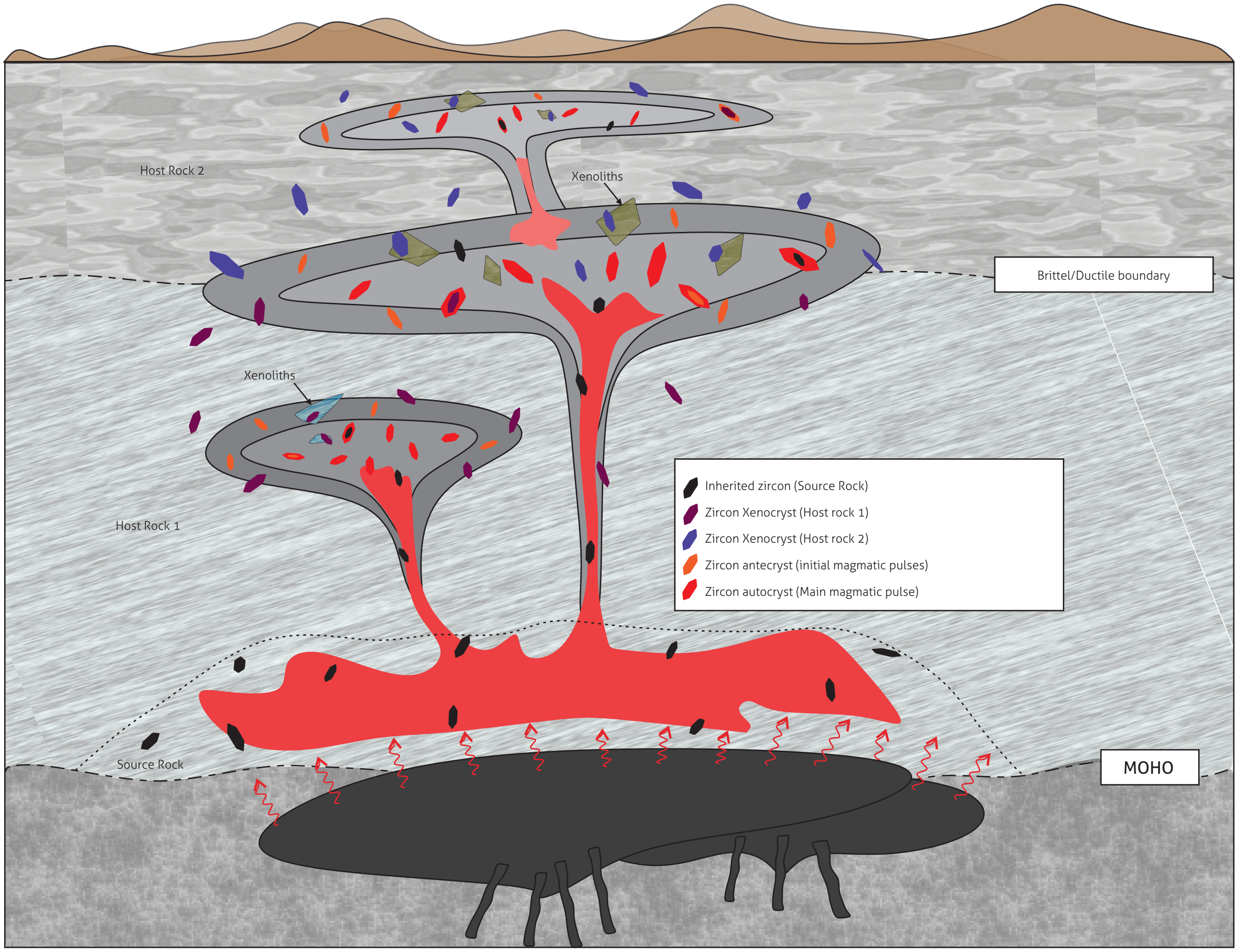

Figure 4. Schematic diagram of the possible types of zircons present in a magmatic system, corresponding to inherited zircons, xenocrysts, anticrysts and autocrysts, according to the criteria by Miller et al. (2007)

phological typology of the crystal (Pupin, 1980); b) classify internal textures using cathodoluminescence images (Corfu et al.,2003); c) cluster the ages obtained from crystals interpreted as xenocrysts, anticrysts and autocrysts; and d) calculate inherited and crystallization ages using the Isoplot (Ludwig, 2009) or IsoplotR (Vermeesch, 2018) programs.

To determine whether the calculated ages are statistically reliable, the statistical parameter mean squared weighted deviation, MSWD (Wendt and Carl, 1991), should be used because this parameter indicates the level of data dispersion (Vermeesch, 2018) and makes it possible to indirectly assess whether individual age weighting and uncertainty represent a single population (Spencer et al., 2016). Accordingly, MSWD = 1 indicates that the calculated age neither underestimates nor overestimates the associated uncertainties; MSWD < 1 indicates overestimated ages, and MSWD > 3 indicates underestimated ages (Spencer et al., 2016; Vermeesch, 2018). Thus, acceptable values of MSWD vary in the range of > 0 to 3, and these values are in turn related to the number of analyses used to calculate the age, as more analyses achieve better MSWD values (see Figure 3 of Spencer et al., 2016). For example, for a number of analyses (or spots) of N = 20, the acceptable MSWD would range from 0.35 to 1.65, for an age calculated with 2σ, which guarantees a reliable age (Spencer et al., 2016). On the other hand, statistically significant ages are those that present a value of P (X^2) 0.05 to 0.95, and this parameter indicates the level of data dispersion with respect to analytical uncertainties around the best-fit line (Vermeesch, 2018).

3.2. Thermobarometry in igneous rocks: emplacement depth

To approximate the emplacement depth of an intrusive body, the magma crystallization pressure and the crystallization temperature near the *solidus* line must be simultaneously estimated (Blundy and Holland, 1990; Holland and Blundy, 1994; Anderson, 1996; Anderson and Smith, 1995; Anderson et al., 2008; Mutch et al., 2016). Various thermobarometers have been proposed in the literature to determine these intensive variables from the composition, equilibrium or saturation of mineral phases present in the intrusive bodies (Table 1). The thermobarometers applied to intrusive rocks are described as follows:

Al-in-Hornblende barometer (Al in Hbl)

This barometer is based on the strong correlation between the total Al content in Hbl and the crystallization pressure of an intrusive (Hammarstrom and Zen, 1986). From this correlation, various equations found in the literature are formulated, generally based on experimental petrology, to estimate the crystallization pressure. The equations differ in the initial experimental parameters, such as the total composition of the host rock, the nature of the fluid phase (H_2O or H_2O-CO_2), the temperature range at which the experiment was performed and the different empirical or experimental calibrations of each equation (Hammarstrom and Zen, 1986; Schmidt, 1992; Anderson and Smith, 1995; Anderson et al., 2008; Mutch et al., 2016).

For a metaluminous granitoid of intermediate to felsic composition with a mineral association of quartz + plagioclase ($An_{25\text{-}35}$) + hornblende + biotite + titanium and iron oxides ± potassium feldspar ± titanite, which was most likely emplaced from 2 kbar to 14 kbar at crystallization temperatures lower than 800 °C, equation 1 (Anderson and Smith, 1995) is applied:

$$P(kbar) = 4.76\ \mathrm{Al}\text{-}3.01\text{-}\frac{[T\,°C - 675]}{85} \times$$

$$[0.530\ Al + 0.005294(T\,°C - 675)] \pm 0.6\ kbar \qquad (1)$$

Applying this barometer requires estimating the crystallization temperature (Anderson and Smith, 1995) because the positive correlation between temperature and $^{[IV]}$Al content in Hbl (Blundy and Holland, 1990) generates overestimated values of pressure at high temperature (>650 °C) (Anderson and Smith, 1995). To use this equation, the authors also recommend ensuring high oxygen fugacity (fO_2) in the system based on Fe/(Fe+Mg) ratios in Hbl ranging from 0.4 to 0.61.

For granitoids with a mineral association of amphibole + plagioclase ($An_{15\text{-}85}$) + biotite + quartz + alkali feldspar + ilmenite/titanite + magnetite + apatite at temperatures near the *solidus* line (725 ± 75 °C), which are emplaced at low pressures (from 2.5 to 0.5 kbar), equation 2 (Mutch et al., 2016) should be used:

$$P\ (kbar) = 0.5 + 0.331(8) \times Al + 0.995(4) \times Al^2 \pm 16\%\ P \qquad (2)$$

Wherein the numbers in parentheses correspond to the uncertainty 1σ expressed in the physical notation with the lowest significant number (Mutch et al., 2016). To correctly apply this equation, the crystallization temperature should also be estimated, thereby ensuring the necessary conditions for its use, which assumes a crystallization temperature of approximately 725 ± 75 °C, as previously mentioned.

Amph+Pl Thermometer

The Amph + Pl thermometer is used to determine the crystallization temperature of a granitoid of variable composition (even with rocks unsaturated in quartz) with a mineral association between amphibole and plagioclase over a temperature range of 400-1000 °C and a pressure range of 1-15 kbar (Holland and Blundy, 1994). This thermometer is based on the equations of equilibrium between edenite + quartz = tremolite + albite (for associations with quartz, termed *thermometer A*) and edenite + albite = richterite + anorthite (for associations without quartz, termed *thermometer B*). This technique considers a non-ideal mixture in both amphibole and plagioclase compositions and calibrates the equations using a database of natural and synthetic amphiboles to reach uncertainties of ± 35-40 °C or higher for iron-rich amphiboles (Holland and Blundy, 1994). The equations (3) and (4) are proposed by the authors.

Iterative calculations using this thermometer and the Al-in-Hbl barometer can provide reliable pressure and temperature ranges in metaluminous granitoids (cf. Anderson et al., 2008).

Thermobarometers based on the composition of calcic amphiboles

A set of barometers and thermometers based on the chemical composition of amphiboles, which is applicable under conditions of temperature raging from 1130 to 800 °C and under a wide pressure range from 22 to 1.3 kbar, have been reported for calc-alkaline and alkaline rocks with calcic amphibole (Ridolfi et al., 2010; Ridolfi and Renzuli, 2012). These thermobarometers are empirically formulated from data in the literature regarding natural and synthetic amphibole compositions, with multivariate least squares analysis of experimental compositions of this mineral (Ridolfi et al., 2010; Ridolfi and Renzuli, 2012).

Thermobarometers based on the clinopyroxene-liquid equilibrium

Thermobarometers based on the clinopyroxene-liquid equilibrium can be used in intrusive rocks of mafic composition under conditions of pressure ranging from 0 to 30 kbar and temperatures ranging from 1100 to 1475 °C (Putirka et al., 1996). These thermobarometers are recommended for rocks that are not granitoids, because mafic rocks are exposed over wide areas in Western Colombia.

Other barometers

In peraluminous granitoids without the required mineral associations to use the Al-in-Hbl barometer and without a suitable composition of calcic amphiboles, pressure can be estimated using empirical garnet + biotite + plagioclase + quartz (Wu et al., 2004a) or garnet + muscovite + plagioclase + quartz (Wu et al., 2004b) barometers developed for metapelitic rocks, which are recommended for granitoids with this mineralogy (Anderson et al., 2008). Similarly, in peraluminous plutons with garnet and muscovite, where muscovite contains celadonite, pressure can be estimated by barometry developed in high-pressure metapelites (cf. Wei and Powell, 2004; 2006; Anderson et al., 2008).

Moreover, the identification of stable mineral phases under specific pressure conditions can constrain the calculation, such

$$\text{Thermometer A:} \quad \frac{-76.95 + 0.79P + Y_{ab} + 39.4X_{Na}^{A} + 22.4X_{Na}^{A} + (41.5 - 2.89\,P)\,.\,X_{Al}^{M_2}}{-0.0650 - \mathrm{R}\,.\,ln\left(\dfrac{27\,.\,X_{\square}^{A}\,.\,X_{Si}^{T_1}\,.\,X_{ab}^{plag}}{256\,.\,X_{Na}^{A}\,.\,X_{Al}^{T_1}}\right)} \tag{3}$$

where the term $Y_{ab} = 0$, if > 0.5; otherwise, $Y_{ab} = 12.0(1 - X_{ab})^2 - 3.0\ kj$; the empty box in $X_{\square}^{A}$ corresponds to the vacancy in the crystallographic site A of amphiboles.

$$\text{Thermometer B:} \quad \frac{78.44 + Y_{ab-an} - 33.6X_{Na}^{M4} - (66.8 - 2.92\,P)\,.X_{Al}^{M2} + 78.5X_{Al}^{T1} + 9.4\,X_{Na}^{A}}{0.0721 - \mathrm{R}\,.\,ln\,\dfrac{27\,.\,X_{Na}^{M4}\,.\,X_{Si}^{T_1}\,.\,X_{an}^{plag}}{64\,.\,X_{Ca}^{M4}\,.\,X_{Al}^{T_1}\,.\,X_{ab}^{plag}}} \tag{4}$$

where the term $Y_{ab-an} = 0$, if $X_{ab} > 0.5$; otherwise, $Y_{ab-an} = 12.0\,(2X_{ab} - 1) + 3.0\ kj$, expressing the temperature as Kelvin, the pressure as kbar, the composition X_i^{Φ} as the molar fraction of element i in mineral phase $^{\Phi}$, and gas constant $R = 0.0083144\ kjK^{-1}mol^{-1}$ (Holland and Blundy, 1994).

as the presence of magmatic epidote, which suggests a pressure > 5 kbar (Zen and Hammarstrom, 1984; Schmidt, 1993). The emplacement depth of an intrusive body can also be estimated when knowing the pressure and temperature conditions at the contact aureole (e.g., garnet + biotite + cordierite equilibrium [cf. Treloar, 1981] and with the aforementioned barometry in peraluminous granitoids applied to the contact rocks [cf. Wu et al., 2004 a, b]). Moreover, the depth of an intrusive body can be qualitatively estimated in terms of epizonal (0-10 km), mesozonal (6-16 km) and catazonal (> 10 km) emplacement by characterizing the type of contact and by describing micro- and mesostructures of the intrusive body and host rock (Buddington, 1959; Paterson et al., 1996), although the resulting ranges should be taken with caution.

Other thermometers

Other thermometers, which can be applied to intrusive bodies of different compositions, are based on the saturation of accessory phases or on the content of the trace elements of these phases (cf. Anderson et al., 2008), such as zircon (Watson and Harrison, 1983) and apatite (Tollari et al., 2006) saturation thermometers and titanium (Ti)-in-zircon (Watson et al., 2006; Ferry and Watson, 2007) and zirconium (Zr)-in-titanite (Hayden et al., 2008) thermometers.

Crystallization temperatures obtained by zircon saturation and Ti-in-zircon thermometers are not always comparable, and the crystallization temperatures tend to be more closely associated with the temperature derived from the Ti-in-zircon method (Harrison et al., 2007) because zircon saturation temperature can be affected by the presence of pre-magmatic zircons (xenocrysts) in the granitic systems that saturate the magma with zircon during the melting process and not during the crystallization process.

The Ti-in-zircon thermometer is based on both empirical and experimental calibration, according to the abundance ratio of titanium in zircon and to its variation as a function of the crystallization temperature, and it is derived from equation 5 (Watson et al., 2006):

$$logTi(ppm)_{zircon} = 5.69 - \left[\frac{3765}{T(K)}\right] \tag{5}$$

However, the substitution of Ti in zircon is related to the activities of TiO_2 and SiO_2. Therefore, a new experimental calibration is required in a temperature range from 1450 to 590 °C, which emphasizes the effect of these activities (Ferry and Watson, 2007):

$$logTi(ppm)_{zircon} = 5.711 - \left[\frac{4800}{T(K)}\right] - log\,(a_{SiO2}) + log\,(a_{TiO2}) \tag{6}$$

In turn, the Zr-in-titanite thermometer was empirically and experimentally calibrated by Hayden et al. (2008), based on experiments at temperatures ranging from 800 to 1000 °C and at pressures ranging from 10 to 24 kbar, and the variation in the Zr abundance in titanite as a function of temperature and pressure is described by using equation 7:

$$logZr(ppm)_{titanite} = 10.52 - \left[\frac{7708}{T(K)}\right] - \left[960 \times \left(\frac{\mathrm{P}\ (Gpa)}{T(K)}\right)\right]$$
$$- log\,(a_{SiO2}) - log\,(a_{TiO2}) \tag{7}$$

Table 1. Thermobarometers that are potentially suitable for estimating pressure and temperature in intrusive rocks

Barometer/thermometer	P and/or T conditions	Compositional characteristics	Reference
Al-in-Hlb Barometer	Pressure range = 2-14 kbar	Metaluminous granitoids	Anderson and Smith (1995)
	Pressure < 2.5 kbar	Metaluminous granitoids	Mutch et al. (2016)
Hbl+Pl Thermometer	Pressure range = 1-15 kbar, temperature range = 400-1000 °C	Granitoids with quartz (thermometer A)	Holland and Blundy (1994)
		Granitoids without quartz (thermometer B)	
Thermobarometers based on the composition of calcic amphiboles	Pressure range = 1.3-22 kbar, temperature range = 1130-800 °C	Calc-alkaline and alkaline rocks	Ridolfi et al., (2010); Ridolfi and Renzulli (2012)
Thermobarometer based on the clinopyroxene-liquid equilibrium	Pressure range = 0-30 kbar, temperature range = 1100-1475 °C	Mafic igneous rocks	Putirka et al. (1996)
Gr+Bt+Pl+Qz barometer	Pressure range = 1-11.4 kbar, temperature range = 515-878 °C	Peraluminous granitoids/ hornfels with this mineralogy	Wu et al. (2004a)
Gr+Ms+Pl+Qz barometer	Pressure range = 1-11.4 kbar, temperature range = 505-745 °C	Peraluminous granitoids/ hornfels and/ or host rock with this mineralogy	Wu et al. (2004b)
Zircon-saturation thermometer	Near-*solidus* temperature	Intermediate to felsic granitoids	Watson and Harrison (1983)
Apatite- saturation thermometer	Near-*liquidus* temperature	Peraluminous granitoids	Tollari et al. (2006)
Ti-in-zircon thermometer	Temperature range = 1450-590 °C	Intermediate to felsic granitoids	Ferry and Watson (2007)
Zr-in-titanite thermometer	Pressure range = 10-24 kbar, temperature range = 800-1000 °C	Intermediate to felsic granitoids	Hayden et al. (2008)

This thermometer may underestimate the temperature if the TiO_2 content is < 1, as expected in common intrusive bodies without rutile (Hayden and Watson, 2007; Anderson et al., 2008). Also, the apatite saturation temperature can be used for peraluminous granitoids (Tollari et al., 2006).

3.3. High-temperature thermochronology: initial cooling age

The interpretation of a cooling age in intrusive rocks is directly related to the concept of closure temperature. Closure temperature is defined as the temperature at which a radiometric system starts to accumulate the daughter isotopes produced by the decay of the parent isotope, which reduces the diffusion loss to almost zero (Dodson, 1973; 1979). Based on this concept, various thermochronometers are sensitive to temperature variations and provide information on the thermal history of the rock, rather than mineral crystallization ages (cf. Dodson, 1973; Zeitler, 1985; Gallagher et al., 1998; Kelley, 2002; Reiners and Brandon, 2006; Peyton and Carrapa, 2013a).

Thus, the cooling ages of intrusive rocks correspond to the ages obtained using thermochronological systems with a closure temperature lower than the crystallization temperature of the intrusive body (cf. Dodson, 1979; Zeitler, 1985; Kelley, 2002; Reiners and Brandon, 2006). The initial cooling ages correspond to the post-emplacement ages that are close to the crystallization age of the intrusive body. To calculate these ages, high-temperature thermochronology is the most suitable approach (cf. Harrison, 1982; Zeitler, 1985; Reiners and Brandon, 2006; Schaen et al., 2020). To clarify, the closure temperatures of the systems will depend on the cooling rate of the rock and on kinetics, geometry, composition and size crystal (cf. Dodson, 1979; Harrison, 1982; Donelick et al., 2005; Reiners and Brandon, 2006; Reiners et al., 2017, pp. 97-101; Oriolo et al., 2018; Bernet et al., 2019).

Among the high-temperature thermochronometers (Figure 3), hornblende and muscovite $^{40}Ar/^{39}Ar$ methods stand out because the radiogenic isotope argon is a noble gas, which can be easily affected by diffusion in the minerals and which is only fully retained when the intrusive rock is already at a cooling stage (Dalrymple and Lanphere, 1969). Furthermore, these thermochronometers have considerably higher closure temperatures than other thermochronometers suitable for calculating initial cooling ages (Harrison, 1982; Zeitler, 1985; Harrison et al., 2009; Reiners et al., 2017, pp. 231-253; Schaen et al., 2020) (Figure 3). In the biotite $^{40}Ar/^{39}Ar$ method, the thermometer is considered to be a low-temperature thermometer (Figure 3) because the closure temperatures range from 330 to 280 °C (cf. Harrison et al., 1985; Grove and Harrison, 1996), thus recording younger cooling ages, which would not correspond to the initial cooling ages of an intrusive rock. The potassium feldspar $^{40}Ar/^{39}Ar$ method shows a wide range of closure temperatures (~350-150 °C) (Figure 3) and frequently contains complex microstructures and degrees of alteration. Thus, the potassium feldspar $^{40}Ar/^{39}Ar$ thermochronometer is not recommended for plutonic and metamorphic rocks and is accordingly more often applied to the geochronology of volcanic rocks (cf. Reiners et al., 2017, p. 240; Schaen et al., 2020).

$^{40}Ar/^{39}Ar$ dating can lead to interpretation problems and ages without geological significance. These caveats are related to a) ^{39}Ar recoil, which disturbs the $^{40}Ar/^{39}Ar$ ratio and the accuracy of age and affects fine-grained minerals and minerals with a high surface/volume ratio (e.g., micas) (cf. Kelley, 2002; Reiners et al., 2017, p. 240; Schaen et al., 2020); b) low K concentrations (~< 2% wt K_2O), which makes it difficult to detect ^{39}Ar, and high Ca/K ratios, which can generate interference problems due to reactions in the reactor, two conditions that affect amphiboles (cf. McDougall and Harrison, 1999; Kelley, 2002; Reiners et al., 2017, p. 241); c) argon loss by diffusion, due to the density of defects in the crystalline structure of the mineral (e.g., fractures) and to edge defects (cf. Dahl, 1996; Kramar et al., 2001; Kelley, 2002; Schaen et al., 2020), and d) argon excess in the minerals resulting from fluid, melt or solid inclusions, with the fluid and melt phases being high reservoirs of ^{40}Ar because the element is highly incompatible (cf. Esser et al., 1997; Boven et al., 2001; Kelley, 2002; Schaen et al., 2020).

Considering the above information, step heating should be used in $^{40}Ar/^{39}Ar$ dating because this approach may show the behavior of a partly open system, the presence of non-radiogenic ^{40}Ar in the sample and the ^{39}Ar recoil associated with the surface of the crystal (cf. Turner, 1970; Kelley, 2002; Reiners et al., 2017, pp. 243-246; Schaen et al., 2020). This technique generates an age spectrum as a function of the degassed fraction of the sample from step heating, in which a spectrum with a significant number of continuous steps and with indistinguishable ages will provide a plateau age, and this age is considered to be a concordant age (cf. Lanphere and Dalrymple, 1971; McDougall and Harrison, 1999; Fleck et al., 1977; Faure and Mensing, 2005; Reiners et al., 2017, pp. 243-246; Schaen et al., 2020). The plateau age should comprise at least 50% of the ^{39}Ar

released, at a 95% confidence level for each age encompassing the plateau age (Fleck et al., 1977), as well as include at least five or more consecutive steps (Schaen et al., 2020).

The spectrum of ages shows the excess of ^{40}Ar in the samples, for example, the excess of ^{40}Ar accumulated through fluid inclusions when released at low temperatures, as well as the excess of ^{40}Ar accumulated through melt or solid inclusions when released at high temperatures, which generates a U- or horseshoe-shaped spectrum of ages with older ages at the ends (cf. Lanphere and Dalrymple, 1971; Wartho et al., 1996; Kelley, 2002). Spectra with discordant ages that do not form plateau ages are also observed and are attributed to ^{40}Ar loss by diffusion, ^{39}Ar recoil or ^{39}Ar excess (cf. Turner, 1970; Boven et al., 2001; Reiners et al., 2017, pp. 243-246; Schaen et al., 2020).

Initial cooling rate

The initial cooling rates can be calculated using the hornblende and muscovite ^{40}Ar/^{39}Ar method thanks to the different closure temperatures of these thermochronometers (Figure 3). In this case, the oldest cooling age would be recorded when applying the hornblende ^{40}Ar/^{39}Ar method, which has a higher closure temperature (between 550 and 480 °C) (cf. Harrison, 1982) than the muscovite ^{40}Ar/^{39}Ar method, which has a relatively lower closure temperature (between 440 and 390 °C) (cf. Harrison et al., 2009), thereby yielding younger ages. By calculating these ages, including the crystallization age, the initial cooling rates of the intrusive rock can be estimated.

This initial cooling rate can be interpreted as a) cooling associated with heat transfer by conduction or advection (cf. Peacock 1989; Zeitler, 1985; Ehlers, 2005), or b) cooling attributed to tectonic exhumation processes that decrease the ambient temperature of the intrusive body (cf. Zeitler, 1985; England and Molnar, 1990; Ring et al., 1999). To infer the process that controlled the initial cooling, the tectonic context in which the intrusive body was emplaced and the physical parameters that describe the heat transfer processes should be considered (Ehlers, 2005). For example, one-dimensional heat diffusion in a given intrusive body could be estimated using equation 8 (Carslaw and Jaeger, 1959; Ehlers, 2005):

$$\frac{\partial T}{\partial t} = K \frac{\partial^2 T}{\partial z^2} \tag{8}$$

where ∂T is the temperature difference between the intrusive body and the host rock, ∂t is the time that the system spends decreasing its temperature, z is the parameter associated with the dimensions of the intrusive body, and K is the thermal diffusivity constant of an intrusive body (approximately 32 km^2/Ma) (Ehlers, 2005). The dimensions of the intrusive body can be estimated with its exposed surface area, field relationships and depth of emplacement, which is combined with geophysical techniques if available (cf. Clarke, 1992; Pitcher, 1997). The variation in temperature as a function of time can be assessed using the previously described thermometers and thermochronometers, including thermobarometry in the host rock, to determine the possible thermal paleogradient.

By applying equation 8 to a one-dimensional model and assuming a flat body shape, the initial temperature of a surface intrusive body with a diameter of 5 km, which affects a host rock at a temperature of 50 °C, decreases from 700 to 500 °C over 100000 years, which is exclusively due to heat conduction processes (Ehlers, 2005). In this model, the intrusive body size (diameter) increases the amount of heat that affects the host rock as its temperature decreases, as well as the duration and distance of the heat source. Under these conditions, an equilibrium should be reached between the temperature of the intrusive body and the host rock, which is controlled by the geothermal gradient of the environment (Ehlers, 2005).

Considering the above information, simple heat transfer models should be applied to identify the prevailing cooling process in each intrusive body, that is, whether cooling results from heat dissipation, from an associated tectonic event or from both (cf. Zeitler, 1985; Ehlers, 2005). For this, it must determine the cooling rates, the closure temperatures of the geothermochronometers, the initial temperatures of both the intrusive body and the host rock (thermobarometry, Table 1) and the relative dimensions of the rock bodies (cf. Clarke, 1992; Pitcher, 1997; Ehlers, 2005).

3.4. Low-temperature thermochronology: cooling/exhumation age in the upper crust

Low-temperature thermochronology is suitable for studying cooling processes at upper levels in the crust (cf. Gallagher et al., 1998; Farley, 2002; Peyton and Carrapa, 2013a; Reiners et al., 2017, pp. 105-127; Bernet et al., 2019) because this approach includes thermochronometers with closure temperatures lower than 300 °C, equivalent to shallow depths not exceeding 10 km, for a geothermal gradient of 30 °C/km (Figure 3, Table 2). In general, this cooling is generated as rocks move toward the surface through exhumation events resulting from erosion processes or tectonic activity (cf. England and

Molnar, 1990; Brandon et al., 1998; Ring et al, 1999; Reiners and Brandon, 2006; Peyton and Carrapa, 2013a). These ages can be associated with the exhumation ages of the rock body. By combining different thermochronometers (with different closure temperatures), exhumation rates can be estimated and thermal histories can be modeled during the passage of rocky bodies through the upper crust (Reiners and Brandon, 2006; Peyton and Carrapa, 2013a; Reiners et al., 2017, pp. 105-127; Bernet et al., 2019; Nieto-Samaniego et al., 2019).

The most commonly used low-temperature thermochronology techniques (cf. Gallagher et al., 1998; Farley, 2002; Donelick et al., 2005; Reiners and Brandon, 2006; Chew and Spikings, 2015; Bernet et al., 2019) are zircon and apatite (U-Th)/He (ZHe and AHe) and fission track (ZFT and AFT) dating. To correctly apply these thermochronological methods, the concepts of partial retention zone (PRZ), applicable to the (U-Th)/He technique, and partial annealing zone (PAZ), applicable to the fission track technique (Gleadow and Fitzgerald, 1987; Wolf et al., 1998; Brandon et al., 1998; Armstrong, 2005; Reiners and Brandon, 2006; Peyton and Carrapa et al., 2013a; Bernet et al., 2019) should be clarified, in addition to the concept of closure temperature. These additional concepts must be considered because the mineral may experience different cooling processes, including a) constant, monotonic and relatively fast cooling with a temperature that is always decreasing over time, in which case the concept of closure temperature would be applied, thereby assessing the cooling age (Table 2, Figure 5A), and b) variable cooling over time, possibly remaining in the temperature ranges of the PAZ and PRZ, in which case the systems are partly open, thus generating partial reset ages (Table 2, Figure 5B) (cf. Gallagher et al., 1998; Wolf et al.,1998; Brandon et al., 1998; Farley, 2002; Donelick et al., 2005; Reiners and Brandon, 2006; Bernet et al., 2019). Hence, thermochronological systems can follow different cooling paths, and each technique must be adequately applied toward understanding their thermal history and modelling cooling and exhumation rates close to reality (cf. Gallagher et al., 1998; Wolf et al., 1998; Farley, 2002; Reiners and Brandon, 2006; Bernet et al., 2019).

(U-Th)/He dating is based on the accumulation of He particles in zircon and apatite crystals derived from alpha decay in $^{238}\text{U}\rightarrow{}^{206}\text{Pb}$, $^{235}\text{U}\rightarrow{}^{207}\text{Pb}$, and $^{232}\text{Th}\rightarrow{}^{208}\text{Pb}$ decay systems (Wolf et al., 1996). Because He undergoes diffusion processes at high temperatures, He is only retained in the crystal below the closure temperature of each mineral (Figure 3, Table 2), thereby recording the cooling age (Wolf et al., 1996; Farley, 2000; Farley, 2002), or He might be partly accumulated in the partial retention zones (PRZ) established for each thermochronometer (Table 2), whereby the ages would be considered to be partial reset ages (Wolf et al., 1998).

Fission track dating is based on the spontaneous fission of ^{238}U that occurred in the crystalline structure of the minerals that contain U (Fleischer et al., 1975). This fission generates tracks (or damage) in the crystalline structure that are formed constantly over time, as long as they are generated below the closure temperature of each system, because fission tracks can quickly annealed due to solid-state diffusion in high-temperature environments (cf. Gallagher et al., 1998; Donelick et al., 2005; Reiners and Brandon, 2006; Bernet et al., 2019). The density of tracks in a crystal sector and the concentration of ^{238}U make it possible to calculate the age at which the mineral cooled below the closure temperature, according to a thermochronometer (Table 2), as long as the mineral has experienced relatively fast, monotonic and constant cooling at rates of approximately 10 to 100 °C/Ma (cf. Bernet et al., 2019) (Figure 5A). Conversely, if the minerals experienced slow cooling (2 °C/Ma), staying in the range of PAZ temperatures (Table 2, Figure 5b), or overheating due to a thermal event (in intrusive bodies), the tracks can partially annealed, thus recording partial reset ages (cf. Bernet et al., 2019).

Table 2. Closure temperatures and temperatures in the PAZ and PRZ corresponding to the ZFT, ZHe, AFT and AHe methods under average conditions

Thermochronometers	Closure temperature (cooling rate at 10 °C/Ma)	PAZ/PRZ		Reference
		Temp. upper	Temp. lower	
ZFT (zircon with natural radiation damage)	~230 °C	237.9°C	180.5 °C	Bernet et al., (2019) and references therein
ZHe	~190 °C	197 °C	159.2 °C	
AFT	~110 °C	114 °C	61 °C	
AHe	~70 °C	73.2 °C	47.9 °C	
Conditions	Monotonic and relatively fast cooling	Slow cooling or overheating		Cf. Peyton and Carrapa (2013a); Bernet et al. (2019)
Age interpretation	Cooling age	Partial reset age		

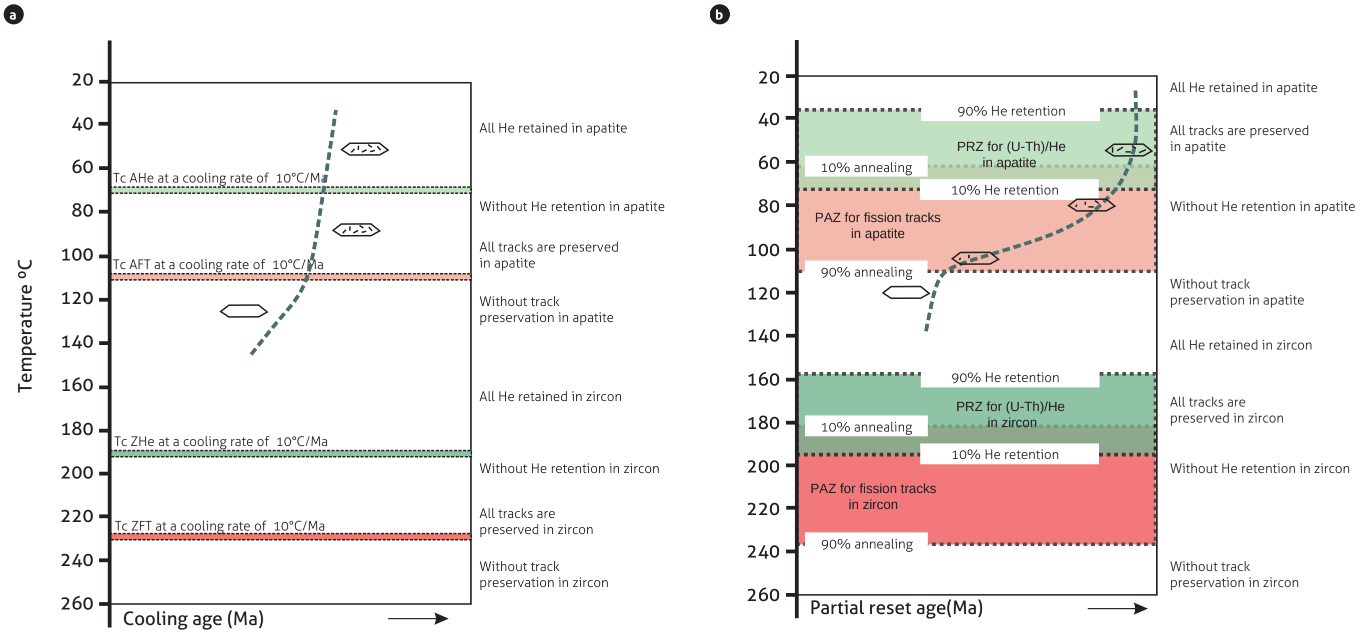

Figure 5. Possible cooling/exhumation curves of paths in the upper crust. a) Relatively fast and monotonic cooling curve; age derived from the closure temperature step (cooling age calculation). b) Slow cooling curve with prolonged passage in the PAZ and PRZ (partial reset age calculation). Temperature thresholds retrieved from Bernet et al. (2019) and references therein (see Table 2).

The AFT technique, in addition to calculating ages, requires studying/understanding of partial annealing degree experienced by the fission track (that is, how much they are shortened or anneling) necessary to know if the sample remained at PAZ temperatures, and for modeling the thermal history of the mineral (Gleadow et al.,1983; Green et al., 1986; Green, Duddy, Laslett et al., 1989; Gallagher et al., 1998; Ketcham et al., 1999; Donelick et al., 2005; Peyton and Carrapa, 2013a). The partial annealing process is mainly controlled by the time-temperature factor that affected the sample and by the direction of tracks with respect to the crystallographic axis, which is correlated with apatite composition (Gleadow et al., 1983; Green et al., 1986; Ketcham et al., 1999; Donelick et al., 2005). The temperature-time factor is determined by the distribution of horizontally confined track lengths, and the crystallographic direction of tracks (and apatite composition) is obtained using kinetic parameters (Gleadow et al., 1983; Green et al., 1986; Green, Duddy, Laslett et al., 1989; Gallagher et al., 1998; Ketcham et al., 1999; Donelick et al., 2005; Peyton and Carrapa, 2013a; Bernet et al., 2019).

The track length distribution method is based on the length-temperature relationship that exists in fission tracks, which could be shortened if the mineral resides within the PAZ temperatures for a significant time, consequently showing a bimodal track length distribution (cf. Green et al., 1986; Donelick et al., 2005; Peyton and Carrapa, 2013a). In this bimodal distribution, the shortest tracks would be the oldest, and the longest tracks would be the most recent, which are formed below the PAZ temperatures (cf. Green et al., 1986; Donelick et al., 2005; Peyton and Carrapa, 2013a).

One of the kinetic parameters is the chemical composition of apatite, which is based on a strong track annealing dependence on the chlorine/fluorine ratio, whereby chlorine-rich apatites are more resistant to track annealing, whereas apatites with fluoride experience faster partial annealing (Green et al., 1985; Barbarand et al., 2003; Donelick et al., 2005). Because determination of the apatite composition requires using destructive or complex and costly analytic techniques, an alternative kinematic parameter is Dpar (Donelick, 1993; Barbarand et al., 2003; Donelick et al., 2005).

Dpar is based on the solubility of the crystal to acid digestion to reveal tracks (etching) and is defined as the diameter of the geometric figure formed by the intersection between the fission track and the polished surface of the crystal; low Dpar values are typical of fluorine apatites, characterized by low annealing temperatures, whereas high Dpar values are commonly found in chlorine-rich apatites, characterized by high annealing temperatures (Donelick, 1993; Barbarand et al., 2003; Donelick et al., 2005).

In summary, the distribution of horizontally confined fission track lengths and the kinetic parameter Dpar should be determined to modeling the thermal history of apatite (cf. Green et al., 1985; Donelick, 1993; Gallagher et al., 1998; Barbarand, 2003; Donelick et al., 2005).

In the ZFT method, partial track annealing is controlled by the temperature, time and accumulation of alpha radiation damage (cf. Nasdala et al., 2001; Garver et al., 2002; Rahn et al., 2004; Reiners and Brandon, 2006). Alpha radiation damage occurs during ^{238}U, ^{232}Th and ^{235}U decay and causes changes in the crystallography of the mineral (or metamictisation), as well as color accumulation in zircon due to point defects in the crystals (Nasdala et al., 2001; Garver and Kamp, 2002, Garver et al., 2002; Rahn et al., 2004).

Various studies suggest that zircons with alpha radiation damage are more likely to show partial annealing at temperatures below those faced by zircons with little radiation damage and lower closure temperatures (cf. Brandon et al., 1998; Garver et al., 2002; Rahn et al., 2004; Reiners and Brandon, 2006). Thus, experiments with zircons without alpha radiation damage indicate a closure temperature of approximately 342 °C, at a cooling rate of 10 °C/Ma (Rahn et al., 2004; Reiners and Brandon, 2006), which is considerably higher than that estimated in zircons with natural radiation damage of approximately 230 °C under the same cooling conditions (Brandon et al., 1998) (Table 2).

The closure temperature of zircons with radiation damage is the most recommended value for most geological processes (Brandon et al., 1998; Reiners and Brandon, 2006). In turn, the closure temperature of zircons with zero radiation damage can be applied to environments where zircons show rapid cooling and derive from high-temperature environments (> 350-400 °C), causing little alpha radiation damage to these zircons during closure (Reiners and Brandon, 2006).

Cooling and partial reset age

Various cooling ages can be calculated when an intrusive body experiences a monotonic and relatively fast cooling (Figure 5a). Based on the age vs. closure temperature correlation, the oldest ages would be recorded by ZFT and ZHe (closure temperatures that would vary between approximately 230 and 190 °C, respectively; Table 2), which would provide data on the time when the intrusive passed to a depth ranging from 7 to 5.6 km, assuming a geothermal gradient of 30 °C/km and a surface temperature of 20 °C (cf. Gallagher et al., 1998; Farley, 2002; Reiners and Brandon, 2006; Peyton and Carrapa, 2013a; Bernet et al., 2019). Similarly, the youngest ages would be assessed with AFT and AHe (Table 2), which would indicate the time when the rock body passed at a depth of 3 km with AFT and 1.6 km with AHe (depths close to the surface) (cf. Gallagher et al., 1998; Farley, 2002; Reiners and Brandon, 2006; Peyton and Carrapa, 2013a; Bernet et al., 2019). Therefore, when combining the four thermochronological techniques (or at least two), the cooling ages associated with exhumation processes can be calculated at upper crust levels, as well as the cooling/exhumation rates (cf. Zeitler et al., 1982; Zeitler, 1985; Brandon et al., 1998; Ring et al., 1999; Reiners and Brandon, 2006; Deeken et al., 2006).

Conversely, if the rock body experienced slow and variable cooling (Figure 5) or reheating events, such as through magmatism, hydrothermalism or burial metamorphism, it could reside in the PAZ and PRZ, and the ages calculated using the ZFT, ZHe, AZT and AHe methods would correspond to partial reset ages, whose interpretation requires direct or indirect thermal modeling based on numerical methods (Ehlers, 2005; Peyton and Carrapa, 2013a; Bernet et al., 2019). The literature contains programs and routines for modelling the thermal history of one or more samples based on thermochronological data, such as the HeFty (Ketcham, 2005), QTQt (Gallagher, 2012) and Pecube (Braun et al., 2012) programs. The last program solves the heat transfer equation in three dimensions, which reduces exhumation scenarios, tectonic configurations and time-temperature paths (thermal history) of study samples (cf. Braun et al., 2012).

Considering the above information, two or more low-temperature thermochronometers should be applied when studying the cooling/exhumation processes that intrusive bodies have experienced in their passage through the upper crust, and to thermal modeling when the calculated ages are interpreted as a product of partial reset.

4. CONCLUSIONS AND FINAL CONSIDERATIONS

The path of an intrusive body from emplacement to final exhumation at the surface should be studied to determine its cooling and exhumation history. For this purpose, geothermochronology and thermobarometry techniques can be combined with field observations and relationships.

The present review highlights the application of geothermochronological and thermobarometric methods to determine temperature-time-depth variables in intrusive bodies.

Granitoid emplacement ages are determined using the zircon U-Pb method, and their depths can be estimated with thermobarometry techniques (Table 1). Initial cooling ages can be calculated with high-temperature thermochronology techniques, including hornblende and muscovite $^{40}Ar/^{39}Ar$ methods. Initial cooling rates can also be calculated by combining the crystallization age with the initial cooling age. These cooling rates can be associated with heat diffusion processes (by conduction or advection) or with tectonic events.

Low-temperature thermochronology techniques can be applied to study the passage of intrusive bodies in the upper crust level (<10 km): zircon and apatite fission track (ZFT and AFT) and (U-Th)/He (ZHe and AHe) dating. The ZFT and ZHe thermometers provide data on cooling/exhumation ages at depths ranging approximately from 8 to 6 km (assuming a geothermal gradient of 30 °C/km), and AFT and AHe thermometers record cooling/exhumation ages at near-surface depths (approximately from 4 to 2 km). If the mineral has remained in the PAZ and/or PRZ zones, the calculated ages are considered to be partial reset ages and require thermal modeling for correct interpretation. Two or more low-temperature thermochronology techniques should be combined to calculate exhumation rates at upper crust levels and their possible correlations with tectonic events.

The different techniques proposed in this review may present sources of uncertainty that are not normally included in the error propagation calculation, such as sampling bias, number of statistically representative data, human errors in laboratory work and interlaboratory standard calibration errors, which increase the uncertainty around the final curve or path.

Finally, establishing the cooling/exhumation history of an intrusive body is crucial for understanding the thermal and tectonic evolution of a region. Furthermore, determining the cooling and exhumation rates helps to limit the main tectonic pulses associated with the construction of an orogenic belt or with its collapse during crustal evolution.

Acknowledgements

This study was conducted by the Tectonics Group of the Technical Dirección técnica de Geociencias Básicas of the Servicio Geológico Colombiano (SGC) within the framework of the project entitled *Modelo Tectónico de Colombia* [Tectonic Model of Colombia]. We would like to sincerely thank the anonymous reviewers for their valuable comments and suggestions, which helped to improve the manuscript. We also thank geologists Carlos Augusto Quiroz Prada and Ana María Patiño for their important suggestions and technical comments.

References

Anderson, J. (1996). Status of thermobarometry in granitic batholiths. *Earth and Environmental Science Transactions of the Royal Society of Edinburgh*, *87*(1-2), 125-138. https://doi.org/10.1017/S0263593300006544

Anderson, J., & Smith, D. (1995). The effects of temperature and $f0_2$ on the Al-in-hornblende barometer. *American Mineralogist*, *80*, 549-559. https://doi.org/10.2138/am-1995-5-614

Anderson, J., Barth, A., & Young, E. (1988). Mid-crustal Cretaceous roots of Cordilleran metamorphic core complexes. *Geology*, *16*(4), 366-369. https://doi.org/10.1130/0091-7613(1988)016<0366:MCCROC>2.3.CO;2

Anderson, J., Barth, A., Wooden, J., & Mazdab, F. (2008). Thermometers and thermobarometers in granitic systems. *Reviews in Mineralogy and Geochemistry*, *69*(1), 121-142. https://doi.org/10.2138/rmg.2008.69.4

Armstrong, F. (2005). Thermochronometers in sedimentary basins. *Reviews in Mineralogy and Geochemistry*, *58*, 499-525. https://doi.org/10.2138/rmg.2005.58.19

Barbarand, J., Carter, A., Wood, I., & Hurford, T. (2003). Compositional and structural control of fission-track annealing in apatite. *Chemical Geology*, *198*, 107-137. https://doi.org/10.1016/S0009-2541(02)00424-2

Bernet, M., Piraquive, A., Urueña, C., López Isaza, J., Bermúdez, M., Zuluaga, C., Amaya, S., & Villamizar, N. (2019). Multidisciplinary petro-geo-thermochronological approach to ore deposit exploration. *Ore Geology Reviews*, *112*, 1-17. https://doi.org/10.1016/j.oregeorev.2019.103017

Bernet, M., Van der Beek, P., Pik, R., Huyghe, P., Mugnier, J. L., Labrin, E., & Szulc, A. (2006). Miocene to recent exhumation of the central Himalaya determined fromcombined detrital zircon fission-track and U/Pb analysis of Siwalik sediments, Western Nepal. *Basin Research*, *18*(4), 393-412. https://doi.org/10.1111/j.1365-2117.2006.00303.x

Blundy, J., & Holland, T. (1990). Calcic amphibole equilibria and a new amphibole-plagioclase geothermometer. *Contributions to Mineralogy and Petrology*, *104*, 208-224. https://doi.org/10.1007/BF00306444

Boven, A., Pasteels, P., Kelley, S., Punzalan, L., Bingen, B., & Demaiffe, D. (2001). ^{40}Ar/^{39}Ar study of plagioclases from the Rogaland anorthosite complex (SW Norway); an attempt to understand argon ages in plutonic plagioclase. *Chemical Geology*, *176*(1-4), 105-135. https://doi.org/10.1016/S0009-2541(00)00372-7

Brandon, M., Roden Tice, M., & Garver, J. (1998). Late Cenozoic exhumation of the Cascadia accretionary wedge in the Olympic Mountains, Northwest Washington State. *GSA Bulletin*, *110*(8), 985-1009. https://doi.org/10.1130/0016-7606(1998)110<0985:LCEOTC>2.3.CO;2

Braun, J., Van Der Beek, P., Valla, P., Robert, X., Herman, F., Glotzbach, C., Pedersen, V., Perry, C., Simon-Labric, T., & Prigent, C. (2012). Quantifying rates of landscape evolution and tectonic processes by thermochronology and numerical modeling of crustal heat transport using Pecube. *Tectonophysics*, *524*, 1-28. https://doi.org/10.1016/j.tecto.2011.12.035

Buddington, A. (1959). Granite emplacement with special reference to North America. *Bulletin of The Geological Society of America*, *70*, 571-747. https://doi.org/10.1130/0016-7606(1959)70[671:GEWSRT]2.0.CO;2

Caggianelli, A., Prosser, G., & Del Morro, A. (2000). Cooling and exhumation history of deep-seated and shallowlevel, late Hercynian granitoids from Calabria. *Geological Journal*, *35*, 33-42. https://doi.org/10.1002/(SICI)1099-1034(200001/03)35:1<33::AID-GJ836>3.0.CO;2-U

Cardona, A., Valencia, V., Weber, M., Duque, J., Montes, C., Ojeda, G., Reiners, P., Domanik, K., Nicolescu, S., & Villagómez, D. (2011). Transient Cenozoic tectonic stages in the southern margin of the Caribbean plate: U-Th/He thermochronological constraints from Eocene plutonic rocks in the Santa Marta massif and Serranía de Jarara, Northern Colombia. *Geological Acta*, *9*(3-4), 445-466. https://doi.org/10.1344/105.000001739

Carroll, M., & Wyllie, P. (1990). The system tonalite-H_2O at 15 kbar and the genesis of calc-alkaline magmas. *American Mineralogist*, *75*(3-4), 345-357.

Carslaw, H., & Jaeger, J. (1959). *Conduction of heat in solids*. Clarendon Press. https://doi.org/10.2307/3610347

Cherniak, D., & Watson, E. (2001). Pb diffusion in zircon. *Chemical Geology*, *172*(1-2), 5-24. https://doi.org/10.1016/S0009-2541(00)00233-3

Chew, D., & Spikings, R. (2015). Geochronology and thermochronology using apatite: Time and temperature lower crust to surface. *Elements*, *11*, 189-194. https://doi.org/10.2113/gselements.11.3.189

Clarke, D. (1992). *Granitoid rocks*. Chapman y Hall. Topics in the Earth Sciences, 7.

Coleman, D., Gray, W., & Glazner, A. (2004). Rethinking the emplacement and evolution of zoned plutons: Geochronologic evidence for incremental assembly of the Tuolumne Intrusive Suite, California. *Geology*, *32*(5), 433-436. https://doi.org/10.1130/G20220.1

Corfu, F., Hanchar, J., Hoskin, P., & Kinny, P. (2003). Atlas of zircon textures. *Reviews in Mineralogy and Geochemistry*, *53*(1), 469-500. https://doi.org/10.2113/0530469

Corrigan, J. (1991). Inversion of apatite fission track data for thermal history information. *Journal of Geophysical Research*, *96*(B6), 10347-10360. https://doi.org/10.1029/91JB00514

Cortés Calderón, E. (2015). *Geochemical behavior and emplacement conditions of the Ibagué Batholith: Regional implications* (tesis de grado), Universidad de los Andes.

Dahl, P. (1996). The crystal-chemical basis for Ar retention in micas: Inferences from interlayer partitioning and implications for geochronology. *Contributions to Mineralogy and Petrolpgy*, *123*, 22-39. https://doi.org/10.1007/s004100050141

Dalrymple, G., & Lanphere, M. (1969). *Potassium-argon dating: Principles, techniques and applications to geochronology*. Freeman.

Deeken, A. S. (2006). Development of the Southern Eastern Cordillera, NW Argentina, constrained by apatite fission track thermochronology: From early Cretaceous extension to middle Miocene shortening. *Tectonics*, *25*(6). https://doi.org/10.1029/2005TC001894

Dodson, M. (1973). Closure temperature in cooling geochronological and petrological systems. *Contributions to Mineralogy and Petrology*, *40*(3), 259-274. https://doi.org/10.1007/BF00373790

Dodson, M. (1979). Theory of cooling ages. En E. Jäger y J. C. Hunziker (eds.), *Lectures in isotope geology* (pp. 194-202), Springer. https://doi.org/10.1007/978-3-642-67161-6_14

Donelick, R. (1993). Apatite etching characteristics versus chemical composition. *Nuclear Tracks and Radiation Measurements*, *21*(604), 1359-0189

Donelick, R., O'Sullivan, P., & Ketcham, R. (2005). Apatite fission-track analysis. *Reviews in Mineralogy and Geochemistry*, *58*, 49-94. https://doi.org/10.2138/rmg.2005.58.3

Ehlers, T. (2005). Crustal thermal processes and the interpretation of thermochronometer data. *Reviews in Mineralogy and Geochemistry*, *58*(1), 315-350. https://doi.org/10.2138/rmg.2005.58.12

England, P., & Molnar, P. (1990). Surface uplift, uplift of rocks, and exhumation of rocks. *Geology*, *18*(12), 1173-1177. https://doi.org/10.1130/0091-7613(1990)018<1173:SUUORA>2.3.CO;2

Esser, R., McIntosh, W., Heizler, M., & Kyle, P. (1997). Excess argon in melt inclusions in zero-age anorthoclase feldspar from Mt Erebus, Antarctica, as revealed by the ^{40}Ar/^{39}Ar method. *Geochimica et Cosmochimica Acta*, *61*(18), 3789-3801. https://doi.org/10.1016/S0016-7037(97)00287-1

Farley, K. (2000). Helium diffusion from apatite: General behavior as illustrated by Durango fluorapatite. *Journal of Geophysical Research: Solid Earth*, *105*(B2), 2903-2914. https://doi.org/10.1029/1999JB900348

Farley, K. (2002). (U-Th)/He Dating: Techniques, calibrations, and applications. *Reviews in Mineralogy and Geochemistry*, *47*(1), 819-844. https://doi.org/10.2138/rmg.2002.47.18

Faure, G., & Mensing, T. (2005). *Isotopes: Principles and applications*. John Wiley & Sons.

Ferry, J., & Watson, E. (2007). New thermodynamic models and revised calibrations for the Ti-in-zircon and Zr-in-rutile thermometers. *Contribution to Mineralogy and Petrology*, *154*, 429-437. https://doi.org/10.1007/s00410-007-0201-0

Fleck, R., Sutter, J., & Elliot, D. (1977). Interpretation of discordant ^{40}Ar-^{39}Ar age-spectra of Mesozoic tholeiites from Antarctica. *Geochimica et Cosmochimica Acta*, *41*, 15-32.

Fleischer, R., Price, P., & Walker, R. (1975). *Nuclear tracks in solids: Principles and applications.* University of California Press.

Foster, D., Miller, C., Harrison, T., & Hoisch, T. (1992). ^{40}Ar/^{39}Ar thermochronology and thermobarometry of metamorphism, plutonism, and tectonic denudation in the Old Woman Mountains area, California. *GSA Bulletin*, *104*, 176-191. https://doi.org/10.1130/0016-7606(1992)104<0176:AATATO>2.3.CO;2

Foster, D., Schafer, C., Fanning, C., & Hyndman, D. (2001). Relationships between crustal partial melting, plutonism, orogeny, and exhumation: Idaho-Bitterroot batholith. *Tectonophysics*, *342* (3-4), 313-350. https://doi.org/10.1016/S0040-1951(01)00169-X

Gallagher, K. (2012). Transdimensional inverse thermal history modeling for quantitative thermochronology. *Journal of Geophysical Research: Solid Earth*, *117*(B2). https://doi.org/10.1029/2011JB008825

Gallagher, K., Brown, R., & Johnson, C. (1998). Fission track analysis and its applications to geological problems. *Annual Review of Earth and Planetary Sciences*, *26*, 519-572. https://doi.org/10.1146/annurev.earth.26.1.519

Garver, J. I., & Kamp, P. J. (2002). Integration of zircon color and zircon fission-track zonation patterns in orogenic belts: Application to the Southern Alps, New Zealand. *Tectonophysics*, *349*(1-4), 203-219. https://doi.org/10.1016/S0040-1951(02)00054-9

Garver, J. I., Riley, B. C. D., & Wang, G. (2002). Partial resetting of fission tracks in detritai zircon. *Geotemas*, (4), 73-76.

George, P. (1993). *Tectonic implications of fission-track thermochronology and amphibole thermobarometry studies of the Northern Peninsular Ranges Batholith, Southern California* (tesis Ph. D.), The Louisiana State University.

Gil Rodríguez, J. (2014). Petrology of the Betulia Igneous Complex, Cauca, Colombia. *Journal of South American Earth Sciences*, *56*, 339-356. https://doi.org/10.1016/j.jsames.2014.09.016

Gleadow, A., & Fitzgerald, P. (1987). Uplift history and structure of the Transantarctic Mountains: New evidence from fission track dating of basement apatites in the Dry Valleys area, Southern Victoria Land. *Earth and Planetary Science Letters*, *82*, 1-14.

Gleadow, I., Duddy, I., & Lovering, J. (1983). Fission track analysis: A new tool for the evaluation of thermal histories and hydrocarbon potential. *The APPEA Journal*, *23*(1), 93-102. https://doi.org/10.1071/AJ82009

Glorie, S., Alexandrov, I., Nixon, A., Jepson, G., Gillespie, J., & Jahn, B.-M. (2017). Thermal and exhumation history of Sakhalin Island (Russia) constrained by apatite U-Pb and fission track thermochronology. *Journal of Asian Earth Sciences*, *143*, 326-342. https://doi.org/10.1016/j.jseaes.2017.05.011

Gómez, J., Montes, N., Alcárcel, F., & Ceballos, J. (2015). Catálogo de dataciones radiométricas de Colombia en ArcGIS y Google Earth. En J. Gómez, & M. F. Almanza (eds.), *Compilando la geología de Colombia: Una visión a 2015*. Publicaciones Geológicas Especiales, vol. 33. Servicio Geológico Colombiano.

Green, P., Duddy, I., Gleadow, A., & Lovering, J. (1989). *Apatite fission track analysis as palaeotemperature indicator for hydrocarbon exploration.* En N. D. Naeser & T. H. McCulloh (eds.) *Thermal history of sedimentary* (pp. 181-195), Springer-Verlag. https://doi.org/10.1007/978-1-4612-3492-0_11

Green, P., Duddy, I., Gleadow, A., Tingate, P., & Laslett, G. (1985). Fission-track annealing in apatite: Track length measurements and the form of the Arrhenius plot. *Nuclear Tracks and Radiation Measurements*, *10*(3), 323-328. https://doi.org/10.1016/0735-245X(85)90121-8

Green, P., Duddy, I., Gleadow, A., Tingate, P., & Laslett, G. (1986). Thermal annealing of fission tracks in apatite: 1. A qualitative description. *Chemical Geology* (Isotope Geoscience Section), *59*, 237-253. https://doi.org/10.1016/0168-9622(86)90074-6

Green, P., Duddy, I., Laslett, G., Hegarty, K., Gleadowa, A., & Lovering, J. (1989). Thermal annealing of fission tracks in apatite: 4. Quantitative modelling techniques and extension to geological timescales. *Chemical Geology*, *79*: 155-182. https://doi.org/10.1016/0168-9622(89)90018-3

Grove, M., & Harrison, T. (1996). ^{40}Ar* diffusion in Fe-rich biotite. *American Mineralogist*, *81*(7-8), 940-951. https://doi.org/10.2138/am-1996-7-816

Hammarstrom, J., & Zen, E.-A. (1986). Aluminum in hornblende: An empirical igneous geobarometer. *American Mineralogist*, *71*, 1297-1313.

Harrison, T. (1982). Diffusion of ^{40}Ar in hornblende. *Contributions to Mineralogy and Petrology*, *78*(3), 324-331. https://doi.org/10.1007/BF00398927

Harrison, T., Armstrong, R., Naeser, C., & Harakal, J. (1979). Geochronology and thermal history of the Coast Plutonic Complex, near Prince Rupert, British Columbia. *Canadian Journal of Earth Sciences*, *16*(3), 400-410. https://doi.org/10.1139/e79-038

Harrison, T., Celerier, J., Aikman, A., Hermann, J., & Heizler, M. (2009). Diffusion of ^{40}Ar in muscovite. *Geochimica et Cosmochimica Acta*, *73*(4), 1039-1051. https://doi.org/10.1016/j.gca.2008.09.038

Harrison, T., & Clarke, G. (1979). A model of the thermal effects of intrusion and uplift as applied to Quottoon pluton British Columbia. Canadian *Journal of Earth Sciences*, *16*(3), 411-420. https://doi.org/10.1139/e79-039

Harrison, T., Duncan, I., & Mcdougall, I. (1985). Diffusion of ^{40}Ar in biotite: Temperature, pressure and compositional effects. *Geochimica et Cosmochimica Acta*, *49*(11), 2461-2468. https://doi.org/10.1016/0016-7037(85)90246-7

Harrison, T., Watson, E., & Aikman, A. (2007). Temperature spectra of zircon crystallization in plutonic rocks. *Geology*, *35*(7), 635-638. https://doi.org/10.1130/G23505A.1

Hayden, L. A., & Watson, E. B. (2007). Rutile saturation in hydrous siliceous melts and its bearing on Ti-thermometry of quartz and zircon. *Earth and Planetary Science Letters*, *258*, 561-568. https://doi.org/10.1016/j.epsl.2007.04.020

Hayden, L., Watson, E., & Wark, D. (2008). A thermobarometer for sphene. *Contributions to Mineralogy and Petrology*, *155*(4), 529-540. https://doi.org/10.1007/s00410-007-0256-y

Holland, T., & Blundy, J. (1994). Non-ideal interactions in calcic amphiboles and their bearing on amphibole-plagioclase thermometry. *Contributions to Mineralogy and Petrology*, *116*, 433-447. https://doi.org/10.1007/BF00310910

Hunziker, J., Desmons, J., & Hurford, A. (1992). *Thirty-two years of geochronological work in the Central and Western Alps: A review on seven maps.* Mémoires de Géologie (Lausanne), 13.

Hurford, A. (1986). Cooling and uplift patterns in the Lepontine Alps South Central Switzerland and an age of vertical movement on the Insubric fault line. *Contributions to Mineralogy and Petrology*, *92*, 413-427. https://doi.org/10.1007/BF00374424

Kelley, S. (2002). K-Ar and Ar-Ar Dating. *Reviews in Mineralogy and Geochemistry*, *47*(1), 785-818. https://doi.org/10.2138/rmg.2002.47.17

Ketcham, R. (2005). Forward and inverse modeling of low-temperature thermochronometry data. *Reviews in Mineralogy and Geochemistry*, *58*(1), 275-314. https://doi.org/10.2138/rmg.2005.58.11

Ketcham, R., Donelick, R., & Carlson, W. (1999). Variability of apatite fission-track annealing kinetics: III. Extrapolation to geological time scales. *American Mineralogist*, *84*, 1235-1255. https://doi.org/10.2138/am-1999-0903

Kramar, N., Cosca, M., & Hunziker, J. (2001). Heterogeneous Ar-^{40*} distributions in naturally deformed muscovite: In situ UV-laser ablation evidence for micro structurally controlled intra-grain diffusion. *Earth and Planetary Science Letters*, *192*(3), 377-388. https://doi.org/10.1016/S0012-821X(01)00456-3

Lanphere, M., & Dalrymple, G. (1971). A test of the ^{40}Ar/^{39}Ar age spectrum technique on some terrestrial material. *Earth and Planetary Science Letters*, *12*, 359-372. https://doi.org/10.1016/0012-821X(71)90020-3

León, S., Cardona, A., Parra, M., Sobel, E., Jaramillo, J., Glodny, J., Valencia, V. A., Chew, D., Montel, C., Posada, G., Monsalve, G., & Pardo Trujillo, A. (2018). Transition from collisional to subduction-related regimes: An example from Neogene Panama-Nazca-South America interactions. *Tectonics*, *37*, 119-139. https://doi.org/10.1002/2017TC004785

Ludwig, K. (2009). *User's manual for Isoplot 3.7: A geochronological toolkit for Microsoft Excel.* Special Publication n.° 4. Geochronology Center.

Martínez, L., & Zuluaga, C. (2010). Thermal modeling of pluton emplacement and associated contact metamorphism: Parashi stock emplacement in the Serranía de Jarara (alta Guajira, Colombia). *Earth Sciences Research Journal*, *14*(2), 145-152.

McDougall, I., & Harrison, T. (1999). *Geochronology and thermochronology by the ^{40}Ar/^{39}Ar method*. Oxford University Press.

McInnes, B., Farley, K., Sillitoe, R., & Kohn, B. (1999). Application of apatite (U-Th)/He thermochronometry to the determination of the sense and amount of vertical fault displacement at the Chuquicamata porphyry copper deposit, Chile. *Economic Geology*, *94*(6), 937-947. https://doi.org/10.2113/gsecongeo.94.6.937

Miller, J., Matzel, J., Miller, C., Burguess, S., & Miller, R. (2007). Zircon growth and recycling during the assembly of large, composite arc plutons. *Journal of Volcanology and Geothermal Research*, *167*, 282-299. https://doi.org/10.1016/j.jvolgeores.2007.04.019

Mutch, E., Blundy, J., Tattitch, B., Cooper, F., & Brooker, R. (2016). An experimental study of amphibole stability in low-pressure granitic magmas and a revised Al-in-hornblende geobarometer. *Contributions to Mineralogy and Petrology*, *171*(85), 1-27. https://doi.org/10.1007/s00410-016-1298-9

Nasdala, L., Wenzel, M., Vavra, G., Irmer, G., Wenzel, T., & Kober, B. (2001). Metamictisation of natural zircon: Accumulation versus thermal annealing of radioactivity-induced damage. *Contributions to Mineralogy and Petrology*, *141*(2), 125-144. https://doi.org/10.1007/s004100000235

Nieto Samaniego, A., Olmos Moya, M., Levresse, G., Alaniz Álvarez, S., Abdullin, F., Pilar Martínez, A., & Xu, S. (2019). Thermocronology and exhumation rates of granitic intrusions at Mesa-Central, Mexico. *International Geology Review*, *62*(3), 311-319. https://doi.org/10.1080/00206814.2019.1602789

Oriolo, S., Wemmer, K., Oyhantçabal, P., Fossen, H., Schulz, B., & Siegesmund, S. (2018). Geochronology of shear zones; A review. *Earth-Science Reviews*, *185*, 665-683. https://doi.org/10.1016/j.earscirev.2018.07.007

Parada, M., Féraud, G., Fuentes, F., Aguirre, L., Morata, D., & Larrondo, P. (2005). Ages and cooling history of the Early Cretaceous Caleu pluton: Testimony of a switch from a rifted to a compressional continental margin in central Chile. *Journal of the Geological Society*, *162*, 205, 273-287. https://doi.org/10.1144/0016-764903-173

Paterson, S., Fowler, T., & Miller, R. (1996). Pluton emplacement in arcs: A crustal-scale exchange process. *Earth and Environmental Science Transactions of The Royal Society of Edinburgh*, *87*(1-2), 115-123. https://doi.org/10.1017/S0263593300006532

Peacock, S. (1989). Thermal modeling of metamorphic pressure-temperature-time paths: A forward approach. *Metamorphic Pressure-Temperature-Time Paths*, *7*, 57-102. https://doi.org/10.1029/SC007p0057

Peyton, S., & Carrapa, B. (2013a). An introduction to low-temperature thermochronologic techniques, methodology, and applications. En C. Knight, J. Cuzella & L. D. Cress (eds.), *Application of structural methods to Rocky Mountain hydrocarbon exploration and development* (pp. 15-36), AAPG Studies in Geology, 65. https://doi.org/10.1306/13381688St653578

Peyton, S., & Carrapa, B. (2013b). An overview of low-temperature thermochronology in the Rocky Mountains and its application to petroleum system analysis. En C. Knight, J. Cuzella & L. D. Cress (eds.), *Application of structural methods to Rocky Mountain hydrocarbon exploration and development* (pp. 37-70), AAPG Studies in Geology, 65. https://doi.org/10.1306/13381689St653578

Pitcher, W. (1997). *The nature and origin of granite.* Springer Science+Business Media Dordrecht. https://doi.org/10.1007/978-94-011-5832-9

Pupin, J. (1980). Zircon and granite petrology. *Contributions to Mineralogy and Petrology*, *73*(3), 207-220. https://doi.org/10.1007/BF00381441

Putirka, K., Johnson, M., Kinzler, R., Longhi, J., & Walker, D. (1996). Thermobarometry of mafic igneous rocks based on clinopyroxene-liquid equilibria, 0-30 kbar. *Contributions to Mineralogy and Petrology*, *123*, 92-108. https://doi.org/10.1007/s004100050145

Rahn, M. K., Brandon, M. T., Batt, G. E., & Garver, J. I. (2004). A zero-damage model for fission-track annealing in zircon. *American Mineralogist*, *89*(4), 473-484. https://doi.org/10.2138/am-2004-0401

Reiners, P., & Brandon, M. (2006). Using thermochronology to understand orogenic erosion. *Annual Review of Earth and Planetary Sciences*, *34*, 419-466. https://doi.org/10.1146/annurev.earth.34.031405.125202

Reiners, P., Carlson, R., Renne, P., Cooper, M., Granger, D., McLean, N., & Schoene, B. (2017). *Geochronology and thermochronology*. John Wiley & Sons. https://doi.org/10.1002/9781118455876

Restrepo Moreno, S., Foster, D., Bernet, M., Min, K., & Noriega, S. (2019). Morphotectonic and orogenic development of the Northern Andes of Colombia: A low-temperature thermochronology perspective. En F. Cediel, R. P. Shaw (eds.), *Geology and tectonics of Northwestern South America,* Frontiers in Earth Sciences. https://doi.org/10.1007/978-3-319-76132-9_11

Restrepo Moreno, S., Foster, D., Stockli, D., & Parra Sánchez, L. (2009). Long-term erosion and exhumation of the "Altiplano Antioqueño", Northern Andes (Colombia) from apatite (U-Th)/He thermochronology. *Earth and Planetary Science Letters*, *278*(1-2), 1-12. https://doi.org/10.1016/j.epsl.2008.09.037

Ridolfi, F., & Renzulli, A. (2012). Calcic amphiboles in calc-alkaline and alkaline magmas: Thermobarometric and chemometric empirical equations valid up to 1130 °C and 2.2 GPa. *Contribution to Mineralogy and Petrology*, *163*, 877-895. https://doi.org/10.1007/s00410-011-0704-6

Ridolfi, F., Renzulli, A., & Puerini, M. (2010). Stability and chemical equilibrium of amphibole in calc-alkaline magmas: An overview, new thermobarometric formulations and application to subduction-related volcanoes. *Contribution to Mineralogy and Petrology*, *160*(1), 45-66. https://doi.org/10.1007/s00410-009-0465-7

Ring, U., Brandon, M., Willett, S., & Lister, G. (1999). *Exhumation processes*. Special Publications, 154, Geological Society. https://doi.org/10.1144/GSL.SP.1999.154.01.01

Sáenz, E. (2003). *Fission track thermochronology and denudational response to tectonics in the north of The Colombian Central Cordillera* (tesis de maestría), Shimane University.

Sáenz, E., Paucar, C., & Restrepo, J. (1996). Estudio de la evolución térmica del Batolito Antioqueño por huellas de fisión. 7th Congreso Colombiano de Geología, Bogotá.

Schaen, A. J., Jicha, B. R., Hodges, K. V., Vermeesch, P., Stelten, M. E., Mercer, C. M. Phillips, D., Rivera, T., Jourdan, F., Matchan, E., Hemming, S., Morgan, L., Kelley, S., Cassata, W., Heizler, M., Vasconcelos, P., Benowitz, J., Koppers, A., Mark, D., Niespolo, E., … Singer, H. (2020). Interpretingandreporting40Ar/39Ar geochronologicdata. *GSA Bulletin*. https://doi.org/10.1130/B35560.1

Schmidt, M. (1992). Amphibole composition in tonalite as a function of pressure: An experimental calibration of the AI-in-hornblende barometer. *Contributions to Mineralogy and Petrology*, *110*, 304-310. https://doi.org/10.1007/BF00310745

Schmidt, M. (1993). Phase relations and compositions in tonalite as a function of pressure: An experimental study at 650 C. *American Journal of Science*, *293*, 1011-1011.

Spencer, C. J., Kirkland, C. L., & Taylor, R. J. (2016). Strategies towards statistically robust interpretations of in situ U-Pb zircon geochronology. *Geoscience Frontiers*, *7*(4), 581-589. https://doi.org/10.1016/j.gsf.2015.11.006

Tollari, N., Toplis, M., & Barnes, S.-J. (2006). Predicting phosphate saturation in silicic magmas: An experimental study of the effects of melt composition and temperature. *Geochimica et Cosmochimica Acta*, *70*, 1518-1536. https://doi.org/10.1016/j.gca.2005.11.024

Treloar, P. (1981). Garnet-biotite-cordierite thermometry and barometry in the Cashel thermal aureole, Connemara, Ireland. *Mineralogical Magazine*, *44*, 183-189. https//doi.org/10.1180/minmag.1981.044.334.11

Turner, G. (1970). ^{40}Ar/^{39}Ar dating of lunar rock samples. *Science*, *167*, 466-468.

Van der Lelij, R., Spikings, R., & Mora, A. (2016). Thermochronology and tectonics of the Mérida Andes and the Santander Massif, NW South America. *Lithos*, 248-251, 220-239. https://doi.org/10.1016/j.lithos.2016.01.006

Vermeesch, P. (2018). IsoplotR: A free and open toolbox for geochronology. *Geoscience Frontiers*, *9*(5), 1479-1493. https://doi.org/10.1016/j.gsf.2018.04.001

Villagómez, D., & Spikings, R. (2013). Thermochronology and tectonics of the Central and Western Cordilleras of Colombia: Early Cretaceous-Tertiary evolution of the Northern Andes. *Lithos*, *160*(161), 228-249. https://doi.org/10.1016/j.lithos.2012.12.008

Villagómez, D., Spikings, R., Mora, A., Guzmán, G., Ojeda, G., Córtes, E., & Van der Lelij, R. (2011). Vertical tectonics at a continental crust oceanic plateau plate boundary zone: Fission track thermochronology of the Sierra Nevada de Santa Marta, Colombia. *Tectonics*, *30*, 1-18. https://doi.org/10.1029/2010TC002835

Wagner, G., Reimer, G., & Jager, E. (1977). Cooling ages derived by apatite fission-track, with Rb-Sr and K-Ar dating: The uplift and cooling history of the Central Alps. *Memorie degli Istituti di Geologia e Mineralogia dell' Universita di Padova*, *30*(28), 1-27.

Wartho, J., Rex, D., & Guise, P. (1996). Excess argon in amphiboles linked to greenschist facies alteration in Kamila amphibolite belt, Kohistan island arc system, Northern Pakiston: Insights from 40Ar/39Ar step-heating and acid leaching experiments. *Geological Magazine*, *133*, 595-609. https://doi.org/10.1017/S0016756800007871

Watson, E., & Harrison, T. (1983). Zircon saturation revisited' temperature and composition effects in a variety of crustal magma types. *Earth and Planetary Science Letters*, *64*, 295-304. https://doi.org/10.1016/0012-821X(83)90211-X

Watson, E., Wark D. A., & Thomas, J. (2006). Crystallization thermometers for zircon and rutile. *Contributions to Mineral and Petrology*, *151*, 413-433. https://doi.org/10.1007/s00410-006-0068-5

Wei, C., & Powell, R. (2004). Calculated phase relations in high pressure metapelites in the system NKFMASH (Na_2O-K_2O-FeO-MgO-Al_2O_3-SiO_2-H_2O). *Journal of Petrology*, *45*, 183-202. https://doi.org/10.1093/petrology/egg085

Wei, C., & Powell, R. (2006). Calculated phase relations in the system NCKFMASH (Na_2O-CaO-K_2O-FeO-MgO-Al_2O_3-SiO_2-H_2O) for high pressure metapelites. *Jounal of Petrology*, *47*, 385-408. https://doi.org/10.1093/petrology/egi079

Wendt, I., & Carl, C. (1991). The statistical distribution of the mean squared weighted deviation. *Chemical Geology Isotope Geoscience Section* 86, 275-285. http://dx.doi.org/10.1016/0168-9622(91)90010-T

Wolf, R., Farley, K., & Kass, D. (1998). Modeling of the temperature sensitivity of the apatite (U-Th)/He thermochronometer. *Chemical Geology*, *148*(1-2), 105-114. https://doi.org/10.1016/S0009-2541(98)00024-2

Wolf, R., Farley, K., & Silver, L. (1996). Helium diffusion and low-temperature thermochronometry of apatite. *Geochimica et Cosmochimica Acta*, *60*(21), 4231-4240. https://doi.org/10.1016/S0016-7037(96)00192-5

Wu, C.-M., Zhang, J. & Ren, L.-D. (2004a). Empirical Garnet-Biotite-Plagioclase-Quartz (GBPQ) Geobarometry in Medium- to High-Grade Metapelites. *Journal of Petrology*, *45*(9), 1907-1921. https://doi.org/10.1093/petrology/egh038

Wu, C.-M., Zhang, J., & Ren, L.-D. (2004b). Empirical garnet-muscovite-plagioclase-quartz geobarometry in medium- to high-grade metapelites. *Lithos*, *78*, 319-332. https://doi.org/10.1016/j.lithos.2004.06.008

Zeitler, P. (1985). Cooling history of the NW Himalaya, Pakistan. *Tectonics*, *4*(1), 127-151. https://doi.org/10.1029/TC004i001p00127

Zeitler, P., Johnson, N., Naeser, C., & Tahirkheli, R. (1982). Fission-track evidence for Quaternary uplift of the Nanga Parbat region, Pakistan. *Nature*, *298* (5871), 255-257. https://doi.org/10.1038/298255a0

Zen, E., & Hammarstrom, J. (1984). Magmatic epidote and its petrologic significance. *Geology*, *12*, 515-518. https://doi.org/10.1130/0091-7613(1984)12<515:MEAIPS>2.0.CO;2

Boletín Geológico

SERVICIO GEOLÓGICO COLOMBIANO

Boletín Geológico, 47, 107–122, 2020
https://doi.org/10.32685/0120-1425/boletingeo.47.2020.495

Received: May 22, 2020

Revised: August 28, 2020

Accepted: November 4, 2020

Quantitative analysis of micromorphological images in edaphosedimentary sequences of the archaeological sites of Tequendama and Aguazuque, Sabana de Bogotá, Colombia

Análisis cuantitativo de las imágenes micromorfológicas en secuencias edafosedimentarias de los sitios arqueológicos de Tequendama y Aguazuque, sabana de Bogotá, Colombia

Angélica Viviana **Triana Vega**[1], Santiago **Vélez Bedoya**[2], Sergey **Sedov**[3], Elizabeth **Solleiro Rebolledo**[3], Jaime **Díaz**[3]

1. Departamento de Antropología, Facultad de Ciencias Sociales, Universidad de los Andes, and Facultad de Estudios del Patrimonio Cultural, Programa de Arqueología, Universidad Externado de Colombia, Bogotá, Colombia.
2. Universidad Nacional de Colombia, Medellín, Colombia.
3. Instituto de Geología, Universidad Nacional Autónoma de México, Mexico City, Mexico.
Corresponding author: Angélica Triana, av.triana177@uniandes.edu.co

ABSTRACT

The Bogotá savanna is a very important site for Colombian archeology. At this site, researchers have identified the settlements of hunter-gatherers and agricultural farmers who inhabited the territory from the late Pleistocene to the late Holocene. These archaeological studies have established the ways of life, social dynamics and environmental interactions of these groups. To clarify settlement processes, this article presents a detailed micromorphological and micromorphometric analysis of sediments collected in archeological excavations conducted at the Tequendama and Aguazuque sites in the municipality of Soacha, Cundinamarca. This analysis quantifies the contents of archaeological materials, such as bone and coal, as well as carbonate remains, which are associated with various activities. The results show differences in the abundance of bones and charcoal between settlement levels. Level 7A (dated 6,897-7,001 BP) of the Tequendama site shows the highest density of occupation and activities of all levels analyzed in this study. Furthermore, based on paleoenvironmental interpretation, the presence of secondary carbonates indicates arid conditions in the Bogotá savanna matching the regional climatic records.

Keywords: micromorphometry, hunter-gatherers, geoarchaeology, settlement processes, Holocene.

Citation: Triana, A. V., Vélez, S., Sedov, S., Solleiro, E., & Díaz, J. (2020). Quantitative analysis of micromorphological images in edaphosedimentary sequences of the archaeological sites of Tequendama and Aguazuque, Sabana de Bogotá, Colombia. *Boletín Geológico*, *47*, 107-122. https://doi.org/10.32685/0120-1425/boletingeo.47.2020.495

RESUMEN

La sabana de Bogotá representa un sitio muy importante para la arqueología colombiana. Allí se han identificado asentamientos de grupos humanos de cazadores recolectores, horticultores y agricultores que habitaron dicho territorio desde finales del Pleistoceno hasta el Holoceno tardío. Los estudios arqueológicos han permitido establecer formas de vida, dinámicas sociales e interacciones con el medio ambiente de esos grupos humanos. Para esclarecer los procesos de ocupación, en este artículo se presenta un estudio micromorfológico y micromorfométrico detallado de los sedimentos obtenidos de las excavaciones arqueológicas realizadas en los sitios de Tequendama y Aguazuque, en el municipio de Soacha, Cundinamarca. El análisis cuantifica los contenidos de materiales arqueológicos como hueso y carbón, y restos de carbonatos, que pudieron estar asociados a diversas actividades. Los resultados muestran diferencias en la abundancia de huesos y carbón, de acuerdo con los pisos de ocupación, de manera que en el nivel 7A (datado en 6,897-7,001 AP) del sitio de Tequendama se observa la mayor densidad de ocupación y actividades, de todos los analizados. Con respecto a la interpretación paleoambiental, la presencia de carbonatos secundarios permite establecer condiciones áridas en la sabana de Bogotá, que coinciden con los registros climáticos regionales.

Palabras clave: micromorfometría, cazadores-recolectores, geoarqueología, procesos de ocupación, Holoceno.

---

1. INTRODUCTION

The archaeological sites of Tequendama and Aguazuque are located in the Bogotá savanna. These sites are very important because they contain evidence of the settlements of hunter-gatherers who inhabited Tequendama from the late Pleistocene to the late Holocene (12,500-2,500 BP, approximately) and Aguazuque from the middle Holocene to the early late Holocene (8,000-2,500 BP, approximately). These sites were excavated in the 1970s and 1990s (Correal and Van der Hammen, 1977; Correal, 1990) and again in 2014 in smaller columns (Triana, 2019; Triana et al., 2019). The identification of human burials, lithic artifacts and animal skeletal and macroscopic plant remains has shed light on the social dynamics of these groups; in addition, the continuous presence of such archaeological materials across different stratigraphic units suggests that humans established permanent settlements at these sites.

Features of the Tequendama section show that groups of hunter-gatherers inhabited the rock shelter during the early and middle Holocene (125,000-6,000 BP, approximately), followed by a period without data corresponding to the middle Holocene. Toward the beginning of the initial late Holocene, humans returned to the site, as documented by human skeletal remains, some ceramic fragments and animal skeletal remains (Correal and Van der Hammen, 1977). In turn, the Aguazuque section shows a permanent settlement from approximately 8,000 to 2,500 BP. Abundant human burials, lithic artifacts and animal skeletal and macroscopic plant remains provide data on potential hunter-gatherers, with a transition to farming around 4,000 BP (Correal and Van der Hammen, 1977; Correal, 1990; Triana, 2019; Triana et al., 2019; Triana et al., 2020) (Table 1).

Micromorphological analyses of sediments from both sites (Triana et al., 2019) account for different periods of occupation and reflect activities developed during those periods. Similarly, magnetic susceptibility and electrical conductivity values, sediment micromorphology and archaeological data collected by stratigraphic level show different activities of exposure to fire and long periods of occupation in each stratigraphic level at the Tequendama site during the middle Holocene. The period that reflects the most intensive occupation spans from 9,000 to 6,000 BP. At Aguazuque, soil micromorphology and the aforementioned analyses mark a peak in occupation from 4,000 to 2,500 BP. The main modifications that suggest these occupation lapses are high exposure to fire, strong compaction of stratigraphic levels and an abundance of microscopic components, such as fish spines, plant tissues and sand aggregates (Triana et al., 2019).

In turn, micromorphometric analyses performed on thin films observed under the microscope provide evidence of both ancient human impacts (marked by the presence of bone fragments, coal and other anthropic materials) and pedogenetic processes such as newly formed carbonates, soil aggregates, Fe nodules and other pedofeatures). The resulting evidence forms the “edaphic memory” (Targulian and Goryachkin, 2004) that records environmental changes and ancient human activity. The term *micromorphometry* was coined by Kubiëna to designate techniques for quantifying the soil fabric, especially changes in porosity and structure caused by soil management

Table 1. Radiocarbon dates corresponding to Tequendama and Aguazuque

Archaeological site	Stratigraphic level	Dated material	Conventional ^{14}C age	Calibrated ^{14}C age (2 sigma)	Laboratory code	Reference
Tequendama	9 grainy brown	Coal	2225 ± 35 BP	2182-2308 BP	Col 159 GrN-6536	Correal and Van Der Hammen, 1977
Tequendama	8A slightly brownish gray	Coal	6990 ± 110 BP 7090 ± 75 BP	7719-7926 BP 7844-7979 BP	Col 163 GrN-6728 Col 164 GrN-6729	Correal and Van Der Hammen, 1977
Tequendama	5B light brown	Coal	10130 ± 150 BP 10590 ± 90 BP 10920 ± 260 BP	11456-12080 BP 12327-12680 BP 12580-13111 BP	Col 176 GrN-6732 Col 167 GrN-6505 Col 170 GrN-6539	Correal and Van Der Hammen, 1977
Tequendama	7A grayish brown to brownish gray	Human bone	6080 +/- 40 BP	6897-7001 BP	Col-AAA	Triana et al., 2019
Aguazuque	5(2) dark gray loam	Human bone	2725 ± 35 BP	2789-2856 BP	GrN 14.479. Col. 594	Correal, 1990
Aguazuque	4(2) brown loam	Human bone	3850 ± 35 BP	4200-4365 BP	GrN 14.478. Col. 593	Correal, 1990
Aguazuque	4(1) sandy loam	Human bone	4030 ± 35 BP	4453-4550 BP	GrN 12.930. Col. 477	Correal, 1990
Aguazuque	3 reddish sandy loam	Human bone	5025 ± 40 BP	5713-5866 BP	GrN 14.477. Col. 1592	Correal, 1990
Aguazuque	5(2) dark gray loam	Human tooth	3600 +/- 40 BP	3865-3965 BP	Col-AAA	Triana et al., 2019

(Stoops, 2009). However, these techniques have also been successfully used to account for carbonate accumulations in soils (Bui and Mermut, 1989), to evaluate porosity (Skwortsova et al., 2000) and to determine the distribution of soil components (Gutiérrez Castorena et al., 2017).

Triana et al. (2019) performed a qualitative micromorphological study in which informative features were recorded and interpreted in both profiles. In this study, quantitative morphological methods were applied to extract a record of these features to compare them with archaeological evidence and regional environmental proxies. This document focuses on evaluating the morphological quantities and parameters of microscopic anthropic materials (microartifacts). Rosen (1989, 1991) confirmed the importance of these components for detecting the intensity and type of ancient human activity in archaeological sediments; nevertheless, micromorphometric studies of these features in sedimentary sequences are scarce.

1.1 Study area

The Bogotá savanna is located south of the *Altiplano Cundiboyacense* [Cundiboyacense highlands] in the department of Cundinamarca, which is located in the geographic center of Colombia. The municipality of Soacha is located in this region, at an average height of 2,600 meters above sea level (m.a.s.l.). Soacha is characterized by two physiographic zones: the zone of highlands and mountains, with Páramo and Subpáramo ecosystems, and the zone of dry and humid High Andean forests. The archaeological sites of Tequendama and Aguazuque are located in the municipality of Soacha. Due to their proximity, these sites have similar environmental and ecological conditions.

The Tequendama archaeological site is located in a rocky shelter on the Tequendama hacienda, near the Chusacá tollbooth, in the municipality of Soacha, Cundinamarca. Aguazuque is an open-air archaeological site located on private property known as Aguazuque Hacienda. Currently, this property is called Fute Hacienda and is located on the road to Mondoñedo (Figures 1 and 2).

In geological terms, the sediments deposited in both archaeological sites are part of the Guadalupe Formation, which corresponds to the Upper Cretaceous (Correal, 1990). Triana et al. (2019) mention evidence of a sequence of fluvial and colluvial deposits, which are described as red and brown sediments deposited during the Quaternary, in the periphery of the archaeological sites (Julivert, 1961) and a complex of black soils that define the Siecha Formation (Helmens and Van der Hammen, 1994). The presence of sandstone in the rock shelter of the Tequendama site contributes to the accumulation of sediments. In Aguazuque, additional colluvial deposits are present along with the components resulting from fluvial processes.

The landscapes that originated in both sites were shaped irregularly due to an atypical sedimentation of alluvial materials, with changes in the facies and the direction of transport, which fostered a particular accumulation and erosion that generated a diverse stratigraphy. The archaeological sites are located in rocky shelters carved in the Guadalupe Formation, which consists of fossiliferous limestones and sandstones from the Upper Cretaceous, the alteration products of which contribute to the alluvial and colluvial sediments found in Tequendama and Aguazuque. However, Triana et al. (2019) determined that only sandstone is found in the Tequendama rock shelter. Therefore, this rock shelter does not provide calcareous material to the alluvial and colluvial sediments.

Source: Esri, Maxar, GeoEye, Earthstar Geographics, CNES/Airbus DS, USDA, USGS, AeroGRID, IGN, and the GIS User Community; Esri, HERE, Garmin, (c) OpenStreetMap contributors, and the GIS user community

Figure 1. Location map of the Aguazuque and Tequendama archaeological sites

2. METHOD

During the excavation phase, conducted in 2014, soil samples were collected from each stratigraphic level. These samples were identified and classified based on the presence of archaeological material, the characteristics of the profile and the stratigraphic levels identified by Correal and Van der Hammen (1977) and Correal (1990). Although the samples were not oriented, they were exposed as little as possible to avoid destroying the soil aggregates collected during the total sediment sampling of each level. Thus, samples from each soil level were collected in bags to preserve the original structure. Subsequently, in the laboratory, an unaltered soil aggregate—which retained the original characteristics of the outcrop and its original position, such as pores, coarse and fine particles, pedofeatures and even anthropogenic materials—was impregnated with polyester resin, prepared and processed to assemble thin sections of each stratigraphic level at each site.

The soil aggregate was impregnated to prevent disintegration, thereby preserving the natural relationships between different components. These thin sections were prepared at the Soil and Sediment Thin Section Workshop of the Institute of Geology (*Instituto de Geología* – IGL), National Autonomous University of Mexico (*Universidad Nacional Autónoma de México* – UNAM) by impregnation. The impregnated blocks were cut and polished to prepare 30-µm-thick thin sections, which were observed under an Olympus optical microscope and analyzed using the 2D image analysis software Image-Pro Plus.

In total, 14 thin soil sections were prepared from the two sites using six samples from Tequendama and eight from Aguazuque. The microscopic study focused on quantifying the materials, rather than assessing their distribution. The entire slides were scanned in a high-resolution scanner to generate a complete image of the components. The thin sections were micromorphologically described using terminology from Stoops et al. (2003) and adopted by Loaiza et al. (2015). In turn, the anthropic components (microartifacts) were identified based on the work of Courty et al. (1989) and Nicosia and Stoops (2017).

The method was applied in two sections. Initially, coal, bones and carbonates present throughout the thin section were counted manually and semiautomatically to determine the percentage of coal and bones in each thin section, with respect to the solid matrix. The porous space was subtracted from the measurement because the thin sections were derived from disaggregated materials and thus could not be considered *in situ*. For this purpose, the pore space was selected using the "Color selection and area calculation" dialog box of the Image-Pro Plus software. Subsequently, this area was subtracted from the total area of the thin section. The bone fragments were selected by visual observation, in both the microscopic and scanned images, thus providing two observation and control scales. The coal and carbonate fragments of each thin section were selected, counted and measured automatically.

The second methodological part focused on identifying three soil aggregates in each thin section. These aggregates were selected after a careful analysis to identify those that re-

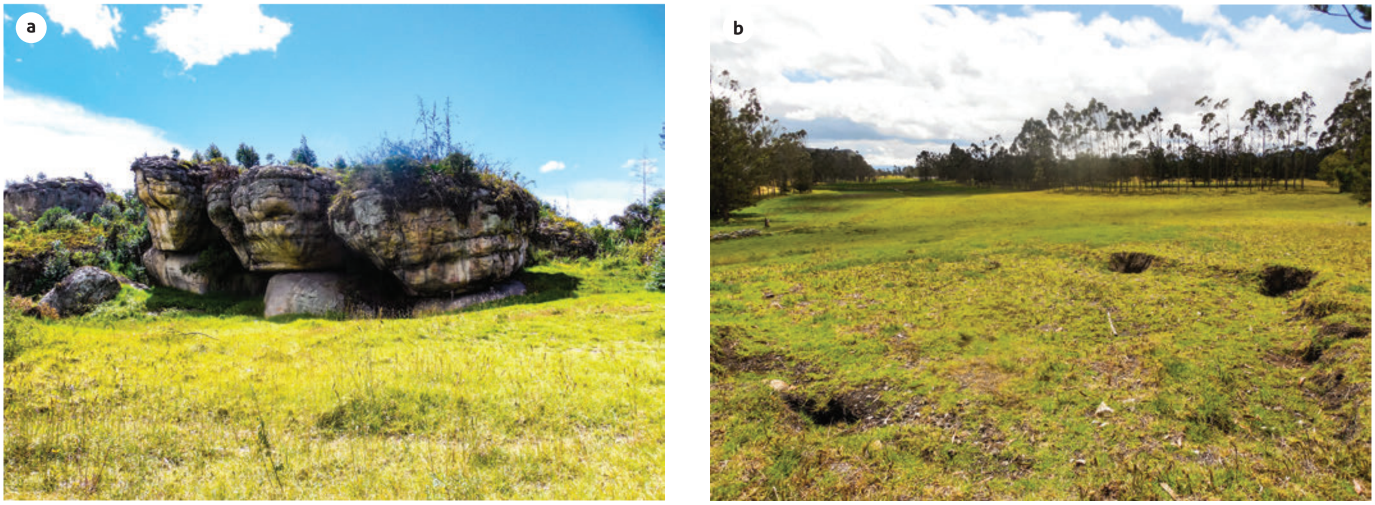

Figure 2. Archaeological excavations in Tequendama (a) and Aguazuque (b)

mained unchanged and contained coal, carbonates and bone fragments. Once selected, each aggregate was measured, and all coal, carbonate and bone fragments were automatically counted in detail using the "Color selection" dialog box of the Image-Pro Plus software.

3. Results

The results section is divided into two subsections because, methodologically, general counts were performed in the thin sections, and detailed counts were performed in aggregates of the same thin sections.

Semiautomatic counting

The results show that bone and coal are less abundant at the Tequendama archeological site than at the Aguazuque site. The highest percentages of bone were found in the topsoil level and in stratigraphic level 7A, dated from 8,500 to 9,500 BP (Figures 3c and 4a-b). The other levels showed low proportions of bone. In stratigraphic level 7A, the burial of a woman was identified, dated at 6,897-7,001 BP (Triana et al., 2019). In addition, in the coal counts at Tequendama, only level 7A had a representative percentage of coal. These data corroborate the previously observed increase in magnetic susceptibility values related to burning (Triana et al., 2019). These findings indicate that this

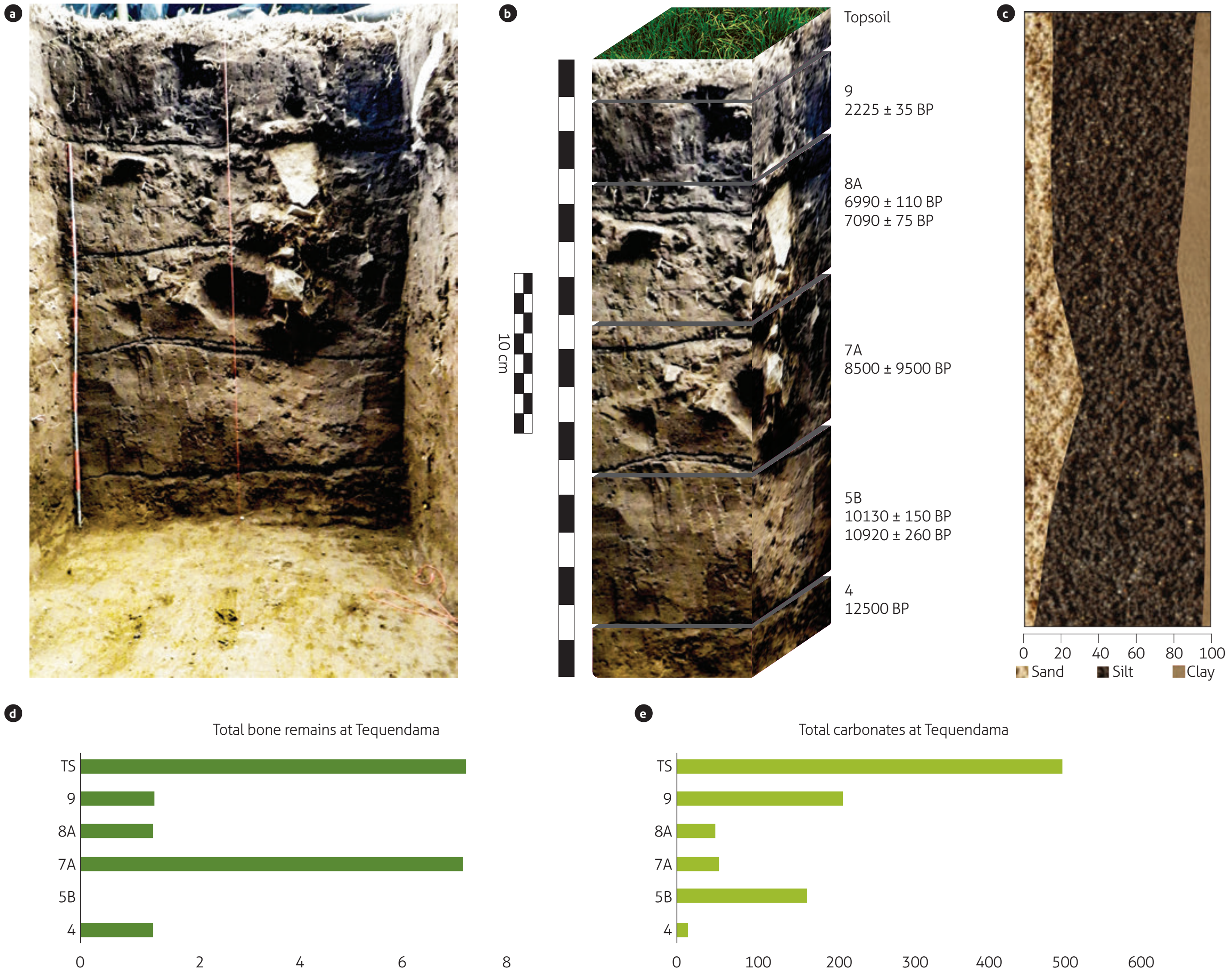

Figure 3. Stratigraphic profile (a) and micromorphological counts by stratigraphic level (b) at Tequendama; variation in texture (% sand, silt and clay fractions) across the stratigraphic profile (c) and total bone (d) and carbonate (e) remains by stratigraphic level

stratigraphic level had a high human occupation during the transition from the Lower Holocene to the Middle Holocene. The average size of the coals is 336 µm, and they present a high degree of thermal alteration.

The carbonates present at the Tequendama archeological site appear more frequently in the first stratigraphic levels, topsoil and level 9 (dated at approximately 2,500 BP) (Figures 3d and 4c-d). Similarly, though to a lesser extent, level 5B (dated at approximately 10,000 BP) also contains carbonates.

In the manual count at Aguazuque, the highest percentages of bones occur between 2,500 and 4,000 BP. In these levels, the frequency of bone remains increases, decreases and increases again toward the earliest stratigraphic level (Figures 5c and 6a-b), in contrast to Tequendama, where the percentage of bones is not as high as that in Aguazuque. In the coal count, the highest percentages are found in the topsoil and in the first stratigraphic level, dated at 8,000 BP (Figure 5d). These values differ from those of Tequendama because the highest percentage of carbon occurs only in stratigraphic level 7A. In the carbonate count, the highest frequencies are found in stratigraphic level 6 and are associated with late periods (Figure 5e); toward the middle Holocene, the frequency decreases and then increases again in stratigraphic level 3, corresponding to the initial middle Holocene (Figure 6c-d).

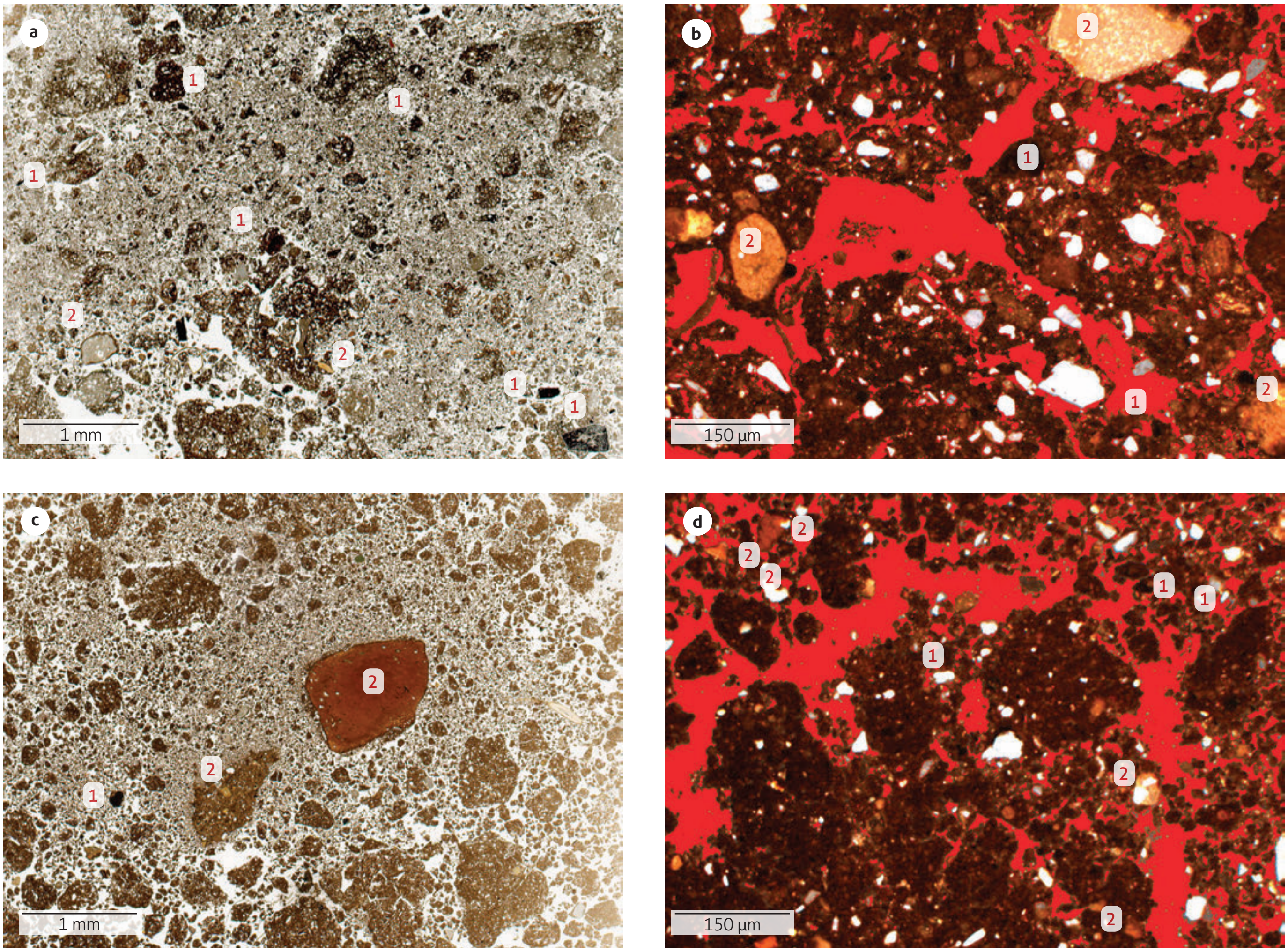

Figure 4. Semiautomatic count at Tequendama;
a) thin section of stratigraphic level 7A; b) total coal (1) and bone remains (2) at level 7A (Image-Pro Plus); c) thin section of stratigraphic level 9; d) total coal (1) and bone remains (2) at level 9 (Image-Pro Plus)

Detailed counts in aggregates

In the counts performed in three soil aggregates of each thin section, coals, bones and carbonates were also identified. These counts were performed using the Image-Pro Plus software. At Tequendama, 1,638 bone fragments with medium-to-small sizes and an average size of 32.59 µm were detected in the topsoil (Figure 7a). Coals were abundantly found in aggregates from level 9 (2,500 BP, approximately) and level 7A (8,500-9,500 BP, approximately). Levels 8A (6,000-7,000 BP, approximately) and 4 (12,500 BP) also showed carbon fragments, but in lower proportions than in the previous levels (Figures 7b and 8b). The percentages of coals in the counts performed using the software are higher than in those performed manually.

The percentage of carbonates present in aggregates at Tequendama increases in the earliest periods, that is, in levels 8A, 7A and 5B, which represent the transition from the early to the middle Holocene (Figures 7c and 8c). Carbonate sizes are larger in the later levels, averaging 30 µm, and decrease toward the earliest levels.

At the Aguazuque archeological site, the aggregate counts by stratigraphic level showed that bone remains were only present in stratigraphic level 3 (associated with 5,025 BP), in which 3,657

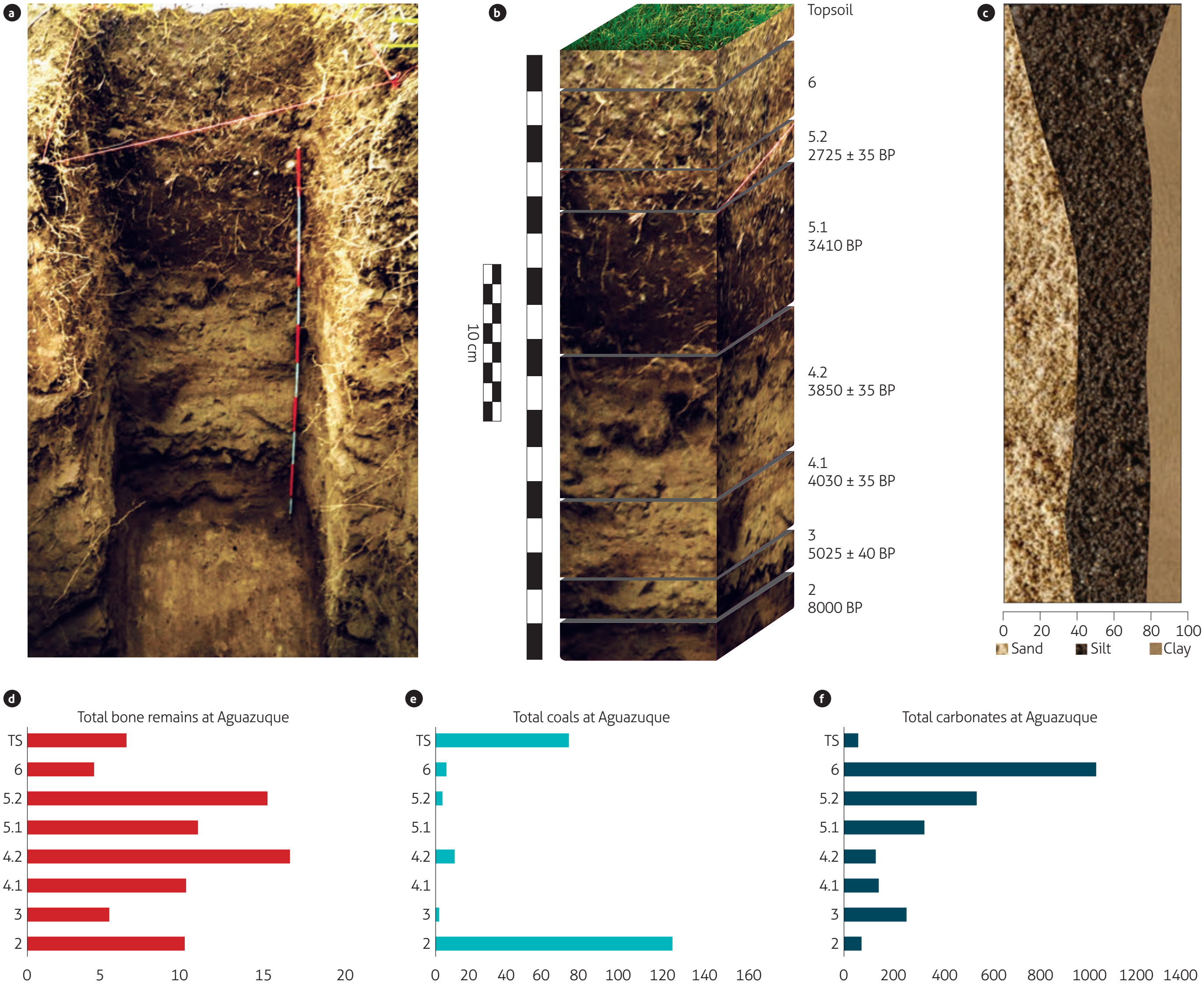

Figure 5. Stratigraphic profile (a) and micromorphological counts by stratigraphic level (b) at Aguazuque; variation in texture (% sand, silt and clay fractions) across the stratigraphic profile (c) and total bone (d), coals (e) and carbonates (f) by stratigraphic level

very small fragments were counted (Figure 9a), in contrast to Tequendama, where the bone counts showed a lower proportion in the latest levels and were not as early as those at Aguazuque. The average size was 0.32 µm. The coal counts showed that the frequency of occurrence is high in the earliest level, subsequently decreases, slightly increases toward the middle Holocene (between 4,000 and 2,500 BP), then decreases toward late periods and finally increases in the topsoil (Figures 9b and 10b). The coals found in Aguazuque had higher counts and larger average sizes than those found in Tequendama.

At Aguazuque, the carbonates values are low in the earliest levels; however, they rise and fall during the middle Holocene, between 4,000 and 2,500 BP. In level 6, toward the late period, carbonates considerably increase (Figures 9c and 10c); although the presence of carbonates is higher at Tequendama, the variation is similar, with values increasing toward later periods. At Tequendama, the carbonates show an average size larger than 10 µm and are thus larger than the carbonates found in Aguazuque.

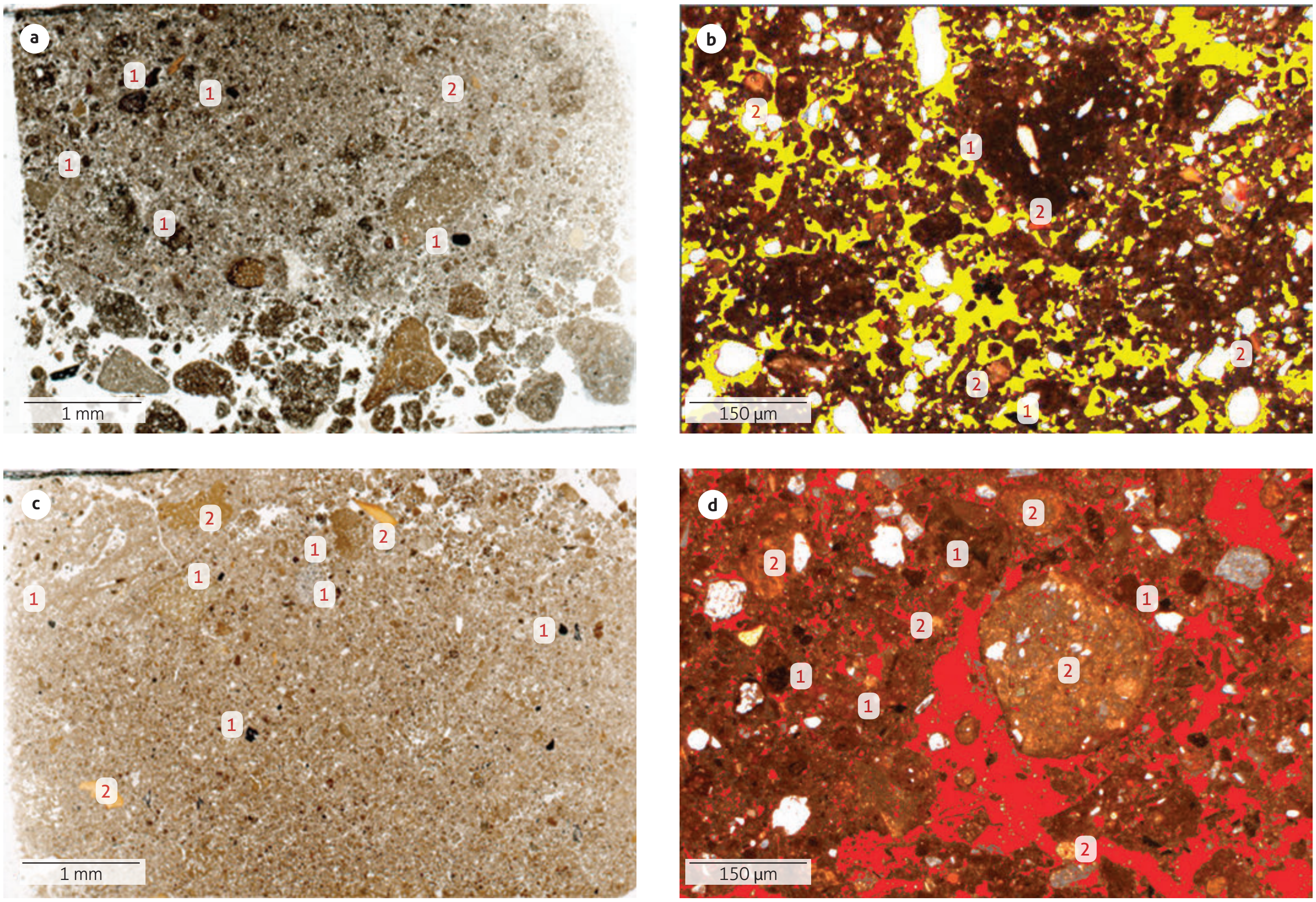

Figure 6. Stratigraphic profile and micromorphological counts at Aguazuque;
a) thin section of stratigraphic level 5.2; b) total coal (1) and bone remains (2) at level 5.2 (Image-Pro Plus); c) thin section of stratigraphic level 2; d) total coal (1) and bone remains (2) at level 2 (Image-Pro Plus)

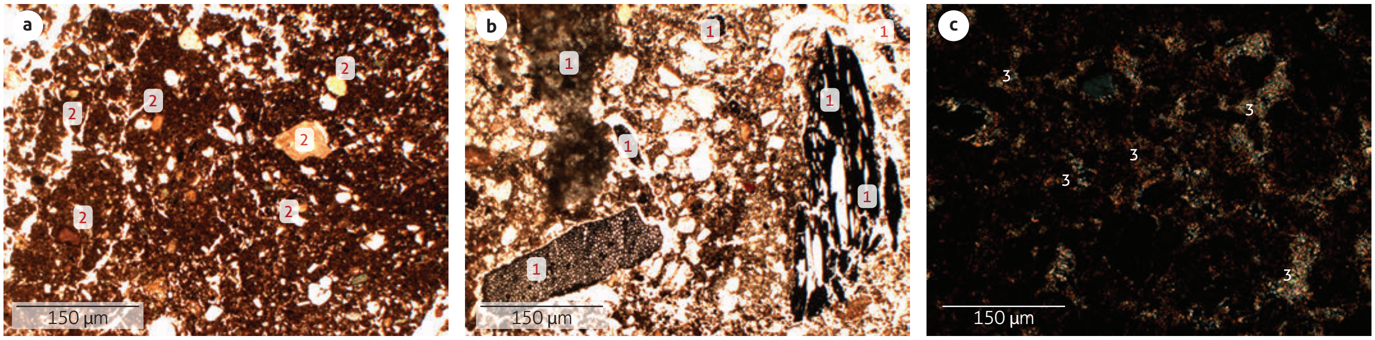

Figure 7. Detailed count by aggregate at Tequendama;
a) topsoil level; total bone remains (2); b) level 7A; total coals (1); c) level 5B, total carbonates (3)

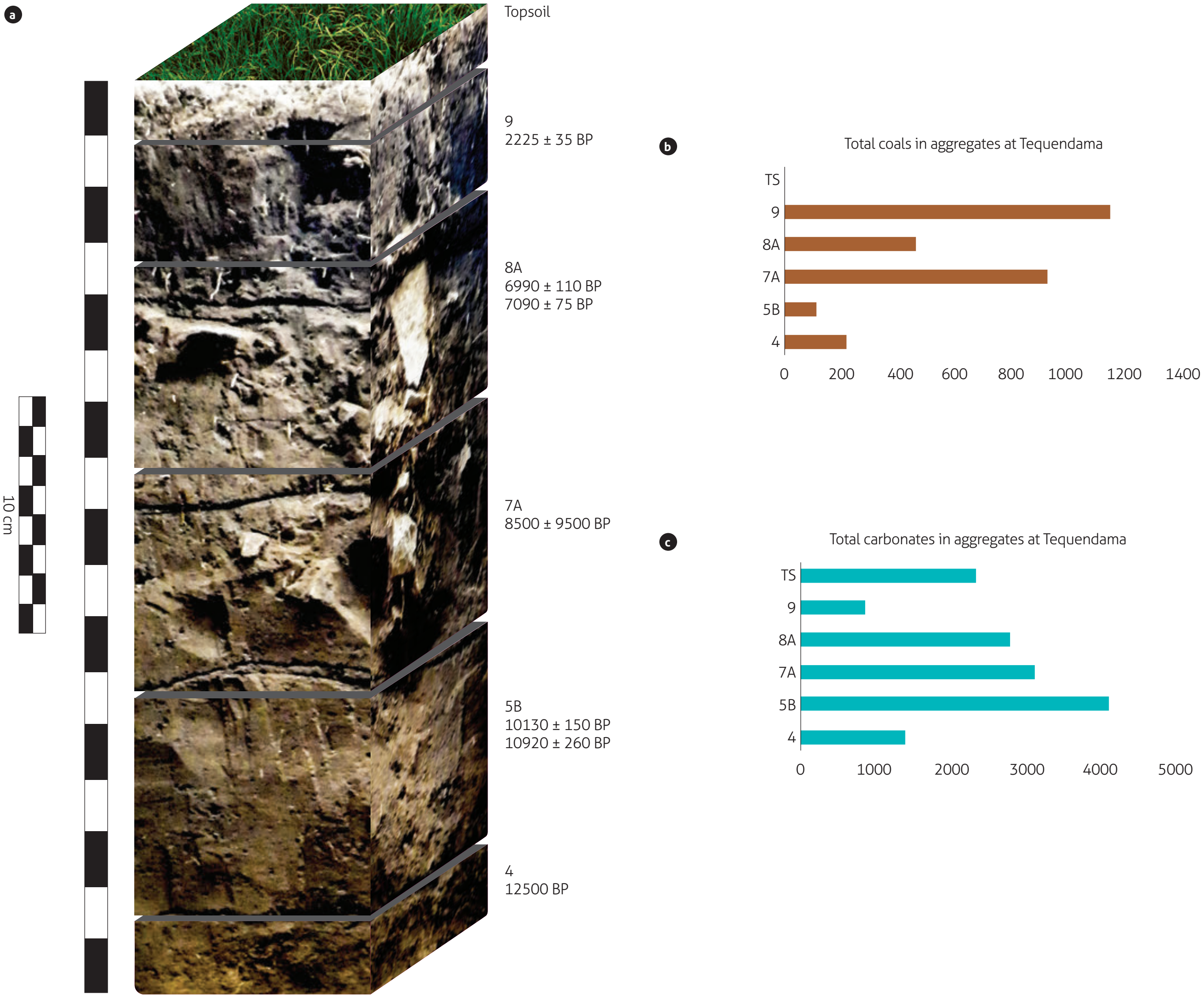

Figure 8. Stratigraphic profile (a) and total aggregate counts at Tequendama with total coals (b) and carbonates (c) by stratigraphic level

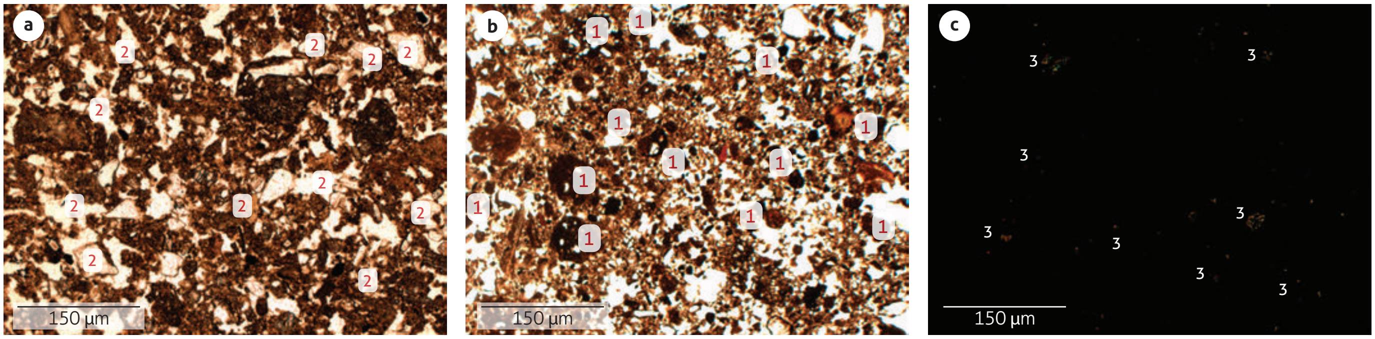

Figure 9. Detailed count in aggregates at Aguazuque
a) level 3, total bone remains (2); b) level 2, total coals (1); c) level 6, total carbonates (3)

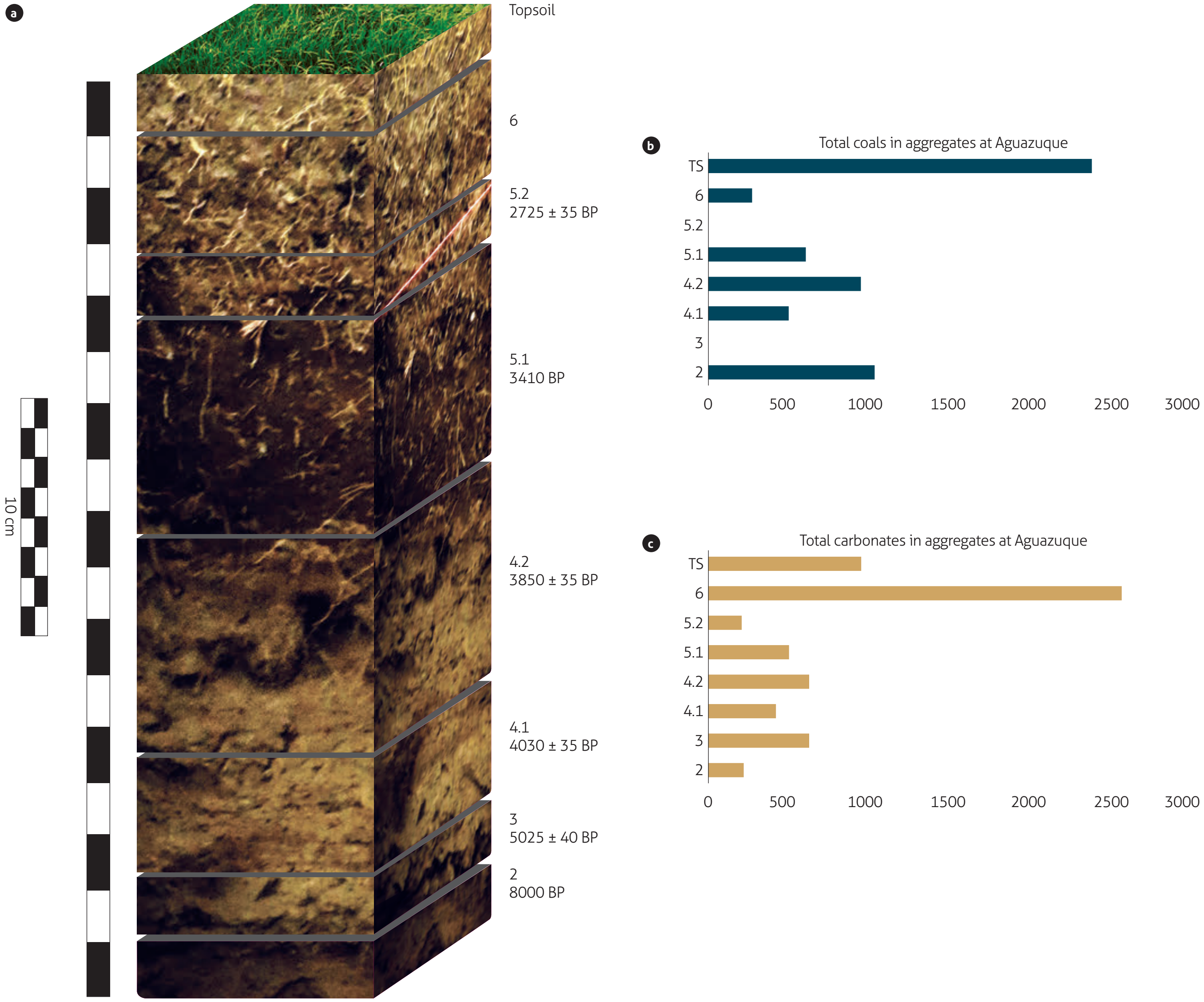

Figure 10. Stratigraphic profile (a) and counts in aggregates at Aguazuque with total coals (b) and carbonates (c) by stratigraphic level

4. DISCUSSION

Activities of the groups that inhabited the Bogotá savanna in the Holocene

The manual counts show that the topsoil and 7A levels of the Tequendama site contain bone remains in abundance. In turn, coals are only identified in level 7A, whereas carbonates are highly prevalent in the topsoil, in level 9 and, to a lesser extent, in level 5B, thus matching the periods of highest human occupation of the site (Correal and Van der Hammen, 1977).

Conversely, at the Aguazuque site, the percentage of bone remains increases and then decreases over the occupation of the site (Correal, 1990; Triana, 2019; Triana et al., 2019; Triana et al., 2020), although it sporadically and considerably increases from approximately 3,800 to 2,500 BP (initial late Holocene). Coals are only evident in the topsoil and in the first level of occupation. Carbonates behave similarly to coals: they are present in the latest levels, such as 6, and in the earliest levels, such as 3, dated at 5,025 BP.

The automatic counts at the Tequendama site show that bone remains are only present in the topsoil. Coals are present in almost all stratigraphic levels, except in the topsoil; however, levels 7A and 9 show high values. Lastly, carbonates increase toward the earliest periods, dated from approximately 6,000 to 10,000 BP (levels 8A, 7A and 5B). The automatic counts at Aguazuque show that bone remains are only present in level 3 (5,025 AP). Coal fragments are present in all stratigraphic levels, but the topsoil has the highest values, followed by level 2, the earliest level of occupation. Carbonates are present in the latest levels, such as level 6.

The results from both counts at the Tequendama site indicate that bone remains are present in the latest levels, such as topsoil; however, general micromorphological counts (Triana et al., 2019) and the frequency of the material during excavation (Triana, 2019) have shown that bone remains are present in all stratigraphic levels, although primarily in levels 9, 8A and 7A (early and middle Holocene), and decrease toward the late Holocene. This indicates that, in late levels, such as topsoil, the frequency of microfragments is high, which can be observed and quantified in both manual and automatic counts. The frequency of bone remains in level 7A is in line with the abundance of bone remains observed during the excavation phase and with micromorphological observations. The above findings support the hypothesis that the highest period of occupation of the Tequendama site is level 7A, with an absolute date of approximately 6,897-7,001 BP (Triana, 2019; Triana et al., 2019; Correal and Van der Hammen, 1977).

The data from the coal counts show a higher presence of microfragments in the automatic counts, and levels 7A and 9 have the highest values. These data indicate that occupation is again identified in level 7A. In addition, level 9 (dated at 2,500 BP) also contains coals, which has not been identified in micromorphological observations or even in manual counts. This level contained a stone floor in that period of occupation, associated with the late Holocene (Correal and Van der Hammen, 1977), as well as ceramic fragments. The body of evidence suggests that some activities were performed during this period in which human groups were possibly developing farming practices; similarly, the presence of coals at this stratigraphic level may be associated with food processing and cooking practices that could have been conducted at the site.

This information can be complemented with reports on changes in the social dynamics of the groups that occupied the Bogotá savanna. More specifically, some authors have argued that the populations were more sedentary, that agriculture markedly outlined a subsistence economy and that the population density would have increased around 2,500 BP. Accordingly, different studies on individuals from this period confirm these hypotheses because they show dietary changes that suggest a dependence on crops, such as maize, and variable percentages in protein intake (Van der Hammen et al., 1990; Cárdenas, 2002; Delgado, 2018; Triana, 2019; Triana et al., 2020).

The manual counts of Tequendama show that carbonates tend to decrease in the latest levels (topsoil and layer 9) and toward the earliest periods. However, level 5B (dated at 10,000 BP) shows an increase in these components. The automatic counts are different because they show a significant increase in carbonates; similarly, the latest levels, such as the topsoil and layer 9, do not show a higher frequency of carbonates; apparently, the frequency of these components increases toward the earliest levels, especially in level 5B, where carbonates peak, which corresponds to the transition from the end of the Pleistocene to the early Holocene. These carbonates are newly formed pedogenic phases, as explained below; as such, they indicate the driest environmental conditions of that period.

Conversely, the peak of carbonates in level 5B at Tequendama matches the presence of lithic artifacts, bone fragments and coals identified in micromorphological observations during the excavation phase. This suggests the presence of human groups in the Bogotá savanna during the transition from the

Pleistocene to the early Holocene, in an environment with conditions very different from those of the late Holocene (Triana et al., 2019; Triana, 2019; Correal and Van der Hammen, 1977; Aceituno et al., 2013; Correal, 1993 and 1981; Correal et al., 2005). The counts of bone remains at the Aguazuque site are consistent with the frequency of archaeological material found during the excavation phase; however, they differ from the automatic counts because bone remains are only identified in level 3 (dated at 5,025 BP; that is, the results show a high presence of previously undetected microfragments.

The occupation of Tequendama lacks data toward the middle Holocene, and the stratigraphic levels with abundant coals at Aguazuque are levels 5.1, 4.2 and 4.1 of this period. These findings suggest that, during the middle Holocene, the social dynamics of the human groups were not limited to hunting and gathering. The archaeological evidence–lithic artifacts such as anvils, hammers, metates and quern stones used for plant processing; dietary changes reported based on different analyses of stable isotopes; burial patterns and diseases of individuals who lived during this period–suggests that the inhabitants of the Bogotá savanna went from hunter-gatherers to potential crop farmers. These data are complemented by the presence of charred plants at Aguazuque from around the same period (Correal 1990; Cárdenas, 2002; Delgado, 2018; Triana et al., 2019, Triana 2019).

Paleoenvironment in the Bogotá savanna based on the counts

An important result is the presence of carbonates at both sites, the morphology of which is related not to primary carbonates, but to secondary carbonates, formed in the soil environment. In the region, the Guadalupe Formation is composed of fossiliferous limestones from the Upper Cretaceous; however, in the thin sections, none of the carbonates match the petrography of a fossiliferous limestone (Figure 11). In turn, the carbonates are related neither to lacustrine calcareous sediments, the morphology of which is linked to bodies of water, with lamellae or nodules with tangentially distributed crystals (Gutiérrez Castorena et al., 1998), nor to coarse textures, such as sand or gravel (which would show an alluvial or colluvial origin), but they are instead micritic carbonates. Micrite and microsparite form nodules or incrustations of plant tissue fragments, which is typical of newly formed pedogenic carbonates (Triana et al., 2019). These carbonates are formed by dissolution and reprecipitation processes when the substrate is calcareous and a primary carbonate source, serving as the basis for the initial dissolution. At Tequendama, the rock shelter is formed by sandstone without carbonates (Triana et al., 2019).

Consequently, the genesis of these carbonate accumulations requires more complex processes: 1) the formation of carbonic acid from CO_2, a product of plant respiration; 2) the formation of soluble bicarbonates $(HCO_3)_2$ from the weathering of primary, calcium-rich minerals, such as plagioclase and amphibole, which were identified in the thin sections (Triana et al., 2019), as well as the dissolution and migration of primary carbonates present in local rocks, and 3) the precipitation of carbonates. This precipitation process is conditioned by the loss of water, as the main mechanism (Rabenhorst et al., 1984); therefore, high ambient temperatures and low levels of rainfall are required because carbonate leaches under humid conditions. Therefore, its presence indicates arid and semiarid conditions (Tanner, 2010). Importantly, no carbonates were identified in the basal layers of the Tequendama section (Triana et al., 2019).

Based on the above, the carbonates present in the thin sections indicate arid conditions starting from the transition from the Pleistocene to the early Holocene (12,500-10,000 BP). This shift represents a notable climate change at the beginning of the Holocene, a period for which cold-humid conditions have been documented, with Subpáramo and forest vegetation (Delgado, 2018; Marchant et al., 2002; Van der Hammen, 1992). Toward the beginning of the early Holocene (10,000 BP) a temperature change is recorded: the environmental conditions became more temperate, in line with the presence of ferruginous nodules and Aristeidae and Gramineae phytoliths, which are

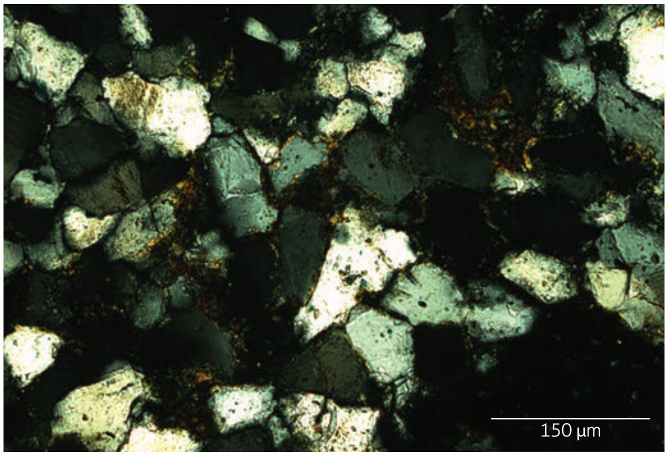

Figure 11. Thin section of rock from the rock shelter of the Tequendama archeological site showing no evidence of carbonates

generally associated with temperate-to-warm environments, in the lower stratigraphic levels of the study sequences (Triana et al., 2019; Triana, 2019). From the initial early Holocene (10,000-7,000 BP), the environmental conditions were warmer and drier and gradually became more arid toward the middle Holocene (Helmens and Van der Hammen, 1994; Torres et al., 2005; Van Geel and Van der Hammen, 1973; Van der Hammen, 1992). Lastly, toward the late Holocene, the climate became more humid on a regional scale. These climatic trends match the presence of carbonates in the study sections.

At the Bogotá savanna, in the middle Holocene, from approximately 8,000 to 6,000 BP, the climate was dry and cold, with dry and open areas and abundant Quercus plants throughout the savanna. From 5,000 to 2,500 BP, the water level of the lakes decreased, and the forest variety increased; species of the genera Quercus, Podocarpus, Urticaceae and Cecropia were identified in this period (Triana et al., 2019; Delgado, 2018; Marchant et al., 2002; Van der Hammen, 1992). The above is confirmed by the pH, electrical conductivity and phytolith values from this period, which corroborate the permanent settlement at the Aguazuque site; similarly, the high concentrations of silica skeleton phytoliths, which were apparently deposited in the soil without being altered and were observed in both the thin sections and the sediments, confirm the constant occupation of the site during these periods (Triana, 2019; Triana et al., 2019; Nicosia and Stoops, 2017).

5. CONCLUSIONS

The data collected during the present study confirm that human groups settled at Tequendama and Aguazuque. At Tequendama, the longest period of occupation spans from approximately 8,500 to 6,000 BP, while that at Aguazuque spans from 4,000 to 2,500 BP. Interestingly, the differences between the manual and automatic counts show the high numbers of anthropogenic components that had not been identified when using qualitative micromorphological techniques. The Image-Pro Plus software more clearly defines the presence of anthropogenic elements that are not visible to the naked eye. These computer techniques enable us to determine features related to early human settlements (transition from the Pleistocene to the early Holocene) in levels such as 5B at Tequendama.

On the one hand, at Aguazuque, low concentrations of bone remains were found during the excavation and qualitative analysis phases (Triana et al., 2019). Those counts were redefined during the present study. Thus, high percentages of bone fragments were detected in level 3 (5,025 BP), thus indicating an intensification of human activities in the middle Holocene. Most likely, this high concentration of bone fragments is related to the processing of faunal resources. On the other hand, variables related to environmental conditions, such as the presence of pedogenic carbonates, can be identified at the microscopic level.

Consequently, quantitative analysis in archeological contexts identifies elements related to human occupation. In the study of the Tequendama and Aguazuque sites, the implementation of this technique highlights the importance of approaching data from different multidisciplinary perspectives by integrating the data and more clearly understanding the contexts of each floor of occupation, as well as the corresponding social and cultural dynamics. The information on the Tequendama and Aguazuque sites has been expanded thanks to quantitative microscopic techniques, which provide very important data on the occupation and environmental changes that may have occurred at these sites.

ACKNOWLEDGMENTS

The present study was made possible thanks to collaboration with Universidad Nacional Autónoma de México, especially the Instituto de Geología, Edaphology Group, Paleosols Laboratory and Lamination Workshop. Support and funding were also provided by the Fundación Nacional de Investigaciones Arqueológicas, the Instituto Colombiano de Antropología e Historia (ICANH), the Fundación CeiBA, which granted a doctoral scholarship, and the Universidad de los Andes. The authors also thank the owners of the Tequendama and Fute haciendas, who endorse and support archaeological research in Colombia.

References

Aceituno, F. J., Loaiza, N., Delgado Burbano, M. E., & Barrientos, G. (2013). The initial human settlement of Northwest South America during the Pleistocene/Holocene transition: Synthesis and perspectives. *Quaternary International*, *301*, 23-33. https://doi.org/10.1016/j.quaint.2012.05.017

Bui, E. N., & Mermut, A. R. (1989). Quantification of soil calcium carbonates by staining and image analysis. *Canadian Journal of Soil Science*, *69*(3), 677-682. https://doi.org/10.4141/cjss89-066

Cárdenas, F. (2002). *Datos sobre la alimentación prehispánica en la sabana de Bogotá, Colombia*. Instituto Colombiano de Antropología e Historia.

Correal, G. (1981). *Evidencias culturales de la fauna pleistocénica en Colombia*. Fundación de Investigaciones Arqueológicas Nacionales, Banco de la Republica.

Correal, G. (1990). *Aguazuque: evidencias de cazadores, recolectores y plantadores en la altiplanicie de la cordillera Oriental*. Fundación de Investigaciones Arqueológicas Nacionales, Banco de la República.

Correal, G. (1993). *Nuevas evidencias culturales pleistocénicas y megafauna en Colombia*. Vol. 8. Fundación de Investigaciones Arqueológicas Nacionales, Banco de la República.

Correal, G., Gutiérrez, J., Calderón, K., & Villada, D. (2005). Evidencias arqueológicas y megafauna extinta en un salado del Tardiglacial superior. *Boletín de Arqueología*, (20), 3-58.

Correal, G., & Van der Hammen, T. (1977). *Investigaciones arqueológicas en los abrigos rocosos del Tequendama: 12.000 años de historia del hombre y su medio ambiente en la altiplanicie de Bogotá*. Fondo de Promoción de la Cultura del Banco Popular.

Courty, M. A., Goldberg, P., & Macphail, R. (1989). *Soils and micromorphology in archaeology*. Cambridge University Press.

Delgado, M. (2018). Stable isotope evidence for dietary and cultural change over the Holocene at the Sabana de Bogotá region, Northern South America. *Archaeological Anthropological Sciences*, (10), 817-832. https://doi.org/10.1007/s12520-016-0403-3

Gutiérrez Castorena, M. C., Gutiérrez Castorena, E. V., González Vargas, T., Ortiz Solorio, C. A., Suástegui Méndez, E., Cajuste Bontemps, L., & Rodríguez Mendoza, M. N. (2018). Thematic micro-maps of soil components using high-resolution spatially referenced mosaics from whole soil thin sections and image analysis. *European Journal of Soil Science*, *69*(2), 217-231. https://doi.org/10.1111/ejss.12506

Gutiérrez Castorena, M. C., Stoops, G., & Ortiz Solorio, C. A. (1998). Carbonato de calcio en los suelos del exlago de Texcoco. *Terra Latinoamericana*, *16*(1), 11-19.

Helmens, K. F., & Van der Hammen, T. (1994). The Pliocene and Quaternary of the high plain of Bogota (Colombia): A history of tectonic uplift, basin development and climatic change. *Quaternary International*, *21*, 41-61. https://doi.org/10.1016/1040-6182(94)90020-5

Julivert, M. (1961). Observaciones del Cuaternario sobre la sabana de Bogotá. *Boletín de Geol*ogía, (7), 5-34.

Loaiza, J. C., Stoops, G., Poch R. M., & Casamitjana, M. (eds.). (2015). *Micromorfología de suelos y técnicas complementarias*. Fondo Editorial Pascual Bravo.

Marchant, R., Behling, H., Berrío, J., Cleef, A., Duivenvoorden, J., Hooghiemstra, H., Kuhry, P., Melief, B., Schreve-Brinkman, E., Van Geel, B., Van der Hammen, T., Van Reenen, G., & Wille, M. (2002). Pollen-based biome reconstructions for Colombia at 3000, 6000, 12000, 15000 and 18000 14C yr ago: Late Quaternary tropical vegetation dynamics. *Journal of Quaternary Science*, *17*(2), 113-129. https://doi.org/10.1002/jqs.669

Nicosia, C., & Stoops, G. (eds.). (2017). *Archaeological soil and sediment micromorphology*. John Wiley & Sons.

Rabenhorst, M. C., Wilding, L. P., & West, L. T. (1984). Identification of pedogenic carbonates using stable carbon isotope. *Soil Science Society of American Journal*, *48*(1), 125-132. https://doi.org/10.2136/sssaj1984.03615995004800010023x

Rosen, A. M. (1989). Ancient town and city sites: A view through the microscope. *American Antiquity*, *54*(3), 564-578. https://doi.org/10.2307/280783

Rosen, A. M. (1991). Microartifacts and the study of ancient societies. *Biblical Archaeologist*, *54*(2), 97-103. https://doi.org/10.2307/3210218

Stoops, G. S., Vepraskas, M. J., & Jongmans, A. G. (eds.). (2003). *Guidelines for analysis and description of soil and regolith thin sections*. Soil Science Society of America.

Skvortsova, E. B., Makeev, A. O., & Kulinskaya, E. V. (2000). Micromorphometry of the pore space of covering and loesslike loams. *Eurasian Soil Science*, *33*(5), 516-522.

Stoops, G. (2009). Seventy years' "Micropedology" 1938-2008: The past and future. *Journal of Mountain Science*, (6), 101-106. https://doi.org/10.1007/s11629-009-1025-3

Tanner, L. H. (2010). Continental carbonates as indicators of paleoclimate. En A. M. Alonso Zarza y L. H. Tanner (eds.), *Carbonates in continental settings: Geochemistry, diagenesis and applications* (pp. 179-214). Vol. 62. Elsevier, Developments in Sedimentology.

Targulian, V. O., & *Goryachkin*, S. V. (2004). Soil *memory*: Types of record, carriers, hierarchy and diversity. *Revista Mexicana de Ciencias Geológicas*, *21*(1), 1-8.

Triana, A. V. (2019). *Dieta y acceso a recursos determinadas a partir del sexo en grupos de cazadores recolectores de la* *sabana de Bogotá durante el Holoceno temprano y medio* (tesis de doctorado). Universidad de los Andes.

Triana Vega, A. V., Casar, I., Morales, P., & Salinas, J. (2020). Análisis de Isótopos estables en restos óseos humanos y de fauna en los sitios arqueológicos del Holoceno temprano y medio, Tequendama y Aguazuque (sabana de Bogotá, Colombia). *Jangwa Pana*, *19*(1), 10-22. https://doi.org/10.21676/16574923.3432

Triana Vega, A. V., Sedov, S., Salinas Acero, J., Carvajal Contreras, D., Moreano, C., Tovar Reyes, M., Solleiro Rebolledo, E., & Díaz Ortega, J. (2019). Environmental reconstruction spanning the transition from hunter/gatherers to early farmers in Colombia: Paleopedological and archaeological indicators from the pre-ceramic sites Tequendama and Aguazuque. *Quaternary International*, *516*, 175-189. https://doi.org/10.1016/j.quaint.2018.09.048

Torres, V., Vandenberghe, J., Hooghiemstra, H., (2005). An environmental reconstruction of the sediment infill of the Bogota basin (Colombia) during the last 3 million years from abiotic and biotic proxies. *Palaeogeography, Palaeoclimatology, Palaeoecology*, *226*(1-2), 127-148. https://doi.org/10.1016/j.palaeo.2005.05.005

Van der Hammen, T. (1992). *Historia, ecología y vegetación*. Corporación Colombiana para la Amazonia.

Van der Hammen, T., Urrego, G., & Klinken, G. (1990). Isótopos estables y dieta del hombre prehistórico en la sabana de Bogotá (un estudio inicial). *Boletín Arqueología FIAN*, *5*(2), 3-10.

Van Geel, B., & Van der Hammen, T. (1973). Upper quaternary vegetational and climatic sequence of the Fuquene area (Eastern Cordillera, Colombia). *Palaeogeography, Palaeoclimatology, Palaeoecology*, *14*(1), 9-55. https://doi.org/10.1016/0031-0182(73)90064-3

Boletín Geológico

SERVICIO
GEOLÓGICO
COLOMBIANO

Boletín Geológico
Editorial Policy

Boletín Geológico is a serial scientific publication of the Servicio Geológico Colombiano (SGC), active since 1953, aiming to promote and disseminate research in the Earth sciences. *Boletín Geológico* publishes original scientific manuscripts of research, reflections, reviews, data and case reports on the Earth sciences, in Spanish or English.

Objective and scope

To disseminate scientific knowledge in the following fields of research:

- Stratigraphy, sedimentology, structure and evolution of basins.
- Geochemistry, geophysics, volcanology, igneous and metamorphic petrology.
- Tectonics, seismotectonic and geodynamic modeling.
- Hydrogeology, oceanography and geothermal energy.
- Economic geology, mineralogy, metallogenesis, hydrocarbon genesis and reservoirs.
- Geomorphology, geological hazards, environmental geology, soil research, climate change and geological heritage.
- Paleontology, paleoclimatology, Quaternary geology and geoarcheology.
- Software applications and artificial intelligence in Earth sciences.

Boletín Geológico may also include compilations, short notes and manuscripts on the state of knowledge and special research on critical and relevant issues.

Articles from authors linked or not linked to the Servicio Geológico Colombiano are accepted.

Periodicity

Annual publication with online publishing in June of each year.

Publishing costs

The contents of the journal are freely available without charge to readers and can be reused after download with proper bibliographic reference.

The journal does not charge authors any fees for sending or receiving their article, for the editorial process, or for publishing. It is completely funded by the Servicio Geológico Colombiano.

Open Access Statement

The content of the journal is protected under a Creative Commons - attribution license. Consequently, the work may be copied, redistributed, remixed, adapted, transformed, and built upon to create new works from the content for any purpose (including commercial purposes). The journal guarantees open access to all published content, users can read, download, copy, distribute,

Archive and preservation

Boletín Geológico uses the LOCKSS system to create a storage system that allows the creation of permanent files for conservation and restoration purposes.

Boletín Geológico

SERVICIO GEOLÓGICO COLOMBIANO

Instructions to Authors

Authorship

The authorship of a postulated article should include those who actively and substantially contributed to the intellectual content and the analysis or interpretation of the data; as such, the authors are publicly responsible for the article submitted. The list and order of the authors should be reviewed before submitting the work the first time for publication. After submitting an article, authorship changes are not accepted.

Transfer of patrimonial copyright to the Servicio Geológico Colombiano

The authors of an article approved for publication transfer patrimonial copyright to the Servicio Geológico Colombiano for its subsequent dissemination, reproduction and distribution in the printed and digital media available to the Servicio Geológico Colombiano, as well as for its inclusion in national or international databases and indexes.

Author requirements

- Understand the editorial policy of the *Boletín Geológico* and the derived processes, and be in agreement with them.
- Include all the people who contributed to the preparation of the manuscript as authors.
- Abide by all ethical guidelines for authors and reviewers.
- In the event that the reviewers of the article/publication suggest the need to make changes or adjustments before their approval, the authors agree to make such adjustments in the time required by the *Boletín Geológico*.

The obligations of the authors are included in the letter of authorship found HERE, or in the corresponding steps when submitting an article. Sending the letter of authorship is an essential requirement for the submission of an article.

1. SUBMISSION CRITERIA

All articles submitted for consideration for publication must meet the following submission criteria:

- Only original and unpublished articles are accepted. The content of the articles must not have been published, totally or partially, in another journal or publication.
- Articles must be sent in Word format by the web page https://revistas.sgc.gov.co/index.php/boletingeo, in the “Submit article” tab.
- The title, in Spanish and English, should be concise and reflect the subject matter.
- The name, the complete institutional affiliation of each author, and the email of the corresponding author must be included.
- The abstract and keywords must be included in both Spanish and English. Images must be attached as individual graphics files, with a minimum resolution of 300 dpi.
- If acknowledgments, acknowledgments to entities, publication permits, etc., are required, they should be included at the end of the text and before the references.
- The text must comply with the references and style requirements indicated in the editorial standards.

2. EDITORIAL GUIDELINES

a. Tables

Tables must be submitted in an editable format, not as images, and they must be accompanied by an explicit legend and source. They must be referenced in the text, and they must be essential to explain or further support the argument of the article.

b. Figures

Figures, such as diagrams, photographs or maps, should be sent in graphics files with a minimum resolution of 300 dpi. Each figure must be cited in the text and be accompanied by an explanatory legend that includes the source.

Images from sources other than the authors of the article must have the permission from the authors of the original image, be free of copyright conflicts or have a Creative Commons license (for further information, please refer to: https://co.creativecommons.org/). Maps, aerial photographs and satellite images should include a graphic scale.

c. Citations

The citation format of *Boletín Geológico* is APA style (Seventh Edition). In the text, citations must include the author's name and date of publication, and all references must be listed in the references section.

When several works by the same author are cited, they must be organized in chronological order and will be shown separated by a comma: (Groat, 2014).

When a reference has two authors, the surnames of both authors must be cited and separated by the conjunction "&": (Pokrovski and Dubessy, 2014) or Pokrovski and Dubessy (2014).

When the reference has three or more authors, only the first author must be cited, followed by the abbreviation "et al.": (Feneyrol et al., 2013) or Feneyrol et al. (2013).

In the case of a corporate author, the name of the organization must be written the first time with the acronym in parentheses, followed by the year; subsequently, only the acronym will be mentioned (Servicio Geológico Colombiano (SGC), 2017).

When citing several references, they must be chronologically sorted and separated by semicolons: (Mantilla et al., 2013; Van der Lelij et al., 2016; Rodríguez et al., 2017). When a specific page of a reference is cited, the page number must be included after the year and be preceded by the abbreviation p., or pp. in the case of several pages: (Groat, 2014, p. 48).

d. Quotes

When the quote is shorter than forty words, it must be written within the paragraph, in quotation marks and without italics. The reference must be included at the end of the quote (Groat, 2014, p. 48).

When the quote is longer than forty words, it must be written in a separate paragraph, with a 2.5-cm left indent, without quotation marks or italics and with a font size one point smaller than the body text. The reference must be included at the end of the quotation (Groat, 2014, p. 48).

e. References

According to the APA format, only the first letter (initial) of the first names of the authors is provided. In the case where two surnames are included, they must not be separated by a hyphen. References must be written in single-space format and with a 1-cm hanging indent (in a hanging indent, the first line of the paragraph is not indented, and all subsequent lines are indented, in this case, 1 cm). If the documents have a Digital Object Identifier (DOI), this identifier must be included at the end of the reference.

Books

Only the first letter (initial) of the first word and of proper names, if any, in the titles of books are capitalized. The titles should be italicized, and the subtitle separated from the title by a colon, not by a period. In Spanish, the first letter of a word following a colon is written in uppercase font; in English, this letter is capitalized.

The information provided must strictly match that included in the following examples and follow the same rules of punctuation between each element of the reference:

Lee, M. S. (2012). *Mass Spectrometry Handbook* (Vol. 1). Wiley.

Bormann, P. (2013). *New Manual of Seismological Observatory Practice 2 (NMSOP-2)*. Deutsches GeoForschungsZentrum. https://doi.org/10.2312/GFZ.NMSOP-2_DS_3.1

Book chapters

Book chapters follow the same rules as those of book titles, except for one difference: the titles of book chapters must not be italicized. The title of the book must be italicized and preceded by the preposition "In".

The information provided must strictly match that included in the following examples and follow the same rules of punctuation between each element of the reference:

Horstwood, M. (2008). Data reduction strategies, uncertainty assessment and resolution of LA–(MC–) ICP–MS isotope data. In P. Sylvester (Ed.), *Laser ablation–ICP–MS in the Earth Sciences: Current practices and outstanding issues*. Mineralogical Association of Canada.

Reimann, C., Birke, M., Demetriades, A., Filzmoser, P., & O'Connor, P. (2014). The gemas project - concept and background. In C. Reimann, A. Demetriades, M. Birke, & I. Schoeters (Eds.). *Chemistry of Europe's Agricultural Soils, Part A*. Bundesanstalt fur Geowissenschaften und Rohstoffe.

Journal articles

Titles of journal articles follow the same rules as those of titles of book chapters, except for one difference: the first letters of all meaningful words (first word, names, verbs and adjectives) of titles of journal articles must be written in uppercase font and italicized, but they must not be preceded by the preposition "In".

The information provided must strictly match that included in the following examples and follow the same rules of punctuation between each element of the reference:

Domeier, M., & Torsvik, T. (2014). Plate tectonics in the late Paleozoic. *Geoscience Frontiers*, *5*(3), 303-350. https://dx.doi.org/10.1016/j.gsf.2014.01.002

Konstantinou, K. (2015). Tornillos modeled as self-oscillations of fluid filling a cavity: application to the 1992-1993 activity at Galeras volcano, Colombia. *Physics of the Earth and Planetary Interiors, 238*, 23-33. https://dx.doi.org/10.1016/j.pepi.2014.10.014

Thesis works

Saylor, J. (2008). *The Late Miocene Through Modern Evolution of the Zhada Basin, South-Western Tibet* (Ph. D. Thesis). The University of Arizona, Tucson.

Conferences, seminars and others

The titles of talks given in these contexts are written without italics, and only the first letter of the first word and proper nouns, if included, are capitalized. All meaningful words in event names are capitalized.

The information provided must strictly match that included in the following example and follow the same rules of punctuation between each element of the reference:

Sulochana, V., Francis, A., & Tickle, A. (2015). Morphology based radon processed neural network for transmission line fault detection. 2015 International Conference on Advances in Computing, Communications and Informatics (ICACCI).

Maps

The information provided must strictly match that included in the following example and follow the same rules of punctuation between each element of the reference:

Bacchin, M., Miligan, P. R., Wynne, P., & Tracey, R. (2008). *Gravity anomaly map of the Australian region, 3rd edn, 1:5,000,000*. Geoscience Australia.

Web pages

EURAQUEM/CITAC. (2016). *Guide to quality in analytical chemistry an aid to accreditation*. Retrieved from www.eurachem.org

Suggested links

- Keywords in the Geosciences: https://www.americangeosciences.org/georef/georef-thesaurus-lists
- Creative Commons: https://co.creativecommons.org/

CONTENTS

SERVICIO
GEOLÓGICO
COLOMBIANO

El futuro
es de todos

Minenergía

ISSN 0120-1425